

Modelling Diffusion: Around Particles and into Plants

A thesis submitted for the degree of

Doctor of Philosophy

in Physical and Theoretical Chemistry

Joseph R Elliott

St. John's College

University of Oxford

Trinity Term 2023

Abstract

This thesis investigates diffusional mass transport about particles on a planar surface through numerical simulation. The results of these simulations are applied to physically significant systems involving particles at electrode and bio-membrane interfaces, with the bio-membrane referring specifically to plant cuticles and foliar uptake across them.

Chapter 1 introduces diffusion as a mass transport process and justifies this thesis' focus upon it. Chapter 1 also introduces the electrochemical concepts that constitute necessary background for the work presented in Chapters 4-6. Chapter 2 introduces plant biology underpinning the models and simulations of agrochemical foliar uptake that are the subject of discussion in Chapters 5 and 6, including leaf structure and function, the epidermal plant cuticle, and practicalities of foliar uptake for plant chemical treatment.

Chapter 3 introduces the numerical methods used in this thesis. The finite difference solution framework is presented, including its explicit and implicit formulations. The problem is linearised to a matrix multiplication. Three solution methods are presented: the Thomas algorithm, the alternating direction implicit method, and fully implicit methods. Dimension reduction, grid construction, and the simulation validation is discussed.

Chapter 4 represents this thesis' first "Results & Discussion" chapter. Simulations results are presented for diffusion at an electroactive particle on a supporting inert planar surface under chronoamperometry. Such simulations are pertinent to particle-modified electrodes and nano-impact electrochemistry. This chapter also serves as an introduction to the sphere-on-a-surface geometry for later chapters.

Chapter 4 introduces the diffusion indicator: a tool for quantifying the linearity/convergence of the diffusion regime behaviour. Total and local flux profiles at the particle surface are

presented and discussed for a range of contact angles. Local diffusional stagnation is a consequence of the geometry and the diffusion indicator is used to characterise it. The simulation results are well-approximated by a mapping we propose to an isolated sphere. We introduce a novel, local variant of the diffusion indicator and discuss its utility. The gradient of the local diffusion indicator is shown to provide additional information about mass transport perpendicular to the electrode surface and general diffusional convergence.

Chapter 5 focusses on foliar uptake across the plant cuticle from a particulate under kinetic chemical release. Significant attention is given to establishing the model for the simulation of the uptake of lipophilic material from particulate. The uptake's dependence on the particle's contact angle, release kinetics, and the relative aqueous and cuticular solubilities and diffusion coefficients are demonstrated, including 4 limiting regimes. A direct and an indirect route are demonstrated for uptake: either via particle-cuticle contact or via dissolution into a surrounding medium. A factor for approximating the relative contributions of these two pathways is presented. A leaching effect, hitherto unrecognised for agrochemicals, is demonstrated. The model is finally compared against other models in the literature.

In Chapter 6, experimental results are presented for the study of foliar uptake into living maize plants of a propriety fungicide. We present data for the transfer of fungicidal material between leaf compartments over 24 hours and images from reflected light and cryogenic scanning-electron microscopy of the leaf surface with analysis. Alongside insights from Chapter 5, we establish a simplest viable model for this system. Dimensionless simulation results are presented and compared with experimental results: validating the model and providing an inference for the cuticular solubility and diffusion coefficient.

Acknowledgements

Completing this DPhil has been the most challenging experience of my life. I have had the honour of working with such talented individuals and enjoyed the love and support of such treasured persons throughout the past 3 years that these words of acknowledgement are insufficient to convey my gratitude.

First and foremost, my most sincere thanks go to my academic supervisor, Professor Richard Guy Compton. Richard has supported me every step of the way from 1st year undergraduate to now. I have the utmost respect for Richard: not only due to his enviable knowledge and keen intelligence, but also due to his dedication to his students and the selfless effort he gives to maximising their success. Richard has been an ideal mentor, and I shall value our time working together with the highest esteem for the rest of my life. He has been an inspiration, without which this project could not have occurred.

No man is an island, and this is especially true in academia. Just as I have given thanks to Professor Compton himself, I am also extraordinarily grateful to the wonderful people that have congregated into his Research Group and who have helped, inspired, and supported me both in their work and also in the environment we cultivated together. I would like to give particular thanks to several outstanding people in my time here. Dr Haotian Chen, I like to think we have leaned on each other mutually to represent the Theoretical sub-group throughout both of our DPhils! Working with you has been a joy, and I am so grateful for the laughs and conversations we shared. Dr Minjun Yang, you have been a role model for me throughout my time at Oxford. I am always impressed by your skill, resilience, and dedication, and I cannot wait to see what fortunes the future will bring to you. Dr Chris Batchelor-McAuley, you have repeatedly taken me under your wing and have taught me so much. It is thanks to you that I was able to start in this group without being entirely

overwhelmed. Your patience and knowledge are inspirations to me, and I aspire to your level of success.

I would like to thank all of my collaborators from Syngenta, who have supported me to branch into unfamiliar biology and helped me to navigate such a project as a previously narrow-minded physical chemist! Dr Colin Brennan, thank you for all of your work as my industrial supervisor, advising on our project direction, and facilitating my development. Dr Federica Cattani, thank you for all of your advice and assistance throughout my DPhil, especially when I was still finding my feet! I would like to thank all of the members of the Bioscience Team at Jealott's Hill Research Centre for welcoming me and supporting the work on which Chapter 6 is dedicated. In particular I would like to thank Joseph Cortvriend and Dr Giovambattista Depietra, without it would not have been possible. Furthermore, I would like to thank Mark Johnston, Faheem Padia, Emily Stratford, Rafael Campos, and Ben Holt for their help and support on this project.

I would like to thank St John's College for providing a home, a sanctuary, and a community in both my undergraduate and postgraduate days.

I would like to thank my friends, close and far, past and present, who have kept me sane throughout this struggle! I am so grateful for the happiness you have each brought into my life.

To my family, I owe everything. Your support and love have made me who I am, every day I am grateful for what you have done for me. It is a debt I cannot repay, and I am endlessly thankful for how you have empowered me and given me the foundation for my life.

Finally, thank you to my darling, Annie Davis. You are the love and light of my life, and I am so thankful that you are a part of it.

Glossary of symbols

Symbol	Meaning
A	Surface area
c_i^j or $[i]^j$	Concentration of species i in medium j
D_i	Diffusion coefficient of species i
$\vec{E}$	Electric field
E	Electrode potential
E^0	Standard electrode potential
E_f^0	Formal electrode potential
F	Faraday constant
I	Dimensional current
I_{ss}	Steady-state current
j_i	Flux of species i
K	Equilibrium constant
K_{cpw}	Cuticle proper-water partition coefficient
K_{cw}	Cuticle-water partition coefficient
K_{ow}	Octanol-water partition coefficient
k_B	Boltzmann constant
k_b	Dimensional first-order rate constant for absorption into a particle surface
k_f	Dimensional zero-order rate constant for release from a particle surface
P_w	Water potential
R	Universal gas constant
r_e	Electrode radius
r_p	Particle radius
t	Dimensional time
T	Temperature
$\vec{v}$	Flow velocity
V	Volume
V_m	Molar volume

z_{cut}	Cuticle membrane thickness
z_i	Charge of species i
z_p	Particle truncation parameter
$\{x, y, z\}$	Cartesian coordinates
$\{r, z, \phi\}$	Cylindrical coordinates
$\{\rho, \theta, \phi\}$	Spherical coordinates
$\{x_{max}, r_{max}, z_{max}\}$	Length of a simulation space in x-, r-, or z-directions
α	Diffusion indicator
α_{local}	Local diffusion indicator
γ_i	Activity coefficient of species i
δ_l	Diffusion layer thickness
θ_c	Contact angle
μ_i	Chemical potential of species i
ϕ	Electric potential
ω	Expansion/contraction factor

General summary of dimensionless conversions

Dimensional Parameter	Dimensionless Transformation
Spatial coordinate, x	$X = x / x_{ref}$
Diffusion coefficient, D	$d = D / D_{ref}$
Concentration, c	$C = c / c_{ref}$
Time, t	$T = D_{ref} \cdot t / x_{ref}^2$
Local flux, j	$J = (j \cdot x_{ref}) / (c_{ref} \cdot D_{ref})$
Mass, m	$M = m / (c_{ref} \cdot x_{ref}^3)$
Zero-order surface rate constant, k_0	$K_0 = (k_0 \cdot x_{ref}) / (c_{ref} \cdot D_{ref})$
First-order surface rate constant, k_1	$K_1 = (k_1 \cdot x_{ref}) / D_{ref}$

Table of contents

Abstract ..... **i**

Acknowledgements ..... **iii**

Glossary of symbols ..... **v**

Table of Contents ..... **vii**

Chapter 1 Mass transport at interfaces **1**

1.1 Types of mass transport 1

1.2 Diffusion 4

1.2.1 Fick's Laws 4

1.2.2 Diffusional displacement 5

1.3 Fundamentals of electrochemistry 7

1.3.1 Electrochemistry at equilibrium 8

1.3.2 Electrochemical cell 10

1.3.3 Electrochemical methods 12

1.3.4 Electrode geometries 14

References 23

Chapter 2 Introduction to foliar uptake **26**

2.1 The plant leaf 26

2.1.1 Functions 27

2.1.2 Structures 30

2.2 The cuticle 36

2.2.1 Function 36

2.2.2 Chemistry 37

2.2.3 Cuticle ultrastructure 38

2.3 Pathways for transcuticular transport 41

2.3.1 Lipophilic pathway 42

2.3.2 Hydrophilic pathway 44

2.3.3 Stomatal uptake 46

2.4 Foliar uptake as an agricultural practice 47

2.4.1 Purpose of chemical treatment via foliar uptake 48

2.4.2 Agrochemical properties 50

2.4.3 Additional barriers 52

2.4.4 Formulation design 53

2.4.5 Drive towards sustainability....56
References....57
Chapter 3 Modelling diffusion....61
3.1 Model construction....61
3.1.1 Fick's Second Law as a PDE for describing mass transport....62
3.1.2 Boundary conditions....64
3.1.3 Normalisation....66
3.2 Solving the PDE....68
3.2.1 Finite difference....68
3.2.2 Spatial & temporal derivatives....69
3.2.3 Explicit versus implicit solution....71
3.2.4 Thomas algorithm....73
3.2.5 Alternating Direction Implicit method (ADI)....75
3.2.6 Fully implicit methods....77
3.3 Dimensionality & co-ordinate systems....79
3.4 Grid construction....81
3.5 Convergence, validation & testing....83
References....84
Chapter 4 Diffusion at a particle on a surface....86
4.1 Introduction....86
4.2 Theory....89
4.2.1 The diffusion indicator....93
4.3 Results for hemisphere and full-sphere-on-a-surface....94
4.3.1 Model validation....95
4.3.2 Modified-sphere equation....96
4.3.3 Applying the diffusion indicator....98
4.4.4 Local effects....99
4.4 Results for a spherical cap....103
4.4.1 Generalising the modified-sphere equation....103
4.4.2 Reducing the contact angle: $\pi/2<\theta_c\leq\pi$....104
4.4.3 Reducing the contact angle: $0<\theta_c<\pi/2$....106
4.5 Conclusions....114
References....115

Chapter 5 Foliar uptake: single-particle simulations.....119
5.1 Introduction.....120
5.2 Theory.....123
5.3 Modelling release from the particle into the aqueous phase.....135
5.4 Modelling direct uptake with perfect sink.....141
5.5 Modelling competing uptake pathways.....149
5.5.1 Comparing release rates into aqueous and cuticular phases for typical pesticides.....149
5.5.2 Model of the indirect pathway.....152
5.5.3 Competing direct and indirect pathways.....153
5.6 Additional insights.....155
5.6.1 The G-factor.....155
5.6.2 Considering evaporation times.....156
5.7 Comparison with other models.....158
5.8 Conclusions.....159
References.....161
Chapter 6 Foliar uptake: experiment and modelling.....166
6.1 Introduction.....166
6.2 Experimental methods.....168
6.2.1 Uptake study.....168
6.2.2 Microscopy.....170
6.3 Experimental results.....171
6.3.1 Characterisation of leaf surface by microscopy.....171
6.3.2 Droplet evaporation.....174
6.3.3 Characterisation of deposit by microscopy.....175
6.3.4 Uptake data & analysis.....181
6.4 Theory.....186
6.5 Simulation results.....196
6.6 Model application to experimental data.....200
6.7 Conclusions.....202
References.....203

1 Mass transport at interfaces

This chapter provides an overview of concepts and theories critical to the study of mass transport and, more specifically, diffusion, the focus of this thesis. This chapter also introduces fundamental aspects of electrochemistry and electroanalytical theory, the historical study of which has provided critical insights to mass transport behaviours at interfaces through the utility of analysing Faradaic currents at electrode surfaces, discussed further in Section 1.3. The concepts introduced in this Chapter are foundational background information for each following chapter in this thesis and are well-developed in several seminal textbooks[1, 2].

1.1 Types of mass transport

There are three processes that are generally considered to characterise the net movement of dissolved species in a condensed phase: diffusion, advection, and migration. Diffusion is the movement of material down a concentration gradient driven by Brownian motion, advection is movement of the dissolved species induced by bulk motion of the fluid (an example of which is the motion induced by a density gradient), and migration is movement induced by an electric field if the transported material is charged.

A schematic illustration of the three processes acting in a system is provided in Figure 1.1. Two components (orange and red) are presented as dissolved in a blue solvent, which is illustrated as a continuum. A positively charged surface is shown in grey. We see that there is a concentration gradient for the orange particles (their concentration decreases as one approaches the surface). This concentration gradient induces a net flux of orange particles towards the surface by diffusion since the Brownian motion of the particles will result in more particles moving down the concentration gradient than up it, simply as a result of there

being more particles moving stochastically at higher concentrations and so more particles moving left than right at any given cross-section.

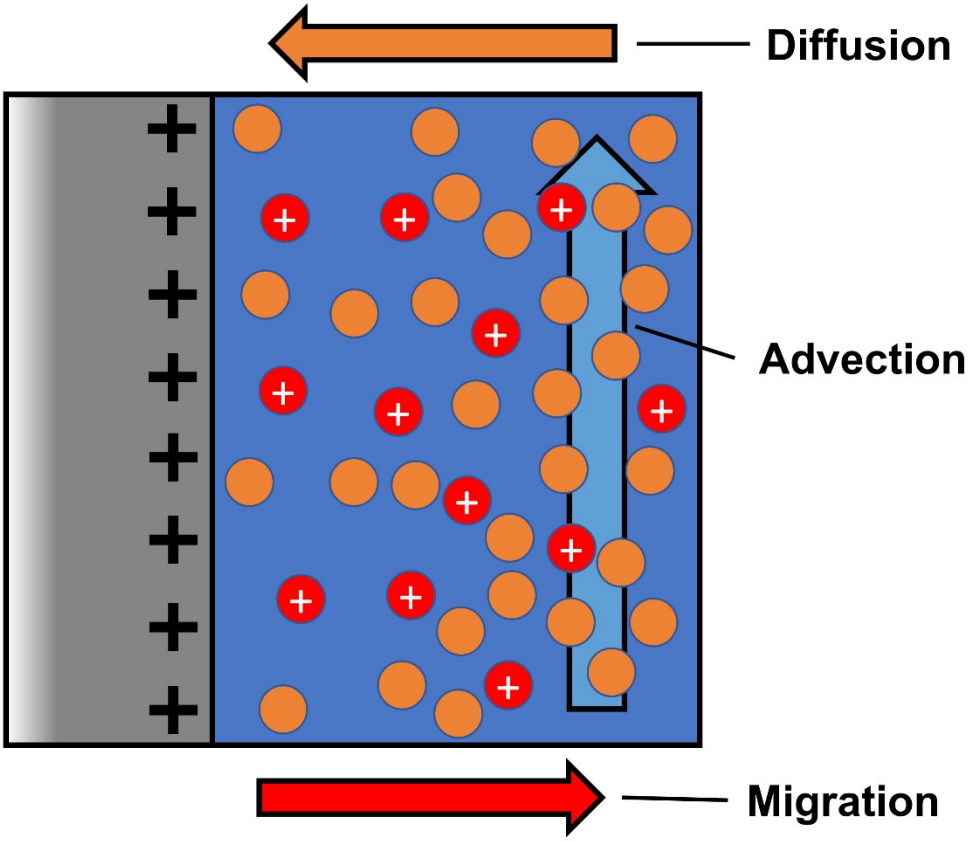


Figure 1.1: The mass transport processes of diffusion, migration, and advection illustrated schematically. Two components (uncharged species in orange and positively charged species in red) are dissolved in blue a solution phase (demonstrated here as a continuum) adjacent to a positively charged surface (grey). A flow of solvent perpendicular to the surface is represented by a light blue arrow. The net movement of orange particles by diffusion is represented by an orange arrow and the net movement of red particles by migration from the charged surface is represented by a red arrow.

The red species do not have a concentration gradient. However, the red particles are said to be positively charged: as such they experience a Coulombic repulsion from the similarly charged surface according to the external potential gradient they experience. This shall induce a net movement of red particles away from the electrode. Later, this shall be counteracted by consequent diffusion down the induced concentration gradient until a steady-state is achieved (assuming the conditions are held constant). This is an example of migration induced by simple electrostatics, however more complex migration effects induced by an electric field are possible.

Close to the surface we have approximated the blue solvent as stationary. This approximation is viable for cases where the solvent-surface friction is suitably high to prevent bulk movement of solvent at the interface and the solvent viscosity is suitably high to propagate that reduction in flow away from the surface. However, at a sufficient distance from a surface, it is likely that the solvent phase will move in bulk with a particular flow velocity. The flow of the bulk phase shall induce a corresponding flow of material dissolved in it. In Figure 1.1 this bulk flow is represented by a blue arrow perpendicular to the surface, which will induce a corresponding movement of red and orange particles perpendicular to the surface. This induced net movement by the bulk flow of the surrounding medium is advection. While migration is a response to a force on the species themselves, advection is a bulk response of all species to a net force. This net force corresponds to a pressure gradient in the medium: examples of what might cause this are gradients in surface tension, density, or temperature. Advection may be induced deliberately, such as in a flow system[3]. Some natural flow velocity in the bulk phase is practically unavoidable, although efforts to mitigate it during electrochemical experiments are described in Section 1.3.

The Nernst-Planck equation describes the net mass transfer arising from these processes acting in tandem through the conservation of mass. The flux vector $\vec{j}$ is given as:

$$\vec{j} = -D\nabla c + c\vec{v} + \frac{Dze}{k_B T} c\vec{E} \qquad \text{Equation 1.1}$$

where D is the diffusion coefficient, c is the concentration, $\vec{v}$ is the flow velocity of the bulk fluid, z is the valence of the ionic species, e is the elementary charge, k_B is the Boltzmann constant, T is the temperature, and $\vec{E}$ is the electric field. The Nernst-Planck equation refers to the evolution of the concentration with time t, given as:

$$\frac{\partial c}{\partial t} = -\nabla \circ \cdot \vec{j}$$ Equation 1.2

Convection typically refers to mass or heat transfer that involves simultaneous advective and diffusive processes. One example of this is Marangoni flow in evaporating droplets induced by temperature gradients arising from endothermic evaporation at the liquid-air interface[4]. Another example is capillary flow induced by contact line pinning during droplet evaporation, which drives the deposition of insoluble material as a ring[5]. These shall be discussed further in Chapter 6.

1.2 Diffusion

In this thesis, we focus on cases where the advection and migration terms are negligible and thus cases where the action of diffusion is dominant. This simplifies the problem and is commonly sought after in experiment to ease analysis, motivating complementary computational analysis.

In typical electrochemical experiments, advection is minimised by temperature control, vibration damping, and Faraday cages. Furthermore, the experimental timescale is typically short enough for mass transport to only occur close to the electrode surface and thus be weakly influenced by natural convection. Similarly, migration is minimised by ensuring that the fluid is well-supported by inert ions that screen potentials arising from electron transfer at the electrode. These practises are discussed further in Section 1.3. Discussion with respect to advection and migration effects in the modelling of mass transport in the context of biological media, specifically foliar uptake, is given in Chapter 2 .

1.2.1 Fick's Laws

The Nernst-Planck equation (given in Equation 1.1) is in truth an extension of the earlier derived Fick's Laws[6]. These are recovered when the advection and migration terms are set to

zero (for example by assuming zero fluid velocity and an uncharged species). Fick's First Law is:

$$\vec{j} = -D \nabla c \qquad \text{Equation 1.3}$$

while Fick's Second Law is:

$$\frac{\partial c}{\partial t} = D \nabla^2 c = D \left\{ \frac{\partial^2 c}{\partial x^2} + \frac{\partial^2 c}{\partial y^2} + \frac{\partial^2 c}{\partial z^2} \right\} \qquad \text{Equation 1.4}$$

The solutions to Fick's Second Law give the concentration profiles $c(x, y, z, t)$ predicted by diffusion, with unique solutions for different boundary conditions. Numerous analytical results have been derived using various mathematical approaches including the method of reflection and superposition, the method of separation of variables, and the method of Laplace transform. The seminal work by Crank[7] is suggested as an overview of the principal solution cases and traditional solution techniques. However, for more complex boundary conditions and interfacial geometries (some of which shall be introduced in Section 1.3.4), deriving analytical results is currently not possible. Today, great academic focus is instead given to numerical solutions for the simulation of diffusion behaviours in environments of interest and this is the primary work of this thesis. Techniques used for simulating diffusion at interfaces by computation are described in Chapter 3.

1.2.2 Diffusional displacement

Diffusion is a macroscopic observation, resulting from the underlying Brownian motion of molecules, whereby concentration gradients induce a corresponding net movement of material (Equation 1.3). If one considers the expected distance that a particle or molecule shall diffuse over a given period of time, one shall have an approximate measure of the distance to which diffusion shall propagate a response to a local perturbation in the concentration field. The problem of predicting the expected displacement of a particle under

Brownian motion with time was considered by Einstein in 1905[8] and the following relationship was derived for the expected root-mean-square displacement:

$$\sqrt{\langle r^2 \rangle} = \sqrt{\xi D t} \qquad \text{Equation 1.5}$$

where $\xi = 2n$, where n is the dimensionality of the space considered, and r is the displacement of the particle in the n-dimensional space. Note that since the Brownian motion is stochastic with respect to direction: $\langle r \rangle = 0$.

The expression in Equation 1.5 can be used to estimate the thickness δ_l of the "diffusion layer", a volume within which the concentration has been perturbed from a bulk value by an action starting at $t = 0$ due to dominant diffusion. It predicts $\delta_l \propto \sqrt{t}$. However, this only considers a root-mean-squared of a distribution and so is typically an underestimate.

An alternative estimate for the thickness of a diffusion layer is the Nernst diffusion layer. This is defined as the intersection between the bulk concentration value and the tangent of the concentration profile at the origin of perturbation. While in most cases this is unrealistic (the concentration profile is rarely linear between two constant values, requiring two perfect Dirichlet boundaries, as shall be described in Section 1.4), it provides an easy estimate within an order of magnitude. For the case of one-dimensional diffusion to a surface, $\delta_l = \sqrt{\pi D t}$ is predicted[9], similar to the $\delta_l = \sqrt{2\,Dt}$ prediction above.

A plot of a concentration profile for diffusion in one dimension, x, between a bulk solution at concentration c_{bulk} and an instantaneously equilibrated interface at zero concentration is given in Figure 1.2. The black line indicates the concentration profile, the blue dotted lines indicate the means of calculating the Nernst diffusion layer thickness δ_{Nernst}, and the positions of the Nernst diffusion layer and $\sqrt{\langle x^2 \rangle} = \delta_{rms}$ are indicated on the x-axis. The concentration profile is

derived from the Cottrell Equation, described in Section 1.3.4. The distance at which the bulk condition is applied as a limiting boundary to semi-infinite solution simulations presented in this thesis is $6\sqrt{Dt}$ and this is also indicated; this application of a bulk condition at this distance is discussed further in Chapter 3.

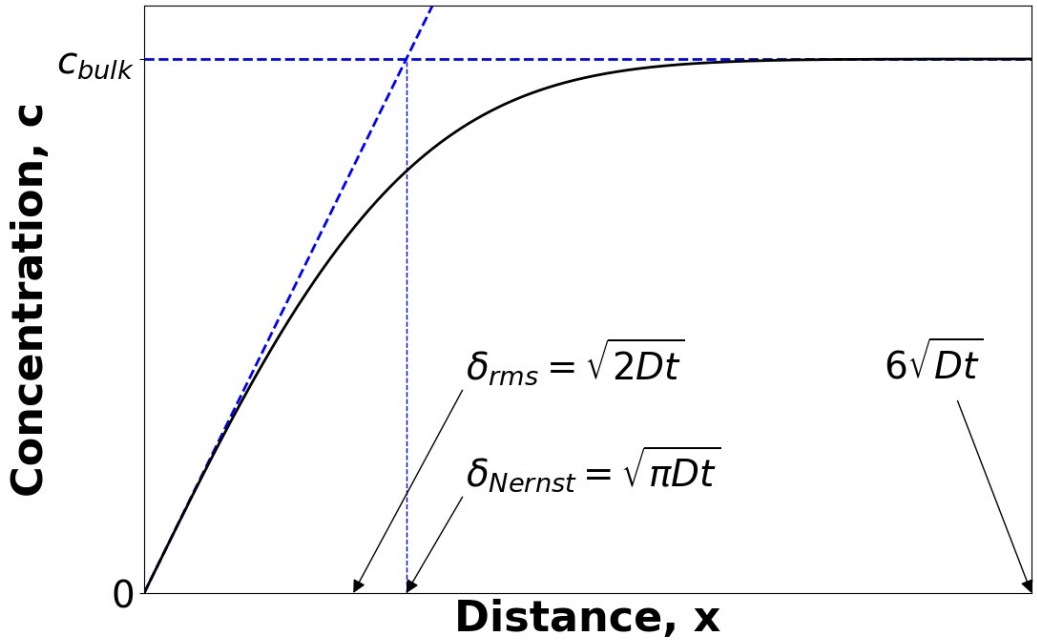


Figure 1.2: Illustration of a one-dimensional concentration profile $c(x)$ as a black solid line at an arbitrary time t after a diffusion-limited reaction occurs at an interface at $x=0$ and beginning at $t=0$. The diffusion layer thicknesses predicted by the root-mean-squared displacement of a particle under Brownian motion δ_{rms} and by the Nernst diffusion layer δ_{Nernst} are indicated. The distance at which a bulk condition is often applied in simulations, $6\sqrt{Dt}$, is also indicated. The blue dotted lines indicate where the bulk concentration value c_{bulk} and concentration profile tangent at $x=0$ intersect.

Knowledge of the thickness of the diffusion layer at a given time is useful for considering the distance from an action at a surface at which the concentration profile is impacted by diffusion. This is impactful for the field of electrochemistry, which shall be introduced in Section 1.3, since this plays a vital role in analysing the currents induced by an electrochemical reaction at an electrode surface. The diffusion layer is also significant for justifying the diffusion behaviour at different timescales for particular system geometries. This shall be discussed further in Section 1.4.

1.3 Fundamentals of electrochemistry

We next turn to considering the fundamentals of electrochemistry. This field is acutely associated with the simulation of interfacial mass transport due to the importance of understanding electron transfers at an electrode surface. Results presented in this thesis directly contribute to this field (see Chapter 4) and electrochemical insights and theory are applied in Chapters 5 & 6. Herein, we establish some relevant underlying theoretical principles of this discipline.

1.3.1 Electrochemistry at equilibrium

The essential process to which electrochemists dedicate their study is the movement of charge at the metal-electrolyte interface, particularly when this induces measurable currents. The mechanisms by which this commonly occurs can be divided into Faradaic and non-Faradaic categories, as described by David Grahame[10]. Faradaic processes involve the reduction or oxidation of chemical material through the transfer of electrons across the interface. Non-Faradaic processes do not involve the transfer of charged particles across the interface but instead involve the accumulation of charge at the interface, for example through the charging and discharging of the electric double layer at the electrode interface or through adsorption/desorption processes. Faradaic processes are intrinsically dependent on the net movement of chemical species from or to a bulk phase and so it is to these that we restrict the scope of this thesis.

We thus consider the following electron transfer reaction between molecules in solution phase and a solid electrode:

$$A^{z}(aq) + n\,e^{-} \rightleftharpoons B^{z-n}(aq) \qquad \text{Equation 1.6}$$

where z is the charge of species A and n is the number of electrons transferred from the electrode. We can consider such a reaction at equilibrium such that the stoichiometric sums

of the chemical potentials μ_j of the reactants and products are equal. The electrochemical potential $\overline{\mu_j}$ was introduced by Butler[11] and Guggenheim[12, 13] to differentiate a conception of the chemical potential from its electrostatic contributions for a species of charge z in a medium α, whose potential is represented as $\phi(\alpha)$:

$$\overline{\mu_j}(\alpha) = \mu_j(\alpha) + z_j F \phi(\alpha) \qquad \text{Equation 1.7}$$

while the chemical potential independent of electrostatics is expressed as:

$$\mu_j(\alpha) = (\mu_j(\alpha))^{\ominus} + R T \ln(\gamma_j c_j) \qquad \text{Equation 1.8}$$

where $(\mu_j(\alpha))^{\ominus}$ is the standard chemical potential of species j, c_j is the concentration of species j, and γ_j is the activity coefficient of species j accounting for deviation from non-ideality in solution.

If we now consider the balanced sum of chemical potentials,

$$(\mu_A(aq) + zF\phi(aq)) + n¿ \qquad \text{Equation 1.9}$$
$$¿(\mu_B(aq) + (z-n)F\phi(aq))$$

where $\phi(aq)$ and $\phi(el)$ are the electric potentials experienced by species in solution and species in the electrode respectively (where *el* refers to the electrode). This simplifies to

$$\phi(el) - \phi(aq) = \mu_A(aq) + n\frac{\mu_{e^{-¿}(el)} - \mu_B(aq)}{nF}¿ \qquad \text{Equation 1.10}$$

Substituting in Equation 1.8 gives

$$\phi(el) - \phi(aq) = \frac{\Delta\mu^{\ominus}}{nF} + \frac{RT}{nF}\ln\left(\frac{\gamma_A c_A}{\gamma_B c_B}\right) \qquad \text{Equation 1.11}$$

where $\Delta\mu^{\ominus} = (\mu_A(aq))^{\ominus} + n¿¿$. In practise, the value of $\phi(el) - \phi(aq)$, known as the electrode potential, at an electrode-solution interface is not measurable. However, by introducing a

second electrode-solution interface and thus completing a circuit through the solution medium, we can consider the difference in electrode potentials. If the second electrode potential is chosen to correspond to a reference electrode whose electrode potential is held constant (typically by passing a minimal current through it to maintain constancy of composition and/or by maintaining a saturated environment local to the electrode surface) then we can calculate the electrode potential *relative* to the reference chosen, E:

$$E = (\phi(el) - \phi(aq)) - (\phi(el) - \phi(aq))_{ref} \quad \text{Equation 1.12}$$

$$\text{¿}\ \frac{\Delta\mu^{\ominus}}{nF} + \frac{RT}{nF}\ln\left(\frac{\gamma_A c_A}{\gamma_B c_B}\right) + c$$

where the c term arises from the constant chemical potentials involved with the reference electrode. Typical reference electrodes[14] include the standard hydrogen electrode (SHE), the saturated calomel electrode (SCE), and the silver/silver chloride electrode. Therefore, since

$E = (\phi(el) - \phi(aq)) - (\phi(el) - \phi(aq))_{ref}$ and $E^0 = \frac{\Delta\mu^{\ominus}}{nF} + c$ is the standard electrode potential:

$$E = E^0 + \frac{RT}{nF}\ln\left(\frac{\gamma_A}{\gamma_B}\right) + \frac{RT}{nF}\ln\left(\frac{c_A}{c_B}\right) \quad \text{Equation 1.13}$$

$$\text{¿}\ E_f^0 + \frac{RT}{nF}\ln\left(\frac{c_A}{c_B}\right)$$

where $E_f^0 = E^0 + \frac{RT}{nF}\ln\left(\frac{\gamma_A}{\gamma_B}\right)$ is the formal electrode potential, introduced to allow simpler measurements without requiring knowledge of the activity coefficients. This equation is the well-known Nernst equation[15, 16] which describes the thermodynamics of electron transfer.

1.3.2 Electrochemical cell

While at least two electrodes are required to form a circuit through an electrolytic phase, which is necessary for electrochemical experiments, a three-electrode cell is much preferred

for precise measurements. These three electrodes consist of the working electrode, the reference electrode, and the counter electrode. Figure 1.3 provides a schematic illustration of such a cell.

The working electrode is the interface at which the reaction of interest occurs. The reference electrode has been described above. It is desirable for it to maintain a constant electrode potential against which we can measure the relative electrode potential at the working electrode, while minimising the current that passes through the reference electrode. This helps to maintain constancy of composition and thus a constant reference electrode potential, while also minimising the influence of the *IR* ohmic drop in potential induced by the resistivity of the intervening electrolyte.

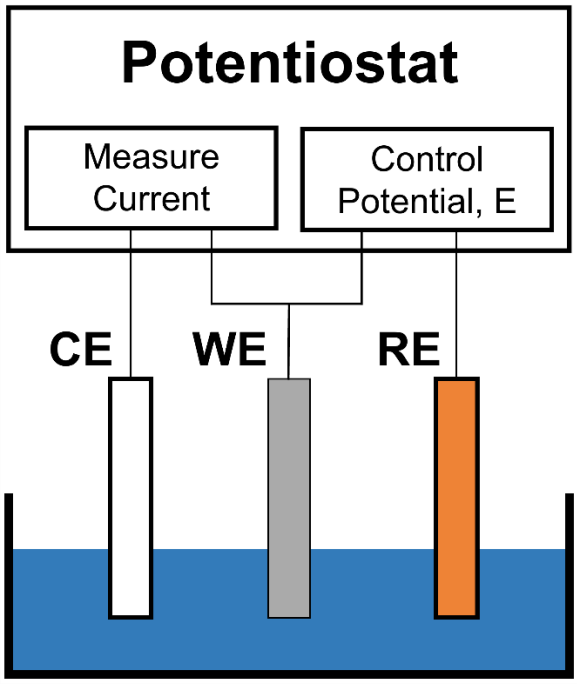


Figure 1.3: Schematic illustration of a three-electrode electrochemical cell. The electrodes from left to right are: the counter electrode (CE), the working electrode (WE), and the reference electrode (RE). The potentiostat and its functionality relative to the electrodes is demonstrated. The electrodes are illustrated as submerged in a thermostatted bath of electrolyte.

To provide control over the flow of current, and thus minimise its flow through the reference electrode, the counter electrode is introduced. The potential maintained at this electrode is chosen to balance the flow of current through the electrolyte from the working electrode such

that minimal current flows through the reference electrode while still allowing a measurement of the difference in potential between the reference and working electrodes. The material and shape of the counter electrode is usually irrelevant so long as it is chemically inert and supports a kinetically rapid electron transfer on its surface. Platinum and graphite are typical counter electrode materials.

The three-electrode system is typically managed by a computer-controlled potentiostat. The potentiostat allows the user to control the potential difference applied between the working and reference electrodes while measuring the current that passes through the working and counter electrodes (amperometry) or vice versa (potentiometry).

Typically, the electrolyte shall have a high ionic strength in order to minimise the influence of migration on mass transport at the working electrode. The compression of the electric double layer to distances compatible with electron transfer by tunnelling ensures that migration does not affect the mass transport to or from the working electrode. A medium that is well-supported by ionic electrolyte will also exhibit a reduced uncompensated resistance, and thus a smaller *IR* ohmic drop in potential between the working and reference electrodes.

Furthermore, the timescale of the experiment is typically chosen to maintain a diffusion layer ($\sqrt{\pi Dt}$) of less than 100 μm, as it has been observed that advection effects become significant at such a distance from a static surface in aqueous solution. At smaller distances from a rigid, non-porous surface, friction forces reduce natural flow velocity, so-called ‘natural convection’ which is induced by temperature inhomogeneity and/or evaporation at room temperature, to negligibility such that diffusion is the dominant mass transport process close to the electrode surface. Temperature control, vibration damping, and the use of a Faraday cage also help to mitigate natural flow.

1.3.3 Electrochemical methods

As mentioned above, two categories of electrochemical analysis are amperometry (controlled potential difference and measured current) and potentiometry (controlled current, including zero current, and measured potential difference). A typical potentiometric technique involves maintaining a negligibly small current through a circuit involving two electrodes connected by an electrolyte and measuring the potential difference between the two electrodes. This experiment provides a very powerful tool for probing the thermodynamics of electrochemical reactions, since, by maintaining a zero current, equilibrium is reached at both the working and reference electrodes, allowing the accurate measurement of the potential difference induced by the chemical reaction(s) of interest according to the Nernst equation (derived above). Potentiometry remains a commonly used tool for electroanalysis[17], for example in pH sensors[18] and ion-selective electrodes (ISEs)[19].

However, a significant body of modern academic work applies amperometric techniques instead since these experiments typically provide both thermodynamic and kinetic information. This is possible thanks to the work conducted to overcome the greater practical challenge and the analytical difficulties associated with interpreting the more data-rich results. Amperometric techniques allow observations to be made of the mass transport, typically the diffusion, at the electrode surface, and are thus the focus of our electrochemical considerations moving forward.

Within the field of amperometry we can distinguish two broad subclasses in typical use: chronoamperometry and voltammetry. Chronoamperometry involves applying discrete steps in potential to the cell and observing the resulting decay in current with time. Voltammetry involves a continuous change in potential with time and observing the associated variation in the current. The nature of a voltametric experiment is usually characterised by the potential-

time waveform employed. Linear sweep voltammetry is the default, while more exotic waveshapes are also used, such as square-wave[20, 21] and semi-circular[22] voltammetry. The potential-time waveforms and expected current-time transients for chronoamperometry and linear sweep voltammetry are illustrated in Figure 1.4.

Since the focus of this thesis is on the mass transport behaviours, chronoamperometric results and theory are of principal concern, since a chronoamperometric step can be chosen to overpotentials that provide an electrochemical driving force that overwhelms any potential electrode kinetics and thus the current decay with time becomes entirely a function of the mass transport. While voltametric techniques capture the mass transport and electrode kinetics, the resulting analysis and simulation are more complex and so this is outside the scope of this thesis.

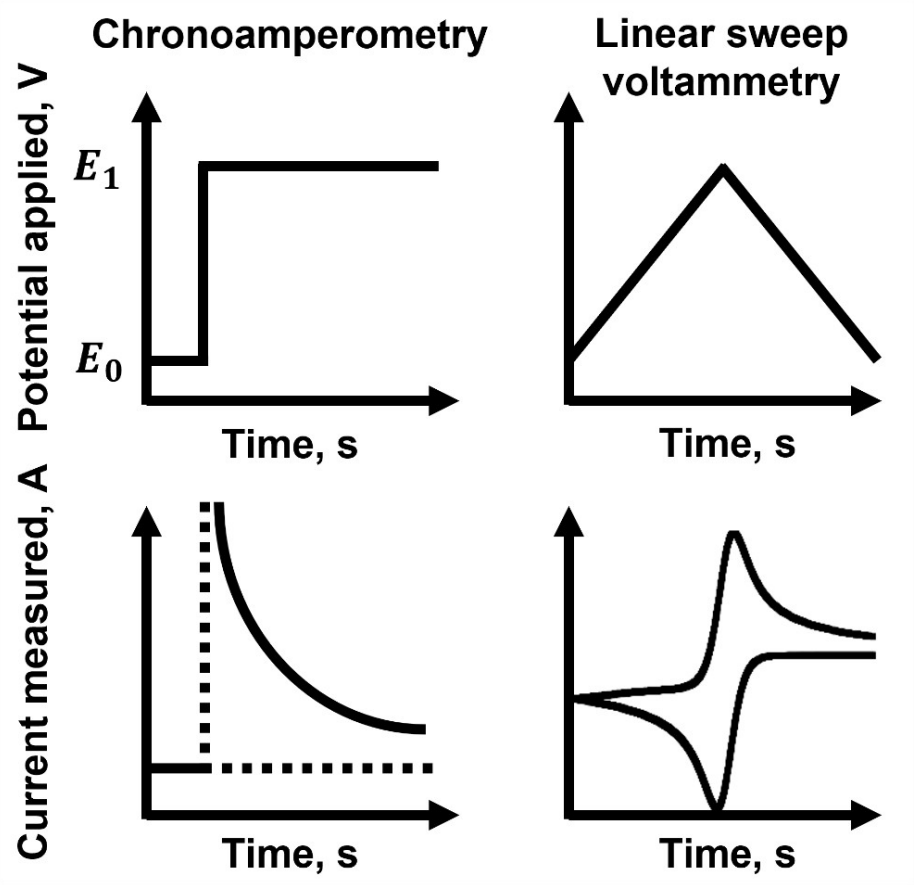


Figure 1.4: Potential-time waveforms (top row) applied to an electrochemical cell during chronoamperometry (left column) and linear sweep voltammetry (right column) and the corresponding shapes of the current-time responses (bottom row).

1.3.4 Electrode geometries

After a chronoamperometric step an instantaneous surface equilibration can be considered to have occurred at the electrode surface, resulting in the complete conversion of an initially present material by a given electron transfer if a sufficient potential is applied (see Equation 1.13). This results in a spike in current, ignoring non-Faradaic effects, which decays as mass transport brings material from greater and greater distances from the electrode to engage in electron transfer while the product species is removed from the electrode interface. A system in which the surface flux j, which is related to the current by $I=nAFj$, is entirely dependent on the mass transport, rather than the kinetics of the process confined to the surface, is considered to be under a thermodynamic or mass transport limit. The decay in current is thus

characteristic of the mass transport active at the surface only. In the case of dominant diffusion, it is the diffusion coefficient that determines the decay rate.

However, the shape of this curve is dependent on the shape of the surface at which the reaction occurs. Different shapes result in different diffusion regimes, which can vary with time.

The simplest case is linear diffusion. In this example, the size of the electrode surface greatly exceeds the size of the diffusion layer such that any curvature or complex geometry is negligible on the scale of diffusion. The diffusion appears to occur unidimensionally in the dimension perpendicular to a surface of seemingly negligible curvature, hence the 'linear' label. All geometries exhibit this behaviour at short times while the diffusion equation holds, since the diffusion layer (Chapter 1.2.2) begins infinitesimally small relative to the surface and grows with time $\left(\delta_l \propto \sqrt{t}\right)$. Any curvature of the electrode surface is thus initially negligible on the scale of the diffusion layer and thus the electrode shape is initially irrelevant.

Depending on the size and timescale of the experiment, the diffusion behaviour might not deviate from the linear regime at all. This is the case with macro-electrodes, typically on the scale of millimetres and acting on the timescale of seconds. Some electrodes may exhibit prolonged linear diffusion behaviour by maintaining a unidimensional geometry along a channel, such as is seen for recessed electrodes[23-25] and electrodes with microporous films[26].

The Cottrell equation[27] provides an analytical solution to the problem of purely linear diffusion after a chronoamperometric step with the following boundary conditions:

$$t = 0, all\ x, c = c^{¿}$$

$$t>0, x=0, c=0$$

$$t>0, x\to\infty, c=c^{¿}$$

where one considers the transport of the initially homogeneous species to the electrode at which instantaneous and complete electron transfer occurs. Introducing the substitution variable $\Gamma=\frac{x}{2\sqrt{Dt}}$ converts Fick's 2nd Law to:

$$\frac{d^2c}{d\Gamma^2}+2\Gamma\frac{dc}{d\Gamma}=0 \qquad \text{Equation 1.14}$$

which gives, by integration:

$$\frac{dc}{d\Gamma}=a\exp\left(-\Gamma^2\right) \qquad \text{Equation 1.15}$$

$$\int_c^{c^{¿}} dc=a\int_\Gamma^\infty \exp\left(-\Gamma^2\right)d\Gamma \qquad \text{Equation 1.16}$$

where we have applied the bulk boundary condition of an infinitely distant perfect source and the initial condition. Given that $\int_0^\infty \exp\left(-\Gamma^2\right)d\Gamma=\frac{\sqrt{\pi}}{2}$ and since $c=0$ when $\Gamma=0$ (the boundary condition at the electrode surface at a non-zero time-point after the step):

$$c=c^{¿}\frac{2}{\sqrt{\pi}}\int_0^\Gamma \exp\left(-\Gamma^2\right)d\Gamma=c^{¿}\,erf\left(\frac{x}{2\sqrt{Dt}}\right) \qquad \text{Equation 1.17}$$

$$j=D\frac{\partial c}{\partial x}\bigg|_{x=0}=\frac{\sqrt{D}}{2\sqrt{T}}\frac{dc}{d\Gamma}\bigg|_{\Gamma=0}=\frac{\sqrt{D}c^{¿}}{\sqrt{\pi t}} \qquad \text{Equation 1.18}$$

Since the advent of micro-electrodes, on the scale of micrometres, alternative diffusion behaviours are practically observable. The electrode geometries described by an isolated sphere or a hemisphere on an inert plane, which is isomorphic with a half-space of an isolated sphere, demonstrate the same amperometric behaviour. Electrodes possessing either of these geometries are common, with perhaps the most characteristic being the mercury hanging drop

electrode[28-31], which benefits from a renewable surface and variable dropping rate. Instead of continual current decay to zero, a steady-state current is instead observed at long times. This can be rationalised by conversion of Fick's 2nd Law into radial coordinates, representing 3-dimensional space with one spatial parameter by exploiting the two angular symmetries of the system:

$$\frac{\partial c}{\partial t} = D\left\{\frac{\partial^2 c}{\partial r^2} + \frac{2}{r}\frac{\partial c}{\partial r}\right\} \qquad \text{Equation 1.19}$$

A substitution of $u = rc$ converts this expression back to Fick's 2nd Law under linear diffusion conditions:

$$\frac{\partial u}{\partial t} = D\frac{\partial^2 u}{\partial r^2} \qquad \text{Equation 1.20}$$

which can be subjected to the same treatment as was used to derive the Cottrell equation above (Equation 1.17 and Equation 1.18). This gives the following results:

$$c/c^{¿} = \frac{r_e}{r} erf\left(\frac{r - r_e}{2\sqrt{Dt}}\right) \qquad \text{Equation 1.21}$$

$$|j| = D\frac{\partial c}{\partial r}\bigg|_{r=r_e} = Dc^{¿}\left(\frac{1}{\sqrt{D\pi t}} + \frac{1}{r_e}\right) \qquad \text{Equation 1.22}$$

where the electrode surface boundary condition is imposed at $r = r_e$ instead of at $x = 0$, where r_e is the radius of the (hemi-)spherical electrode. A constant value in the flux expression (and therefore the current transient) does not vanish as $t \to \infty$ in this case, resulting in a steady-state current! The current-time transient is illustrated in Figure 1.5 with the limiting Cottrellian and steady-state currents indicated.

At short times ($\sqrt{D\pi t} \ll r_e$) the flux approximates that predicted by the Cottrell equation at short times: $j \to \frac{\sqrt{D}c^{¿}}{\sqrt{\pi t}}$. The long-time ($\sqrt{D\pi t} \gg r_e$) steady-state flux $j \to \frac{Dc^{¿}}{r_e}$ corresponds to

the convergent diffusion regime. In this regime, the surface at which the reaction occurs is finite in each dimension and also has a scale much smaller than the diffusion layer. The diffusion then acts as if to a point in space rather than to a finite surface since the morphology of the concentration field becomes less dependent on the shape of the electrode at greater distances from the electrode.

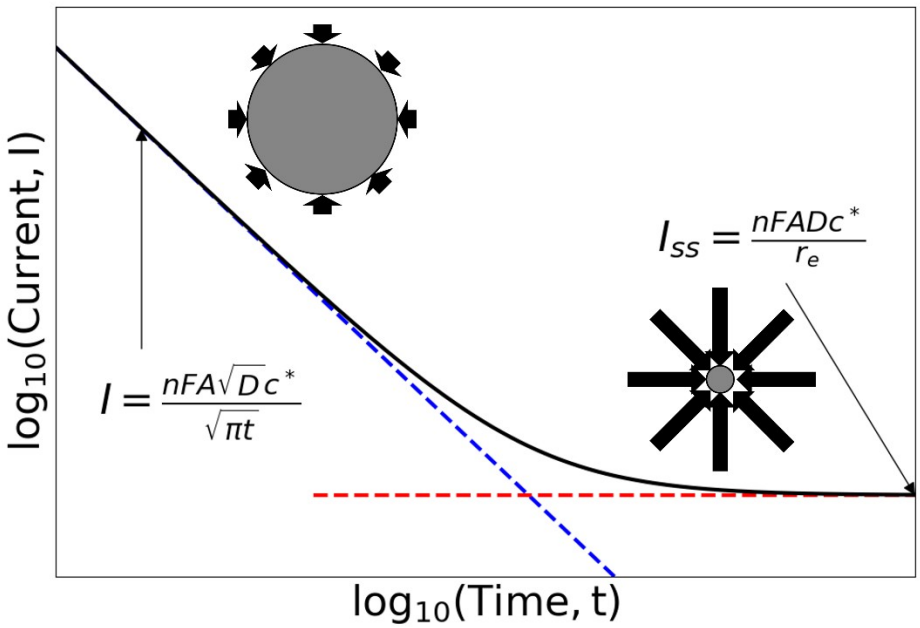


Figure 1.5: The Faradaic current-time transient observed for a chronoamperometric step to a large overpotential using a hemispherical electrode. The limiting Cottrell (blue) and steady-state (red) currents are indicated as dotted lines annotated with equations for their current.

If we consider a set of infinitesimally thin shells originating at the electrode surface, where each shell contains all points at a distance between R and $R+dR$ from the electrode, the shell volumes shall increase at greater distances from the electrode:

$$V_{shell} = 4\pi R^2 dR + O\left((dR)^2\right) \qquad \text{Equation 1.23}$$

where V_{shell} is the shell volume, R is the radius of the inner shell surface and dR is the infinitesimal thickness of the shell. The big-O notation $O\left((dR)^2\right)$ demonstrates that the following terms are on the order of $d\,R^2$ or greater and thus negligible relative to the first term in the limit of $dR \to 0$. Thus, as the diffusion layer expands, i.e. R increases, it encounters an

increasing amount of material to transport to the electrode since V_{shell} also increases for a constant dR. At long times, the diffusion layer is sufficiently large that the rate at which it encounters new material by expansion is greater than the rate at which material is transferred to the electrode surface, resulting in a steady-state system, so long as the diffusion layer continues to expand uninterrupted.

If one of the dimensions of the electrode surface is not finite, then truly convergent diffusion is not possible. An example of this is the infinite cylinder, whose diffusion is characterised by a similar partial differential equation to the sphere:

$$\frac{\partial c}{\partial t} = D\left\{\frac{\partial^2 c}{\partial r^2} + \frac{1}{r}\frac{\partial c}{\partial r}\right\} \qquad \text{Equation 1.24}$$

where r here represents the radial coordinate in cylindrical coordinates, not spherical. The cylinder instead exhibits a quasi-steady-state at long times and the current never reaches a constant value under diffusion control. This was first noted for electrochemical experiments by Delahay[32]. Notable equations predicting the current-time relationship for chronoamperometry proposed by Aoki et al[33] and Szabo et al[34] also predict this behaviour and showed 1% accuracies.

An infinitely large dimension is not required for diffusion behaviour to/from an electrode to follow a diffusion regime that is neither linear nor truly convergent. In the case of the cylinder, if the length is simply much greater than the radius, the current at the ends are negligible relative to at the sides and the current transient follows that predicted for an infinite cylinder (once suitably scaled to the finite length). Evidently, this lasts until the size of the diffusion layer also exceeds the length, in which case truly convergent diffusion does eventually occur. However, for the majority of applications in which treating the active

surface as a cylinder is worthwhile, insufficient time passes to practically observe the truly convergent diffusion regime.

While convergent and linear diffusion are both inevitable (for finite surfaces), unlike linear diffusion, the shape of the surface is significant for the convergent diffusion regime beyond its surface area alone. The steady-state flux is dependent on the electrode shape, as is the transitory diffusion behaviour between the two regimes, which is typically most difficult to characterise analytically and by numerical simulation.

An example of an electrode geometry which is as popular as the spherical cases and also engages in truly convergent diffusion on an experimental timescale is the inlaid disk electrode. An advantage of analysing the spherical electrode was the greater symmetry of the system and the uniformity of the mass transport across the electrode surface. This is not the case for the disk electrode where the edges are more exposed to diffusing material than the centre. In a derivation by Aoki[35, 36] it is observed that the steady state flux at the disk is predicted to tend to infinity. While not physically possible, this indicates the significance of the contribution to the total flux of such edge effects. Similar edge effects are also observed with other geometries involving sharp edges, for example at the corners and vertices of the cube electrode[37].

The disk electrode possesses reduced symmetry relative to the spherical electrode and so requires (at least) two spatial dimensions to describe its diffusion. Cylindrical coordinates $\{r, z, \phi\}$ are an intuitive choice, giving Fick's 2nd Law as:

$$\frac{\partial c}{\partial t} = D\left\{\frac{\partial^2 c}{\partial r^2} + \frac{1}{r}\frac{\partial c}{\partial r} + \frac{\partial^2 c}{\partial z^2}\right\} \qquad \text{Equation 1.25}$$

Alternative coordinates that have been used for the disk geometry include the rotational elliptical coordinate system $\{\xi, \eta, \phi\}$ with the two foci at the electrode edges[38].

Despite its significance to electrochemistry, analytical results for the time-dependent current transient at the disk electrode are lacking. The Shoup-Szabo equation[39] is a well-established equation derived by fitting to a simulation, reporting a maximum error of 0.6%, and is often used as a benchmark for simulation. Additional study by numerical computation is highly valuable and performed at numerous points in this thesis as a benchmark (Chapter 5), comparison case (Chapter 4), or as a geometry of interest in its own right (Chapters 5 & 6).

One assumption underpinning the discussion thus far on electrode geometry is that these electrodes exist in an infinite medium from which material can be eternally sourced by mass transport. While an accurate approximation for certain experimental conditions, there are circumstances in which this is not the case. Typically, this involves the diffusion layer encountering another interface.

The influence of another interface depends on the condition it places on the concentration of material at said interface (Dirichlet boundary), on the flux of material through it (Neumann boundary), or a condition on both concentration and flux (Cauchy or Robin boundary).

A simple case of a Dirichlet boundary is the perfect source/sink. At such an interface, some process acts to continually replenish or remove material and thus maintain a constant concentration. This may be a perpendicular advective flow, natural convection, saturation at an equilibrated solid surface, or some other process. The electrode surface is usually modelled as a Dirichlet boundary after a chronoamperometric step, which originates the diffusion, imposing surface equilibration according to an applied potential and the Nernst equation. A diffusion layer does not expand through a Dirichlet boundary as the concentration cannot change. In the case of linear diffusion, the influence of a perfect source and perfect sink pair is to provide a steady-state result with a linear concentration profile and

constant concentration gradient at all points in space leading to $\frac{\partial^2 c}{\partial x^2}=0=\frac{\partial c}{\partial t}$. Once the diffusion layer reaches the opposing interface, the flux decay slows and tends to the limiting value. In numerous models of diffusion across bio-membranes[40-45], this steady-state concentration profile is assumed, whereby the compartments either side of the membrane are treated as perfect sink and perfect source. Despite neglecting membrane curvature, depletion effects, time-dependence, and surface kinetics, such an approach is highly attractive due to the simplification of complex systems to a constant flux value which depends only on membrane thickness and solubility parameters.

Alternatively, a simple case of a Neumann boundary is the inert wall through which no flux of material can occur. A typical example would be a phase in which the diffusing material is negligibly soluble (e.g. a solid or gaseous phase). This leads to depletion effects whereby the material before the 'wall' is exhausted over time. "Thin-layer" experiments may be designed to exhibit this response[46, 47].

A relevant example of a Robin boundary condition is used to describe kinetically limited surface reactions, such as a hindered dissolution involving zero-order release kinetics (with rate constant k_f) and first-order re-absorption (with rate constant k_b):

$$j=k_f-k_b\cdot c=k_b(K-c)=k_f(1-c\cdot K^{-1}) \qquad \text{Equation 1.26}$$

where $K=k_f/k_b$ is the equilibrium constant. Such a condition is applied to simulate dissolving particles in Chapters 5 and 6.

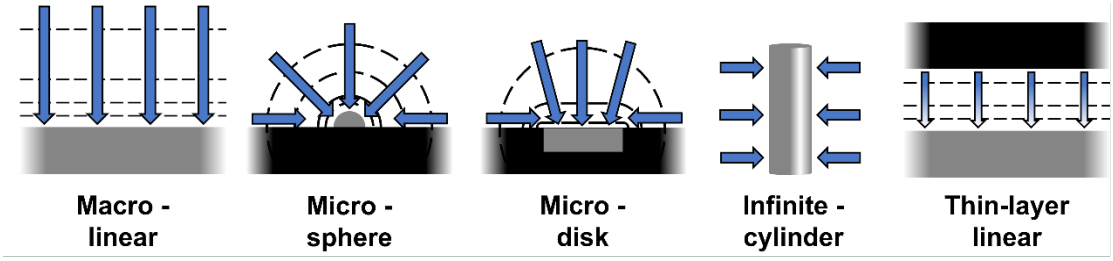


Figure 1.6: Schematic illustrations of the electrode geometries relevant to the study presented in this thesis. Grey represents the electroactive surface, black represents an inert, insulating material, blue arrows indicate directions of diffusive transport to the electroactive surface, and black dashed lines represent example isoconcentration lines. The macro-linear geometry corresponds to a unidimensional system above a flat plane which only ever exhibits linear diffusion. The micro geometries (sphere and disk) demonstrate initial linear diffusion which transitions to truly convergent diffusion. The infinite cylinder demonstrates initial linear diffusion which transitions to quasi-convergent diffusion. The thin-layer systems exhibit typical behaviour for the corresponding geometry followed by a depletion process upon the diffusion layer encountering the zero-flux interface; only the linear example is demonstrated here.

The system geometries and diffusion regimes we have hitherto discussed and on which we will continue to focus in this thesis are illustrated schematically in Figure 1.6. These are: the "macro-linear" unidimensional geometry with a flat and infinite electrode surface which exhibits only linear diffusion, a model system for macro-electrodes; the "micro-sphere" unidimensional geometry where the spatial dimension is spherically radial and truly convergent diffusion results at long times (with linear diffusion at short times); the "micro-disk" two-dimensional geometry which also exhibits linear transitioning into truly convergent diffusion, although with a differing steady state; the "infinite-cylinder" two-dimensional geometry which exhibits quasi-convergent diffusion at long times; and the set of "thin-layer" systems, with the linear case illustrated in Figure 1.6, where a zero-flux boundary is proximal to the electrode surface, resulting in a depletion effect and more rapid chronoamperometric flux decay.

As such, the geometry of the system has a marked effect on the diffusion behaviour, both due to the geometry of the active surface of interest and interaction with other interfaces in the medium. The typical transition is from linear to convergent diffusion, but characterising intermediate behaviour for different geometries and the interaction with other interfaces are challenges in analytical and computational study. Achieving physical insight through the

simulation of diffusion in such environments relevant to electrochemistry and uptake transfer across a bio-membrane, specifically the plant leaf cuticle, is the goal of this thesis. Having covered the fundamental concepts of electrochemistry relevant to this work, we now turn to the concepts underpinning the study of the foliar uptake of agrochemicals in the next chapter.

References

1. A. J. Bard, L. R. Faulkner, C. G. Zoski and J. Leddy, *Electrochemical methods : fundamentals and applications*, Second edn., 2001.
2. R. G. Compton and C. E. Banks, *Understanding Voltammetry*, World Scientific, Third edn., 2018.
3. T. Noël, Y. Cao and G. Laudadio, *Accounts of Chemical Research*, 2019, **52**, 2858-2869.
4. H. Hu and R. G. Larson, *Langmuir*, 2005, **21**, 3972-3980.
5. R. D. Deegan, O. Bakajin, T. F. Dupont, G. Huber, S. R. Nagel and T. A. Witten, *Nature*, 1997, **389**, 827-829.
6. A. Fick, *The London, Edinburgh, and Dublin Philosophical Magazine and Journal of Science*, 1855, **10**, 30-39.
7. J. Crank, *The Mathematics of Diffusion*, Clarendon Press, 1979.
8. A. Einstein, *Annalen der Physik*, 1905, **322**, 549-560.
9. Á. Molina, J. González, F. Martínez-Ortiz and R. G. Compton, *The Journal of Physical Chemistry C*, 2010, **114**, 4093-4099.
10. D. C. Grahame, *Journal of The Electrochemical Society*, 1952, **99**, 370-385.
11. J. A. V. Butler and F. G. Donnan, *Proceedings of the Royal Society of London. Series A. Containing Papers of a Mathematical and Physical Character*, 1926, **112**, 129-136.
12. E. A. Guggenheim, *The Journal of Physical Chemistry*, 2002, **33**, 842-849.
13. E. A. Guggenheim, *The Journal of Physical Chemistry*, 2002, **34**, 1540-1543.
14. D. J. G. Ives and G. J. Janz, *Reference electrodes*, Academic Press, New York, 1961.
15. W. Nernst, *Zeitschrift für physikalische Chemie*, 1889, **4**, 129-181.
16. J. Butler, *Transactions of the Faraday Society*, 1924, **19**, 729-733.
17. E. Bakker and E. Pretsch, *Angew Chem Int Ed Engl*, 2007, **46**, 5660-5668.
18. F. Haber and Z. Klemensiewicz, *Z. Physik. Chem.(Leipzig)*, 1909, **67U**.
19. W. E. Morf, *The principles of ion-selective electrodes and of membrane transport*, Elsevier, 2012.
20. J. J. O'Dea, J. Osteryoung and R. A. Osteryoung, *Analytical chemistry*, 1981, **53**, 695-701.
21. V. Mirceski, R. Gulaboski, M. Lovric, I. Bogeski, R. Kappl and M. Hoth, *Electroanalysis*, 2013, **25**, 2411-2422.
22. Y. Uchida, E. Kätelhön and R. G. Compton, *Journal of Electroanalytical Chemistry*, 2018, **818**, 140-148.
23. A. C. West and J. Newman, *Journal of The Electrochemical Society*, 1991, **138**, 1620.
24. R. Ferrigno, P. F. Brevet and H. H. Girault, *Electrochimica Acta*, 1997, **42**, 1895 - 1903.
25. P. N. Bartlett and S. L. Taylor, *Journal of Electroanalytical Chemistry*, 1998, **453**, 49-60.

26. F. G. Chevallier, L. Jiang, T. G. J. Jones and R. G. Compton, *Journal of Electroanalytical Chemistry*, 2006, **587**, 254-262.
27. F. G. Cottrell, *Zeitschrift für Physikalische Chemie*, 1903, **42U**, 385-431.
28. R. DeMars and I. Shain, *Analytical Chemistry*, 1957, **29**, 1825-1827.
29. J. M. Markowitz and P. J. Elving, *Chemical Reviews*, 1958, **58**, 1047-1079.
30. A. M. Bond and K. B. Oldham, *Journal of Electroanalytical Chemistry and Interfacial Electrochemistry*, 1983, **158**, 193-215.
31. T. R. Ralph, M. L. Hitchman, J. P. Millington and F. C. Walsh, *Journal of Electroanalytical Chemistry*, 2006, **587**, 31-41.
32. P. Delahay, *New Instrumental Methods in Electrochemistry*, Interscience Publishers Inc., New York, 1954.
33. K. Aoki, K. Honda, K. Tokuda and H. Matsuda, *Journal of Electroanalytical Chemistry and Interfacial Electrochemistry*, 1985, **186**, 79-86.
34. A. Szabo, D. K. Cope, D. E. Tallman, P. M. Kovach and R. M. Wightman, *Journal of Electroanalytical Chemistry*, 1987, **217**, 417--423.
35. K. Aoki and J. Osteryoung, *Journal of Electroanalytical Chemistry*, 1981, **122**, 19--35.
36. K. Aoki, *Electroanalysis*, 1993, **5**, 627--639.
37. C. Batchelor-McAuley and R. G. Compton, *Journal of Electroanalytical Chemistry*, 2020, **877**, 114607.
38. J. Newman, *Journal of The Electrochemical Society*, 1966, **113**, 501-502.
39. D. Shoup and A. Szabo, *Journal of Electroanalytical Chemistry and Interfacial Electrochemistry*, 1982, **140**, 237-245.
40. K. J. Laidler and K. E. Shuler, *The Journal of Chemical Physics*, 1949, **17**, 851-855.
41. J. S. Turi, N. F. H. Ho, W. I. Higuchi and C. Shipman, *Journal of Pharmaceutical Sciences*, 1975, **64**, 622-626.
42. L. Masaro and X. X. Zhu, *Progress in Polymer Science*, 1999, **24**, 731-775.
43. J. Siepmann and N. A. Peppas, *International Journal of Pharmaceutics*, 2011, **418**, 6-12.
44. J. Schönherr and P. Baur, *Pesticide Science*, 1994, **42**, 185-208.
45. N. M. Satchivi, E. W. Stoller, L. M. Wax and D. P. Briskin, *Pesticide Biochemistry and Physiology*, 2000, **68**, 85-95.
46. D. Oglesby, S. Omang and C. N. Reilley, *Analytical Chemistry*, 1965, **37**, 1312-1316.
47. E. Laviron, *Journal of Electroanalytical Chemistry and Interfacial Electrochemistry*, 1972, **39**, 1-23.

2 Introduction to foliar uptake

In this chapter we introduce the central concepts of foliar uptake, specifically the biological structures and physical processes involved. We introduce a broad overview of what the structure and function of the plant leaf is and how it can be viewed from mass transport and modelling perspectives. We focus on the influence of the cuticle on uptake and its biological significance. We discuss how the transport of chemicals can be achieved across the leaf-environment interface and how this depends on the chemical identity. Finally, we review the use of foliar uptake as an uptake route for agrochemicals into plants, with a specific focus on pesticides.

2.1 The plant leaf

It is perhaps taken for granted that the majority of terrestrial plant species possess leaves as an organ[1]. They are complex, specialised, and multi-functional[2-6], making them very distinct from the other structures and organs common to plant life, such as the roots and stem. Furthermore, leaf structures are unique to plants out of all life on Earth. As a result, leaves are a unique subject of interest when studying the importance of plant life in our world and its relationship with humanity. The importance of this relationship is emphasised by the growing demands on agriculture[7] and the increasing need for environmental conservation[8-10]. Human efforts to improve both of these aspects rely on an increasing understanding of plant biology and enhancing the efficacy of human involvement. Developing effective models is a necessary step in this pursuit[11].

The leaf phenotype varies widely between and within species. The many functions performed by the leaf organ and their significances depend on the environment, age, and the plant's "survival strategy"[5, 12]; this means that leaves exhibit significant inter- and intra-species diversity, as exhibited in Figure 2.1. This presents a challenge for approaching leaves from a

generalised perspective and necessitates care in the development of plant leaf models. We begin by considering the functions common amongst leaves before considering the structures that support these functions.



Figure 2.1: Illustration of interspecies phenotypic leaf diversity using five examples. From top left clockwise: *Alocasia macrorrhizos* (giant taro), from Jinguashi, Taiwan, with a large leaf area, waxy exterior and simple vein structure; *Nelumbo nucifera* (Indian lotus), from Hyderabad, India, with ultra-hydrophobic upper exterior and rotational symmetry; *Ilex aquifolium* (English holly), from New Jersey, USA, with hardened and spined leaf margin and high tannin content; *Rafflesia arnoldii* (padma) from Bengkulu, Indonesia, with large, mottled red-white petals releasing volatile chemicals smelling of rotting flesh; and *Dionaea muscipula* (Venus flytrap) from Pennsylvania, USA, with terminal leaflets that attract, rapidly close on and digest insects. The above photos have been taken from Wikimedia Commons and their contributors and licenses are (from top left clockwise): Fred Hsu under CC BY-SA 3.0, https://commons.wikimedia.org/w/index.php?curid=9536635; J.M. Garg under CC BY 3.0, https://commons.wikimedia.org/w/index.php?curid=7249919; Famartin under CC BY-SA 4.0, https://commons.wikimedia.org/w/index.php?curid=35352616; SofianRafflesia under CC BY-SA 4.0, https://commons.wikimedia.org/w/index.php?curid=59608279; and Beatriz Moisset under CC BY-SA 4.0, https://commons.wikimedia.org/w/index.php?curid=83312051.

2.1.1 Functions

Arguably, the primary purpose of the leaf structure is to facilitate and optimise the photosynthetic process[2]. This requires a supply of water and carbon dioxide, the capture of energy from sunlight, the removal of the oxygen by-product, and the transport of the nutrient product to the rest of the plant, particularly to areas of growth. Leaves are not necessary for photosynthesis: numerous plant species, such as algae, and non-plant species, such as the sea slug *E. chlorotica*, do not possess leaves and yet photosynthesise. However, the widespread adoption of leaves in terrestrial plants suggests a significant evolutionary benefit, particularly since they appear to be a convergent evolved trait, developing independently in at least six

different plant lineages[13]. We consider here the functions and roles the leaf fulfils (summarised in Figure 2.2), how they conflict and how the differing optimisations lead to such phenotypic diversity among plant leaves.

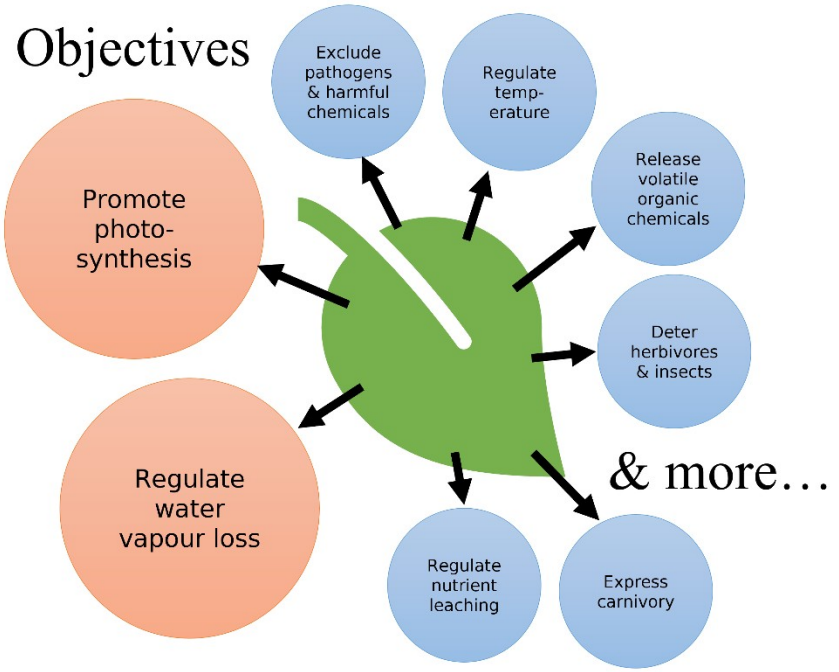


Figure 2.2: Illustration of conflicting objectives for the development of the plant leaf, discussed further in the text. Objectives in the larger orange circles are the primary objectives that all leaves demonstrate some level of optimisation for, while objectives in smaller blue circles are a subset of secondary objectives leaves may also optimise for depending on the plant's survival strategy and environmental pressures, and for which some plant species do demonstrate adaptation (this list of secondary objectives is not exhaustive).

It is intuitive that improving the rate of photosynthesis is likely to improve a plant's "fitness" for a given environment by increasing its ability to capture carbon and produce carbon-based material. This acts as an evolutionary driver for the development of leaf properties. Maximising the capture of energy from sunlight incentivises increasing the leaf's surface area, chlorophyll concentration and photosynthetic pathway efficiency. Maximising the rate of gas exchange at the photosynthesising zones incentivises porosity at the interface to the environment and the extension of leaves into the air (gas diffusion and convection is a significant improvement to dissolution and diffusion of gases through water, as is the case for aquatic species). Maximising the transfer of water to, and photosynthetic products from, the

leaf incentivises the use of rapid transport processes through specialised structures, rather than relatively slow diffusion between cells.

However, these adaptations do have disadvantages. There are inhibitory drivers complicating the evolutionary optimisation of the leaf structure. While an efficient gas exchange, large surface area and improved water transport promote photosynthesis, these adaptations also exacerbate a significant route for the loss of water from the plant through the leaves as vapour[5, 14, 15]. If the loss of water is more rapid than the uptake through the roots, this will cause water stress in the plant. Furthermore, if the loss of water from the leaf is greater than its supply, this can lead to local desiccation, causing structural damage and halting photosynthesis. The significance of this evolutionary driver depends on the temperature, humidity, and wind speed in the environment, which affect the rate of water loss, as well as its aridness, which affects the rate of water uptake. Leaf structures must therefore adapt to reduce and/or control the loss of water as well as increase the rate of photosynthesis, producing conflicting objectives. The relative significance of these depends on the environment and thus promotes diversity.

There are other inhibitory drivers against the optimisation of the leaf structure for photosynthesis alone. Porosity to the aerial environment provides an entrance route for bacteria, fungi, and other pests to infiltrate and parasitize the plant. It also provides an entrance route for harmful chemicals, such as pollutants. The concentration of carbon content, nitrogen content and water in the leaves also makes it attractive as a food source for herbivores. Mechanical stress due to wind and rainfall necessitates the development of structural integrity. A means to avoid the retention of water droplets on the leaf is also a driver since water droplets block gas exchange, focus excess light onto the leaf through

droplet lensing, can induce nutrient leaching, and may contain harmful chemicals and/or facilitate their uptake.

Additional leaf functions have also been identified. Petals[16] are a modified type of leaf that protects the reproductive organs of the plant; these variants may additionally display unusual colours and release distinctive volatile chemicals for attracting pollinators. The release of volatile chemicals through leaves is also done for a variety of other reasons[17], including to dissuade or harm pests, to attract certain animals, in symbiotic relationships with fungi, to alleviate abiotic stresses such as heat stress, oxidative stress, salt stress and water stress, as a defence to pathogenic attack, and even as a form of communication between plants.

The leaves of some carnivorous plants have also evolved to trap, kill, and digest animals[18], such as the iconic Venus fly trap. Some leaves have evolved to retract or roll[19] in response to abiotic factors (water loss, excessive irradiation, rainfall) and biotic factors (deter herbivores or trap prey). Other defence mechanisms[20, 21] against herbivores include physical defences, such as spines, barbs, and hardened leaves, and chemical defences, such as latex, stings, and toxins.

While the range of roles fulfilled by leaves is wide, with this thesis' focus on interfacial mass transport, we are most concerned with the chemical exchange across this interface, which is relevant both to understand the plant's protection from its environment and how humans might use this pathway as a route to introduce chemicals for our own purposes. We next turn to the relevant structures commonly observed in leaves that are adapted to the above leaf functions.

2.1.2 Structures

In order to achieve the functions listed in the previous section, certain structures have developed to facilitate these demands. While some of these structures are common to many plant species, the diversity of phenotypic expression means that not all leaves exhibit the same structures. With differing selective pressures, different taxonomic branches have evolved correspondingly. The ability for certain structures to fulfil several functions simultaneously, and to variable extents, has led to even greater phenotypic diversity[6]. In this section, we introduce relevant leaf structures common to many, but not necessarily all, plants and discuss their features and purposes. The structures we introduce in this sub-section are presented schematically in Figure 2.3.

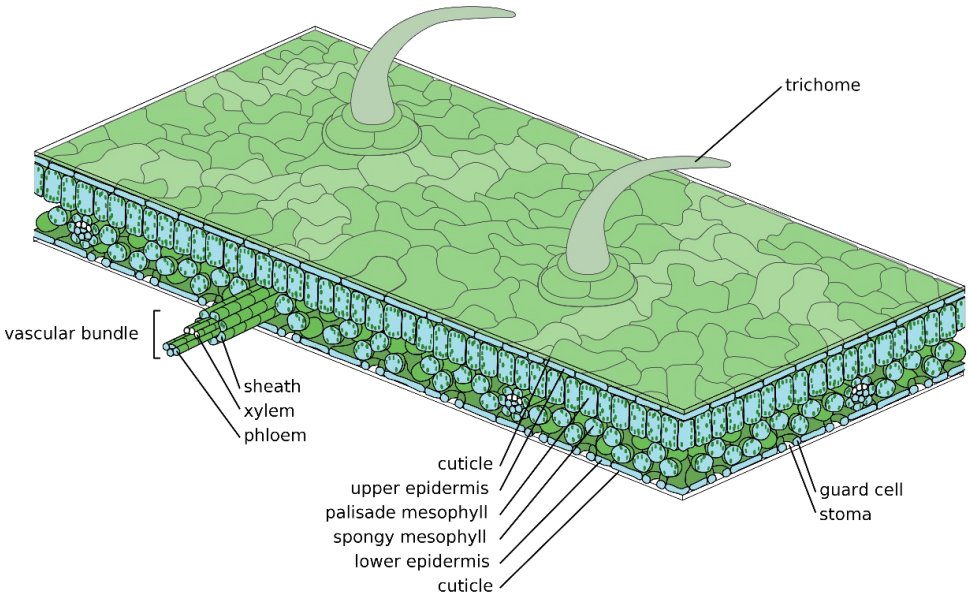


Figure 2.3: A schematic of a leaf structure featuring: upper and lower epidermis (and associated cuticles), palisade and spongy mesophyll, stomata (and associated guard cells), vascular tissue made up of xylem, phloem and sheath cells, and example trichomes. The green spots within cells represent chloroplasts and indicate which tissues undergo photosynthesis. This image is adapted from "Own work" by Zephyris (https://commons.wikimedia.org/w/index.php?curid=15005467) under licensed under CC BY-SA 3.0 (https://creativecommons.org/licenses/by-sa/3.0).

A broadly applicable observation is the differentiation of leaf cells into epidermis, palisade mesophyll and spongy mesophyll[3]. The mesophyll cells provide a high concentration of chlorophyll and perform the bulk of the light-harvesting and photosynthetic action. Depending on demands on gas exchange, light capture, structural integrity, wind load,

transport efficiency and energy budget, the mesophyll may have tightly packed cells or an incredibly porous ultrastructure. Any expression of internal porosity (for the facilitation of CO_2 transport and light scattering) occurs in the spongy mesophyll.

To provide mechanical strength, a tightly packed, rigid epidermis of pavement cells surrounds the mesophyll; other, more specialised cells are also present in the epidermal layer (discussed below). To facilitate light capture by the mesophyll, pavement cells often have high transparency, and some even provide a focussing function. The epidermis reduces the evaporation of water and provides a defence against biotic attack by pathogens and parasites.

Some species develop a palisade mesophyll[22] below the upper epidermis: these cells contain chlorophyll and perform photosynthesis, however, unlike the irregularly shaped spongy mesophyll distributed in a porous structure, they are columnar and tightly packed, providing some additional mechanical strength and more effective light capture at the expense of greater resistance to internal CO_2 diffusion. The palisade cell shapes promote the penetration of light deeper into the leaf, while the spongy mesophyll produces light scattering within the leaf, enhancing light absorption.

Further cell differentiation in the epidermal layer tunes the plant-environment interaction. The development of stomatal complexes[23] is a central example. The non-parallel objectives of maximising gas exchange and controlling water vapour loss means that fully enclosing the mesophyll is a poor solution. A dynamic response is advantageous for the plant to regulate these processes over time, for example in response to water stress and the day/night cycle. The stomata provide an array of controllable apertures between swellable “guard” cells, through which gas exchange occurs. The defensive and mechanical functions of the epidermis are minimally compromised, while the mesophyll remains well-supplied by CO_2.

By closing these stomatal apertures, the plant can respond to its environment with respect to its water loss.

The “water potential” is a metric in botany used to assess the local and total plant water status. It refers to the potential energy (J) of water per unit volume (m^{-3}) under certain conditions relative to pure water, including contributions from the osmotic potential, external pressure, and matrix effects such as fluid cohesion and surface tension. The water potential is related to the chemical potential of the water as: $\mu = P_w \cdot V_m$, where μ is the chemical potential, P_w is the water potential, and V_m is the molar volume. Expression of the metric as a pressure facilitates its measurement. If the water potential at the leaf drops below a certain value (typically in the range -1 to $-5\,MPa$) then the aperture is closed[24], greatly reducing the exchange of gases including water vapour. A decreased epidermal water potential (below that maintained by steady flow from the roots) indicates a risk of desiccation, and that gas exchange should be slowed until the water potential rises again, this also has the effect of slowing the photosynthesis by restricting access to CO_2. Thus, the rate of photosynthesis and rate of water loss are controlled dynamically to maintain a certain water potential at the leaf surface. The closing of the stomatal apertures is responsive to three physiological variables: the concentration of photosynthetic metabolites (to ensure diffusional supply of CO_2 keeps up with its photosynthetic need), the presence of certain hormones and regulators, primarily abscisic acid (to respond to water stress in the roots), and hydraulic linkage involving flow of water along a pressure gradient (coupling the stomatal guard cells to the leaf’s water potential)[25].

Water loss by evaporation does still remain significant. As well as the development of stomata, the risk of desiccation for the plant cells is further alleviated by the efficient supply of water by vascular transport, which also increases a plant’s maximum possible

photosynthetic rate. The xylem describes a system of dead, specialised, low resistance cells, arranged in tubes, that irrigates the whole plant by supporting a pathway for water to flow in response to a gradient of pressure/water potential. Despite accounting for a small fraction of the whole-plant transport distance on this hydraulic system, the leaf accounts for 30% of the whole-plant resistance to water flow[4]. The transport of water and water-soluble chemicals in the xylem is advective. The cohesion-tension theory, postulated by Dixon and Joly in 1894[26] and well-reviewed by Tyree in 1997[27], posits that the flow of water is driven entirely by evaporation at the leaves, while strong cohesion forces maintain the water column under metastable tension and induces a flow from the roots. This whole process is termed transpiration and predicts negative pressure gradients of several mega-pascals for tall plants. However, this theory is increasingly challenged, notably by Zimmerman et al[28], whereby multiple forces are being identified to assist water transport.

The xylem exists in the vascular bundle alongside the phloem. While the xylem transports water and water-soluble chemicals from the roots to the leaves, the phloem provides a hydraulic pathway for the transport of chemicals away from the leaf to zones where those chemicals are consumed. Active mass transport processes transfer chemicals into the phloem at the leaf and removes those chemicals at sites of growth. The subsequent osmosis of water generates a hydrostatic pressure difference, leading again to advection. This is the theory posited by Münch[29] and the Kleier model simulates this process for the prediction of properties to optimise a chemical's phloem mobility[30-32]. The energy cost for producing the vascular bundle is high[33], as is the surrounding tissue that controls the mass transport between the bundle and surrounding tissue. The active transport for the phloem function is also energy intensive. We thus have conflicting objectives of maximising the rate of mass transport to as much of the leaf surface area as possible while minimising the energy cost of doing so. This leads to a diversity of venal leaf architectures from single-vein to dendritic to reticulate[4].

Nevertheless, mass transport within the leaf is much more rapid generally than mass transport at the leaf-environment interface.

Additional features that are observed in leaves can have more diverse functionalities. Leaf pubescence describes the generation of hair-like features on the leaf surface[2, 34, 35]. This may be trichome structures, which are fine appendages extending from specialised epidermal cells; spines, which are hardened leaves or parts of leaves with vascular bundles inside; prickles, which are derived from the epidermis tissue and contain no vascular bundles; or other spinose structures. Pubescence is frequently used to deter herbivores and animals. Some trichomes are specialised to dispense toxins as stings. Pubescence may also be used to direct and/or trap insects, for example in carnivorous plants. However, many other roles can be fulfilled by pubescent structures[35], depending on how they are implemented; this includes shading the leaf, reflecting light onto the mesophyll, reducing the rate of water loss, thermally insulating the leaf, facilitating the excretion of excess salts, protecting stomata from pathogens and blockages by water or particulates, and increasing the advective boundary layer thickness. Pubescence may also be used to reduce the wettability of the leaf surface, for example in the generation of superhydrophobic surfaces[36, 37] and thus avoiding the retention of water droplets. Pubescence thus has a significant effect on the properties of the leaf surface.

However, a feature which is common to all terrestrial plants is the protective waxy cuticle[38-41]. This is a layer of cutinous wax that covers the entire epidermis exposed to the environment (and occasionally parts of the interior mesophyll as well), not just at the leaf. The principal role of the cuticle is to hinder the astomatous (i.e., not at the stomata) transport of chemicals between the plant and environment. The presence of the cuticle minimises water loss, nutrient leaching, and the influx of harmful material. It also plays a complex mechanical role (needing to stretch for growth and flex for wind while also increasing the leaf's mechanical strength),

provides reflective or focussing functions for different species, and also provides a pathogenic and pest defence.

The cuticle is the principal barrier to chemical exchange (at which it is much more effective than the underlying living palisade cells) and a reservoir for lipophilic material on the leaf surface. Due to these roles, the leaf cuticle is henceforth the focus of this thesis and so requires a deeper description than we have erstwhile provided for the other leaf structures above. This is provided in the following section.

2.2 The cuticle

As mentioned above, the cuticle is a layer of wax that covers the epidermis of almost all terrestrial plants. Similar to the overall leaf structure, the development of a cuticle to control water loss is a convergent evolutionary property having developed independently in plants and also arthropods. Approximately 80% of all species on Earth share a cuticle-like integument with low water permeability achieved by associated waxes. As such, it is of vital importance for understanding chemical interactions on the outer surface of living entities. Its importance to the mass transport processes that govern plant biology makes it central to the study presented in this thesis. We thus dedicate this section to introducing the cuticle in sufficient depth for the reader and as background for the studies presented in later chapters. Concepts introduced in this work are reviewed extensively in the literature, with a particularly valuable and general resource being the dedicated volume of the Annual Plant Reviews: “Biology of the Plant Cuticle”[42].

2.2.1 Function

The cuticle is recognised as the principal transport and solubility barrier to chemicals coming into the plant from the environment[40, 43, 44]. It is also the principal barrier against water loss and gas exchange outside of the stomatal pathway[45], aka astomatous transport. The cuticle is far more resistant to mass transfer than the underlying palisade cells, which offer relatively rapid transport facilitated by the vascular system. The development of the cuticle coincides with the arrival of plant life on land[46, 47] during the Cambrian period and it is hypothesised that the evolution of the cuticular barrier was necessary for plant life to survive outside of water.

The cuticle also acts as a reservoir for lipophilic material. As shall be discussed below, the cuticle consists of a semi-crystalline polymer matrix with waxes and other chemicals impregnated within. This highly lipophilic environment acts as a sequestration trap for similarly lipophilic chemicals. It is unclear to what extent the lipophilicity of the cuticle evolved to reduce its permeability to water versus its evolutionary benefit of trapping potentially harmful lipophilic material outside of the plant but this dual-purpose emphasises the significance of the cuticle's appearance in evolutionary history.

Furthermore, the cuticle provides several additional functions that are less relevant to our study but nonetheless important to its role. The hydrophobicity of the cuticle assists with water and particle repellence, epicuticular waxes (introduced in the next sub-section) scatter and reflect visible and UV light to avoid excessive irradiation, cuticles assist in maintaining the structural integrity of the plant tissue, and the cuticle modulates the interaction of the plant with bacteria and fungi. Additionally, the cuticle is plastic (and therefore capable of following growth and movement) and self-healing (despite being a non-living material).

The barrier and reservoir functions are highly relevant to models of uptake of chemical material across the cuticle membrane, whether to model pollutant fates in the biosphere or to

model the uptake of deliberately applied agrochemicals. It is useful to consider the chemistry of the cuticle to understand how it achieves these functions.

2.2.2 Chemistry

The cuticle is a complex, multi-phasic polymer matrix. Different plant species demonstrate a variety of chemical compositions in their cuticles. However, in all cases, the two major components are cutin polymers[48], which consist of C_{16} and C_{18} omega hydroxy acid monomers and their derivatives in polyester chains of indeterminate lengths, and cutan polymers, which are non-saponifiable and believed to be long hydrocarbon chains, although their exact structures and syntheses are still unclear. The polymer matrix is lipophilic and generally contains both amorphous and rigid domains according to the disordered polymer conformations and generally significant flexibility. The monomers involved with these polymers vary between species (and even within species in response to environmental conditions) and it is yet unclear what relationships exist between these chemical compositions and the cuticle's properties and functionality.

Lipid waxes are also commonly present in cuticles[49-52], introducing additional structure. These waxes have complex and varied chemical compositions. The two typical categories are aliphatic waxes, including very-long-chain fatty acids, n-alkanes, n-alcohols, n-aldehydes, ketones and wax esters, and alicyclic waxes, including pentacyclic triterpenoids, tocopherols, and steroids. The chain lengths of these waxes typically constitute a wide range and are longer than the cutin monomers, with the most common lengths being between C_{29} and C_{31}. Unsaturated and branched versions of the major wax components are often also present in smaller quantities. Generally, the wax concentration increases closer to the outer cuticular interface. Intracuticular waxes exist within the cuticle, while epicuticular waxes protrude

from the cuticle surface into the environment, either as a distinct amorphous layer, solid crystals, or both.

2.2.3 Cuticle ultrastructure

It would, however, be a simplification to suppose that the cuticle is a homogeneous mixture of these ingredients. Indeed, the cuticle displays a large degree of heterogeneity and asymmetry in its structure and composition. As a general rule, there is some gradient with respect to depth into the cuticle whereby lipophilic material (such as the waxes) is predominantly deposited towards the outer layer and hydrophilic material (such as carbohydrates) is predominantly located towards the interior of the cuticle at the interface with the epidermal cell wall.

In many models, the cuticle is differentiated into two layers: a “cuticle proper” and a “sorption compartment” or “cuticular layer”[53, 54]. The cuticle proper typically constitutes the top 10% of the cuticle’s depth and is where the majority of intracuticular waxes are found. The sorption compartment is the interior 90%, constituting the majority of the cuticular mass and containing little cuticular wax but all the carbohydrates. It has been shown[55, 56] that penetrant species have significantly lower mobilities in the cuticle proper and are more soluble in the sorption compartment, where sequestration predominantly occurs. The “sorption compartment” may be divided into exterior and interior layers if structures, such as nanofibrils, extend from the cell walls into the interior section but do not extend across the entire cuticular layer.

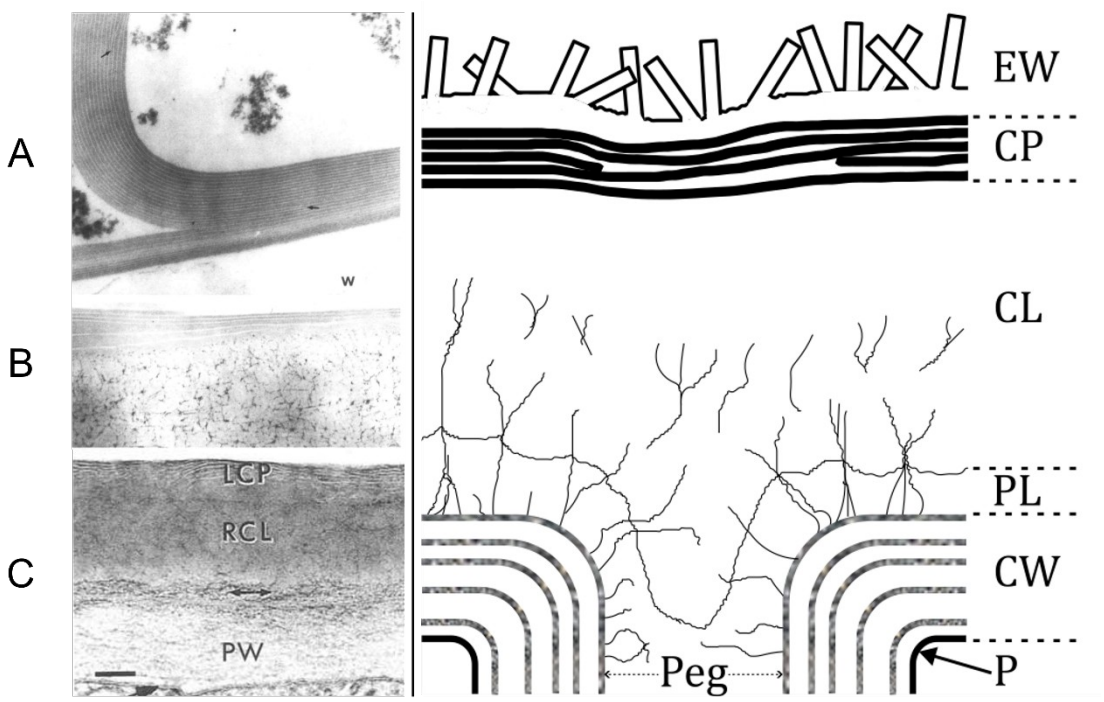


Figure 2.4: On the left are representative images taken, with permission, from literature of transmission electron micrographs of cuticles illustrating the divisions of the cuticle into different layers. Images A and B are from a study by Wattendorff and Holloway[57] of the cuticle of *Agave Americana* L., where A is of a detached cuticle proper and B is of a still attached cuticle proper with the cuticular layer shown, both images at ×73,000 magnification. Such a cuticle is Type 1. Image C is from a study by Heide-Jørgensen[58] of the cuticle of *Utricularia lateriflora*, where LCP is the polylamellate cuticle proper, RCL is the reticulate cuticular layer, and PW is the primary pecto-cellulosic wall, with the image at ×64,400 magnification and a $0.1\,\mu m$ bar included. Such a cuticle is Type 2. On the right is a schematic illustration of the generic ultrastructure of a plant cuticle. Separation into several layers is shown: EW is the epicuticular wax layer, consisting of an amorphous layer and/ or solid epicuticular crystals; CP is the cuticle proper, illustrated here as possessing polylamellate structure, though amorphous and reticulate are also observed; CL is the cuticular layer (sorption compartment); PL is the pectin-rich layer between the cuticle and cell wall (CW); and P is the plasmalemma separating CW from the cell interior (cytoplasm). The cuticular peg between adjacent cells is also shown. This schematic is not to scale. This image is the author's own work but is derived from an image presented in work by A. Buchholz (2006)[59].

Transmission electron microscopy (TEM) of stained cross-sections of cuticles demonstrate a variety of ultra-structures in cuticles[57-62]. A schematic illustrating the differentiation between layers of the cuticle derived from these studies is demonstrated in Figure 2.4. Of particular note are arrangements of electron-dense and electron-lucent regions in the cuticle proper[57]. It is hypothesised that these correspond to chemically distinct domains distributed throughout the cuticle. Amorphous, disordered, lamellate and reticulate structures have been observed in both the cuticle proper and sorption compartment. It is possible that, if diffusion is precluded from certain domains in the cuticle, the pathway to transfer from one side of the cuticle proper to the other shall be highly tortuous[63]. This hypothesis is used to justify various

observations discussed further in Section 2.3.1. Cuticle structures have been grouped by Holloway[42, 64] into six types. Type 1 cuticles have a polylamellate outer region with a sharp delineation to a mainly reticulate inner region; Type 2 have a faintly lamellate outer region which merges with a mainly reticulate inner region; Type 3 have an amorphous outer region and mainly reticulate inner region; Type 4 are all reticulate; Type 5 are all lamellate; and Type 6 are mainly amorphous. As such, the cuticle represented schematically in Figure 2.4 is Type 1.

An additional structural feature to be noted is that the cuticle surface conforms to the epidermal layer beneath it. While generally maintaining a flat overall topology, features that extend from the epidermis (such as trichomes) and features that subtend into the epidermis (such as stomatal apertures) will also be covered by cuticle. Additionally, the outer epidermal cells do not rest entirely flush to each other, leaving a gap in between that must be filled with cuticular material. This translates to a small trough on the outer surface but underneath one can observe that the cuticular depth at points between epidermal cells is much deeper than directly over these cells. This section is called the “cuticular peg”, which forms channels all over the outer leaf structure between the cells. These zones provide additional volume for sequestration and complicate the modelling of transcuticular diffusion from the environment to those epidermal cell walls and beyond. The presence of cuticular pegs and their influence on chemical uptake shall be significant in Chapter 6 where we observe and model cuticular transport.

2.3 Pathways for transcuticular transport

The principal role of the cuticle, and our interest in it, is as a barrier to the loss of water and the influx of chemicals. It has been identified[65] that the transfer across the cuticle depends highly on the size and lipophilicity of the chemical species. While the default route is to

diffuse through the polymer matrix, the so-called lipophilic pathway, the presence of hydrated pores through the cuticle does provide a more effective route for otherwise insoluble hydrophilic species: the hydrophilic pathway.

A schematic of the two astomatous pathways through the cuticle is presented in Figure 2.5 as a symbolic transverse cuticle cross-section, where we present the lipophilic pathway as restricted to a tortuous path in the cuticle proper followed by less restricted and more rapid (lateral) diffusion in the sorption compartment layer and the hydrophilic pathway as restricted to polar channels.

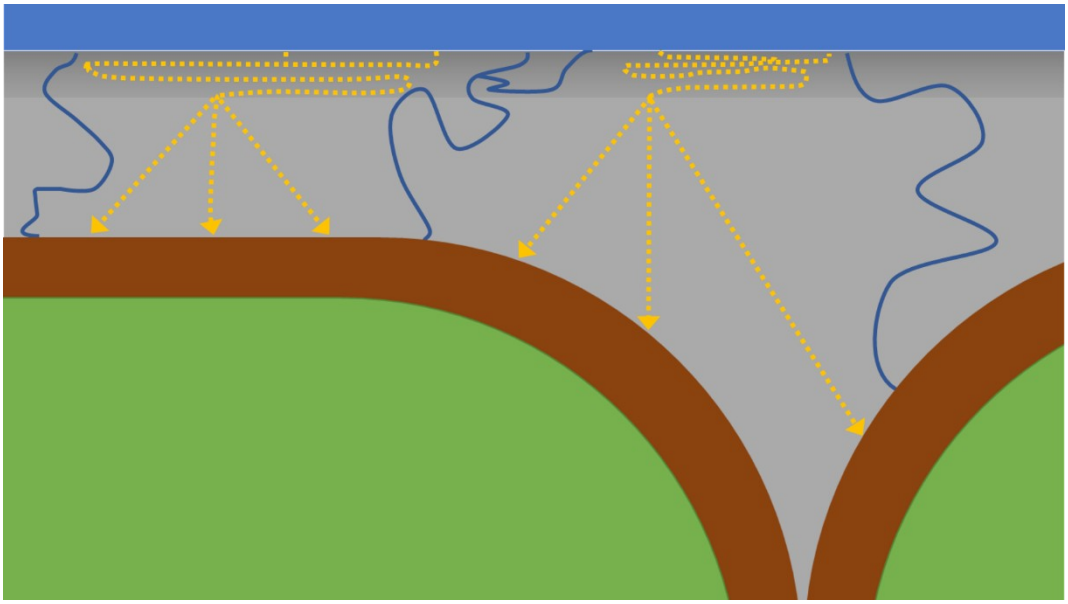


Figure 2.5: A schematic illustration of the cuticular astomatous uptake pathways. The lipophilic pathway is represented as orange dashed arrows, which are restricted to tortuous paths through the cuticle proper (represented as a darker shade of grey) and which represent unrestricted diffusion through the sorption compartment (lighter grey). The hydrophilic pathway is restricted to confined polar channels through the cuticle (blue). We demonstrate the tops of the underlying pavement cells, with the cell walls represented as brown regions and the living section (symplast) in green. A cuticular peg between two pavement cells is also shown. This schematic is not to scale.

It is also worth noting that transfer of chemical material from the environment to the leaf tissue, and thereon to the rest of the plant, is not restricted to these astomatous pathways and may instead be achieved through the stomata. This might be done as a gas or within a low-surface-tension liquid phase, hijacking the route optimised for photosynthetic gas exchange. As such, while the lipophilic path is the focus of this thesis, it is valuable to introduce and

consider the other two pathways as well. In this way we can assess the relevant importance of the lipophilic pathway for different chemicals and accurately present the limitations of considering only the lipophilic pathway during modelling and experimental data analysis.

2.3.1 Lipophilic pathway

The lipophilic pathway[59] represents diffusion through the lipophilic, non-crystalline domains of the cuticle, namely the lipophilic intracuticular wax and cutin polymer matrix. The semi-crystalline and polymeric nature of the cuticle leads to slow diffusion coefficients on the order of $10^{-18} - 10^{-17}\, m^2 s^{-1}$ as calculated from reconstituted and isolated cuticles[43, 66]. The lipophilicity of the domains through which the lipophilic pathway passes is evident by the relative solubility of chemicals in the cuticle equilibrated with aqueous solution, giving a cuticle-water partition coefficient, K_{cw}. The value of this cuticle-water partition coefficient is generally consistent with estimates of the lipophilicity: a common model parameter used in the literature[67] is the octanol-water partition coefficient, K_{ow}.

Tests on the permeance of the cuticle to the diffusion of material across it through the lipophilic pathway have shown a large size selectivity. A 4-fold increase in the molecular weight of the diffusing chemical was shown to have >1000-fold decrease in the mobility[68, 69], emphasising that diffusion is through a polymeric medium where the size of pores through the matrix structure is on a molecular scale. The use of a lipophilic accelerator[70-73], a species which also dissolves into the lipophilic domain and relaxes the energy barrier to diffusion by plasticising the structure, is common in commercial products. This results in an increase in lipophilic chemical mobility as it becomes less energetically prohibitive for the polymer matrix to flex and for diffusion to occur. The accelerator may also increase the matrix porosity and/or pore size. Similarly, increasing the temperature also increases the mobility[74], most likely by reducing the activation energy to diffusion. Removing the intracuticular wax

also greatly increases the mobility[75-77] and it is hypothesised that this is because crystalline intracuticular wax domains represent impenetrable barriers to diffusion, thus introducing tortuosity to the diffusion path whereby chemicals must diffuse around these domains. Critically, while removal of the intracuticular waxes has been shown to have a significant effect on the barrier properties of the cuticle, removal of the epicuticular waxes has been shown not to[76]. However, the epicuticular waxes are significant in affecting the cuticle's wetting properties and have been shown to reduce the contact between the cuticle and any chemical deposit (either as solid, liquid, or dissolved solute) whether by maximising the contact angle or preserving pockets of air between the deposit and cuticle surface. As such, while not relevant to the mass transport mechanism between the cuticle and a chemical deposit in contact with it, the epicuticular waxes do affect the overall uptake from a given array of mixture droplets.

A common model of the cuticle with respect to the lipophilic pathway is the distinction between the outer 'cuticle proper' layer and the inner 'sorption compartment', as discussed in Section 2.2.3. This is highly relevant to lipophilic uptake. The cuticle proper is the principal transport barrier to chemical influx and efflux of the cuticle (itself the principal transport barrier the whole leaf), despite being generally less thick than the sorption compartment. Hence, diffusion across the cuticle proper is the rate determining step for the overall uptake process. It is hypothesised that the greater density of intracuticular wax in this layer is what contributes to the reduced diffusion across this layer, with the hypothesis that the presence of wax results in impermeable, crystalline wax domains which introduce tortuosity to the diffusion being frequently cited[63]. This is evidenced by the large mobility increases associated with intracuticular wax extraction. This argument also applies to the reduced solubility of the layer as a whole compared to the sorption compartment, since the wax crystals represent an excluded volume fraction. Furthermore, the tortuosity argument helps to justify the unusual

observation that no relationship has been observed between the thickness of a plant's cuticle and its lipophilic permeability, since the diffusion pathway may be effectively independent of the total cuticle thickness if it is highly tortuous, especially if this tortuosity is evolutionarily tuned inverse to the cuticle thickness to give the same permeability. Desorption experiments by Schönherr et al[55, 78] were influential in the adoption of this model when two kinetic regimes were observed for desorption from the inner boundary (rapid desorption from the sorption compartment followed by desorption from the cuticle proper through the sorption compartment) but only one kinetic regime for desorption from the outer boundary (rate determining step is transport through the cuticle proper).

As such, the lipophilic pathway corresponds to diffusion through the cutin polymer matrix through the cuticle proper and sorption compartment, with more rapid diffusion through the sorption compartment with a greater propensity for sequestration in the more lipophilic system followed/preceded by slower diffusion through the cuticle proper, possibly induced by the imposition of a tortuous pathway by the intracuticular wax.

2.3.2 Hydrophilic pathway

While lipophilic and small, uncharged chemicals are able to transfer across the cuticle on the lipophilic pathway, hydrophilic chemicals have low solubilities in the lipophilic cuticle and thus the cuticle might be expected to be impermeable for them. Nevertheless, hydrophilic species demonstrate cuticular permeances that are much higher than expected if they were to engage in the lipophilic pathway[79-84]. This is especially notable for charged species since they would need to lose their hydration shells in order to enter the lipophilic polymer matrix, which is severely unfavourable.

There is building evidence that there is a distinct pathway for the transfer of hydrophilic material along diffusional paths through the cuticle[44, 65]. The mobilities of hydrophilic

penetrants are independent of temperature and plasticiser use and are only weakly affected by the extraction of intracuticular wax. Dependence of these chemicals' mobilities on their molecular size was much lower. However, the mobility does depend significantly on the humidity, with higher humidity translating to greater mobility; this is not the case for lipophilic species. This suggests that the transport is fundamentally different for these two pathways and occurs through different chemical environments.

It is hypothesised that transcuticular paths develop along hydrated channels of polar material through the cuticle. These channels may be supported by the polar groups of the cutin polymer matrix and possibly non-esterified clusters of its monomers. Carbohydrates present in the cuticle may also support paths between the outer surface and the cell wall of the epidermal layer. The hydration of these channels with water is necessary for this pathway to be available, hence the dependence on the humidity. The activation energy for diffusion along this hydrated channel is independent of the temperature and plasticising the lipophilic domains surrounding these channels evidently has no effect. The extraction of intracuticular waxes does have a weak effect: these waxes may influence the pathway either by providing polar functional groups of their own, decreasing the polar proportion of material in the cuticle or by introducing additional tortuosity to the channels by forcing them to circumvent the crystalline wax domains. Removal of the epicuticular waxes still has no effect.

It is crucial to recognise that water, as a small and uncharged molecule that is nevertheless hydrophilic and polar engages in both pathways[54, 85], as will other chemicals with similar properties. However, the majority of organic agrochemicals in common use are insufficiently small to engage in both pathways, and as such will only engage with one of these pathways, with their lipophilicity usually being the deciding factor.

2.3.3 Stomatal uptake

The two pathways described above are strictly astomatous. The need to transfer across the cuticle, an effective barrier to transport, may be circumvented through direct access to the mesophyll through the stomata. This would be highly effective as the mesophyll and leaf structure is already optimised to facilitate chemical transfer and mass transport once beyond the epidermal layer. However, crossing the stomatal aperture is no easy feat.

The transfer of gaseous chemicals through the stomata is viable and an effective route for pollutant gases[86-88]. However, from the perspective of deliberate human chemical intervention, it can be an inefficient delivery method to spray a gaseous vapour over a collection of plants under open conditions, especially if wind is a complicating factor. This is also a potentially dangerous technique due to the risk of contaminating adjacent land, unintended environmental effects, additional threat to the user, and the additional complexity of the necessary equipment. Fumigation as a technique is typically restricted to the treatment of enclosed areas[89] or (covered) soil[90], does not rely on transfer into the plant before delivery to the target pest, and is not usually used to protect living plants.

The application of a volatile chemical as a solid, liquid or dissolved in a carrier phase, such as an aqueous mixture, to the leaf surface, such that astomatous uptake is supplemented by volatilisation of the chemical and gaseous transfer through the stomata may also appear viable[91]. Modelling of this system[92] however demonstrates the difficulties involved in designing such an application with high efficiency and low danger: once again wind is a major obstacle.

An alternative is for the liquid phase to penetrate the stomatal aperture itself, with the liquid either being or solvating the chemical of interest. Calculations have been performed to demonstrate that the restrictions on the surface tension of such a liquid formulation and its

contact angle on interacting with the leaf surface are demanding, though not impossible, and this pathway is significant for specific formulations[93].

The viability of the stomatal pathway is incredibly plant-dependent due to variations in the design of the stomatal complex as well as the distribution of stomata over the leaf surface. The greater complexity of this pathway, combined with the restrictions on when it is relevant, means that this is frequently, and justifiably, neglected in models that are not gas conductance models[94] or models dedicated to assessing the viability of this pathway[95, 96].

2.4 Foliar uptake as an agricultural practice

A significant challenge in agriculture is the efficient use of agrochemicals to bolster crops, improve yield and quality, and minimise environmental contamination[97, 98]. Application of chemicals to crops needs to be scalable, efficient, safe, and affordable. The two major interfaces for the exchange of chemicals between a plant and its environment are through its leaves and through its roots: as such these interfaces are frequently exploited by agronomists for chemical treatments[99]. While the treatment of soil and seeds is common as a route to root uptake, this is most often applied on an industrial scale to pre-emergence plants (i.e. before the plant emerges aboveground during growth). Foliar uptake plays a significant role for managing plants industrially post-emergence due to the efficiency and scalability of spraying over foliage and the avoidance of soil and groundwater interactions. Furthermore, leaves and shoots are frequent target sites for a variety of agrochemicals, leading to the most efficient delivery method being through the leaf interface rather than via the soil, roots, and stem.

The focus and scope of this thesis is on the mass transfer at interfaces and membranes, principally via diffusion. Since the major barrier to foliar uptake is the cuticular membrane, our modelling of interfacial diffusion processes lends itself better to the study of foliar uptake than root uptake; as a result, we have restricted our focus to foliar uptake.

We introduce the practical aspects of utilising foliar uptake in agriculture in this section and relate these features to the topics discussed in previous sections. We discuss: the purposes under which foliar uptake is commonly used as a route to chemical treatment, the properties of the agrochemicals of interest and their significance, the typical barriers to biological activity between the product and target site, how tackling this problem of optimising delivery and efficacy has informed modern formulation design, and finally how this relates to improved sustainability.

2.4.1 Purpose of chemical treatment via foliar uptake

There are numerous drives to treat plants chemically in an agricultural context. Two broad categories are: fertilisers, which seek to feed or supplement the target plant, and pesticides, which seek to kill a target species in defence of a crop. Pesticides are differentiated by what they target: herbicides target other plants, such as weeds; insecticides target insects; fungicides target fungi; bactericides target bacteria; and so on.

The action of foliar fertilisers and herbicides generally necessitate the delivery of the chemical into either the immediate plant living tissue or into the vascular system. Herbicides can be contact herbicides, in which case they take action at the leaf at the site of application, for example by disrupting the photosynthetic pathway or inducing oxidative stress, and their primary effect is localised damage that ultimately kills the plant, or they can be systemic herbicides, in which case they do not target the leaf but must be transported elsewhere in the plant, for example a growth site such as the shoots, where their primary effect is not localised and affects the plant generally. Foliar fertilisers also act in a systemic manner.

The design of these chemicals is highly dependent on this distinction since it determines whether their activity is enhanced or hindered by more effective transfer to and along the vascular system. Dilution of contact herbicides by transport across the whole plant and

removal from the leaf target site results in reduced activity if the chemical is effectively transported by the xylem or phloem. Meanwhile the activity of systemic chemicals requires this vascular transport for delivery to their target sites. This informs some of the optimal physicochemical properties for these chemicals, which will be discussed further in the next sub-section.

Nevertheless, both herbicides and foliar fertilisers require transfer across the cuticle. A more rapid transfer minimises exposure to loss processes on the leaf surface, discussed in Section 2.4.3, reduces the time until chemical activity, and may result in more effective action by maintaining a higher concentration at the target site. This is not necessarily the case for pesticides that do not target the plants they are applied to, such as fungicides.

The usual strategy of applying non-herbicidal pesticides to the plants that benefit from protection is to retain the pesticide within or on the plant, for as long as possible, at biologically effective concentrations, and in a location where delivery to the target is most effective or where the plant is vulnerable to pest attack. This will vary from pesticide to pesticide and target to target. It may be that transferring the chemical across the cuticle may be a hindrance to its effect: if the target pest penetrates through the cuticle to parasitise the plant (e.g. fungi) or if the target feeds on the leaves whole (e.g. certain insects and larger herbivores) then concentrating the chemical in the cuticle may be the optimal strategy for delivery to the pest and transcuticular transfer may act as a loss mechanism. In such cases, sequestering the chemical in the cuticle is an instrumental objective, with effective dissolution into the cuticle but ineffective leaching out of it, such as into the epidermis. In other cases, it may be preferred to cross the cuticle and deliver the chemical to other parts of the plant, e.g. via the vascular pathway, such as to defend the vascular pathway itself, e.g.

from bacteria or sap-consuming insects such as aphids, or to defend other sections of the plant, such as the roots.

A complete understanding of the interaction between different agrochemicals and the cuticles of target and non-target plants is thus necessary for the optimisation of the chemical delivery. Having discussed the cuticle in depth in previous sections, we now turn to the physicochemical properties of the agrochemicals, the range they exhibit and their relevance to their activity and delivery.

2.4.2 Agrochemical properties

The key properties that determine an agrochemical's practical viability in the context of transport are its size, its solubility in different media, its lipophilicity, its pK_a, and its diffusion coefficient. Furthermore, its activity at the target site both for the target and for any other species is important in assessing the efficacy and toxicology of the chemical.

For the process of crossing the cuticle, the lipophilicity and size are the two predominant physicochemical parameters to consider as these determine which uptake pathway the chemical may use and inform agronomists on what their likely mobility shall be (as described in Section 2.3). Generally, smaller compounds are always preferred. Lipophilic compounds are also generally preferred due to the greater effectiveness of the lipophilic pathway and the rapid uptake into the cuticle if the carrying medium is less lipophilic. However, if the compound is too lipophilic there is an observed risk of sequestration in the cuticle and an ineffective transfer out of the cuticle into the plant tissue. This may in fact be preferable for certain fungicides and insecticides that reach their targets through contact between the cuticle and target pest.

Additionally, whether the species of interest is charged or has an acid-base dissociation is important for determining the pathway as well as the overall permeance. In the case of an acid-base equilibrium, charged products may progress along the hydrophilic pathway while undissociated moiety may progress along the lipophilic to give a composite uptake behaviour. Furthermore, dissociation while diffusing within the cutin matrix is possible, leading to sequestration and reduced mobility. Evidence suggests that the isoelectric point of plant cuticles, the pH at which they are uncharged when immersed in water, is around 3 [100], which informs whether a weak acid or base will dissolve into the cuticle as its undissociated or dissociated form and how its solubility may depend in each form on the pH of the solution the chemical is applied within. Typically, the undissociated form of a chemical exhibits greater mobility across lipidic bio-membranes such as the plant cuticle and so this is usually sought after for optimising cuticular uptake. The pK_a of a prospective chemical may be of additional importance if dissociation occurs in the plant tissue beyond the cuticle, which can lead to an acid-trapping effect and more effective transcuticular transport, similar to the weak-acid hypothesis for phloem mobility[101].

Agrochemicals may also be designed to maximise or minimise phloem mobility (as discussed in the previous section). The properties for optimal phloem mobility are expressed in the work by Kleier and the development of Münch theory[29-32]: a weak-acid dissociates once inside the phloem, leading to more effective transport into the phloem, while high lipophilicity facilitates transport across the lipidic boundary into the phloem. Attaching weak-acid moiety has been shown to be effective at improving an agrochemical's phloem mobility, although in some cases it can reduce the chemical's activity upon reaching the target site.

2.4.3 Additional barriers

While the plant cuticle is the principal transport barrier for foliar uptake, as well as an effective solubility barrier for hydrophilic compounds and sequestration trap for lipophilic compounds, there are other processes at work that can slow or prevent the delivery of the active agrochemical. While these processes are not the focus of this thesis, it is valuable to mention them here as it emphasises the additional challenges faced by agronomic formulation designers and the invalidity of optimising the formulation and chemical design for the transcuticular uptake only. As such, we recognise the context of the results of this thesis as a part of a much broader picture. The loss processes we consider here are presented schematically in Figure 2.6.

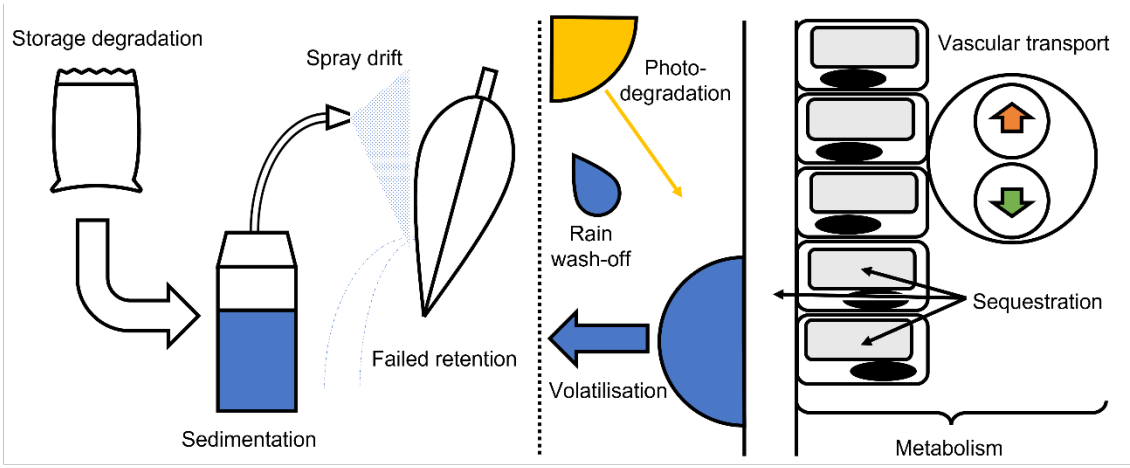


Figure 2.6: Schematic illustration of additional loss processes that affect the efficacy of a foliar applied agrochemical between commercial product and arrival at the target site. Processes on the left-hand side occur before the product is deposited on the leaf surface, right-hand side processes occur once the product has arrived onto the leaf surface. We present the agrochemical as a suspension in water (blue), the cuticle as an infinite white membrane between the environment and leaf epidermal cells (represented with grey vacuoles and black nuclei), and the vascular bundle as one xylem tube (green arrow) and one phloem tube (orange arrow) within a circular sheath bundle. We demonstrate that metabolism can occur at any stages after transcuticular uptake. This figure is not to scale.

Before the agrochemical reaches the leaf, it is packaged, stored, mixed with a carrying solution (most commonly water) and applied as a spray. Chemical, thermal, photo- and bio-degradation are all risks during storage and the compound must be stable to each of these processes to be commercially viable. The chemical must be stable to mixing with water in air

and should not engage in chemical reaction or extreme endo- or exothermicity of mixing. Particulate based formulations must suspend in water and not coagulate or sediment. On spraying, droplets can drift and fail to land on the leaf at all. Upon landing on the leaf, the droplets must be retained on the surface. This involves an interplay of droplet size, spray velocity, surface tension and droplet-cuticle affinity. A poor coverage of the leaf surface with formulation will reduce the surface area of contact and thus reduce the rate of uptake; this can result from drift, poor retention, and also poor wetting.

Once on the leaf surface, the formulation is exposed to wash-off by rain, potentially harsh sunlight leading to photo-degradation, volatilisation and loss into the atmosphere, mechanical removal, and crystallisation of the agrochemical.

After transcuticular uptake, the agrochemical will be subject to chemical reaction within the plant tissue (which may be desirable, e.g. for contact herbicides) and metabolism by the plant (which is a loss process but also a necessary step to prevent persistence of the agrochemical in the plant and bioaccumulation). Mobility of the compound in the xylem or phloem may be desirable or undesirable, depending on whether the chemical's action is systemic or not. Finally, sequestration involves (effectively) irreversible dissolution into a high-affinity phase, such as the cuticle or the cell vacuole, or chemical immobilisation; this also prevents the chemical from reaching its target site while not (necessarily) degrading the chemical.

2.4.4 Formulation design

The design of formulations seeks to overcome these challenges involved in the delivery of an active agrochemical to its target site. Formulations typically consist of an active ingredient (A.I.), a carrier liquid and numerous additives, often called adjuvants. The established formulation types are often given an acronymic abbreviation, such as S or EC (see below), which describe how the form in which they are sold to the user before mixing with the carrier

liquid for spraying. The complexity of formulations has significantly grown in complexity in recent decades[7, 98, 102], increasing the number of tools available to a formulation chemist and the number of viable commercial products. We provide a brief overview of some of the relevant aspects of formulation design that will inform the studies we present in later chapters.

For the effective delivery of the chemical to the leaf surface, a carrier phase is used which is significantly cheaper than the A.I. . Water is the common choice, although oil-based formulations are sometimes preferred. These cheap carrier liquids are chosen for their price, abundance, the familiarity of their physicochemical properties, their safety, and their inertness. Preferably, the active agrochemical, and any additives, will be soluble within the carrier phase. The simplest formulations are thus solutions: S (solution), C (concentrated solution) or LC (liquid concentrate).

However, it may be the case that the A.I. is not soluble in the desired carrier phase. This is common for lipophilic A.I. compounds in water. The formulation may instead be provided as an organic solvent concentrate which emulsifies with water, usually with surfactant adjuvants involved: such as EC (emulsifiable concentrate) formulations. As well as formulations that form emulsions with water, others produce well-dispersed particulate suspensions when mixed with water. The particles may be the A.I. in solid form (suspension concentrates SC, pellets P or PS, wettable powders WP, or water-dispersible granules WDG), have the A.I. bound to the surface of inert particles (dust D and granules G), or contain the A.I. in encapsulated particles with another inert phase (M). Encapsulated particles are of particular interest as complex release profiles are available depending on how the A.I. is released from its encapsulation. This could involve Fickian diffusion[103], a particle burst mechanism[104], particle swelling[105, 106], particle erosion[107, 108], and triggered release[109], such as by pH. As well

as additional control over the timing of the release and thereby uptake, particulate systems provide greater safety to the user and easier decontamination. Many pesticidal compounds are lipophilic and so formulations that form heterogeneous spray solutions are very common.

There are many adjuvants that may be included in a formulation to tweak its properties, such as the surface tension, emulsifiability, stability, particulate dispersity, volatility, hydration after solvent evaporation, surface retention, viscosity, and so on. A particularly interesting application is that of accelerator adjuvants[70, 110] which increase chemical mobility within the cuticle, namely through the lipophilic pathway. The exact mechanisms by which these compounds work to improve the permeability of the cuticle are still debated and there is even disagreement over whether different adjuvants actually are accelerators or not. Some work refers to these adjuvants as plasticisers, however the evidence that their plasticisation is what causes increased uptake when they are included as additives is usually inconclusive. Adjuvants frequently perform several functions at once, making it difficult to extract which effects are influencing the active ingredient's uptake rate. An example would be an accelerator adjuvant which also improves the leaf-droplet wettability: it is then difficult to conclude to what extent any improved uptake is due to an increased surface area per droplet or an adjuvant-cuticle interaction.

It is not uncommon for the active ingredient to exhibit properties that make it undesirable to be applied in its active form. This may be because it is susceptible to a loss process, such as photo-degradation or metabolism, has undesirable physicochemical traits, as a poor lipophilicity for cuticular uptake, or is hazardous to use. An effective solution is to apply a compound that will convert into the active chemical later, ideally after delivery to the target site. A compound that converts to an active pesticide after delivery is called a pro-pesticide. Using pro-pesticides allows agronomists to design safer formulations using chemicals with

improved delivery. It is worth noting that the chemical crossing the cuticle may not be the active chemical itself.

2.4.5 Drive towards sustainability

The use of pesticides in industrial scale agriculture has numerous benefits. It provides a highly scalable, rapid method to tackle pests that is manpower efficient and relatively cheap. It provides the manufacturer and user a large amount of control on the intended effects, as well as the how, when, and where of treatment. However, pesticide use does have its drawbacks. It can be materially inefficient, presents a potential danger to the user and consumer, and represents an environmental contamination risk. Agrochemicals may persist or accumulate in the environment and product. Pesticides also pose a risk to non-pest species and are a threat to biodiversity.

While the study and development of pesticides in the past has been focussed on exploring new options to offer to customers by competing on price, effectiveness, ease of use and, in the case of pesticides, their range of target species, greater pressure is now placed on the responsible and sustainable development of pesticides into the future[9, 111]. While the old drivers are still present, there is now focus on enhancing the selectivity of pesticide activity to reduce damage to the wider ecosystem, on mitigating loss processes to enhance chemical efficiency, on reducing environmental harm, and on ensuring the safety of humans and animals throughout the product cycle.

It is thus vital to develop our understanding of how these chemicals transfer into and across the cuticle as the first and most significant barrier to the successful delivery of these chemicals. The development of models and the performance of meaningful simulation is increasingly central to research in this area[11]. Improved uptake models assist in the screening and design of agrochemicals for their foliar uptake efficacy. This will reduce the exposure of

the environment to the chemical (and vice versa), improve the efficiency of new formulations (thus requiring reduced chemical loads) and allow greater control of how these chemicals interact with the biosphere. This motivates the study conducted in Chapters 5 and 6.

In the next chapter we introduce the concepts that underpin the modelling and simulation work we have performed in this thesis in the pursuit of these goals. These concepts shall be presented generally before we discuss how they might be applied to the specific problems we wish to consider.

References

1. M. Ingrouille, *Diversity and Evolution of Land Plants*, Chapman & Hall, 1992.
2. M. C. Press, *The New Phytologist*, 1999, **143**, 213-219.
3. H. R. Bolhàr-Nordenkampf and G. Draxler, in *Photosynthesis and Production in a Changing Environment: A Field and Laboratory Manual*, eds. D. O. Hall, J. M. O. Scurlock, H. R. Bolhàr-Nordenkampf, R. C. Leegood and S. P. Long, Springer Netherlands, Dordrecht, 1993, DOI: 10.1007/978-94-011-1566-7_7, pp. 91-112.
4. T. J. Brodribb, T. S. Feild and L. Sack, *Functional Plant Biology*, 2010, **37**, 488-498.
5. E. Garnier, *Variation in Leaf Structure: an Ecophysiological Perspective*, Cambridge University Press, Cambridge, UK, 1999.
6. V. P. Gutschick, *The New Phytologist*, 1999, **143**, 3-18.
7. D. L. Shaner and H. J. Beckie, *Pest Management Science*, 2014, **70**, 1329-1339.
8. C. de Perre, K. W. J. Williard, J. E. Schoonover, B. G. Young, T. M. Murphy and M. J. Lydy, *Environmental Toxicology and Chemistry*, 2015, **34**, 197-207.
9. D. K. Hazra, R. Karmakar, R. Poi, S. Bhattacharya and S. Mondal, *Archives of Agriculture and Environmental Science*, 2017, **2**, 232-237.
10. H. Köhler and R. Triebskorn, *Science*, 2013, **341**, 759-765.
11. J. A. Zabkiewicz, *Crop Protection*, 2007, **26**, 312-319.
12. R. B. Primack and H. Kang, *Annual Review of Ecology and Systematics*, 1989, **20**, 367-396.
13. K. J. Niklas, *The Evolutionary Biology of Plants*, University of Chicago Press, Chicago, US, 1997.
14. J. Schönherr, in *Physiological Plant Ecology II*, Springer, 1982, pp. 153-179.
15. M. Riederer and L. Schreiber, *Journal of Experimental Botany*, 2001, **52**, 2023-2032.
16. E. M. Kramer and V. F. Irish, *Nature*, 1999, **399**, 144-148.
17. J. Picazo-Aragonés, A. Terrab and F. Balao, *International Journal of Molecular Sciences*, 2020, **21**, 8956.
18. A. M. Ellison and N. J. Gotelli, *Trends in Ecology & Evolution*, 2001, **16**, 623-629.
19. A. Kadioglu and R. Terzi, *The Botanical Review*, 2007, **73**, 290-302.
20. J. Koricheva, H. Nykänen and E. Gianoli, *The American Naturalist*, 2004, **163**, E64-E75.
21. A. T. Moles, B. Peco, I. R. Wallis, W. J. Foley, A. G. B. Poore, E. W. Seabloom, P. A. Vesk, A. J. Bisigato, L. Cella-Pizarro, C. J. Clark, P. S. Cohen, W. K. Cornwell, W.

Edwards, R. Ejrnæs, T. Gonzales-Ojeda, B. J. Graae, G. Hay, F. C. Lumbwe, B. Magaña-Rodríguez, B. D. Moore, P. L. Peri, J. R. Poulsen, J. C. Stegen, R. Veldtman, H. von Zeipel, N. R. Andrew, S. L. Boulter, E. T. Borer, J. H. C. Cornelissen, A. G. Farji-Brener, J. L. DeGabriel, E. Jurado, L. A. Kyhn, B. Low, C. P. H. Mulder, K. Reardon-Smith, J. Rodríguez-Velázquez, A. De Fortier, Z. Zheng, P. G. Blendinger, B. J. Enquist, J. M. Facelli, T. Knight, J. D. Majer, M. Martínez-Ramos, P. McQuillan and F. K. C. Hui, *New Phytologist*, 2013, **198**, 252-263.

22. A. M. Borsuk, A. B. Roddy, G. Théroux-Rancourt and C. R. Brodersen, *New Phytol*, 2022, **234**, 946-960.
23. B. J. Glover, *Journal of Experimental Botany*, 2000, **51**, 497-505.
24. N. Martin-StPaul, S. Delzon and H. Cochard, *Ecology Letters*, 2017, **20**, 1437-1447.
25. J. A. Bunce, *Plant, Cell & Environment*, 1997, **20**, 131-135.
26. H. H. Dixon and J. Joly, *Philosophical Transactions of the Royal Society of London, Series B*, 1894, **186**, 563-576.
27. M. T. Tyree, *Journal of Experimental Botany*, 1997, **48**, 1753-1765.
28. U. Zimmermann, H. Schneider, L. H. Wegner and A. Haase, *New Phytologist*, 2004, **162**, 575-615.
29. E. Munch, *Stoffbewegungen in der Pflanze*, Gustav Fischer Verlag, Jena, Germany, 1930.
30. B. T. Grayson and D. A. Kleier, *Pesticide Science*, 1990, **30**, 67-79.
31. D. A. Kleier, *Pesticide Science*, 1994, **42**, 1-11.
32. D. A. Kleier and C. H. Francis, *Weed Science*, 1996, **44**, 749-756.
33. H. Lambers and H. Poorter, in *Advances in Ecological Research*, eds. M. Begon and A. H. Fitter, Academic Press, 1992, vol. 23, pp. 187-261.
34. J. R. Ehleringer and H. A. Mooney, *Oecologia*, 1978, **37**, 183-200.
35. D. M. Gates, *Biophysical Ecology*, Springer-Verlag, New York, USA, 1980.
36. B. Bhushan and Y. C. Jung, *Journal of Physics: Condensed Matter*, 2008, **20**, 225010.
37. K. Koch, B. Bhushan and W. Barthlott, *Soft Matter*, 2008, **4**, 1943-1963.
38. J. T. Martin and B. E. Juniper, *The Cuticles of Plants*, Edward Arnold, London, 1970.
39. E. Domínguez, J. A. Heredia-Guerrero and A. Heredia, *New Phytologist*, 2011, **189**, 938-949.
40. V. Fernández, H. A. Bahamonde, J. Javier Peguero-Pina, E. Gil-Pelegrín, D. Sancho-Knapik, L. Gil, H. E. Goldbach and T. Eichert, *Journal of Experimental Botany*, 2017, **68**, 5293-5306.
41. V. Bhanot, S. V. Fadanavis and J. Panwar, *Environmental and Experimental Botany*, 2021, **183**, 104364.
42. M. Riederer and C. Müller, *Biology of the Plant Cuticle*, Blackwell Publishing Ltd, 2006.
43. L. Schreiber, *Journal of Experimental Botany*, 2006, **57**, 2515-2523.
44. V. Fernández and T. Eichert, *Critical Reviews in Plant Sciences*, 2009, **28**, 36-68.
45. R. Bourgault, S. Matschi, M. Vasquez, P. Qiao, A. Sonntag, C. Charlebois, M. Mohammadi, M. J. Scanlon, L. G. Smith and I. Molina, *Annals of Botany*, 2019, **125**, 79-91.
46. B. Xu, L. Taylor, B. Pucker, T. Feng, B. J. Glover and S. F. Brockington, *New Phytologist*, 2021, **229**, 2324-2338.
47. J. L. Morris, M. N. Puttick, J. W. Clark, D. Edwards, P. Kenrick, S. Pressel, C. H. Wellman, Z. Yang, H. Schneider and P. C. J. Donoghue, *Proceedings of the National Academy of Sciences*, 2018, **115**, E2274-E2283.
48. V. Fernández, P. Guzmán-Delgado, J. Graça, S. Santos and L. Gil, *Frontiers in Plant Science*, 2016, **7**.

49. L. Samuels, L. Kunst and R. Jetter, *Annu. Rev. Plant Biol.*, 2008, **59**, 683-707.
50. T. H. Yeats, G. J. Buda, Z. Wang, N. Chehanovsky, L. C. Moyle, R. Jetter, A. A. Schaffer and J. K. C. Rose, *The Plant Journal*, 2012, **69**, 655-666.
51. R. Jetter and M. Riederer, *Plant Physiology*, 2015, **170**, 921-934.
52. L. Kunst and A. L. Samuels, *Progress in Lipid Research*, 2003, **42**, 51-80.
53. R. C. Kirkwood, *Pesticide Science*, 1999, **55**, 69-77.
54. V. Fernández, E. Gil-Pelegrín and T. Eichert, *The Plant Journal*, 2021, **105**, 870-883.
55. J. Schönherr and M. Riederer, *Archives of Environmental Contamination and Toxicology*, 1988, **17**, 13-19.
56. J. Schönherr and M. Riederer, in *Reviews of Environmental Contamination and Toxicology*, Springer, 1989, pp. 1-70.
57. J. Wattendorff and P. J. Holloway, *Annals of Botany*, 1980, **46**, 13-28.
58. H. S. Heide-Jørgensen, *Planta*, 1991, **183**, 511-519.
59. A. Buchholz, *Journal of Experimental Botany*, 2006, **57**, 2501-2513.
60. T. Mérida, J. Schönherr and H. W. Schmidt, *Planta*, 1981, **152**, 259-267.
61. G. J. Buda, T. Isaacson, A. J. Matas, D. J. Paolillo and J. K. C. Rose, *The Plant Journal*, 2009, **60**, 378-385.
62. P. Guzmán, V. Fernández, M. L. García, M. Khayet, A. Fernández and L. Gil, *Plant Physiology and Biochemistry*, 2014, **76**, 1-6.
63. P. Baur, H. Marzouk and J. Schönherr, *Plant, Cell & Environment*, 2002, **22**, 291-299.
64. P. Holloway, presented in part at the Linnean Society symposium series, 1982.
65. L. Schreiber, *Annals of Botany*, 2005, **95**, 1069-1073.
66. L. Schreiber, M. Riederer and K. Schorn, *Pesticide Science*, 1996, **48**, 117-124.
67. F. Kerler and J. Schönherr, *Archives of Environmental Contamination and Toxicology*, 1988, **17**, 1-6.
68. P. Baur, A. Buchholz and J. Schönherr, *Plant, Cell & Environment*, 1997, **20**, 982-994.
69. A. Buchholz, P. Baur and J. Schönherr, *Planta*, 1998, **206**, 322-328.
70. J. Schönherr and P. Baur, *Pesticide Science*, 1994, **42**, 185-208.
71. P. Baur, H. Marzouk, J. Schönherr and B. T. Grayson, *Journal of Agricultural and Food Chemistry*, 1997, **45**, 3659-3665.
72. P. Baur, *Recent Research Developments in Agricultural and Food Chemistry*, 1998, **2**, 809-837.
73. P. Baur, *Journal of Agricultural and Food Chemistry*, 1999, **47**, 753-761.
74. P. Baur and J. Schönherr, *Chemosphere*, 1995, **30**, 1331-1340.
75. S. Santier and A. Chamel, *Plant Physiology and Biochemistry*, 1998, **36**, 225-231.
76. V. Zeisler-Diehl, Y. Müller and L. Schreiber, *Journal of Plant Physiology*, 2018, **227**, 66-74.
77. S. Staiger, P. Seufert, K. Arand, M. Burghardt, C. Popp and M. Riederer, *Pest Management Science*, 2019, **75**, 3405-3412.
78. P. Baur, H. Marzouk, J. Schönherr and H. Bauer, *Planta*, 1996, **199**, 404-412.
79. J. Schönherr and M. Luber, *Plant and Soil*, 2001, **236**, 117-122.
80. J. Schönherr, *Journal of Plant Nutrition and Soil Science*, 2001, **164**, 225-231.
81. J. Schönherr, *Journal of Experimental Botany*, 2006, **57**, 2471-2491.
82. E. C. Tredenick, T. W. Farrell, W. A. Forster and S. T. P. Psaltis, *Frontiers in Plant Science*, 2017, **8**, 746.
83. R. J. L. Ramsey, G. R. Stephenson and J. C. Hall, *Pesticide Biochemistry and Physiology*, 2005, **82**, 162-175.
84. C. Popp, M. Burghardt, A. Friedmann and M. Riederer, *Journal of Experimental Botany*, 2005, **56**, 2797-2806.
85. E. C. Tredenick and G. D. Farquhar, *Nature Communications*, 2021, **12**, 5042.

86. G. A. Beattie and J. R. Seibel, *Chemosphere*, 2007, **68**, 528-536.
87. A. Roth-Nebelsick, *Annals of Botany*, 2007, **100**, 23-32.
88. N. L. L. Steyaert, M. Hauck, S. W. H. Van Hulle and A. Jan Hendriks, *Chemosphere*, 2009, **77**, 727-732.
89. E. J. Bond and H. A. U. Monro, *Manual of Fumigation for Insect Control*, FAO Publishing, Rome, Italy, 1984.
90. https://www.epa.gov/soil-fumigants, 2023).
91. G. Kerstiens, R. Federholzner and K. J. Lendzian, *Agriculture, Ecosystems & Environment*, 1992, **42**, 239-253.
92. M. Riederer, A. Daiß, N. Gilbert and H. Köhle, *Journal of Experimental Botany*, 2002, **53**, 1815-1823.
93. J. r. Schönherr and M. J. Bukovac, *Plant Physiology*, 1972, **49**, 813-819.
94. G. Damour, T. Simonneau, H. Cochard and L. Urban, *Plant, Cell & Environment*, 2010, **33**, 1419-1438.
95. T. Eichert, A. Kurtz, U. Steiner and H. E. Goldbach, *Physiologia Plantarum*, 2008, **134**, 151-160.
96. J. Burkhardt, S. Basi, S. Pariyar and M. Hunsche, *New Phytologist*, 2012, **196**, 774-787.
97. P. Jeschke, *Pest Management Science*, 2016, **72**, 433-455.
98. T. C. Sparks and B. A. Lorsbach, *Pest Management Science*, 2017, **73**, 672-677.
99. I. J. Graham-Bryce, G. W. Cooke, N. W. Pirie and G. D. H. Bell, *Philosophical Transactions of the Royal Society of London. B, Biological Sciences*, 1977, **281**, 163-179.
100. J. Schönherr and R. Huber, *Plant Physiology*, 1977, **59**, 145-150.
101. F. C. Hsu and D. A. Kleier, *Journal of Experimental Botany*, 1996, **47**, 1265-1271.
102. Y. Zhang, B. A. Lorsbach, S. Castetter, W. T. Lambert, J. Kister, N. X. Wang, C. J. R. Klittich, J. Roth, T. C. Sparks and M. R. Loso, *Pest Management Science*, 2018, **74**, 1979-1991.
103. P. L. Ritger and N. A. Peppas, *Journal of Controlled Release*, 1987, **5**, 23-36.
104. X. Huang and C. S. Brazel, *Journal of Controlled Release*, 2001, **73**, 121-136.
105. J. Siepmann, H. Kranz, R. Bodmeier and N. A. Peppas, *Pharmaceutical Research*, 1999, **16**, 1748-1756.
106. J. Siepmann and N. A. Peppas, *Advanced Drug Delivery Reviews*, 2012, **64**, 163-174.
107. H. B. Hopfenberg, in *Controlled Release Polymeric Formulations*, American Chemical Society, 1976, vol. 33, ch. 3, pp. 26-32.
108. J. Heller, *Biomaterials*, 1980, **1**, 51-57.
109. A. P. Esser-Kahn, S. A. Odom, N. R. Sottos, S. R. White and J. S. Moore, *Macromolecules*, 2011, **44**, 5539-5553.
110. C. J. Wang and Z. Q. Liu, *Pesticide Biochemistry and Physiology*, 2007, **87**, 1-8.
111. A. Knowles, *The Environmentalist*, 2008, **28**, 35-44.

3 Modelling diffusion

The goal of this thesis is to develop relevant models for the study of electrochemistry (introduced in Section 1) and foliar plant uptake (introduced in Section 2) and to perform simulations for the prediction of physical behaviours at these interfacial systems under diffusion to achieve practical insights. In this chapter, we introduce the approaches we have taken to perform these numerical simulations through the solution of partial differential equations (PDEs) governing the diffusional mass transport. First, we introduce our approach to constructing a model for simulation. We then present the techniques we have used to perform simulations. We next establish how the simulation space is constructed, including considerations of its dimensionality and gridding. Finally, we illustrate the importance of testing the convergence of simulation results and validating their accuracy for benchmarks to evidence accuracy in similar but unknown systems. Much of the content in this chapter is covered in relevant textbooks[1-5].

3.1 Model construction

It would be unscientific to propose that someone could create a perfect representation of reality and predict its behaviour with exact accuracy. Representing such an abstraction of reality computationally would be even more unbelievable. Our knowledge of physics is finite and incomplete, our computational systems are limited by the capabilities of hardware, and the computational cost of such an endeavour would be incalculable. Nevertheless, it is possible, with today's technology, to perform meaningful and informative simulations of reality that achieve levels of accuracy comparable to experimental results. A perfect digital representation of the universe is not required, we can instead develop a model of the system we wish to study to achieve the accuracy we seek. Indeed, through the development of a model, one can simplify the system of interest and, in so doing, more easily identify relevant

processes and achieve physical insights into how these processes work individually and generally.

The model requires approximations of the system and physics, which must be carefully chosen, clearly explained, and justified in order to maximise the model's utility for generating predictions at the desired accuracy. The model considers a finite subsection of the universe and furthermore only an incomplete representation of that subsection (due to constraints on memory and efficiency). In addition, it is often not necessary to incorporate many of the involved processes and information into a model if their influence over the system is small. The construction of a model is performed to achieve the desired accuracy and precision while minimising the computational requirements to achieve that result (memory, time, component cost, etc). A model is thus usually constructed in a manner that facilitates its computation and interpretation.

In this section, we introduce the approaches taken for constructing the models whose results we present in the following chapters 4, 5, and 6. We first consider our use of Fick's Second Law (introduced in Section 1.2) as a model of mass transport and the simulation of this modelled physics by solving it. Next, we discuss the imposition of boundary conditions, both to contain the simulation space and enforce a unique solution. Finally, we propose the renormalisation of the physical parameters of a system into dimensionless values in order to simplify the problem and generalise a solution's results.

3.1.1 Fick's Second Law as a PDE for describing mass transport

Fick's Second Law[6] is produced by enforcing mass conservation on Fick's First Law (as described in Section 1.2):

$$\frac{\partial c}{\partial t} = D\nabla^2 c = D\left\{\frac{\partial^2 c}{\partial x^2} + \frac{\partial^2 c}{\partial y^2} + \frac{\partial^2 c}{\partial z^2}\right\} \qquad \text{Equation 3.1}$$

where c is the concentration of a species at a given point in space and time, t is the temporal coordinate, D is the diffusion coefficient, $\nabla^2 c$ is the Laplacian of the concentration field, and $\{x, y, z\}$ demonstrate our use of Cartesian spatial coordinates.

We have used this equation to model mass transport in the systems we simulate in future chapters. However, it is important to acknowledge the approximations inherent to this. First of all, diffusion is the only active mass transport process considered by Fick's Second Law, meaning that the bulk fluid is modelled as static and without potential energy gradients. How reasonable this is with respect to advection and migration has been discussed in Chapter 1 and is reiterated in Chapters 4, 5, and 6.

Secondly, this equation models diffusion on a macroscopic scale such that the stochastic movements of individual particles are ignored: the species of interest is modelled as a continuous, concentration field instead of as discrete particles. All of the systems we simulate in this thesis are on the scale of tens of nanometres or larger, while the species whose diffusion we simulate are molecular and at high concentrations. We conclude that macroscopic perspective is valid. Furthermore, we are not interested in individual particle movements but with the expected flux and concentration profiles over time. As such, there is insufficient benefit to justify the computational cost of treating the diffusing particles discretely at the concentrations and relative length-scales we consider.

Finally, under this model, the medium within which diffusion occurs is homogeneous (or at least continuous), with any (significant) heterogeneity described by a boundary condition at an interface. The heterogeneity included within a model should be specific to each system, and so this is considered individually in each chapter. As a broad rule of thumb, different phases should be separated by an interface and a boundary condition, with potentially different diffusion coefficients either side. If the heterogeneity in a phase is microscopic (on

the scale of the model/simulation) and generally isotropic, its influence on the mass transport may be incorporated into the diffusion coefficient by instead using a space-averaged value. If the heterogeneity is very anisotropic, this could be reflected on a macroscopic scale with distinct diffusion coefficients for each direction[5, 7, 8], e.g.:

$$\frac{\partial c}{\partial t} = D_x \frac{\partial^2 c}{\partial x^2} + D_y \frac{\partial^2 c}{\partial y^2} + D_z \frac{\partial^2 c}{\partial z^2} \qquad \text{Equation 3.2}$$

In this thesis, we only consider isotropic media and use a single diffusion coefficient, as per Equation 3.1.

Under these approximations, Fick's Second Law accurately describes diffusional mass transport. Solving the partial differential equation (PDE) produces a family of solutions, each of which satisfies different boundary conditions, which are constraints on the solution that can be used to define a system and generate a unique solution. While in some cases this can be done analytically[5], for more complex sets of boundary conditions a numerical approach is much faster at providing satisfying results. We now describe fully what boundary conditions are and how they are used.

3.1.2 Boundary conditions

Boundary conditions impose constraints on the solution of a partial differential equation. Doing so is necessary to achieve a unique solution and thus make physical predictions. An incomplete set of boundary conditions will lead to a family of possible solutions with no unique answer. If this is the case, we say that the system is ill-posed and that this shall lead to the failure of numerical procedures.

Boundary conditions are typically imposed at interfaces and describe the geometry of the space (and time) contained within the model/simulation. The space included within a simulation is called the simulation space, or simulation domain (which may include the

temporal dimension). Boundary conditions are required at the domain boundaries in order to ensure the solution's uniqueness. Such boundary conditions may be chosen to enforce a symmetry or periodicity. Boundary conditions that present the simulation domain as a closed system are also common. Boundary conditions can also be applied within the simulation domain to describe heterogeneity, such as interfaces between phases. If the simulation is time-dependent, then an initial boundary condition is also generally required for uniqueness. Not all simulations of Fick's Second Law need to be time-dependent: time-independent solutions are valuable for predicting the steady state of a diffusional system where $\frac{\partial c}{\partial t}=0$ after infinite time.

For physical models, five generic categories for boundary conditions have developed, namely Dirichlet, Neumann, Cauchy, Robin, and mixed boundary conditions. Dirichlet conditions impose a constraint on the value of the solution at an interface (for example $c=f(x,y,z,t)$), while Neumann conditions impose a constraint on the first derivative of the solution (for example $\frac{\partial c}{\partial x}=g(x,y,z,t)$), where f and g are appropriate functions. A Cauchy boundary imposes a Dirichlet *and* a Neumann condition. A Robin boundary imposes a constraint on a linear combination of the solution value and its derivative. Finally, a mixed boundary involves the imposition of mutually exclusive Neumann or Dirichlet conditions at disjoint parts of the boundary (for example, on a 2D planar boundary, $c|_{x<0}=1$ and $\left.\frac{\partial c}{\partial y}\right|_{x\geq 0}=0$). These different types of boundary conditions may be used to define a model system.

In Chapter 1, we have already introduced examples of Dirichlet conditions being used to model perfect sources $(c=c_0)$ and perfect sinks $(c=0)$. They may also be used to model a

Nernstian electrode surface: $c_A = c_B e^{\theta} = \frac{c_0 e^{\theta}}{1+e^{\theta}}$, where $\theta = \frac{\left(E - E_f^0\right)nF}{RT}$, as derived for a one-electron transfer in sub-section 1.3.1, and imposing $c_A + c_B = c_0$.

A symmetry condition across a boundary is implemented as a Neumann condition where $\frac{\partial c}{\partial n} = 0$ is imposed (where n is the coordinate vector normal to the boundary) since the value of the solution either side of the boundary must be equal. Defining the boundaries of a closed system is also achieved using this Neumann condition, since no exchange of material can occur.

A periodic boundary condition may be applied as a Cauchy boundary whereby $\frac{\partial c}{\partial n} = 0$ and $c(x=0) = c(x=\lambda)$ are applied, where λ is the period distance.

As demonstrated in sub-section 1.3.4, a Robin boundary condition is useful for modelling a kinetically limited surface reaction, such as dissolution, which depends on the concentration and its gradient: such as $D\frac{\partial c}{\partial x} - k_b \cdot c = -k_f$.

An inset disk electrode may be modelled using a mixed boundary condition set across the 2D plane at $z=0$ whereby an electroactive surface at which $c = f(t)$ exists at $\sqrt{x^2+y^2} \leq r_e$, where r_e is the electrode radius, but an insulating material at which $\frac{\partial c}{\partial n} = 0$ exists at $\sqrt{x^2+y^2} > r_e$.

The most common initial boundary condition is a homogeneous $\left(c(t=0) = c_0\right)$ concentration field. This may be used to reflect a saturated or an empty initial environment, depending on the model.

The boundary conditions used in each of the models we present are expressed clearly and justified when they are introduced in each chapter.

3.1.3 Normalisation

So far, we have considered the modelling of dimensional systems. However, a dimensionless representation is generally preferable. A dimensionless representation can be mapped onto a family of dimensional models via appropriate transformations. The results of one simulation of a dimensionless model will be generalisable across several systems, which is a more computationally efficient way to generate results.

We employ relatively simple transformations between dimensional and dimensionless features whereby we define the dimensional system using a set of reference values and convert to dimensionless values by normalising against those references. A reference length is used to normalise the spatial features. It is convenient to use a length that characterises the system (such as the radius of an electrode or particle). The transformation between dimensional x and dimensionless X, using reference length x_{ref}, is $X = x/x_{ref}$. The diffusion coefficient and concentration are similarly normalised. In a one-component, one-medium system there is only one diffusion coefficient, and so normalisation gives a unitary dimensionless value $\left(D/D_{ref} \equiv 1\right)$, removing a factor from the PDE and simplifying the equation. Simplification of the problem provides another incentive for using a dimensionless representation. A table of the typical transformations used in this thesis is given in Table 3.1.

Table 3.1: Table of typical dimensionless transformations used in this thesis

Dimensional Parameter	Dimensionless Transformation
Spatial distance, x	$X = x/x_{ref}$
Diffusion coefficient, D	$d = D/D_{ref}$
Concentration, c	$C = c/c_{ref}$
Time, t	$T = D \cdot t/x_{ref}^2$

Local flux, j	$J=\left(j\cdot x_{ref}\right)/\left(c_{ref}\cdot D_{ref}\right)$
Zero-order surface rate constant, k_0	$K_0=\left(k_0\cdot x_{ref}\right)/\left(c_{ref}\cdot D_{ref}\right)$
First-order surface rate constant, k_1	$K_1=\left(k_1\cdot x_{ref}\right)/D_{ref}$

It is beneficial to require as few reference values as possible to describe a system as this maximises the generalisability of the dimensionless results. As such, conversion using a combination of other reference values is preferable over defining a reference value for every parameter. An example of this is the transformation between dimensional time t and dimensionless time T without defining a reference time, so long as reference diffusion coefficient and length have been defined: $T=D_{ref}\cdot t/x_{ref}^2$.

3.2 Solving the PDE

By following the approach outlined in the previous section, we can establish a dimensionless model for a set of systems using approximate physics and constrained boundaries. We now turn to the methods we use to numerically solve such a problem, expressed as a PDE, and generate a unique, physically informative solution.

3.2.1 Finite difference

The analytical definition of the derivative dc/dx of a function $c\left(x\right)$ at a is:

$$\frac{dc}{dx}\left(a\right)=\lim_{\delta\to 0}\frac{c\left(a+\delta\right)-c\left(a\right)}{\delta} \qquad \text{Equation 3.3}$$

In order to solve problems involving derivatives numerically, one technique is to approximate the above calculation by using a finite step h:

$$\frac{dc}{dx}\left(a\right)\approx\frac{c\left(a+h\right)-c\left(a\right)}{h} \qquad \text{Equation 3.4}$$

where h is a small but finite value. The smaller h is, the more accurate the approximation.

We can discretise the simulation domain into a grid of points separated by small, finite steps. Each of these points represents a point in space-time and is associated with a concentration value. The derivative at any point in any direction can be estimated by considering the adjacent point's concentration value and the distance between the points according to Equation 3.4. This discretisation into a grid for the purpose of computing derivatives numerically is referred to as the finite difference method.

The initial boundary condition defines the PDE solution at $t=t_0$, and is a solved layer of the discretised grid. The task is then to use finite difference computation of the derivatives, under the constraints of the boundary conditions and PDE, to generate the rest of the solution. This is usually done one step at a time along the time-dimension (respecting the direction of causality), where the previous step's solution is used to calculate the solution for the next step. We shall discuss this further in sub-section 3.2.3.

3.2.2 Spatial & temporal derivatives

The spatial first derivatives have two adjacent points that can be used to compute the derivative at a point X_i: X_{i+1} and X_{i-1}. The forward finite difference (Equation 3.4) involves X_{i+1} and X_i. The backward finite difference uses X_i and X_{i-1}:

$$\frac{dc}{dx}(a) \approx \frac{c(a)-c(a-h)}{h} \qquad \text{Equation 3.5}$$

At the domain boundaries (i.e. X_0 and X_{n-1} where n is the number of points in the X-direction), only one of these pairs is available. However, away from the boundaries, both are viable. However, the average of the forward and backward values gives the more accurate central finite difference value:

$$\frac{dc}{dx}(a) \approx \frac{c(a+h)-c(a-h)}{2h} \qquad \text{Equation 3.6}$$

Let us consider the Taylor series expansion for $c(a+h)$ and $c(a-h)$:

$$c(a+h)=c(a)+h\left(\frac{dc}{dx}(a)\right)+\frac{h^2}{2}\left(\frac{d^2c}{dx^2}(a)\right)+\frac{h^3}{6}\left(\frac{d^3c}{dx^3}(a)\right)+O(h^4) \quad \text{Equation 3.7}$$

$$c(a-h)=c(a)-h\left(\frac{dc}{dx}(a)\right)+\frac{h^2}{2}\left(\frac{d^2c}{dx^2}(a)\right)-\frac{h^3}{6}\left(\frac{d^3c}{dx^3}(a)\right)+O(h^4) \quad \text{Equation 3.8}$$

We thus see that Equation 3.4 and Equation 3.5 each have an error on the order of $O(h)$ with the first of the error terms containing $\frac{d^2c}{dx^2}(a)$, while Equation 3.6 has an error on the order of $O(h^2)$ since the $\frac{d^2c}{dx^2}(a)$ terms cancel. Central finite differencing is thus more accurate. Let us consider the addition of these two Taylor series:

$$c(a+h)+c(a-h)=2c(a)+h^2\left(\frac{d^2c}{dx^2}(a)\right)+\frac{h^4}{12}\left(\frac{d^4c}{dx^4}(a)\right)+O(h^6) \quad \text{Equation 3.9}$$

This corresponds to the three-point central finite difference for the second derivative, with an associated error of $O(h^2)$:

$$\frac{d^2c}{dx^2}(a)=\frac{c(a+h)-2c(a)+c(a-h)}{h^2}+O(h^2) \quad \text{Equation 3.10}$$

The backward, forward, and central finite difference first derivatives and the 3-point central finite difference second derivative for a quartic curve has been illustrated in Figure 3.1 (a quartic curve is used to ensure some error for all finite difference calculations for illustrative purposes). This demonstrates the greater accuracy of the central finite difference as an average of the forward and backward finite differences.

As mentioned in the previous sub-section, we seek to generate solutions for the domain grid by stepping through time, beginning with the initial condition. As such, the temporal derivative will be the finite difference between those two time steps.

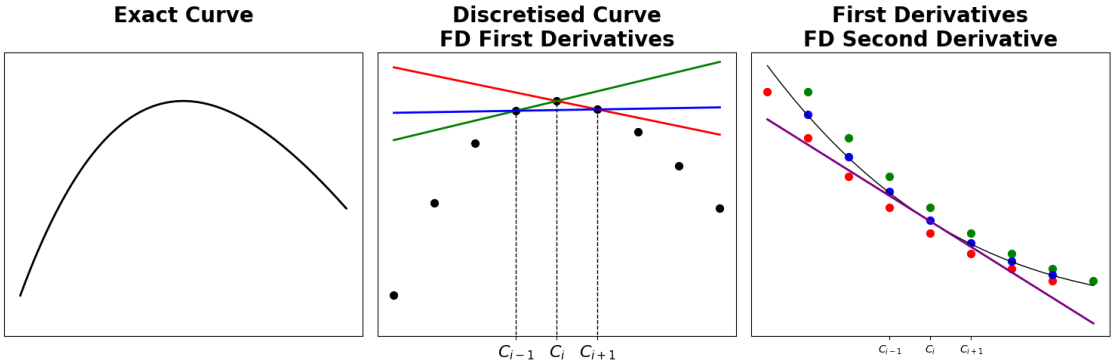


Figure 3.1: Illustration of the use of finite differencing using adjacent values to estimate the first and second derivatives. The first panel displays a section of an exact, quartic curve. The second panel illustrates a discretisation of the curve. The green line demonstrates the backward finite difference estimate of the first derivative at C_i, the forward finite difference is demonstrated by the red line, and the central finite difference is shown as the blue line. The third panel illustrates the values for the first derivatives from these finite difference estimates in matching colours. The exact first derivative has also been included as a black line. The purple line demonstrates the second derivative calculated by 3-point central finite difference.

3.2.3 Explicit versus implicit solution

We have now established a grid of points describing the domain, a method to estimate the derivatives in each direction via finite difference discretisation, an initial condition, and a set of constraints, including the PDE, that allows us to calculate the values at the next time-step. The concentration at a given point in space-time can be evaluated using either the spatial derivatives of the previous, known time-step, or the spatial derivatives of its current time-step (the values at which are as yet unknown). These represent the explicit and implicit solution formulations respectively. An illustration of this difference is shown in Figure 3.2 for a 2D grid in X and T.

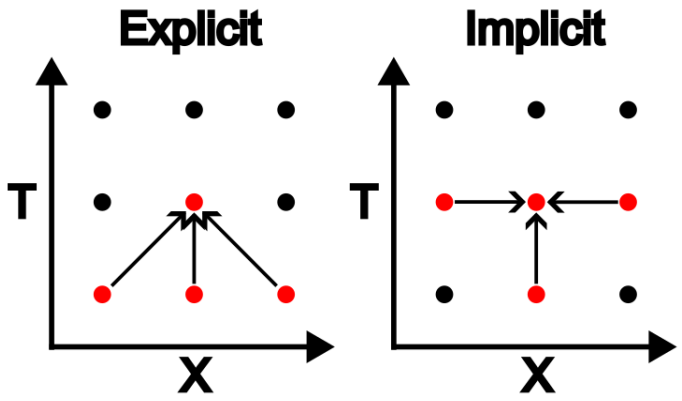


Figure 3.2: Illustration of explicit formulation versus implicit formulation for calculating the concentration at a point in a uniform 2D (X, T) grid. The red dots illustrate the grid-points whose concentrations are involved in the equation and the arrows demonstrate which grid-point is being solved for and the direction of the time-stepping.

In the explicit formulation, the PDE for Fick's Second Law is expressed as

$$\frac{C_i^k - C_i^{k-1}}{\Delta T} = \frac{C_{i+1}^{k-1} - 2C_i^{k-1} + C_{i-1}^{k-1}}{\Delta X^2} \qquad \text{Equation 3.11}$$

where C_i^k is the dimensionless concentration at position (i, k) in the dimensionless, discretised (X, T) domain and ΔT and ΔX are the steps sizes in the T- and X-dimensions respectively. Since all concentration values at $T = 0$ are known from the initial boundary condition, applying Equation 3.11 allows one to calculate the concentration values for the next time-step and, by induction, allows one to calculate the concentration values at all time-steps. However, this method is only guaranteed to be stable when[9]

$$\frac{\Delta T}{\Delta X^2} < \frac{1}{2} \qquad \text{Equation 3.12}$$

For many simulations, an inefficiently small ΔT is required in order to accurately characterise a continuous function spatially while also obeying the above constraint. As such, the implicit method is preferred. The PDE for Fick's Second Law is expressed implicitly as

$$\frac{C_i^k - C_i^{k-1}}{\Delta T} = \frac{C_{i+1}^{k} - 2C_i^{k} + C_{i-1}^{k}}{\Delta X^2} \qquad \text{Equation 3.13}$$

In this case only one of the values is known $\left(C_i^{k-1}\right)$. However, listing the constraints (PDE and boundary) for each of the values at a time-step gives a finite list of simultaneous equations, which can be expressed as a matrix multiplication

$$M\vec{c}=\vec{b} \qquad \text{Equation 3.14}$$

where M is the matrix of coefficients applied to the unknown C_i^k values contained in vector $\vec{c}$, and $\vec{b}$ is the vector of known/explicit constants. The problem then becomes a matter of solving M^{-1} to calculate $\vec{c}$:

$$\vec{c}=M^{-1}\vec{b} \qquad \text{Equation 3.15}$$

There are many algorithmic methods for solving such a problem, including the general Gaussian elimination algorithm[2, 10]. We discuss a more rapid variant of this algorithm in the following sub-section, which has been used in this thesis' work.

3.2.4 Thomas algorithm

One may have noticed that our implementation of finite difference so far has only considered the adjacent points (e.g., C_{i-1} and C_{i+1} in a 1D spatial grid) when calculating a derivative. It is entirely possible to use more and increasingly distant points in a finite difference derivative to achieve greater accuracy by increasing the order of the error (such as in Equation 3.10). An example of doing so would be the 5-point finite difference first derivative, which has an error of $O\left(h^4\right)$:

$$\frac{dc}{dx}(a)=\frac{-C_{i+2}+8C_{i+1}-8C_{i-1}+C_{i-2}}{12\Delta X}+O\left(h^4\right) \qquad \text{Equation 3.16}$$

There are two reasons for not doing so here. Firstly, there are diminishing returns for improved accuracy by increasing the number of points used in the finite difference

discretisation, such that a discretisation error of $O(h^2)$ is already acceptable for our simulations.

Secondly, let us consider the matrix of coefficients M and the vector of constants $\vec{b}$, introduced in Equation 3.14 in one dimension. Let us consider a system where we have the boundary conditions $c=0$ at X_0 and $c=1$ at X_{n-1}, where n is the number of discretised points, and under the PDE described in Equation 3.13.

$$M=\begin{pmatrix} 1 & 0 & & 0 & 0 & & & \\ -\lambda & 1+2\lambda & & -\lambda & 0 & \cdots & 0 & \\ 0 & -\lambda & & 1+2\lambda & -\lambda & & & \\ & & \vdots & & & \ddots & \vdots & \\ & & 0 & & & \cdots & \lambda \quad 1+2\lambda \quad \lambda & \\ & & & & & & 0 \quad 0 \quad 1 & \end{pmatrix}$$

Equation 3.17

$$\vec{b}=\begin{pmatrix} 0 \\ C_1^{k-1} \\ C_2^{k-1} \\ \vdots \\ C_{n-2}^{k-1} \\ 1 \end{pmatrix}$$

Equation 3.18

where $\lambda=\frac{\Delta T}{\Delta X^2}$. Note that the matrix M is diagonal. A branch of algorithms, extending from the general Gaussian elimination, have been developed that are optimised for solving diagonal matrices[2]; their use greatly accelerates simulation. Furthermore, if only adjacent points are used, the matrix is tridiagonal. The Thomas algorithm[2] is optimised for solving tridiagonal matrices and is even more rapid. The computational time saved by employing the Thomas algorithm is worth using 3-point as opposed to 5- or higher-point finite differencing, since this saved time can be used to increase the computational load elsewhere. The Thomas algorithm is the popular choice for one-dimensional problems and underpins at least one method for solving two-dimensional problems: the Alternating Direction Implicit (ADI)

method (which we shall introduce in the next sub-section). As such, it is valuable to briefly outline how the Thomas algorithm operates.

First, we factorise M as a product of a lower and an upper triangular matrix: this process is called LU factorisation.

$$M = LU = \begin{pmatrix} \beta_0 & ¿\,\alpha_1 & \beta_1 & & ¿ & \\ & ¿\,\ddots & & & ¿ & \\ & ¿ & & \ddots & ¿\,\alpha_{n-1} & \beta_{n-1} \end{pmatrix} ¿$$

Equation 3.19

We can now re-arrange the equation to give

$$U\vec{c} = L^{-1}\vec{b} = \vec{d}$$

Equation 3.20

where $\vec{d}^{\,T} = \begin{pmatrix} \delta_0 & \delta_1 & \cdots & \delta_{n-1} \end{pmatrix}$.

The first step is the forward sweep and involves calculating the γ_i and δ_i values. The Thomas algorithm does so by applying the following rules:

$$\gamma_i = \begin{cases} M_{0,1}/M_{0,0} & for\ i = 0 \\ M_{i,i+1}/\left(M_{i,i} - \gamma_{i-1}M_{i,i-1}\right) & for\ i = 1,2,\ldots,n-2 \end{cases}$$

Equation 3.21

$$\delta_i = \begin{cases} b_0/M_{0,0} & for\ i = 0 \\ \left(b_i - \delta_{i-1}M_{i,i-1}\right)/\left(M_{i,i} - \gamma_{i-1}M_{i,i-1}\right) & for\ i = 1,2,\ldots,n-1 \end{cases}$$

Equation 3.22

The second step is the back substitution whereby we evaluate C_i^k from $\vec{c} = U^{-1}\vec{d}$:

$$C_i^k = \begin{cases} \delta_{n-1} & for\ i = n-1 \\ \delta_i - \gamma_i C_{i+1}^k & for\ i = n-2, n-3, \ldots, 0 \end{cases}$$

Equation 3.23

While this approach is sufficient for one-dimensional problems, it is inappropriate for two-dimensional systems since these depend on second derivatives in a second spatial dimension and so rely on more than three-points in a finite difference formulation of the PDE. As such,

the matrix of coefficients is not tridiagonal. The implicit expression of the PDE under three-point finite differencing is

$$C_{i,j}^{k-1} = \lambda_1 C_{i-1,j}^{k} + \lambda_2 C_{i,j}^{k} + \lambda_3 C_{i+1,j}^{k} + \lambda_4 C_{i,j-1}^{k} + \lambda_5 C_{i,j+1}^{k} \qquad \text{Equation 3.24}$$

where λ_i are the appropriate coefficients under the PDE. A generalised n-diagonal form of the Thomas algorithm is available[2] and could be used to solve this, however this is very inefficient. Another method is described in the next sub-section: the ADI method.

3.2.5 Alternating Direction Implicit method (ADI)

The ADI method[11-13] combines explicit and implicit methods and is used to solve two-dimensional problems efficiently without sacrificing the convenience of the Thomas algorithm. Each time-step is divided into two halves. In the first half, the spatial derivatives in one dimension are evaluated using their implicit values, while the spatial derivatives in the other dimension are evaluated using their explicit values. In the second half, the implicit and explicit dimensions are swapped. Thus, for each half time-step and row/column of the 2D spatial grid, we construct an equation $M\vec{c} = \vec{b}$, that we solve using the Thomas algorithm, where M contains the implicit coefficients and $\vec{b}$ contains the explicit values, including the prior concentration. This method maintains guaranteed ΔT stability. A schematic illustrating the process is demonstrated in Figure 3.3.

During a half time-step, each row or column of the 2D grid can be solved independently of the others. This facilitates parallel processing whereby the matrix equations can be solved by different threads simultaneously, accelerating the simulation by a factor of the number of available cores.

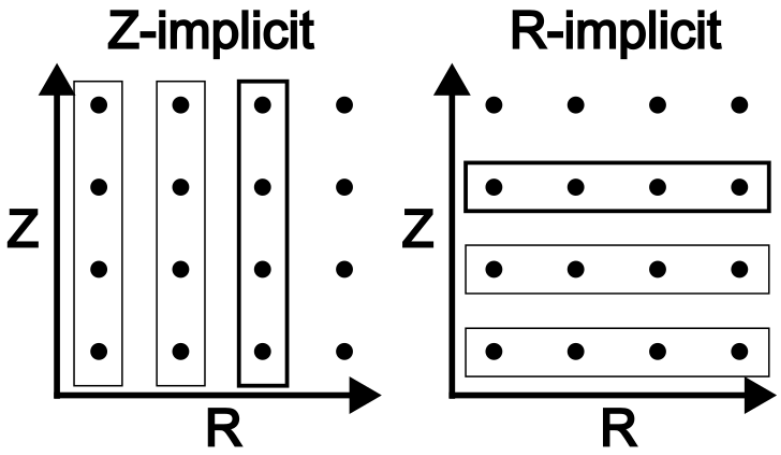


Figure 3.3: Illustration of the directional implicit sweeps used in the ADI method for a problem with two spatial dimensions $\{R, Z\}$. The concentrations are arranged according to their spatial grid discretisation. The thick-lined sections demonstrate a column/row to be solved using contained concentration values implicitly. Thin-lined sections represent columns/rows that have been solved. Note that the implicit sections do not need to be solved sequentially.

This process is not the only method for solving multi-dimensional problems. Over the course of this project, it has been observed that, even though this method maintains ΔT stability, it may not represent the most efficient solution method for certain unusual grid structures, particularly with respect to boundary conditions imposed on curved surfaces. Fully implicit methods without any explicit character have been developed and can be applied to problems more generally. We discuss how such methods have been used in this thesis in the following sub-section.

3.2.6 Fully implicit methods

We have mentioned that the semi-explicit character of the ADI method can compromise its efficiency for solving problems. An alternative approach is thus to maintain the finite difference formulation as fully implicit, meaning implicit terms are used in each direction. If we express the two-dimensional problem as a matrix multiplication equation under 3-point finite difference, we end up with a block tridiagonal matrix with tridiagonal block matrices for our matrix of coefficients for the PDE and boundary conditions[14]:

$$\begin{bmatrix} nw_{ij} & n_{ij} & ne_{ij} \\ w_{ij} & c_{ij} & e_{ij} \\ sw_{ij} & s_{ij} & se_{ij} \end{bmatrix} U_{ij} = nw_{ij} U_{i-1,j+1} + n_{ij} U_{i,j+1} + ne_{ij} U_{i+1,j+1} + \ldots = F \qquad \text{Equation 3.25}$$

¿ Equation 3.26

where

$$c_j = ¿ \qquad \text{Equation 3.27}$$

where U_j is the vector of solutions U_{ij} at (x_i, y_i), F_j represents the vector of known F_{ij} constants, and n and m are the number of points in each direction. Matrices a_j and b_j are defined similarly to c_j but contain the $\{nw_{ij}, n_{ij}, ne_{ij}\}$ and $\{sw_{ij}, s_{ij}, se_{ij}\}$ values respectively. A similar approach would be taken for a three-dimensional system, where the coefficient matrix would be a block tridiagonal matrix whose block matrices are also block tridiagonal with tridiagonal block matrices.

The question now is how to solve these matrix equations efficiently. Krylov subspace methods[4] currently represent the most efficient iterative methods available today. The order-r Krylov subspace generated by an n-by-n matrix A and a vector $\vec{v}$ of dimension n is the linear subspace described by the span of images of $\vec{v}$ under the first r powers of A, i.e., $K_r(A, \vec{v}) = span\{\vec{v}, A\vec{v}, A^2\vec{v}, \ldots, A^{r-1}\vec{v}\}$, where the span of these image vectors is the set of all of their linear combinations. When we refer to an iterative method as a Krylov subspace method, this means that each iteration increases the order of the Krylov subspace that is used to generate the estimate solution. As the Krylov subspace expands, the estimate converges.

There are many approaches that utilise an expanding Krylov subspace in the generation of convergent approximations. The best known methods are conjugate gradient (CG)[15, 16], induced dimension reduction (IDR(s))[17], generalized minimum residual

(GMRES)[18], quasi minimal residual (QMR)[19], minimal residual (MINRES)[20, 21], and, lastly, the stabilized biconjugate gradient (BiCGSTAB)[22]. The rate at which these methods converge depends heavily on the problem. While they all are direct solvers under exact arithmetic when $r=n$, these methods are also susceptible to rounding errors, which result practically in unstable convergence. As such, a tolerance is defined for the norm of the residual vector $\vec{r}_k$ after k iterations, where $\vec{r}_k = M\vec{c}_k - \vec{b}$ and $\vec{c}_k$ is the estimate for $\vec{c}$. The iterative process is halted once this tolerance is achieved. The above methods are tested on each problem to find the most stable and rapidly convergent. In the simulations we applied these methods to, BiCGSTAB was found most consistently to be the optimal method.

The convergence of these Krylov subspace methods is often accelerated if the problem has been pre-conditioned. This involves transforming the problem to one with a lower condition number (i.e. less sensitivity of output error to input) using a preconditioner matrix P, such that

$$M P^{-1}(P\vec{c}) = \vec{b} \qquad \text{Equation 3.28}$$

We then solve $M P^{-1}\vec{y} = \vec{b}$ and $\vec{c} = P^{-1}\vec{y}$ using the preconditioned BiCGSTAB algorithm.

In this work, we use a single cycle of the semi-coarsening multigrid solver (SMG)[14] to act as a preconditioner. This involves calculating P^{-1} by coarsening the grid in one dimension, solving the problem on the coarse grid using the iterative Jacobi method to a high level of tolerance (thus acting as a smoother not a solver), and relaxing the grid to its original, fine structure. This produces the matrix P^{-1}, which is used as input for the preconditioned BiCGSTAB iterative solver.

The *HYPRE C++* library[23, 24] has implemented a wide range of scalable solvers and preconditioners. We have used this library extensively in our own work to benefit from its optimisation on GPU systems.

3.3 Dimensionality & co-ordinate systems

We have already displayed how solving multi-dimensional systems becomes mathematically and computationally more challenging as the number of dimensions increases. There is thus a strong incentive to minimise the dimensionality of the problem where possible by exploiting symmetries where available. An example of this is diffusion to an infinitely long microband electrode (see Figure 3.4).

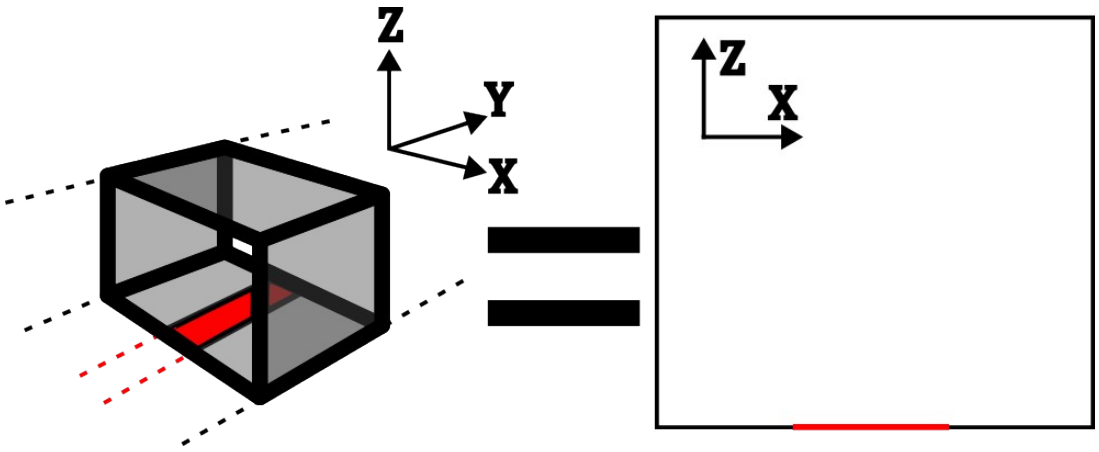


Figure 3.4: Illustration of dimension reduction from a 3D $\{X, Y, Z\}$ microband electrode (indicated in red) to a 2D $\{X, Z\}$ representation by approximating an infinite length in the Y-dimension and therefore translational symmetry, i.e., $\partial c / \partial y = 0$.

Since the band is infinitely long, it possesses translational symmetry in the y-direction, and thus $\frac{\partial c}{\partial y} = 0$ and $\frac{\partial^2 c}{\partial y^2} = 0$ (so long as the boundary conditions also obey this symmetry). We only need to simulate diffusion in the *x*- and *z*- dimensions instead of all three spatial dimensions and the PDE of Fick's Second Law becomes:

$$\frac{\partial c}{\partial t} = D\left(\frac{\partial^2 c}{\partial x^2} + \frac{\partial^2 c}{\partial z^2}\right)$$ Equation 3.29

Modelling a microband as infinitely long can thus significantly enhance the efficiency of the simulation of diffusion-controlled electrochemistry at the expense of neglecting *y*-anisotropy, which shall result in some inaccuracy since the band's edge effects have been ignored. If the relative inaccuracies of such a model are small (such as the length of the band being significantly larger than its width), then this is a valuable approach.

Not all symmetries can be exploited within the Cartesian coordinate system. In order to exploit a rotational symmetry, we may wish to reformulate the problem into cylindrical coordinates: $\{r, z, \phi\}$, where $r = \sqrt{x^2 + y^2}$ and $\tan\phi = \frac{y}{x}$. With some transformations, we can align *z* along the axis of symmetry and exploit $\frac{\partial c}{\partial \phi} = 0$. The PDE then becomes

$$\frac{\partial c}{\partial t} = D\left(\frac{\partial^2 c}{\partial r^2} + \frac{1}{r}\frac{\partial c}{\partial r} + \frac{\partial^2 c}{\partial z^2}\left[\frac{+1}{r^2}\frac{\partial^2 c}{\partial \phi^2}\right]\right)$$ Equation 3.30

where the term in square brackets values to zero.

If the system is spherically symmetric, then conversion to spherical coordinates $\{\rho, \theta, \phi\}$ will be beneficial, where $\rho = \sqrt{x^2 + y^2 + z^2}$, $\cos\theta = \frac{z}{\rho}$, and $\tan\phi = \frac{y}{x}$. With rotational symmetry about the perpendicular axes, the system shall be simplified to one-dimension

$$\frac{\partial c}{\partial t} = D\left(\frac{\partial^2 c}{\partial \rho^2} + \frac{2}{\rho}\frac{\partial c}{\partial \rho}\right)$$ Equation 3.31

These coordinate systems are used for the simulations of this thesis and represented graphically in Figure 3.5.

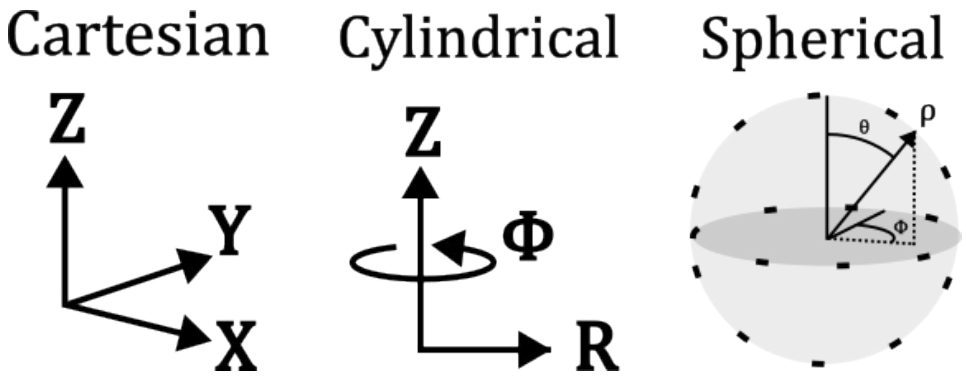


Figure 3.5: Illustration of the three coordinate systems considered in this thesis: Cartesian (useful for translational symmetries), cylindrical (useful for rotational symmetry) and spherical (for spherical symmetry).

3.4 Grid construction

The accuracy of the finite difference method depends on the distances between the discretised grid-points, with smaller distances giving smaller errors. So far, we have assumed that we have used uniform grids to populate our simulation space where the distances between points are constant. However, there are regions where the derivatives with respect to space and time are larger and so a smaller step size is required to characterise these accurately, especially as these errors shall propagate throughout the simulation space. It would be highly inefficient to apply a uniform grid in these cases since an excessive accuracy shall be afforded to regions where it is not required. A grid that is adapted to the local solution derivatives is preferred.

If the region(s) where the derivatives are large are known and static, we use an expanding grid[25, 26] with more concentrated grid-points at areas where higher accuracy is most efficient and increasingly diffuse points at a distance. If there are multiple regions in a given dimension where the higher accuracy is required relative to the rest of the space, then we may wish for the grid to contract as well. The equation we use for calculating the step-sizes in an expanding/contracting grid is

$$\Delta X_i = X_{i+1} - X_i = h \cdot \omega^i \qquad \text{Equation 3.32}$$

where h is the initial grid-step and ω is the expansion/contraction factor. Figure 3.6 illustrates the difference between distributing grid-points along a dimension using a uniform, expanding or expanding/contracting grid.

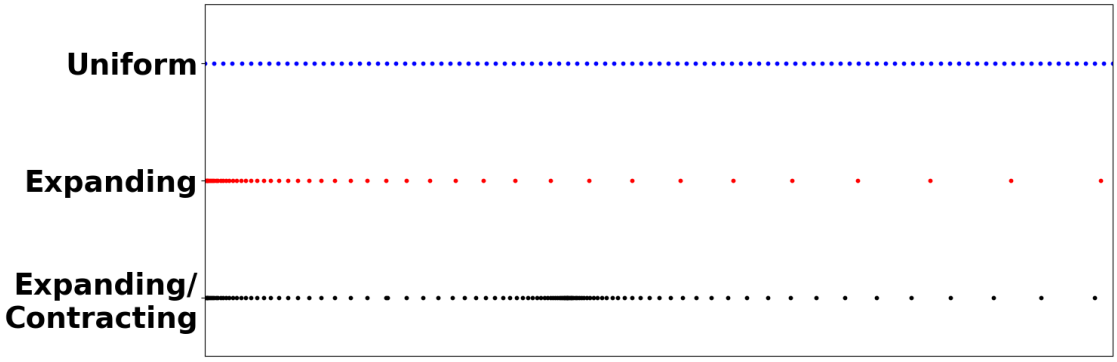


Figure 3.6: Illustration of uniform, expanding grid and expanding/contracting grid distributions to be used for domain discretisation and concentrating grid-points at areas with large gradients to minimise error.

It is important to note that this changes how we calculate finite differences since the distances between points are no longer uniform. The 2-point forward, backward, and central finite differences for the first derivative are

$$\left.\frac{\partial C}{\partial X}\right|_{X_i} \approx \frac{C_{i+1}-C_i}{\Delta X_{+,i}} \approx \frac{C_{i+1}-C_i}{\Delta X_{-,i}} \approx \frac{C_{i+1}-C_{i-1}}{\Delta X_{+,i}+\Delta X_{-,i}} \qquad \text{Equation 3.33}$$

where $\left.\frac{\partial C}{\partial X}\right|_{X_i}$ and C_i are the gradient and concentration at position X_i, $\Delta X_{+,i}=X_{i+1}-X_i$, and $\Delta X_{-,i}=X_i-X_{i-1}$. The three-point central difference for the second derivative is

$$\left.\frac{\partial^2 C}{\partial X^2}\right|_{X_i} \approx \frac{\frac{C_{i+1}-C_i}{\Delta X_{+,i}} - \frac{C_i-C_{i-1}}{\Delta X_{-,i}}}{\frac{1}{2}\left(\Delta X_{i+1}+\Delta X_{i-1}\right)} \qquad \text{Equation 3.34}$$

Expanding grids may be applied in spatial or temporal dimensions. Simulations that have one active boundary, such as many electrochemistry simulations, benefit greatly from expanding spatial grids in terms of computational efficiency. Chronoamperometry simulations and simulations of chemical release into an initially empty medium have the largest

concentration-time first derivatives early in the simulation time and have much greater efficiency with expanding time grids.

3.5 Convergence, validation & testing

As we have seen in the previous sub-sections, the numerical solutions we arrive at are approximate and have multiple sources of error. While these sources of error can be mitigated, this is associated with an increased computational cost. We are incentivised to perform simulations to a minimum acceptable accuracy while also minimising the computational cost. However, when performing simulations of systems whose exact solutions are not known, or for which there is no prior, reliable work, the error of our solution is also unknown, so how can we evidence that we have dedicated sufficient computational resources to achieve an accurate solution?

If the problem is well-posed (i.e., a finite condition number and unique solution) then a solution method should be convergent with respect to diminishing grid step-sizes and/or number of iterations (although this is not guaranteed for BiCGSTAB[22]). This is demonstrated by performing the solution method with increasingly demanding grids and/or iterative tolerances. If the solution is convergent and accurate, then it will asymptotically approach the unknown exact solution. By comparing a set of simulation results using the same method but varying computational demand, one can demonstrate the level of convergence. This can be used as a metric for the simulation's precision.

However, just because the simulation converges does not mean it converges to a correct result. The process of validation involves comparing the solutions generated by a particular method for a similar, benchmark problem against the exact or benchmark solution. A benchmark solution need not be exact but must be demonstrated to have a level of accuracy desired for one's own solution method. If the solution method is demonstrated to converge

towards a benchmark solution for a problem similar to the one we wish to solve, this provides validation that the same method should also converge towards the correct solution for the unknown problem, at least to a degree of accuracy similar to the benchmark solution. Additionally, if the simulated system possesses qualities which we can validate our solution against, such as the conservation of mass, these can also be used. Validation provides an alternative metric for assessing the simulation method's accuracy.

Finally, a solution can be tested by comparing to real-world results. The solution's tested accuracy contains inaccuracies introduced by both the numerical method and also the model itself. Combined with convergence testing and validation, this can provide insight into the combined error of the numerical method and the model itself.

Performing these three tasks rigorously is necessary to evidence the validity of the simulation results and the physical insights they provide[27-29]. Throughout this thesis, we have endeavoured to emphasise the results of these tests when available.

Having provided a brief overview of how we have performed our simulations, in the next chapter we introduce the first problem we apply these techniques to: diffusion about a spherical micro-electrode on a supporting planar surface.

References

1. R. G. Compton, E. Kätelhön, E. Laborda and K. R. Ward, *Understanding Voltammetry: Simulation of Electrode Processes*, World Scientific Europe, Second edn., 2020.
2. W. H. Press, S. A. Teukolsky, W. T. Vetterling and B. P. Flannery, *Numerical Recipes*, Cambridge University Press, Cambridge, Third edn., 2007.
3. A. J. Bard, L. R. Faulkner, C. G. Zoski and J. Leddy, *Electrochemical Methods : Fundamentals and Applications*, Second edn., 2001.
4. J. Liesen and Z. Strakos, *Krylov Subspace Methods: Principles and Analysis*, Oxford University Press, 2012.
5. J. Crank, *The Mathematics of Diffusion*, Clarendon Press, 1979.
6. A. Fick, *The London, Edinburgh, and Dublin Philosophical Magazine and Journal of Science*, 1855, **10**, 30-39.

7. L. A. Evans, M. J. Thomasson, S. M. Kelly and J. Wadhawan, *The Journal of Physical Chemistry C*, 2009, **113**, 8901-8910.
8. J. E. Halls, N. S. Lawrence and J. D. Wadhawan, *The Journal of Physical Chemistry B*, 2011, **115**, 6509-6523.
9. G. D. Smith, *Numerical Solution of Partial Differential Equations: Finite Difference Methods*, Oxford University Press, Oxford, Third edn., 1985.
10. N. J. Higham, *WIREs Computational Statistics*, 2011, **3**, 230-238.
11. J. A. Alden and R. G. Compton, *The Journal of Physical Chemistry B*, 1997, **101**, 8941-8954.
12. D. J. Gavaghan and J. S. Rollett, *Journal of Electroanalytical Chemistry and Interfacial Electrochemistry*, 1990, **295**, 1-14.
13. D. W. Peaceman and J. Rachford, H. H. , *Journal of the Society for Industrial and Applied Mathematics*, 1955, **3**, 28-41.
14. S. Schaffer, *SIAM Journal on Scientific Computing*, 1998, **20**, 228-242.
15. M. R. Hestenes and E. Stiefel, *Journal of Research of the National Bureau of Standards*, 1952, **49**, 409-436.
16. W. W. Hager and H. Zhang, *Pacific Journal of Optimization*, 2006, **2**, 35-58.
17. P. Wesseling and P. Sonneveld, Berlin, Heidelberg, 1980.
18. Y. Saad and M. H. Schultz, *SIAM Journal on Scientific and Statistical Computing*, 1986, **7**, 856-869.
19. R. W. Freund and N. M. Nachtigal, *Numerische Mathematik*, 1991, **60**, 315-339.
20. C. C. Paige and M. A. Saunders, *SIAM Journal on Numerical Analysis*, 1975, **12**, 617-629.
21. S.-C. T. Choi, C. C. Paige and M. A. Saunders, *SIAM Journal on Scientific Computing*, 2011, **33**, 1810-1836.
22. H. A. Van der Vorst, *SIAM Journal on Scientific and Statistical Computing*, 1992, **13**, 631-644.
23. R. D. Falgout and U. M. Yang, presented in part at the Computational Science — ICCS 2002, Berlin, Heidelberg, 2002.
24. R. D. Falgout, J. E. Jones and U. M. Yang, in *Numerical Solution of Partial Differential Equations on Parallel Computers*, eds. A. M. Bruaset and A. Tveito, Springer, Berlin, Heidelberg, 2006, vol. 51, pp. 267-294.
25. M. Rudolph, *Journal of Electroanalytical Chemistry*, 2002, **529**, 97-108.
26. D. J. Gavaghan, *Journal of Electroanalytical Chemistry*, 1998, **456**, 1-12.
27. E. Kätelhön and R. G. Compton, *Analyst*, 2015, **140**, 2592-2598.
28. E. Kätelhön and R. G. Compton, *Analyst*, 2015, **140**, 3290-3290.
29. E. Kätelhön and R. G. Compton, *Analyst*, 2016, **141**, 1154-1154.

4 Diffusion at a particle on a surface

This chapter introduces and analyses diffusion to a particle on an inert supporting surface when subjected to potential-step chronoamperometry. Particular attention is given to the local behaviours of diffusion and the development of concentration profiles beyond the particle surface. The diffusion indicator, a tool for interpreting diffusional effects, is introduced, and applied. The work has been published in the Journal of Electroanalytical Chemistry[1].

Simulations are reported for particles on an inert planar surface with a chronoamperometric boundary condition applied. The geometries simulated vary according to a contact angle, θ_c, between the particle and the planar surface, encompassing a range from fully spherical $(\theta_c = \pi)$ to an infinitesimally thin spherical cap $(\theta_c \to 0)$. Diffusion indicator and local diffusion indicator time-profiles are shown to reflect relative contributions of thin-layer, linear and convergent diffusion regimes. We demonstrate the convergence towards results for chronoamperometry at a disk electrode. These results have implications for the study of nanoparticle-modified surfaces, hanging mercury drop electrodes, and single-entity electrochemistry. The geometry is also synonymous with that of release of material from particles in contact with bio-membranes, which is applicable for chemical delivery on plant leaves, within cells and via digestion. The results presented in this chapter provide a foundation for the results investigated in the following chapters of this thesis.

4.1 Introduction

The study of micro-electrodes is associated with numerous advantages for fundamental and analytical electrochemists over their macroscopic counterparts, which are well-described in the literature[2]. These include access to shorter timescales, greater current densities and reduced total interfacial capacitances. Numerous electrode geometries have risen to prominence, with perhaps the most notable being spheres[3, 4] and disks[5-7].

One key feature of micro-electrodes is that, on the experimental timescale, the diffusion layer that arises due to electroactivity at the electrode surface grows to a length-scale that approaches or exceeds the characteristic length of the electrode geometry itself. In this way, the behaviour deviates from linear to convergent diffusion (as described in Section 1.3.4). The electrode geometry thereby determines the diffusional behaviour and thus influences the observed current transient. In the case of spheres and disks, this leads to a steady-state limiting current I_{ss} in the diffusion-controlled limit of simple Faradaic processes. For the reaction $A \pm n e^{-} \rightarrow B$, the steady-state current at a micro-sphere electrode is calculated to be[8]:

$$I_{ss}(sphere) = 4\pi r_e nF c^{\circ} D \qquad \text{Equation 4.1}$$

while for micro-disks, the steady-state current is calculated[9, 10] as:

$$I_{ss}(disk) = 4 r_e nF c^{\circ} D \qquad \text{Equation 4.2}$$

where r_e is the radius of the sphere or disk, n is the number of electrons transferred in the electrode reaction, F is the Faraday constant, c° is the reference concentration, typically the initial concentration of A for the reaction described, and D is the reference diffusion coefficient, typically that of A for this reaction.

The study of recently developed nanoparticle-modified electrodes[11-15], nano-impact electrochemistry[7, 16-19], and single-entity electrochemistry[20-22], as well as the more traditional, but still popular, hanging mercury drop electrode[23-26] demand the further development of a complete understanding of diffusional transport towards electrochemically active spheres in contact with supporting, planar surfaces.

Numerical simulation[27-29] and multipole methods[30] have been used to derive results for systems involving spheres on surfaces under both steady-state conditions and during voltammetry. The limiting steady-state current for a full sphere on a surface is well-

established[27-30] and requires a correction factor of $\ln(2)$ relative to the corresponding expression for an isolated sphere (Equation 4.1):

$$I_{\lim} = 4\pi \ln(2) r_e n F c^{\infty} D$$ Equation 4.3

Additional correction factors have been proposed for the steady-state current to spheres of differing contact angles via a 'shape factor' by Bobbert[30]. Theory and experiment have been combined to describe the behaviour of randomly-distributed arrays of spherical nanoparticles on a surface, namely the transitions between 4 diffusional regime cases[28].

However, insufficient consideration has been given to physically realistic cases where the physical contact between the particle is finite and non-zero. These cases are effectively modelled in this chapter as truncated spheres on a surface with contact angles, θ_c, below $180°$ or π (see Figure 4.1).

Additionally, little attention has been previously given to the non-uniformity of the current distribution across the sphere's surface induced by the adjacent inert surface and consequent reduction in symmetry. The influence of the inert surface on the local diffusion is of great interest for explaining the total current transients. It is also vital as a foundation for understanding more complex systems, such as those in which the surface also possesses activity, and the behaviour of diffusion at a distance from the electrode. An example of such a system would be the simulation of diffusive uptake from a particulate on a leaf, a case study for diffusion across bio-membranes from localised sources more generally, which is discussed in Chapter 5. The development of a tool for interpreting local diffusional effects would also be of use for this benchmark system, which may be generalised to any other complex geometry.

In this chapter, we present numerical simulations of chronoamperometry at a variably truncated sphere on a supporting plane. We focus on producing high-accuracy simulations to correctly characterise local fluxes and concentration profiles distal from the electrode surface. We also present a simple mapping of results for an isolated sphere to approximate the flux transient for a sphere on a surface with an error of ¿1.5% throughout the current transient; this mapping may also be applied to truncated spheres, with similar accuracy for $\theta_c \geq \pi/4$. We also introduce the diffusion indicator and present and discuss its application to local fluxes for interpreting results.

4.2 Theory

The electrode system of interest involves a single, conductive, truncated, spherical particle of radius r_p in contact with a supporting infinite planar surface. This system is described using cylindrical polar coordinates (r, z, ϕ) with the origin at the centre of the contact area between the sphere and surface, where r is the perpendicular distance from the axis of symmetry, z is the coordinate normal to the planar surface, and ϕ is the angle about the axis of symmetry relative to an arbitrary reference direction normal to the axis. Symmetrical considerations demonstrate that no concentration gradients can develop along the ϕ coordinate; we thus simplify the system to a 2-dimensional simulation using (r, z) coordinates considering a single half-plane.

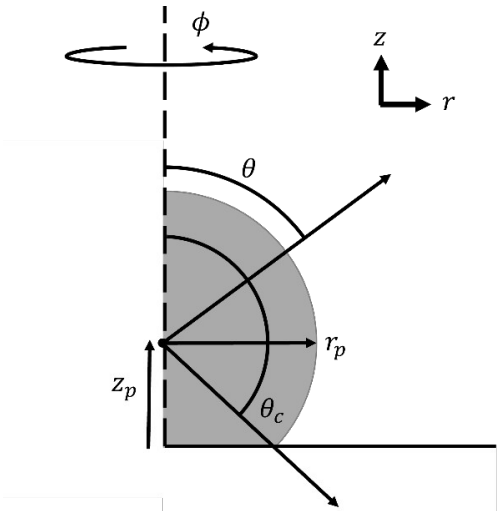


Figure 4.1: Illustration of the simulation space used for a truncated spherical grey particle on a surface. The cylindrical polar coordinate system (r, z, ϕ) is presented along with the axis of symmetry (dashed). Other key spatial parameters are also illustrated: the polar angle θ, the polar contact angle θ_c, the particle radius r_p, and the perpendicular distance from the plane to the particle centre z_p.

The polar angle, θ, measured from the axis of symmetry away from the inert plane, is also used in this work to describe the position of a point on the particle surface; this is related to θ_c which describes the polar angle to the point of contact between the particle and cuticle, as illustrated in Figure 4.1, which is equivalent to the particle's contact angle. The perpendicular distance between the plane and particle centre describes the extent of truncation and is represented by z_p.

We consider a simple one-electron transfer:

$$A + e^{-} \rightleftharpoons B \qquad \text{Equation 4.4}$$

Both species A and B are soluble and are assumed to possess equal diffusion coefficients. Only A is initially present in solution. We simulate the current transient produced by a potential jump to a large overpotential corresponding to diffusion-controlled reduction of A: therefore,

$$At\ t = 0: \qquad \begin{cases} c_A = c_A^{\circ} \ \forall \ (r, z) \\ c_B = 0 \end{cases} \qquad \text{Equation 4.5}$$

$$At\ t>0: \qquad \begin{cases} c_A = 0 \\ c_B = c_A^{¿} \end{cases} at\ r^2 + z^2 = 1 \qquad \text{Equation 4.6}$$

where c_i and $c_i^{¿}$ denote the concentration and bulk concentration of species i, respectively.

The mass transport of A and B in solution is described by Fick's second law of diffusion according to Equation 4.7 for species i:

$$\frac{\partial c_i}{\partial t} = D_i \cdot \nabla^2 c_i = D_i \left\{ \frac{\partial^2 c_i}{\partial r^2} + \frac{1}{r} \frac{\partial c_i}{\partial r} + \frac{\partial^2 c_i}{\partial z^2} \right\} \qquad \text{Equation 4.7}$$

where D_i denotes the diffusion coefficient of species i. Since mass must be conserved within the system and the diffusion coefficients for A and B are set to be identical, $c_A + c_B = c_A^{¿}$ at all points in the system. As a result, only species A need be simulated in order to produce the current transient and concentration profiles of A and B.

Zero-flux boundary conditions are applied normal to the symmetry axis and the inert, supporting planar surface. The bulk solution condition is enforced at a distance of $6\sqrt{Dt}$ from the particle surface, which is far into the tail of diffusion with a probability of diffusing below 0.001, such that the boundary has a negligible influence, recalling that[31, 32] $\langle x \rangle_{rms} = \sqrt{6\,Dt}$.

The system is normalised according to the dimensionless conversions given in Table 4.1.

Table 4.1: Dimensionless conversions used for the simulation system

Dimensionless Parameter	Expression
Radial coordinate	$R = r/r_p$
Normal coordinate	$Z = z/r_p$
Normal distance from plane to sphere centre	$Z_p = z_p/r_p$
Time	$T = D_A t/r_p^2$
Concentration of species A	$C = c_A/c_A^{¿}$
Local electrode flux	$J = \frac{j \cdot r_p}{D_A \cdot c_A^{¿}}$

Total electrode flux	$J_{Tot} = \frac{I}{F D_A c_A^{\infty} r_p} = 2\pi \int_0^{\theta_c} J \cdot \sin(\theta)\, d\theta$

I is the total current to the particle electrode and relates the dimensionless J_{Tot} to an experimental value.

Fick's second law of diffusion in dimensionless form is:

$$\frac{\partial C}{\partial T} = \frac{\partial^2 C}{\partial R^2} + \frac{1}{R}\frac{\partial C}{\partial R} + \frac{\partial^2 C}{\partial Z^2} \qquad \text{Equation 4.8}$$

The dimensionless flux of species A to the particle is equal to the dimensionless concentration gradient normal to the particle surface through Fick's first law of diffusion. Using the cylindrical coordinate system, the dimensionless flux must be determined from its R- and Z- components:

$$J = \frac{\partial C}{\partial R}\sin(\theta) + \frac{\partial C}{\partial Z}\cos(\theta) \qquad \text{Equation 4.9}$$

The total dimensionless flux is calculated by the integration of J across the electrode surface:

$$J_{Tot} = 2\pi \int_0^{\theta_c} J \cdot \sin(\theta)\, d\theta \qquad \text{Equation 4.10}$$

The mass transport equation and associated boundary conditions are discretised according to the following scheme and as illustrated in Figure 4.2.

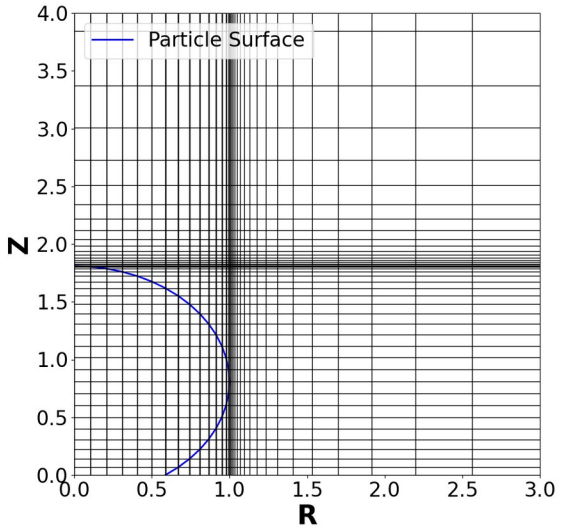


Figure 4.2: Illustration of the spatial discretisation scheme used in this work proximal to the truncated sphere particle. The particle surface is represented by a blue line. Spatial coordinates are in dimensionless forms. The spatial parameters used are chosen purely for illustrative purposes and are as follows: $Z_p = 0.8$, $d\theta = \pi/30$ and $\omega_R = \omega_Z = 1.3$.

The coordinate system chosen requires a high mesh density about the curved surface of the sphere to accurately describe the surface and diffusion proximal to it. This is ensured by arranging the grid such that each row within $0 < Z < 1 + Z_p$ contains a single point on the sphere surface satisfying $R = \sqrt{1 - (Z - Z_p)^2}$: thus the curved surface is described by consistent steps in the grid and the spatial mesh density about the sphere is described singly by the constant $d\theta$. Since less precision is required at a distance from the sphere, the grid expands as it moves beyond $R = 1$ and $Z = 1 + Z_p$. The grid expansion is achieved exponentially[33-36] such that:

- For $R > 1$: $R_i = R_{i-1} + h_R \omega_R^{i-1}$
- For $Z > 1 + Z_p$: $Z_i = Z_{i-1} + h_Z \omega_Z^{i-1}$

where h_R and h_Z are the smallest spacings possible in the R- and Z- directions respectively, and ω_R and ω_Z are expansion factors in the R- and Z- directions respectively.

A backward implicit discretisation[37-39] is used to resolve the steps in time. An exponentially expanding time grid is used for the temporal discretisation.

This discretised, finite difference system is solved fully implicitly and iteratively using the Biconjugate Gradient Stabilised method (BICGSTAB), with a relative convergence tolerance of 1×10^{-6}, with a semi-coarsening multigrid (SMG) preconditioner. The numerical simulation was performed on a Linux(Centos) machine with an Intel Core i7-6800K CPU (3.40GHz, 6 cores), 32GB of RAM, and an Nvidia Quadro GP100. The simulation program was written in C++, utilising the *HYPRE* software package (version 2.18.2)[40, 41] executed with CUDA enabled GPU support. Construction of the discretised grid, data analysis, and plotting were performed with *python*, including the *NumPy*, *SciPy* and *matplotlib* packages.

The flux transient was divided into windows of time which were simulated simultaneously with individually tailored grid parameters and then concatenated to efficiently produce a full flux transient.

4.2.1 The diffusion indicator

The diffusion indicator, α, has been recently established by Le et al[42] as a means to quantitatively characterise the extent to which diffusion to the electrode is convergent ($\alpha = 1$) or linear/Cottrellian ($\alpha = 0$), and is defined by:

$$\alpha = 2\frac{d\left(\log\left(J\right)\right)}{d\left(\log\left(T\right)\right)} + 1 \qquad \text{Equation 4.11}$$

where J and T are surface flux and time, respectively, in either dimensional or dimensionless forms. Several subsequent investigations into diffusion-limited interfacial processes occurring on various geometries have made use of this indicator[43-46]. This diffusion indicator is used in this chapter to analyse the transition from linear to convergent diffusion[2, 8] for a (variably truncated) sphere on a surface and to compare with the transitions observed for isolated spheres and disks.

Novelly, we applied the diffusion indicator to the local flux J_{local} to give α_{local}, rather than as hitherto to the total flux, allowing observation of changes to the diffusion regime local to specific points on the electrode surface. These results evidence the temporal development of a stagnation zone between the sphere and plane and demonstrate an α_{local} minimum associated with the growth of this zone. This result is comparable with the results observed for thin-layer systems[45]. Results are presented for the full sphere on a surface, variably truncated spheres, and for a disk. α_{local} is thus presented as a means for investigating how diffusion-limited currents are affected by complex electrode geometries.

4.3 Results for hemisphere and full-sphere-on-a-surface

In this section we consider the simplest cases of the truncated spherical particle on a plane: that of a hemisphere and of a full sphere. We present flux profiles resulting from an applied potential jump from zero current to one such that complete reduction of A occurs on the particle surface. We consider total flux and local fluxes across the electrode surface and introduce the local diffusion indicator, α_{local}, and how it varies across time and across the electrode surface, to understand the causes underpinning the observed diffusion-controlled response and identifying the role of local thin-layer like behaviour.

4.3.1 Model validation

The simplest possible case of a variably truncated sphere on a plane is the hemisphere, for which $\theta_c = \pi/2$. This case possesses polar angular isotropy; thus, the diffusion is unidimensional with respect to the distance from the particle centre ρ. The dimensionless total flux transient to a hemispherical particle after a potential jump is soluble analytically[47] as

$$J_{Tot} = 2\pi\left(\frac{1}{\sqrt{\pi T}} + 1\right)$$ Equation 4.12

The resulting flux transient is exactly one half that produced by a potential jump on a sphere isolated in solution. Due to its relative simplicity, this unidimensional system has been used to describe various problems involving a truncated sphere on a surface, such as the mercury drop electrode[48-50] and electrodes modified by mercury micro-droplets[26].

A second case is that of a perfect sphere with an infinitesimal point contact to a surface, and for which $\theta_c = \pi$. This has been considered previously both via theoretical analysis[30] and numerical simulation[27-29] and is frequently used for the analysis of nanoparticle-modified electrode surfaces[11] and nano-impacts[18, 51-53]. Figure 4.3 illustrates the flux transient produced by numerical simulation for a full sphere on a surface compared to that of an isolated sphere and an empirical "modified sphere" equation discussed in Section 4.3.2.

The full transition from linear diffusion to convergent diffusion is observed within the window $-4 \le \log(T) \le 3$. At short times the transients superimpose and the response is Cottrellian[54, 55]. The dimensionless total flux thus evolves according to the equation:

$$J_{Tot} = \frac{4\sqrt{\pi}}{\sqrt{T}},$$ Equation 4.13

reflecting linear diffusion across the full surface of the sphere. At longer times the response of the sphere on a surface drops below that of the isolated sphere as diffusional blocking by the surface becomes increasingly significant. In both cases at long times a steady-state current is established corresponding to convergent diffusion[2]. The steady-state current for the sphere on a plane has been shown[27, 30] to be:

$$I_{\lim} = 4\pi \ln(2) nFDr_p[A]_{bulk}$$ Equation 4.14

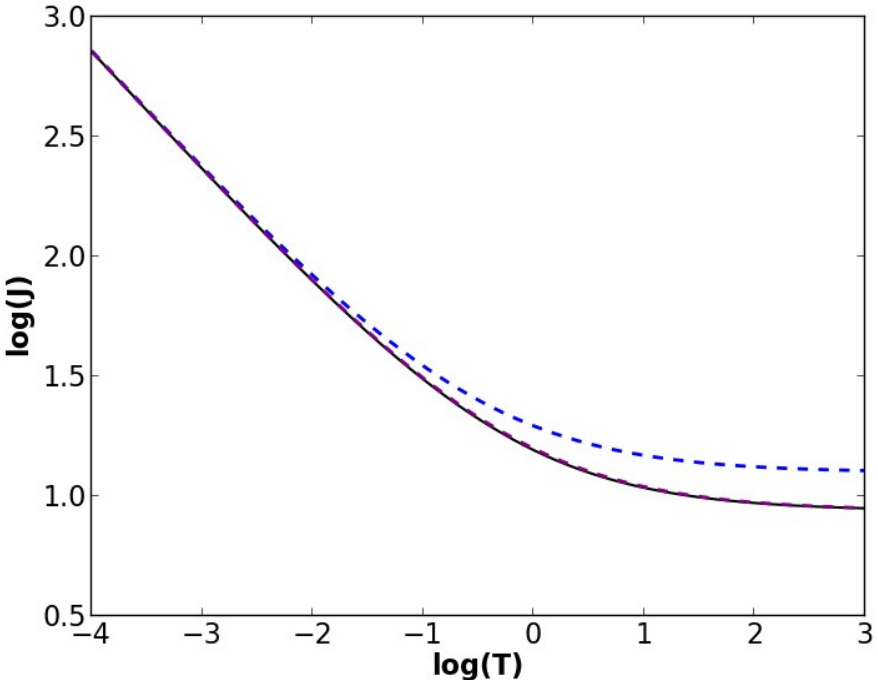


Figure 4.3: Log-log plot of the simulated dimensionless total flux transient for a sphere on a surface (black solid) and results for the isolated sphere (blue dashed) and the empirical "modified sphere" (purple dashed) co-presented. It is observed that there is significant overlap between the simulated results and the empirical "modified sphere" equation which makes the curves difficult to distinguish graphically. The purple dashed curve of the "modified sphere" equation slightly overestimates the simulation results around $\log(T)=0$.

4.3.2 Modified-sphere equation

It is useful to generate an analytical expression, analogous to Equation 4.12, to approximate the full flux transient after a potential step. On comparison of Equation 4.14 with the steady-state current to an isolated sphere, the difference is the $\ln(2)$ factor. Thus we intuitively[29] modify the analytical result for the isolated sphere such that the theoretical short- and long-time limits of the sphere on a plane are accurately described. The resulting "modified sphere" equation, used to approximate the flux transient for a sphere on a plane, is:

$$J_{Tot}=4\pi\left(\frac{1}{\sqrt{\pi T}}+\ln(2)\right) \qquad \text{Equation 4.15}$$

This transient, approximating a sphere on a plane of radius r_p bathed in a solution of bulk concentration $c^{¿}$, can be replicated by an isolated sphere with the radius $r_{isolated}$ in a solution of concentration $c^{¿}_{isolated}$ if $r_{isolated}=1.44\times r_p$ and $c^{¿}_{isolated}=0.48\times c^{¿}$.

The approximation in Equation 4.15 was compared with the fully converged simulation results for chronoamperometry on a sphere on a plane and found to be an excellent approximation, as shown in Figure 4.3. Figure 4.4 shows the relative error of the “modified sphere” equation from the simulated results for a sphere on a plane as given by

$$Relative\,Error = \frac{J_{Modified} - J_{Simulated}}{J_{Simulated}} \times 100\,\% \qquad \text{Equation 4.16}$$

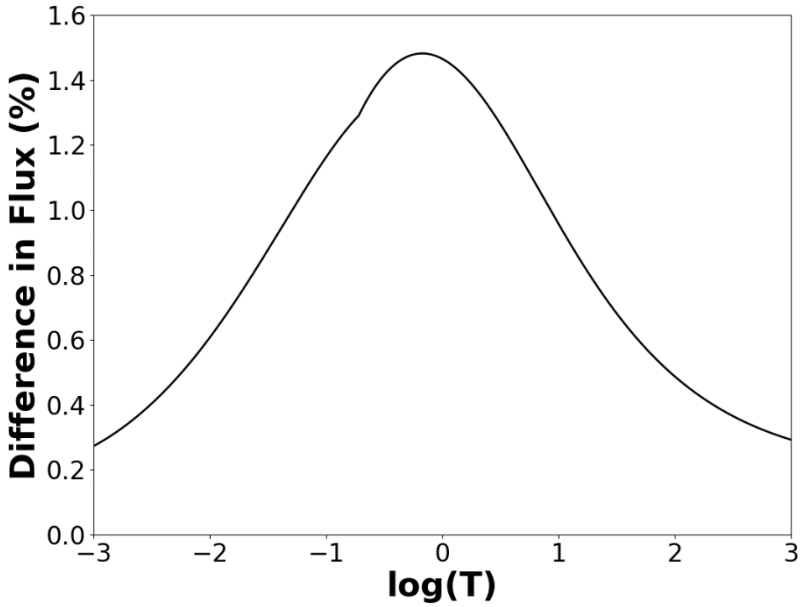


Figure 4.4: Relative error of the total flux predicted by the "modified sphere" equation relative to the simulated results for a sphere on a surface expressed as a percentage of the simulated flux and as a function of logarithmic time. The discontinuity occurs at $\log T = -0.7$: the point of transition between differently gridded zones of simulated time.

While the approximation is excellent in the short- and long-time limits (error ¿0.3%), a maximum error of 1.48% is observed at $T = 0.67$. Since the converged simulation results are themselves accurate to within 0.1% of literature results[27-30] within the range $-4 \le \log(T) \le 3$, the total maximum error is 1.58%, which is likely to be more than adequate for most applications. The small error corresponds to an overestimation of the flux during the transition from linear to convergent diffusion.

4.3.3 Applying the diffusion indicator

It is insightful to apply the diffusion indicator, $\alpha = 2\frac{d(\log(J))}{d(\log(T))} + 1$, to the flux transients shown in Figure 4.3 and the resulting profiles produced for the sphere on a surface, the isolated sphere, and the "modified sphere" equation are presented in Figure 4.5.

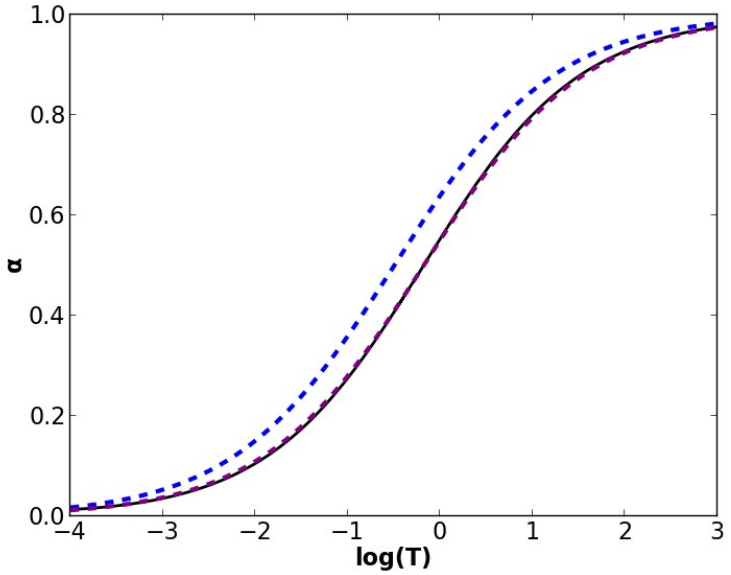


Figure 4.5: Diffusion indicator (α) profile produced by simulation for a sphere on a surface (black solid) compared to the predictions for an isolated sphere (blue dashed) and the empirical "modified sphere" (purple dashed). It is observed that significant overlap between the purple dashed line and the solid black line makes them difficult to distinguish graphically. The purple dashed curve slightly overestimates the black curve before $\log(T) = 0$ and slightly underestimates it after $\log(T) = 0$ with good agreement at the short and long time limits.

Each profile shows a smooth transition between 0 and 1 corresponding to the transition from linear to convergent diffusion. It is seen that the sphere on a plane and "modified sphere" equation deviate in their diffusional behaviour from the isolated sphere only during the transition between the limiting regimes. Although α has been previously demonstrated to act as a sensitive means to visualise changes in diffusional behaviour[42, 43, 45, 46], only slight deviations of the simulated result from the "modified sphere" profile are noted. For developing a deeper understanding of the diffusional behaviour during this transitory period we introduce the idea of a local diffusion indicator, α_{local}, in the next section to provide further insights.

4.4.4 Local effects

A benefit of simulated systems is the ability to extract local flux transients from points on the electrode surface. For electrodes of complex geometry which exhibit non-uniform flux, these local flux transients can possess valuable information on how the geometry affects the diffusion to the electrode. Just as the diffusion indicator, α, applied to the total flux transient provides information on the general diffusional behaviour of the system about the electrode, a local diffusion indicator, applied to a local flux transient, can similarly quantify changes in the diffusional behaviour at a specific region of the system:

$$\alpha_{local} = 2\frac{d\log\left(J_{local}\right)}{d\log\left(T\right)} + 1 \qquad \text{Equation 4.17}$$

Figure 4.6 and Figure 4.7 present the local flux and local diffusion indicator, α_{local}, profiles for the sphere on a surface at regular θ-intervals about the surface. These are compared to the flux profiles and α profiles expected for an isolated sphere and the "modified sphere" equation. At short times, the local fluxes and α_{local} obey the profiles given by the isolated sphere as opposed to the "modified sphere" equation. However, the profiles for each θ negatively deviate from the isolated sphere at different points in time. A minimum in α_{local} develops for θ values above $\pi/2$, with a negative α_{local}^{min} observed for θ values close to π. The closer to θ_c, the earlier this deviation occurs and the more negative the α_{local}^{min}. At long time, all α_{local} values converge on to the "modified sphere" equation's α profile irrespective of θ.

At short times, the diffusion layer is insufficiently thick for the presence of the inert surface to affect the diffusion behaviour local to the electrode surface and thus the surface flux, and so the local fluxes initially obey the transient predicted for an isolated sphere. However, for $\theta > \pi/2$, at some point in time, the diffusion layer will reach the inert plane and the amount of material arriving to the surface solely along the vector normal to the sphere will begin to deplete.

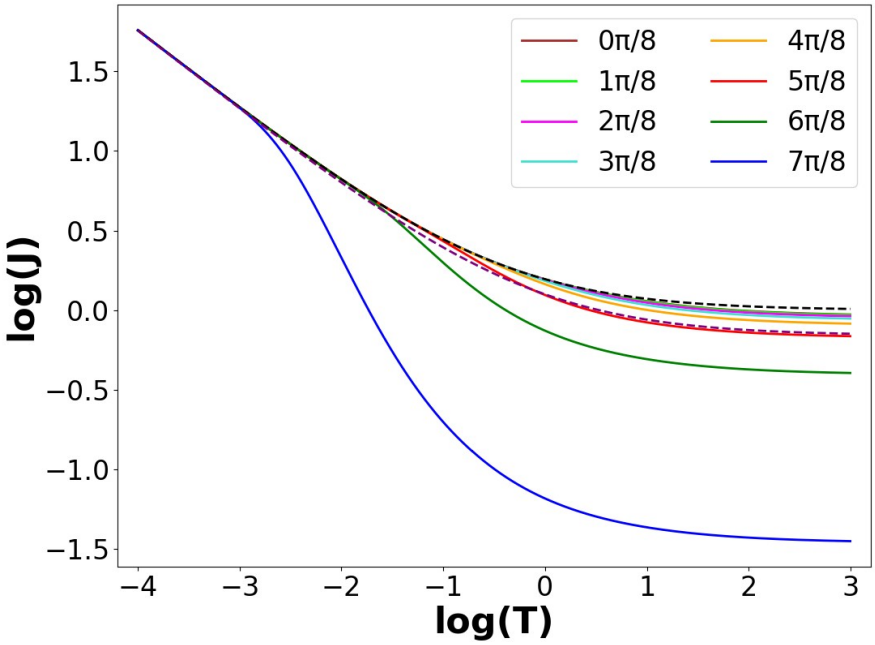


Figure 4.6: Local flux transients for the sphere on a surface at different positions on the sphere surface. θ-values are used to describe the position on the surface and are given in the Figure legend. Flux transients for the isolated sphere (black dashed) and the "modified sphere" equation (purple dashed) are also presented.

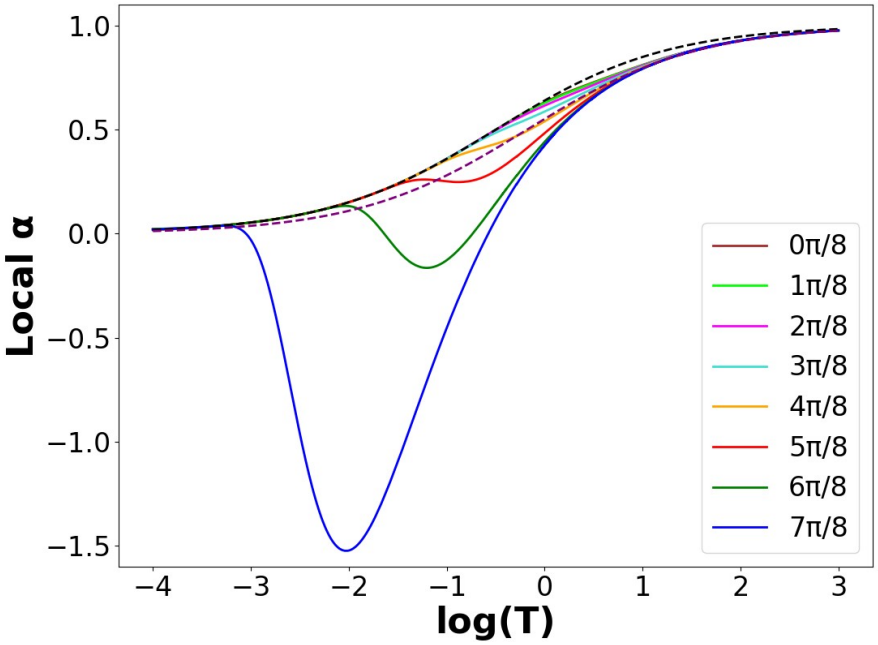


Figure 4.7: Local diffusion indicator (α_{local}) profiles for the sphere on a surface at different positions on the sphere surface. θ-values are used to describe the position on the surface and are given in the Figure legend. Local diffusion indicator profiles for the isolated sphere (black dashed) and the "modified sphere" equation (purple dashed) are also presented.

This depletion of material between the sphere and plane is to some extent comparable to the depletion of a thin layer above a planar electrode, which has been investigated previously[45]. The analytically derived flux transient at a planar electrode under thin layer conditions[8] is:

$$J = 2\sum_{m=1}^{\infty} \exp\left(\frac{-(2m-1)^2\pi^2 T}{4}\right)$$ Equation 4.18

We present the resulting diffusion indicator for a depleting thin layer above a planar electrode:

$$\alpha = 2T\frac{\sum_{m=1}^{\infty}\left(\frac{-(2m-1)^2\pi^2}{4}\right)\exp\left(\frac{-(2m-1)^2\pi^2 T}{4}\right)}{\sum_{m=1}^{\infty}\exp\left(\frac{-(2m-1)^2\pi^2 T}{4}\right)} + 1$$ Equation 4.19

$$¿\ 1 - \frac{\pi^2 T}{2} - \frac{2\pi^2 T\sum_{m=2}^{\infty} m(m-1)\exp\left(\frac{-(2m-1)^2\pi^2 T}{4}\right)}{\sum_{m=1}^{\infty}\exp\left(\frac{-(2m-1)^2\pi^2 T}{4}\right)}$$

The diffusion indicator in the long-time limit for a depleting thin-layer above a planar electrode can be approximated as: $\alpha \approx 1 - \frac{\pi^2}{2}T$ since the ratio of the sums of the exponential terms decays to zero (evident from the first terms, which dominate at long times); thus, the diffusion indicator evidently tends towards negative infinity at long times in this system.

The zero-flux boundary at the plane in contact with the electro-active sphere also produces a depletion of material between it and the electrode. However, unlike the planar thin-layer system described by Equation 4.18, additional material can arrive along the θ-coordinate for the sphere-on-a-plane system. This additional source of material counteracts the falling α_{local}, producing a finite minimum in α_{local}, and causes eventual convergence with the "modified sphere" equation's α profile in the long-time limit.

A similar minimum, caused by the thin-layer-like depletion of material but replenished in part by arrival of material from an additional source, is also observed in the diffusion indicator profiles demonstrated in recent work by Yang et al[56] in which layers of blocking spheres rest

on a planar electrode. Material on the underside of the first layer of spheres is initially depleted until material above the sphere's meridian acts as a new source of material. The diffusion indicator thus decreases to a finite minimum before increasing towards convergent diffusion as material on the sphere's topside is forced to diffuse through a narrow pore between spheres. As the diffusion layer extends beyond the layer(s) of blocking spheres, α tends towards zero and Cottrellian behaviour asserts itself again. Additional layers of spheres can produce a second peak in α. Features of these two peaks can then be analysed to determine geometrical features of the environment such as number of layers of spheres and the pore size between adjacent spheres.

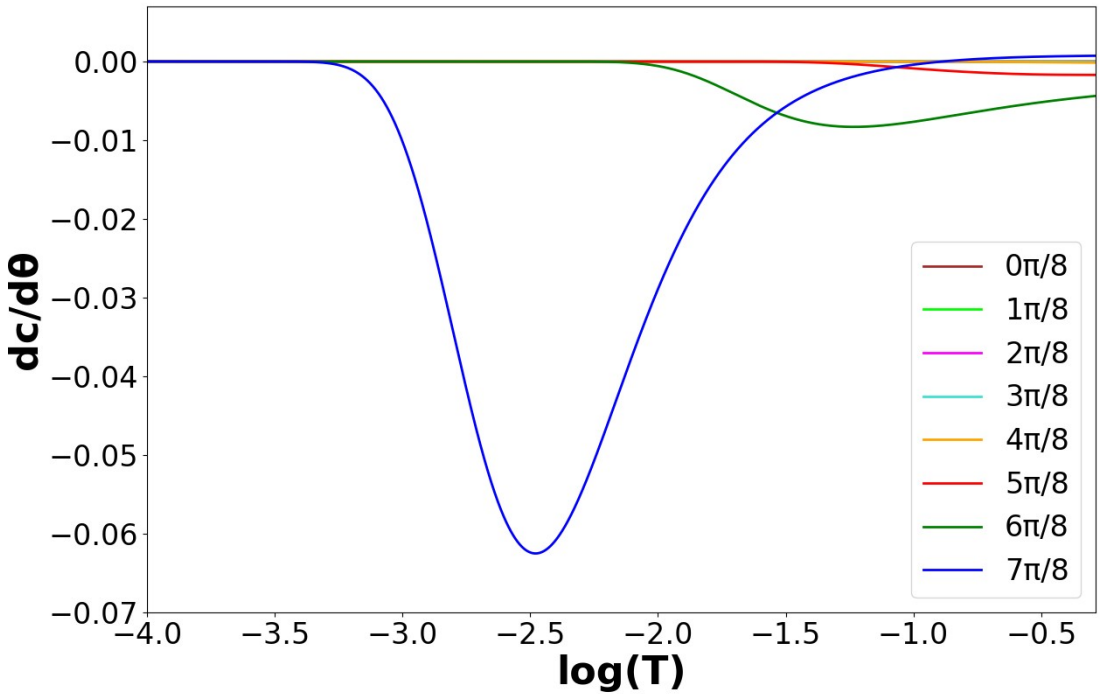


Figure 4.8: Plots of local $\partial C/\partial\theta$ profiles on the surface of a sphere-on-a-plane electrode during chronoamperometry. These profiles are extracted from varying positions on the surface denoted by the θ-positions given in the Figure legend.

Figure 4.8 demonstrates the evolution with time of the $\frac{\partial C}{\partial \theta}$ gradient local to the electrode surface at various θ. It can be seen that, for $\theta<\pi/2$, the depletion of material at the planar surface results in the development of a relatively large, negative $\frac{\partial C}{\partial \theta}$ concentration gradient.

$\frac{\partial C}{\partial \theta}$ goes through a minimum before tending towards a smaller steady state value. This corresponds to a reduction in the local flux normal to the surface and a negative gradient of the α_{local} profile, which generates a α_{local}^{min}. The point at which α_{local} converges on to the "modified sphere" equation is the moment at which the $\frac{\partial C}{\partial \theta}$ gradient ceases to evolve with time at a given θ. Thus, α_{local} offers an elegant means of insight into the evolution of local concentration gradients parallel to the particle surface as well as perpendicular to it.

4.4 Results for a spherical cap

In this section we investigate the effect of the inert, supporting plane to correctly characterise the diffusional behaviour for truncated spherical electrodes when the contact angle θ_c is neither π nor $\pi/2$. In order to effectively observe diffusional effects beyond the Cottrellian to convergent diffusion transition, the "modified sphere" equation (Equation 4.15) is generalised for any θ_c. We present simulated results for the total and local diffusion indicator profiles. We also discuss the convergence towards the case of a microdisk as θ_c tends to zero.

4.4.1 Generalising the modified-sphere equation

The "modified sphere" equation (Equation 4.15) has been used in this chapter as an approximation of the flux transient for a sphere on a plane and comparison to it is used as a means to assess how the diffusion to the sphere is affected by the presence of the inert plane in the limits of short and long time. The "modified sphere" equation is derived by modifying results for an isolated sphere to approximate results for a sphere on a plane. Our use of this equation builds on work by Ward et al[29] in which steady-state voltammograms for a sphere on a plane were accurately generated by performing an inexpensive, one dimensional simulation of an isolated sphere followed by an appropriate mapping of the results using a conversion of

$c^{¿}$ (bulk analyte concentration) and E_f (formal potential of the electron transfer). For chronoamperometry, we propose the mapping of results through the conversion of $c^{¿}$ and r_p (the spherical particle radius).

The "modified sphere" equation is generally applicable for any truncated sphere in the form:

$$J = 2\pi\left(\frac{1-\cos(\theta_c)}{\sqrt{\pi T}} + x\right) \qquad \text{Equation 4.20}$$

where the $1-\cos(\theta_c)$ factor corrects for the electrode surface area during the Cottrellian regime and $x = \int_0^{\theta_c} j_{ss}\sin(\theta)\,d\theta$ corresponds to the limiting dimensionless total steady-state flux for a given (r, z) slice. x may be calculated either using Bobbert's table of shape factors[30] or from numerical simulation of $\frac{\partial c}{\partial t} = D\nabla^2 c = 0$ as we have done.

Assuming a consistent value of the diffusion coefficient D, the flux transient produced by the "modified sphere" equation for a certain truncated sphere on a surface can be replicated by an isolated sphere under the following conditions:

$$r_{isolated} = r_{truncated}\frac{1-\cos(\theta_c)}{x} \qquad \text{Equation 4.21}$$

$$c^{¿}_{isolated} = c^{¿}_{truncated}\left(\frac{x^2}{1-\cos(\theta_c)}\right) \qquad \text{Equation 4.22}$$

We next apply the "modified sphere" equation to truncated spheres generally starting with the case of $\theta_c = 3\pi/4$.

4.4.2 Reducing the contact angle: $\pi/2 < \theta_c \leq \pi$

We next seek insight into how the diffusional effects vary between the cases of a full sphere and a hemisphere on a plane. Numerical simulation of a potential jump on a spherical electrode truncated to produce a contact angle of $\theta_c = 3\pi/4$ was performed.

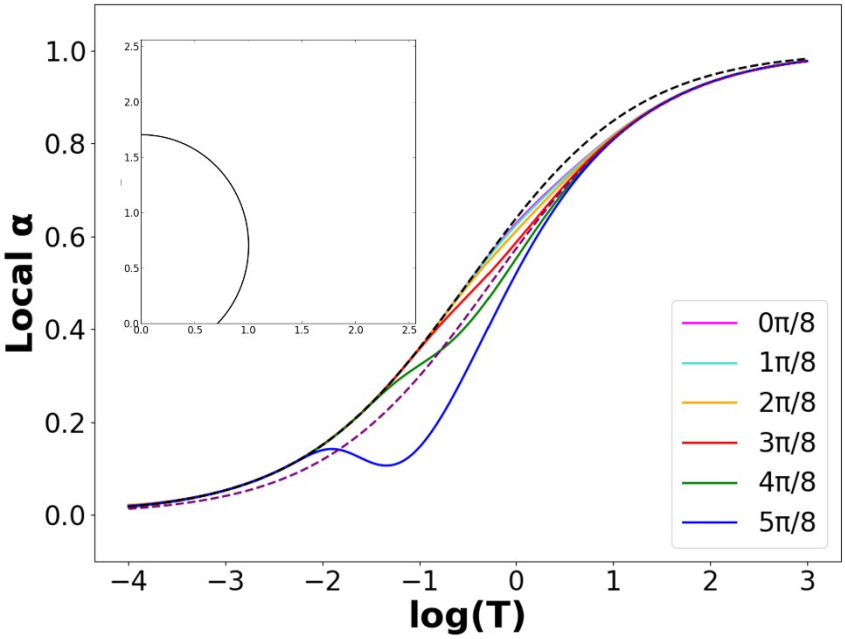


Figure 4.9: Local diffusion indicator (α_{local}) profiles for the truncated sphere with contact angle of $\theta_c = 3\pi/4$. The θ-values at these positions are given in the Figure legend. The values for the isolated sphere (black dashed) and the "modified sphere" equation (purple dashed) are also presented. The inlaid diagram illustrates the shape of this truncated sphere electrode on the supporting plane.

Figure 4.9 shows the local diffusion indicator profiles produced with comparison to the isolated sphere and the “modified sphere” equation (Equation 4.20). The values of θ were chosen to facilitate comparison with the α_{local} profiles produced for the full sphere, demonstrated in Figure 4.7. Trends in the α_{local} profiles for $\theta_c = 3\pi/4$ are qualitatively similar to trends observed for the $\theta_c = \pi$ case. For the same θ, if $\theta > \pi/2$, an earlier and more pronounced minimum is observed, since that section of the sphere is now closer to the new contact point and also closer to the inert surface, giving a more pronounced local ‘thin-layer’ effect and an earlier development of local $\frac{\partial C}{\partial \theta}$. For $\theta < \pi/2$, the decreased θ_c results in a later

and less pronounced deviation of α_{local} from the isolated sphere and a weaker overall $\frac{\partial C}{\partial \theta}$. This is a consequence of greater overall accessibility to the sphere-plane contact by diffusion and the greater similarity of the system to the hemisphere case.

4.4.3 Reducing the contact angle: $0<\theta_c<\pi/2$

Spheres truncated to a level beyond a hemisphere (i.e., $\theta_c<\pi/2$) are expected to display very different diffusional behaviour to what has been seen thus far. Rather than the contact point being concealed from the solution in a local thin-layer-like geometry, the contact point is instead more exposed to convergent diffusion from the bulk solution than the rest of the electrode surface. In the limit of small contact angle this geometry approaches that of the intensely studied[9, 10, 57-63] micro-disk, which possesses a fully exposed edge; the micro-disk is a limiting case for the truncated sphere[30] since the surface asymptotically approaches a flat surface as $\theta_c \to 0$.

In this section, we seek to investigate the transition between the limiting cases of near-sphere-like and near-disk-like diffusional behaviour as θ_c is decreased from a hemisphere ($\theta_c=\pi/2$) towards $\theta_c=0$. The former limit is characterised by the "modified sphere" equation (Equation 4.20) which considers only terms arising from linear and convergent diffusion such that no edge effect or local thin-layer is seen. The latter limit is characterised by the Shoup-Szabo equation[10] (with a surface area correction to dimensionless time, according to θ_c), with significant edge diffusion which increases with time:

$$\frac{J_{Tot}}{A_d}=\frac{4}{\pi}\left(0.7854+\frac{0.8863}{2\sqrt{T_d}}+0.2146\,e^{\frac{-0.7823}{2\sqrt{T_d}}}\right) \qquad \text{Equation 4.23}$$

where A_d is the dimensionless surface area of the truncated sphere, J_{Tot} is the dimensionless total flux, and T_d is the corrected dimensionless time to correct for changing area of an equivalent disk such that $T_d = \frac{T}{r_d^2}$, where $r_d = \sqrt{2\left(1-\cos\theta_c\right)}$ is the ratio of the radius of a micro-disk whose surface area equals a truncated sphere of contact angle θ_c with the radius of that truncated sphere and T is the dimensionless time normalised against the radius of the truncated sphere.

While more recent approximations are available for characterising the limiting disk behaviour, such as those presented by Mahon and Oldham[61, 62] and Bieniasz[63], the Shoup-Szabo equation is a simple and highly familiar result for electrochemists, whose maximum error of 0.6% satisfies experimental demands and the demands of our own work.

$\theta_c = \pi/4$ and $\theta_c = \pi/8$ are presented as informative cases. Profiles of α are presented in assessment of the utility of α for characterising the diffusional behaviour relative to the two limiting cases described above: namely the sphere-like behaviour with no edge effect and the disk behaviour with considerable edge effect.

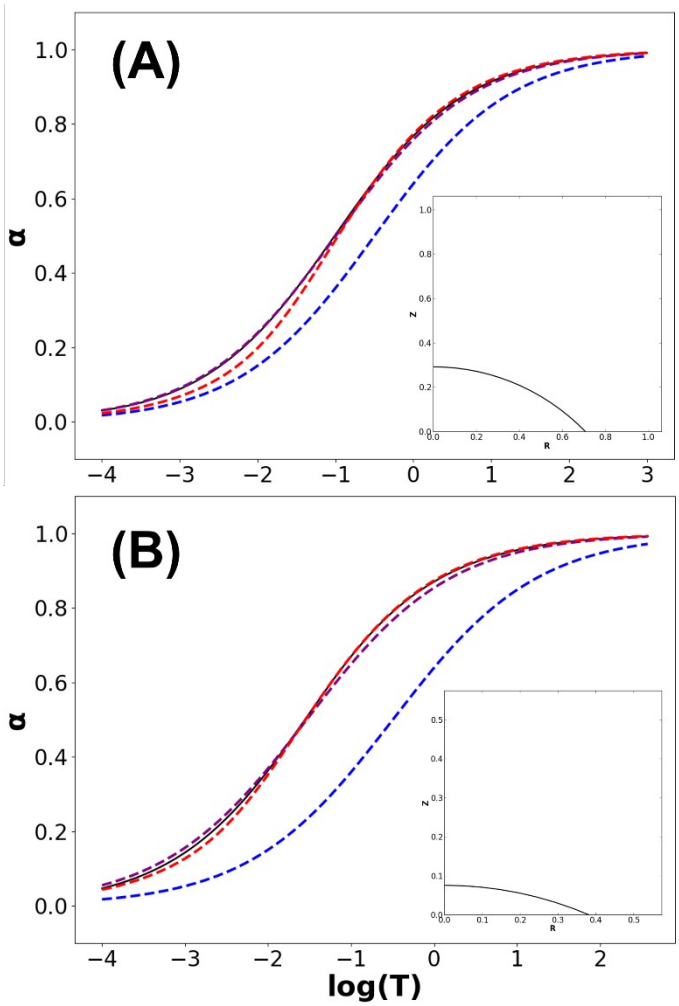


Figure 4.10: Diffusion indicator (α) profiles for the truncated spheres with contact angles of (A) $\theta_c = \pi/4$ and (B) $\theta_c = \pi/8$ illustrated as black solid lines. Also presented are curves illustrating profiles for the isolated sphere (blue dashed), the "modified sphere" equation (purple dashed), and the Shoup-Szabo equation for a disk of equal surface area (red dashed). Inlaid diagrams illustrate the shapes of the corresponding truncated sphere electrodes on the supporting plane. Significant overlap between the solid black line and the purple dashed line in (A) and between the solid black line and the red dashed line in (B) makes distinguishing these curves difficult graphically at certain times.

Figure 4.10 shows the α profiles for the cases of $\theta_c = \pi/4$ and $\theta_c = \pi/8$ in plots (A) and (B) respectively. The isolated sphere is presented as a blue dashed line, the generalised "modified sphere" equation is presented as a purple dashed line, and the Shoup-Szabo equation is presented as a red dashed line. The α profile in (A) follows the "modified sphere" equation more closely than the Shoup-Szabo equation, while in (B) the α profile follows the latter equation more accurately. This illustrates a general transition between the two diffusional regimes: namely near-sphere-like to near-disk-like.

In Figure 4.10(A), α follows the prediction of the "modified sphere" equation accurately at short times for $\theta_c = \pi/4$, however, after the "modified sphere" and Shoup-Szabo α profiles cross, α for the truncated sphere follows a curve located between these two limiting cases. Meanwhile in Figure 4.10(B) for $\theta_c = \pi/8$, the Shoup-Szabo describes the diffusional behaviour accurately at intermediate and long times but the α profile follows a curve intermediate between the limiting cases at short times, namely before the curves given by the limiting cases cross. This suggests that, as θ_c is decreased from $\pi/2$, a transition to near-disk-like behaviour occurs first for the flux at long times, followed by a later transition for short times. This complicates determining the diffusional behaviour from the global (non-local) α profile alone as it depends on which point in time one considers.

To better understand this phenomenon, we extract profiles for the local diffusion indicator, α_{local}, to assess local diffusional effects. Figure 4.11 presents α_{local} profiles at various points along the surface of (A) a sphere truncated to $\theta_c = \pi/4$ and (B) a sphere truncated to $\theta_c = \pi/8$. Plots of the curves predicted by the isolated sphere, "modified sphere" and Shoup-Szabo equations are presented by black, purple, and red dashed lines respectively. The position on the electrode surface from which the profiles are derived is given as the θ-coordinate in the Figure legends.

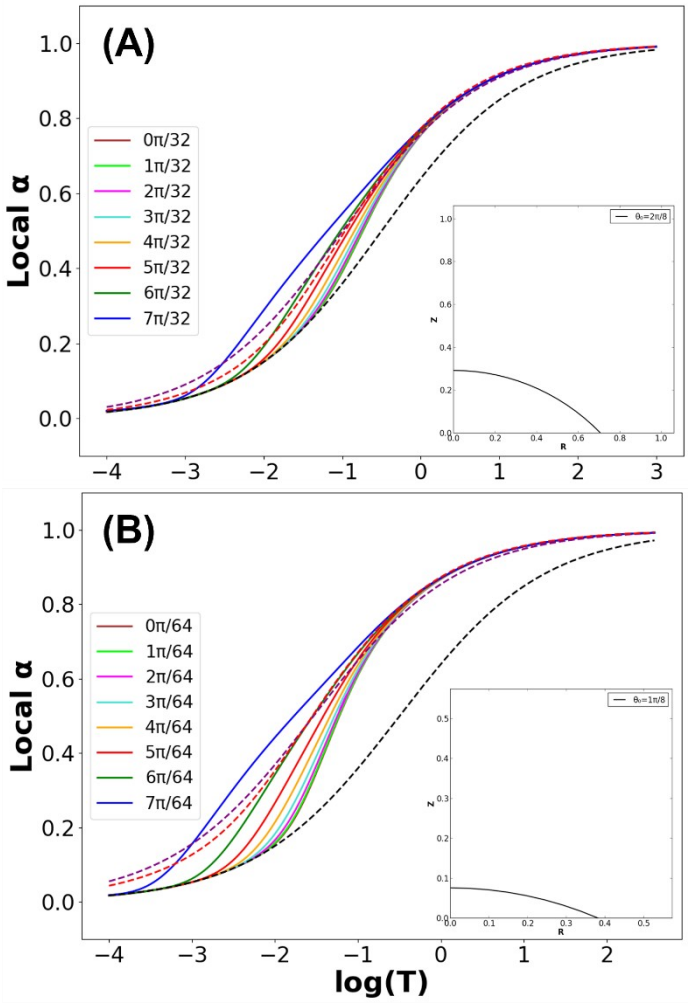


Figure 4.11: Local diffusion indicator (α_{local}) profiles for the truncated spheres with contact angles of (A) $\theta_c = \pi/4$ and (B) $\theta_c = \pi/8$. Profiles for the isolated sphere (black dashed), the "modified sphere" equation (purple dashed), and the Shoup-Szabo equation for a disk of equal surface area (red dashed) are also presented. The position on the electrode surface from which a given α_{local} profile is extracted is given in the Figure legend as the θ-position. Inlaid diagrams illustrate the shape of the corresponding truncated sphere electrodes on the supporting plane.

As was observed for $\theta_c > \pi/2$, all α_{local} profiles in Figure 4.11 follow the same curve at short times, namely that of the isolated sphere. For the truncated spheres this curve is given by the isolated sphere equation. This curve represents the profiles that would be expected if material were to exclusively diffuse along the vector normal to the electrode surface at all times. Each plot exhibits a deviation from this curve once material begins to arrive along the vector parallel to the electrode surface. The larger the θ from which the α_{local} profile is taken (and thus the closer to the electrode surface's edge), the earlier and the more pronounced the deviation. This is due to the greater influence of material arriving due to the edge effect.

The smaller the θ_c, the earlier this deviation occurs for all θ. This is further evidenced by comparison to the surface-local $\frac{\partial C}{\partial \theta}$ profiles given in Figure 4.12 whereby positive $\frac{\partial C}{\partial \theta}$ maxima, produced by the arrival of material via the edge effect and followed by a decline towards steady state values, occur earlier and are more pronounced as θ_c decreases when comparing positions of equivalent θ/θ_c. As the contact angle decreases, it is seen that the response of the truncated sphere tends towards, but does not reach, the response of a flat disc, as shall be discussed below.

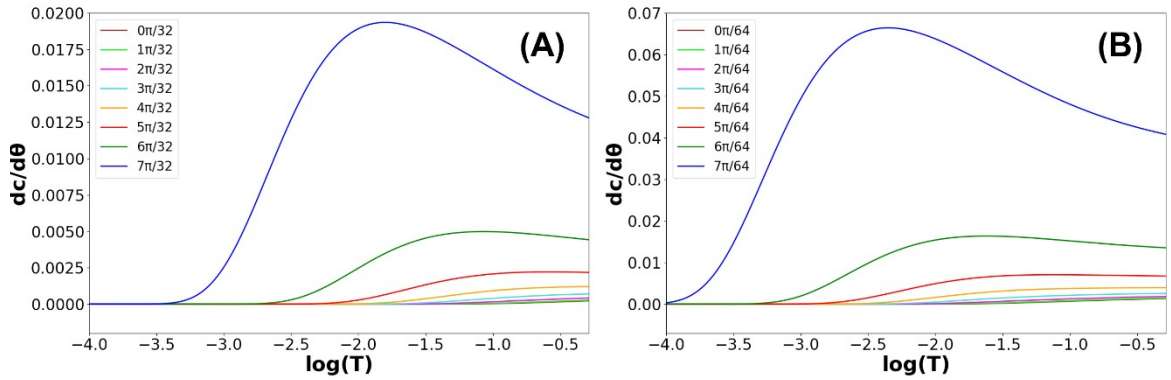


Figure 4.12: Plots of local $\partial C/\partial \theta$ profiles on the electrode surface of truncated spheres with contact angles of (A) $\theta_c = \pi/4$ and (B) $\theta_c = \pi/8$. The θ-positions at which these profiles have been extracted have been given in the Figure legend.

The long-time curve upon which the α_{local} profiles converge is equivalent to the long-time curve for the α profile. The convergence of α_{local} on to the α profile at long time is common to all geometries. Since, at short times, α_{local} obeys the curve of normal diffusion, which depends only on the curvature of the electrode, it is emphasised that α_{local}'s principal utility is in the elucidation of diffusional effects intermediate between the diffusional regimes active at short and long times. As such, α_{local} is not useful for justifying the θ_c required for the truncated spheres to exhibit disk-like behaviour in the late time limit. However, comparison of the α_{local} profiles produced by simulation for the truncated spheres with the α_{local} profiles

produced by simulation for a microdisk yields valuable information about the linear-convergent diffusion regime transition.

Figure 4.13 presents α_{local} profiles for a micro-disk extracted from various R-positions on the electrode surface, where R is the dimensionless perpendicular distance from the axis of symmetry relative to the disk's radius. The profiles at early time all follow the response expected for Cottrellian diffusion of $\alpha=0$, corresponding to the inherent planarity of the electrode's own curvature. A deviation from this regime is seen once material begins to arrive along the dimension parallel to the electrode, which is the R-coordinate in the case of a microdisk. The α_{local} profiles converge at long times on to the long-time curve of the α profile which is accurately predicted by the Shoup-Szabo equation.

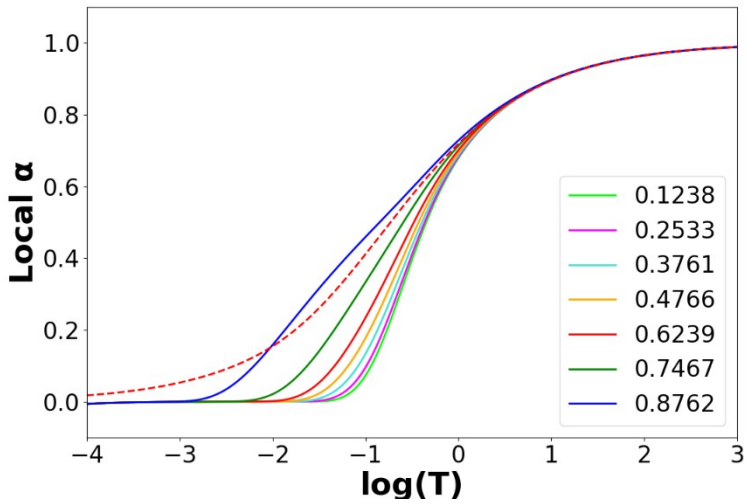


Figure 4.13: Local diffusion indicator (α_{local}) profiles for a micro-disk electrode where variables are normalised to the disk radius as opposed to the radius of a spherical particle. The Shoup-Szabo equation is presented as the red dashed line. The R-position on the electrode surface from which a given α_{local} profile is extracted is given in the Figure legend.

Correspondence of α_{local} for a truncated sphere to that observed for a microdisk is obscured by the influence of the isolated sphere equation, and thus the electrode's inherent curvature, which deviates from Cottrellian diffusion at very early times. For truly disk-like behaviour to be observed across the entire transient for a truncated sphere, the edge effect must contribute greatly to the surface flux before diffusion to the curved surface can deviate from linearity.

Thus we observe that the conditions for near-disk-like behaviour are more demanding at short times for a truncated sphere leading to a time-dependent transition, since the electrode's own curvature dominates more when the diffusion layer is thinner.

Plots of $\frac{\partial \alpha_{local}}{\partial \log(T)}$ are presented in Figure 4.14 to further investigate the shape of the α_{local} curves for truncated spheres of $\theta_c = \pi/4$ (A), $\theta_c = \pi/8$ (B), and for a microdisk (C). Curves corresponding to the isolated sphere (black dashed), the "modified sphere" (purple dashed), the Shoup-Szabo equation (red dashed) and purely linear diffusion (orange dashed) are co-presented for comparison. Note that in Figure 4.14(C), the time domain is normalised to the radius of the disk of contact and not a sphere radius, since the radius of a micro-disk comparable to a given truncated sphere is dependent on θ_c.

It can be seen in Figure 4.14 that two peaks are present in the gradients of α_{local}. The closer to the electrode edge, the greater the peak separation; however, for most of the electrode surface, the peaks are coalesced and indistinguishable. At long times, each profile converges together. The smaller the θ_c, the earlier the convergence. The curve upon which the profiles converge is dependent on the extent of disk-like behaviour at long times and thus intermediate between the predictions of the "modified sphere" and Shoup-Szabo equations for the truncated spheres, as discussed previously, while the microdisk converges on to the Shoup-Szabo equation.

The two overlapping peaks are caused by and thus characterise two distinct diffusional processes. The first process corresponds to the edge effect whereby material arrives along the vector parallel to the electrode surface from the volume beyond the electrode edge. The second process relates to the transition to general convergent diffusion as the diffusion layer

thickness exceeds the electrode dimensions and is independent of diffusion parallel to the electrode surface.

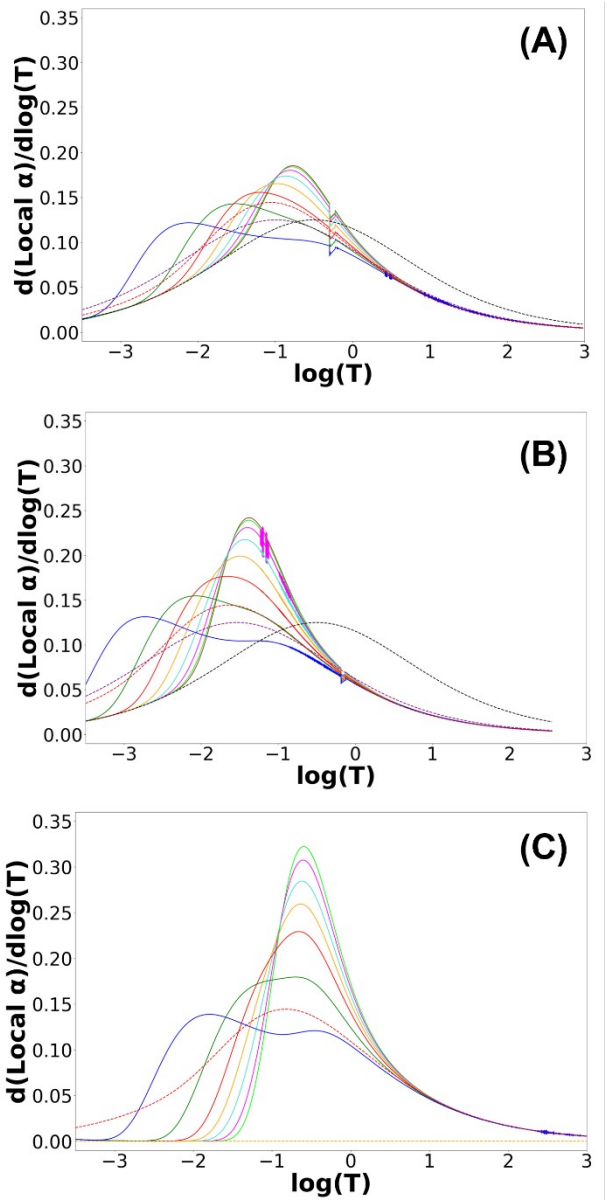


Figure 4.14: Smoothed gradients of simulated α_{local} profiles ($d\alpha_{local}/dlog(T)$) for (A) $\theta_c = \pi/4$, (B) $\theta_c = \pi/8$, and (C) a microdisk. These curves are coloured according to the position on the active surface from which they were extracted in terms of θ/θ_c for (A) and (B) and in terms of R for (C). The colour scheme is as follows with the dimensionless positions given in brackets: dark blue (7/8), green (6/8), red (5/8), orange (4/8), light blue (3/8), purple (2/8), lime (1/8), and brown (at the symmetry axis). The time domain is normalised to the radius of the sphere for subplots (A) and (B) and to the radius of the microdisk for subplot (C). Curves corresponding to the isolated sphere (black dashed), the "modified sphere" (purple dashed), the Shoup-Szabo equation (red dashed) and purely linear diffusion (orange dashed) are co-presented for comparison.

Decreasing θ_c increases the height of each maximum and shifts each maximum to earlier T, with the microdisk (C) acting as the limiting case. This is caused by decreasing the absolute

distance that material diffusing parallel to the surface needs to travel to access a point on the surface. The smaller the θ/θ_c, the greater the sensitivity of the height and position to changes in θ_c.

The features apparent in the $\partial\alpha_{local}/\partial\log(T)$ profiles characterise the processes governing how the diffusional behaviour varies with time and thus provides insightful visualisation of individual local diffusional processes.

4.5 Conclusions

Complex diffusional effects occur during the transition from overall linear to overall convergent diffusion regimes in the current-time transients for (truncated-)sphere-on-a-plane electrode geometries, including a temporary, intermediary, thin-layer-like behaviour for spheres with $\theta_c > \pi/2$ and a θ_c-dependent edge effect for spheres with $\theta_c < \pi/2$. In the limit of a nearly flat electrode, the response tends to that of a disc electrode. Using α_{local} we can observe the effects which cause deviations from simple diffusional behaviour, including the source of error for the "modified sphere" equation. The observation is made that electrodes exhibiting long-time convergent diffusion demonstrate α_{local} profiles which converge under the long-time limit irrespective of position on the surface. α_{local} allows a means to sensitively characterise how the diffusional behaviour affects the local flux and provides effective insight into the effect of concentration gradients parallel to the electrode surface on the normal surface flux. The gradient of α_{local} profiles can distinguish between the action of different diffusional processes which are otherwise indistinguishable. This analytical tool is hence valuable for the understanding of flux transients produced by complex electrode geometries and the visualisation of their diffusional behaviour.

The results presented in this chapter provide a foundation for considering diffusion about a sphere on a surface, a geometry of significance for modelling the uptake of pesticidal material from particulate formulations on plant leaves. In the context of foliar uptake, Chapter 5 continues to investigate the diffusional behaviour about a sphere on a surface and thus the results presented here are also of importance for that work.

References

1. Elliott, J. R.; Compton, R. G., Local diffusion indicators: A new tool for analysis of electrochemical mass transport. *Journal of Electroanalytical Chemistry* **2022,** *908*, 116114.
2. Compton, R. G.; Laborda, E.; Ward, K., *Understanding Voltammetry*. Third ed.; World Scientific: 2018.
3. Bieniasz, L. K.; González, J.; Molina, Á.; Laborda, E., Theory of linear sweep/cyclic voltammetry for the electrochemical reaction mechanism involving a redox catalyst couple attached to a spherical electrode. *Electrochimica Acta* **2010,** *56* (1), 543-552.
4. Liu, Y.; Cai, H.; Li, H., Fabrication of micro spherical electrode by one pulse EDM and their application in electrochemical micromachining. *Journal of Manufacturing Processes* **2015,** *17*, 162-170.
5. Svir, I. B.; Oleinick, A. I., The electrogenerated chemiluminescence kinetics at a microdisc electrode. *Journal of Electroanalytical Chemistry* **2001,** *499* (1), 30-38.
6. Eloul, S.; Compton, R. G., Shielding of a Microdisc Electrode Surrounded by an Adsorbing Surface. *ChemElectroChem* **2014,** *1* (5), 917-924.
7. Eloul, S.; Kätelhön, E.; Batchelor-McAuley, C.; Tschulik, K.; Compton, R. G., Diffusional impacts of nanoparticles on microdisc and microwire electrodes: The limit of detection and first passage statistics. *Journal of Electroanalytical Chemistry* **2015,** *755*, 136 - 142.
8. Bard, A. J.; Faulkner, L. R.; Zoski, C. G.; Leddy, J., *Electrochemical methods : fundamentals and applications*. Second ed.; 2001.
9. Aoki, K.; Osteryoung, J., Diffusion-controlled current at the stationary finite disk electrode: Theory. *Journal of Electroanalytical Chemistry* **1981,** *122* (C), 19--35.
10. Shoup, D.; Szabo, A., Chronoamperometric current at finite disk electrodes. *Journal of Electroanalytical Chemistry and Interfacial Electrochemistry* **1982,** *140* (2), 237-245.
11. Belding, S. R.; Campbell, F. W.; Dickinson, E. J. F.; Compton, R. G., Nanoparticle-modified electrodes. *Physical Chemistry Chemical Physics* **2010,** *12* (37), 11208-11221.
12. Sanghavi, B. J.; Mobin, S. M.; Mathur, P.; Lahiri, G. K.; Srivastava, A. K., Biomimetic sensor for certain catecholamines employing copper(II) complex and silver nanoparticle modified glassy carbon paste electrode. *Biosensors and Bioelectronics* **2013,** *39* (1), 124-132.
13. Messaoud, N. B.; Ghica, M. E.; Dridi, C.; Ben Ali, M.; Brett, C. M. A., Electrochemical sensor based on multiwalled carbon nanotube and gold nanoparticle modified electrode for the sensitive detection of bisphenol A. *Sensors and Actuators B: Chemical* **2017,** *253*, 513-522.
14. Tang, Y.; Cheng, W., Nanoparticle-Modified Electrode with Size- and Shape-Dependent Electrocatalytic Activities. *Langmuir* **2013,** *29* (9), 3125-3132.

15. Miao, R.; Yang, M.; Compton, R. G., The Electro-oxidation of Hydrazine with Palladium Nanoparticle Modified Electrodes: Dissecting Chemical and Physical Effects: Catalysis, Surface Roughness, or Porosity? *The Journal of Physical Chemistry Letters* **2021,** *12* (28), 6661-6666.
16. Cheng, W.; Compton, R. G., Electrochemical detection of nanoparticles by 'nano-impact' methods. *TrAC Trends in Analytical Chemistry* **2014,** *58*, 79-89.
17. Sokolov, S. V.; Eloul, S.; Kätelhön, E.; Batchelor-McAuley, C.; Compton, R. G., Electrode–particle impacts: a users guide. *Physical Chemistry Chemical Physics* **2017,** *19* (1), 28-43.
18. Chang, X.; Batchelor-McAuley, C.; Compton, R. G., Methanol oxidation at single platinum nanoparticles. *Journal of Electroanalytical Chemistry* **2021,** *896*, 115438.
19. Xie, R.-C.; Batchelor-McAuley, C.; Yang, M.; Compton, R. G., Substrate mediated dissolution of redox active nanoparticles; electron transfer over long distances. *Nano Research* **2021**.
20. Bai, Y.-Y.; Wu, Z.; Xu, C.-M.; Zhang, L.; Feng, J.; Pang, D.-W.; Zhang, Z.-L., One-to-Many Single Entity Electrochemistry Biosensing for Ultrasensitive Detection of microRNA. *Analytical Chemistry* **2020,** *92* (1), 853-858.
21. Ren, H.; Edwards, M. A., Stochasticity in single-entity electrochemistry. *Current Opinion in Electrochemistry* **2021,** *25*, 100632.
22. Wang, Y.; Shan, X.; Tao, N., Emerging tools for studying single entity electrochemistry. *Faraday Discussions* **2016,** *193* (0), 9-39.
23. DeMars, R.; Shain, I., Anodic stripping voltammetry using the hanging mercury drop electrode. *Analytical Chemistry* **1957,** *29* (12), 1825-1827.
24. Markowitz, J. M.; Elving, P. J., The Polarographic Diffusion Current - Current-Time Relationship At The Dropping Mercury Electrode. *Chemical Reviews* **1958,** *58* (6), 1047-1079.
25. Ralph, T. R.; Hitchman, M. L.; Millington, J. P.; Walsh, F. C., The reduction of l-cystine in hydrochloric acid at mercury drop electrodes. *Journal of Electroanalytical Chemistry* **2006,** *587* (1), 31-41.
26. Liu, C.; Cheng, W.; Zeng, Q.; Huang, X.; Wang, L., Voltammetric and microscopical investigation of the properties and behaviors of individual mercury micro-droplets. *Journal of Electroanalytical Chemistry* **2017,** *784*, 145-152.
27. Streeter, I.; Compton, R. G., Diffusion-Limited Currents to Nanoparticles of Various Shapes Supported on an Electrode; Spheres, Hemispheres, and Distorted Spheres and Hemispheres. *The Journal of Physical Chemistry C* **2007,** *111* (49), 18049-18054.
28. Belding, S. R.; Compton, R. G., Transient Voltammetry at Electrodes Modified with a Random Array of Spherical Nanoparticles: Theory. *The Journal of Physical Chemistry C* **2010,** *114* (18), 8309-8319.
29. Ward, K. R.; Lawrence, N. S.; Hartshorne, R. S.; Compton, R. G., Modelling the steady state voltammetry of a single spherical nanoparticle on a surface. *Journal of Electroanalytical Chemistry* **2012,** *683*, 37-42.
30. Bobbert, P. A.; Wind, M. M.; Vlieger, J., Diffusion to a slowly growing truncated sphere on a substrate. *Physica A: Statistical Mechanics and its Applications* **1987,** *141* (1), 58-72.
31. Einstein, A., Über die von der molekularkinetischen Theorie der Wärme geforderte Bewegung von in ruhenden Flüssigkeiten suspendierten Teilchen. *Annalen der Physik* **1905,** *322* (8), 549-560.
32. von Smoluchowski, M., Zur kinetischen Theorie der Brownschen Molekularbewegung und der Suspensionen. *Annalen der Physik* **1906,** *326* (14), 756-780.

33. Gavaghan, D. J., An exponentially expanding mesh ideally suited to the fast and efficient simulation of diffusion processes at microdisc electrodes. 1. Derivation of the mesh. *Journal of Electroanalytical Chemistry* **1998,** *456* (1), 1-12.
34. Rudolph, M., Digital Simulations on unequally spaced grids. Part 1. Critical remarks on using the point method by discretisation on a transformed grid. *Journal of Electroanalytical Chemistry* **2002,** *529*, 97-108.
35. Seeber, R.; Stefani, S., Explicit finite difference method in simulating electrode processes. *Analytical Chemistry* **1981,** *53* (7), 1011-1016.
36. Feldberg, S. W., Optimization of explicit finite-difference simulation of electrochemical phenomena utilizing an exponentially expanded space grid: Refinement of the Joslin-Pletcher algorithm. *Journal of Electroanalytical Chemistry and Interfacial Electrochemistry* **1981,** *127* (1), 1-10.
37. Alden, J. A.; Compton, R. G., A general method for electrochemical simulations. 1. Formulation of the strategy for two-dimensional simulations. *The Journal of Physical Chemistry B* **1997,** *101* (44), 8941-8954.
38. Compton, R. G.; Kätelhön, E.; Laborda, E.; Ward, K. R., *Understanding voltammetry: Simulation of electrode processes*. Second ed.; World Scientific Europe: 2020.
39. Laasonen, P., Über eine Methode zur Lösung der Wärmeleitungs-gleichung. *Acta Mathematica* **1949,** *81* (none), 309-317, 9.
40. Falgout, R. D.; Yang, U. M. In *hypre: A Library of High Performance Preconditioners*, Berlin, Heidelberg, Springer Berlin Heidelberg: Berlin, Heidelberg, 2002; pp 632-641.
41. Falgout, R. D.; Jones, J. E.; Yang, U. M. In *The Design and Implementation of hypre, a Library of Parallel High Performance Preconditioners*, Berlin, Heidelberg, Springer Berlin Heidelberg: Berlin, Heidelberg, 2006; pp 267-294.
42. Le, H.; Kätelhön, E.; Compton, R. G., Characterising the nature of diffusion via a new indicator: Microcylinder and microring electrodes. *Journal of Electroanalytical Chemistry* **2019,** *855*, 113602.
43. Le, H.; Compton, R. G., Comparative chronoamperometry: Spheres, discs, cylinders and bands. *Journal of Electroanalytical Chemistry* **2020,** *866*, 114149.
44. Batchelor-McAuley, C.; Compton, R. G., Diffusion to a cube: A 3D implicit finite difference method. *Journal of Electroanalytical Chemistry* **2020,** *877*, 114607.
45. Orrick, O.; Yang, M.; Batchelor-McAuley, C.; Compton, R. G., Characterising Fickian diffusion on the surface of a sphere. *Journal of Electroanalytical Chemistry* **2021,** *900*, 115738.
46. Usha Rani, R.; Rajendran, L., Diffusion indicator for hemispheroidal and ring ultramicroelectrode geometries for E and EC′ reactions. *Electrochemistry Communications* **2021,** *128*, 107071.
47. Crank, J., *The Mathematics of Diffusion*. Clarendon Press: 1979.
48. Delmastro, J. R.; Smith, D. E., Methods for obtaining approximate solutions to the expanding-sphere boundaary value problem in direct current polarography. *The Journal of Physical Chemistry* **1967,** *71* (7), 2138-2149.
49. Lovrić, M.; Branica, M., Application of ASV for Trace Metal Speciation II. Digital Simulation of Neopolarogram Using Hanging-mercury-drop Electrode. *Croatica Chemica Acta* **1980,** *53* (3), 477-483.
50. Bond, A. M.; Oldham, K. B., Potentiostatic voltammetry at the static mercury drop and other spherical electrodes. *Journal of Electroanalytical Chemistry and Interfacial Electrochemistry* **1983,** *158* (2), 193-215.

51. Haddou, B.; Rees, N. V.; Compton, R. G., Nanoparticle–electrode impacts: the oxidation of copper nanoparticles has slow kinetics. *Physical Chemistry Chemical Physics* **2012,** *14* (39), 13612-13617.
52. Guo, Z.; Percival, S. J.; Zhang, B., Chemically Resolved Transient Collision Events of Single Electrocatalytic Nanoparticles. *Journal of the American Chemical Society* **2014,** *136* (25), 8879-8882.
53. Saw, E. N.; Kratz, M.; Tschulik, K., Time-resolved impact electrochemistry for quantitative measurement of single-nanoparticle reaction kinetics. *Nano Research* **2017,** *10* (11), 3680-3689.
54. Cottrell, F. G., Der Reststrom bei galvanischer Polarisation, betrachtet als ein Diffusionsproblem. *Zeitschrift für Physikalische Chemie* **1903,** *42U* (1), 385-431.
55. Oldham, K. B., Edge effects in semiinfinite diffusion. *Journal of Electroanalytical Chemistry and Interfacial Electrochemistry* **1981,** *122*, 1-17.
56. Yang, M.; Batchelor-McAuley, C.; Kätelhön, E.; Compton, R., A New Approach to Characterising the Porosity of Particle Modified Electrodes: Potential Step Chronoamperometry and the Diffusion Indicator. *Applied Materials Today* **2021,** *25*, 101249.
57. Oldham, K. B.; Zoski, C. G., Comparison of voltammetric steady states at hemispherical and disc microelectrodes. *Journal of Electroanalytical Chemistry and Interfacial Electrochemistry* **1988,** *256* (1), 11 - 19.
58. Gavaghan, D. J.; Rollett, J. S., Correction of boundary singularities in numerical simulation of time-dependent diffusion processes at unshielded disc electrodes. *Journal of Electroanalytical Chemistry and Interfacial Electrochemistry* **1990,** *295* (1), 1-14.
59. Ferrigno, R.; Brevet, P. F.; Girault, H. H., Finite element simulation of the chronoamperometric response of recessed and protruding microdisc electrodes. *Electrochimica Acta* **1997,** *42* (12), 1895 - 1903.
60. Aoki, K., Several Derivations for I = 4Fc*Da. *Review of Polarography* **2017,** *63* (1), 21-28.
61. Mahon, P. J.; Oldham, K. B., The transient current at the disk electrode under diffusion control: a new determination by the Cope–Tallman method. *Electrochimica Acta* **2004,** *49* (28), 5041-5048.
62. Mahon, P. J.; Oldham, K. B., Diffusion-Controlled Chronoamperometry at a Disk Electrode. *Analytical Chemistry* **2005,** *77* (18), 6100-6101.
63. Bieniasz, L. K., Highly accurate, inexpensive procedures for computing chronoamperometric current, integral transformation kernel, and related integrals, for an inlaid disk electrode. *Electrochimica Acta* **2018,** *259*, 1068-1080.

5 Foliar uptake: single-particle simulations

Chapters 5 and 6 investigate the modelling of mass transport at droplets containing a lipophilic agrichemical situated on plant leaves and how this leads to the foliar uptake of said agrichemical. Modern formulations containing lipophilic material typically involve particles suspended in an aqueous solution, within which lipophilic pesticide is contained. The work presented in the next 2 chapters is concerned with the modelling of such systems and the measurement of their uptake. In Chapter 6 we present and discuss experimental results relating to foliar uptake from droplets of such a formulation and provide a simplest viable model for its uptake behaviour; in order to facilitate the interpretation of these results and the development of the simplest viable model, we first consider the mass transport at the pesticide-containing particles from a generalised, theoretical perspective and simulate the uptake predicted for different limiting cases and physicochemical properties. A schematic illustration representing these relationships is presented in Figure 5.1.

This chapter focusses on how the release of pesticide from a single particle on the outer cuticular surface and surrounded by an aqueous medium, affects the overall diffusion of pesticide into and across the ‘cuticle proper’, the principal barrier to foliar uptake. Two potential pathways for uptake are identified: direct uptake via physical contact between the cuticle and particle, and indirect uptake via initial release of material into a surrounding medium (such as the carrier phase of a formulation droplet) followed by partitioning into and diffusion across the cuticle. Numerical simulation is performed to investigate the relevance of the particle-cuticle contact angle, the release kinetics of the particle, and the particle size relative to the cuticle thickness. The work presented in this chapter closely follows the work that has been published in ACS Agricultural Science & Technology[1]. The results for release

of pesticide into the surrounding medium build upon the results presented in Chapter 4, which are also published in the Journal of Electroanalytical Chemistry[2].

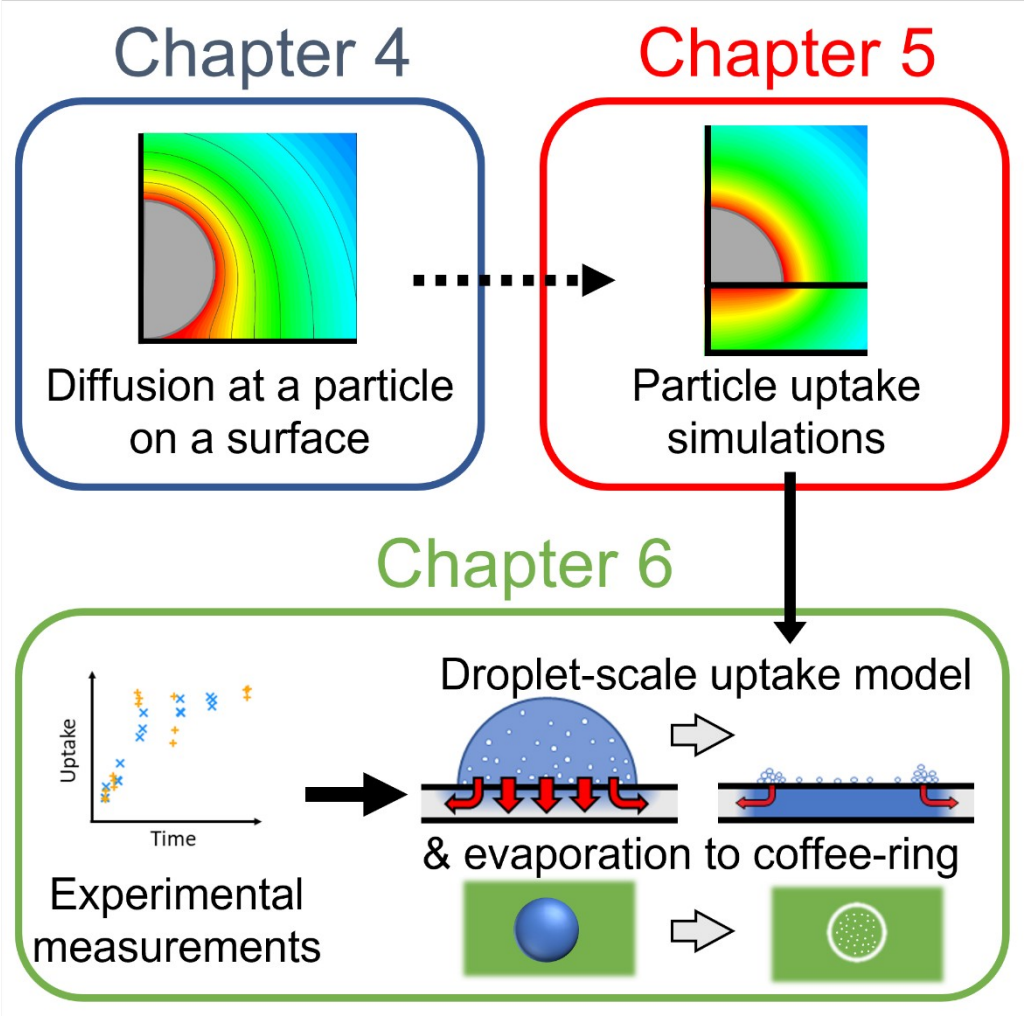


Figure 5.1: Schematic illustrating how results presented in different chapters of this thesis inform the discussion in following chapters.

5.1 Introduction

The improved efficacy of the application of agrochemicals to crops and weeds is vital to the future development of the agricultural industry[3]. Pressure to reduce the agrochemical input in response to its ecological side-effects is increasing[4-6], while common pesticide delivery methods have been demonstrated to be of limited uptake efficacy[7, 8]. Commonly applied agrochemicals are pesticides, which include herbicides, fungicides, and insecticides[9].

Pesticides are frequently sold as spray-applied formulations and many different categories are available. Of particular significance are dispersion-based formulations in which the pesticide, often poorly water-soluble, exists within the droplet as finely dispersed particles of approximately micrometre[10] or sub-micrometer dimensions[10, 11]. These particles may be simply solid pesticide or more complex designs for the purpose of the protection, solubilization, or release control of a pesticide contained within.

The barrier to entry of pesticides of intermediate to high lipophilicity is the plant cuticle, a layer of cutinous polymer matrix and wax which covers the epidermal cells of almost all terrestrial plant leaves and acts as a protective solubility and transport barrier[12, 13]. A mature cuticle typically possesses an inner 'sorption' compartment and an outer 'skin' layer, often referred to as the 'cuticle proper'[14-16]. Intracuticular wax within the 'cuticle proper' often restricts diffusion to greatly tortuous paths[13, 15-17] and slows diffusion. The 'cuticle proper' is accepted to be the limiting step to cuticular uptake[15, 16, 18]. Although alternatives do exist[19, 20], this model of the cuticular environment is widely accepted in the literature and adopted for our work. Diffusion through the lipidic cuticle is the primary route for lipophilic uptake, rather than via stomata[21] or hydrophilic pores[22].

Enhancing the efficacy of foliar uptake of pesticides reduces the use of active ingredient (AI)[23], generating both environmental and economic benefit through improved application efficiency. Accurate modelling and simulation of the processes involved with uptake is preponderant to the effective pursuit of improved efficacy beyond semi-informed trial-and-error testing and pure empiricism[24]. Various models have been proposed for the diffusion of agrochemicals across the cuticular membrane, from simple empirical relationships[25-28] to more complex computational models[29-34]. The study of release of active ingredients from designed particles is also extensive, with the popular Higuchi[35], Ritgar-Peppas[36] and other

models[37-42], including those accounting for particle swelling[43, 44], particle erosion[45-48], multi-layer particles[49, 50], and burst release[51, 52].

The work presented in this chapter is novel for considering simultaneous release of chemical material from a particle *and* the diffusion of this material across a finite barrier. As a result, no prior model accounts for the following effects on foliar uptake: the hindrance of pesticide release from particles proximal to a barrier surface; discrete, localized sources rather than a homogeneous solution source; and competition between direct uptake into the cuticle and indirect uptake via diffusion through the solution medium. These interactions are significant to spray-applied, particulate agrochemicals and particulate contaminants. Application of a model considering only one of these processes is only effective for limiting cases. Modelling release from non-spherical particles is often avoided in the field of controlled release from particles[40], leaving a dearth of knowledge. While Mercer[29] and Tredenick[30, 32] have considered truncated spheres on the cuticle boundary, their models are applied to saturated droplets rather than pesticide-carrying particles.

We couple together the two modelling problems of diffusion across a barrier and release from a discrete particle in the context of foliar uptake into the ‘cuticle proper’. We address several key questions relevant to the overall mechanism of uptake and identify qualitative and quantitative trends for dispersed-particle formulations:

- How does release of pesticide into the aqueous phase, followed by partitioning into the ‘cuticle proper’, compete with release directly into the ‘cuticle proper’ in terms of their contribution to the uptake?

- How does the release rate from discrete particles affect the uptake of pesticide?

- How does the presence of a low permeability barrier affect zero-order release from and diffusion about a particle? How does the geometry of this system affect the transport behavior across such a barrier?

- Does the relative thickness of the ‘cuticle proper’ affect the release from the particle and uptake under this simplified model?

- How does the particle-cuticle-aqueous contact angle affect the uptake for a truncated spherical particle?

- What limiting cases can be identified and how can we use these to understand the system?

These questions are addressed in Sections 5.3-5.8, along with relevant simulated results. A description of the computational model is first provided in Section 5.2.

5.2 Theory

In this chapter, pesticide uptake from a particle on the surface of a plant cuticle is modelled as occurring via two possible routes, illustrated in Figure 5.2. First, a direct pathway with release directly into the ‘cuticle proper’ through the finite particle-cuticle contact area, followed by diffusion through the ‘cuticle proper’. Second, an indirect pathway with initial release into an aqueous phase surrounding the particle, followed by diffusion through the phase to the cuticle surface, partitioning into the ‘cuticle proper’, and subsequent diffusion through the ‘cuticle proper’.

Release and uptake from a particle on the cuticle surface are modelled assuming an isolated, truncated spherical particle and representing the cuticle surface as an infinite slab of finite thickness. Truncation of the sphere by the plane is used to simulate variable physical contact area between the particle and cuticle surface. We simulate the release from the particle into

the cuticle through the circular contact area and approximate a sharp boundary between the ‘cuticle proper’ and the ‘sorption compartment’.

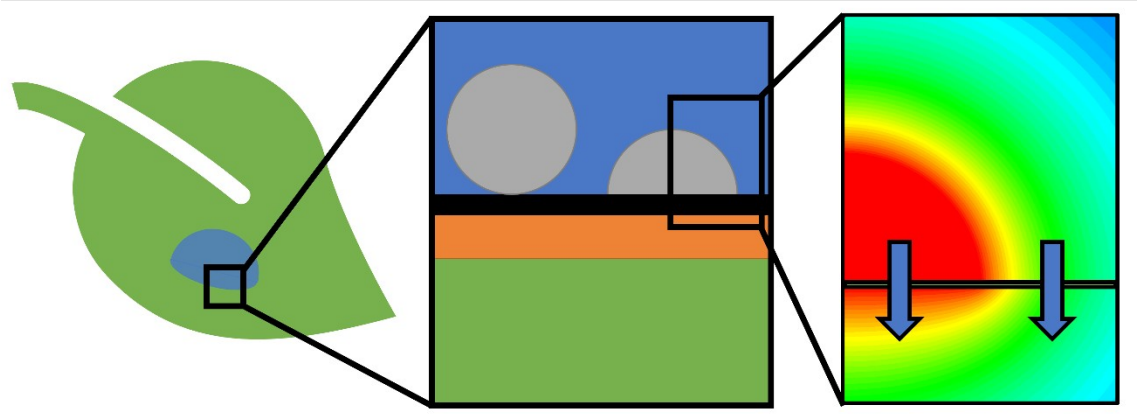


Figure 5.2: Schematic (not to scale) whereby particles in contact with the cuticle and within an aqueous droplet on a generic leaf surface release material either directly into the cuticle or into the aqueous medium prior to uptake through the leaf surface. The second panel provides a schematic of particles (grey) in aqueous droplet (blue) on the cuticle surface (‘cuticle proper’ in black and ‘sorption compartment’ in orange) with plant tissue represented by a green continuum. Fickian diffusion and partitioning across the cuticle-solution interface develops two possible pathways for uptake: directly through the particle-cuticle contact or indirectly via the cuticle-solution interface, represented by the blue arrows. The thick black line in the third panel represents the outer boundary of the ‘cuticle proper’. Illustrative steady-state concentration profiles developed by Fickian diffusion are provided as colormaps in the third panel in the purely illustrative case of 1:1 partitioning.

Figure 5.3 illustrates the whole formulation-leaf system and the simplifying approximations taken. The media involved are as follows: (1) the solid particle (2) the aqueous formulation droplet, (3) the ‘cuticle proper’ layer, (4) the ‘sorption’ layer of the cuticle, (5) the apoplastic leaf tissue, and (6) an open stoma in the leaf surface. The plausibly relevant processes are: (A) release of pesticide from the particle into solution, (B) release of pesticide from the particle into the ‘cuticle proper’, (C) partitioning of pesticide from solution into the ‘cuticle proper’, (D) partitioning of pesticide from the ‘cuticle proper’ into the ‘sorption’ layer of the cuticle, (E) partitioning of pesticide from the ‘sorption’ layer of the cuticle into the apoplastic leaf tissue, (F) vaporization of volatile pesticide from the formulation droplet, (G) uptake of pesticide into open stomata as a vapor, (H) evaporation of water from the formulation droplet, and (I) partitioning of accelerator adjuvant from solution into the ‘cuticle proper’.

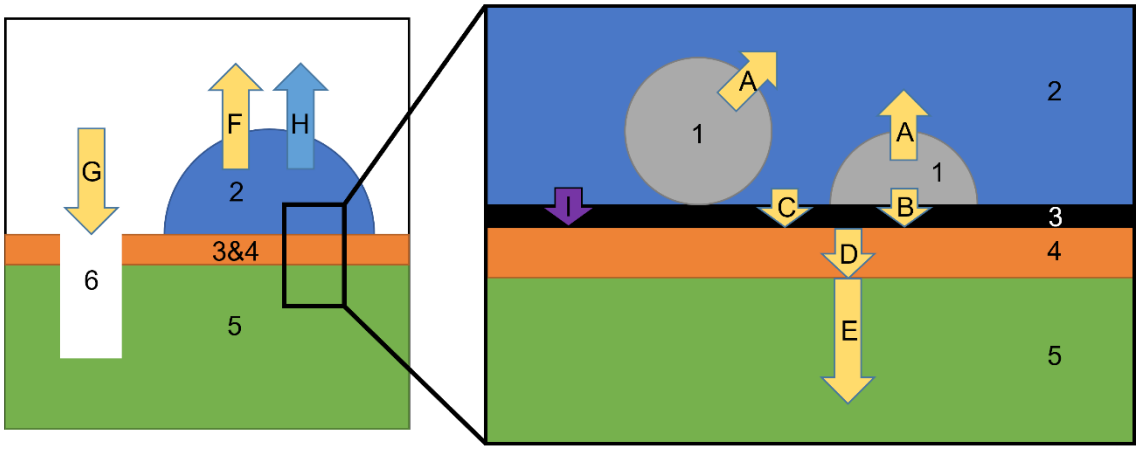


Figure 5.3: General schematic for the different media and processes active during uptake of pesticide from a formulation droplet. The different media are labelled by number while the different processes are represented as arrows and labelled by letter. Explanation of these labels is given in the main text. Not to scale.

In this chapter, stomatal penetration is modelled as a negligible uptake pathway[33]. Penetration of adjuvant species into the cuticle is also neglected for simplicity and transfer from the 'cuticle proper' to the 'sorption compartment' is treated as a significantly faster process than entry to the 'cuticle proper', such that the 'sorption compartment' is treated as a 'perfect sink' due to its greater solubility and diffusion coefficient. Post-cuticular activity within the plant tissue is considered beyond the scope of this thesis. Convective currents and droplet edge effects are ignored. The pesticidal species is assumed to be neutral, a common design choice to maximize cuticular solubility. These assumptions allow us to focus on the coupling of release from the particle with the diffusion across the cuticle barrier and the investigation of fundamental insights into the system's mass transport, which may be generalized to similar systems involving chemical-releasing particles at bio-membranes.

Epicuticular waxes also affect uptake through their wetting properties[53, 54] and trapping of particulate material[55-57]. However, as they have been demonstrated not to act as a transport barrier[58-60], these influences are also considered to be beyond the scope of this thesis.

Zero-order release and first-order re-absorption kinetics are applied at the particle interfaces according to Equation 5.1:

$$j_i = -D_i \frac{\partial c_i}{\partial \eta} = (k_f^i - k_b^i c_i)$$ Equation 5.1

where i represents the aqueous (aq) or cuticular (cut) phase, j_i is the diffusive flux ($mol \cdot m^{-2} \cdot s^{-1}$) into phase i, D_i is the diffusion coefficient within phase i, c_i is the surface concentration of pesticide within phase i, η is the coordinate normal to the interface, k_f^i is the pesticide's release rate constant into phase i, and k_b^i is the pesticide's re-absorption rate constant from phase i. The simple release model given in Equation 5.1 allows focus on the coupling between the diffusive transport and the interfacial kinetics. k_f^i and k_b^i are tunable parameters that can be optimized to reflect specific particle kinetics, such as simple controlled release mechanisms. Mass transport is modelled as purely Fickian diffusion following Fick's 2nd Law[61]:

$$\frac{\partial c}{\partial t} = \nabla \cdot (D \nabla c) = D \nabla^2 c$$ Equation 5.2

where t is time, c is concentration and D is the diffusion coefficient assumed to be constant for a given medium.

The isolated particle on a surface geometry possesses an axis of symmetry, so Fick's 2nd Law in cylindrical coordinates (r, z, ϕ) is expressed as:

$$\frac{\partial c}{\partial t} = D \left[\frac{\partial^2 c}{\partial z^2} + \frac{\partial^2 c}{\partial r^2} + \frac{1}{r} \frac{\partial c}{\partial r} \right]$$ Equation 5.3

since $\frac{\partial c}{\partial \phi} = 0$ at all ϕ, by symmetry.

For the simulation of a sphere in solution, with no proximal planar surface, spherical symmetry is observed. In this geometry,

$$\frac{\partial c}{\partial t} = D \left[\frac{\partial^2 c}{\partial \rho^2} + \frac{2}{\rho} \frac{\partial c}{\partial \rho} \right]$$ Equation 5.4

where ρ is the radial distance from the centre of the sphere.

To produce simulations of the steady state, we simplify Equation 5.3 further by using $\frac{\partial c}{\partial t}=0$, since the concentration at any point is independent of time.

A zero-flux boundary condition, described by $\frac{\partial c}{\partial \eta}=0$, where η is a coordinate perpendicular to the boundary surface, is used at the axis of symmetry[62] and at the outer cuticular interface when simulating without aqueous-cuticle partitioning in the model.

A constant concentration boundary condition of $c(r',z')=c'$ is applied at the boundary to the 'perfect sink', aka the 'sorption compartment', and at the radial boundary at which the solution becomes bulk, as $c'=0$. The distance at which this bulk condition can be imposed accurately is dependent on the rate of diffusion, recalling that $\langle x \rangle_{rms}=\sqrt{6Dt}$ for a diffusing molecule in 3-dimensions as predicted by Brownian motion[63, 64], and whether convective or other transport processes are active. Assuming negligible non-diffusional mass transport and a constant bulk concentration, we impose a constant concentration condition at a distance of $6\sqrt{D t_{max}}$, where the probability of diffusion is below 0.001, where t_{max} is the maximum duration of the simulation. This is tested to demonstrate negligible dependence of the results on this distance.

An active surface boundary follows $\frac{\partial c}{\partial \eta}=f$. This condition is used to describe the release

from the particle as $f=\frac{-1}{D}(k_f-k_b c)$, according to Equation 5.1. The influence of alternative release mechanisms is outside the scope of this thesis.

For modelling release into the aqueous phase from the spherically curved particle surface, $\eta=\rho$. By changing the variables used, the boundary condition is described in cylindrical coordinates as:

$$\left(\frac{\partial c}{\partial \rho}\right)_\theta = \left(\frac{\partial c}{\partial r}\right)_z \left(\frac{\partial r}{\partial \rho}\right)_\theta + \left(\frac{\partial c}{\partial z}\right)_r \left(\frac{\partial z}{\partial \rho}\right)_\theta = \left(\frac{\partial c}{\partial r}\right)_z \sin\theta + \left(\frac{\partial c}{\partial z}\right)_r \cos\theta = \frac{1}{1}$$ Equation 5.5

since $r = \rho \sin\theta$, and $z = \rho \cos\theta$. A boundary condition is also required in the temporal domain. The initial concentration at each point outside the particle is set to the bulk concentration of zero.

Schematics illustrating the boundary conditions and coordinate systems used for the truncated sphere and disk geometries are shown in Figure 5.4.

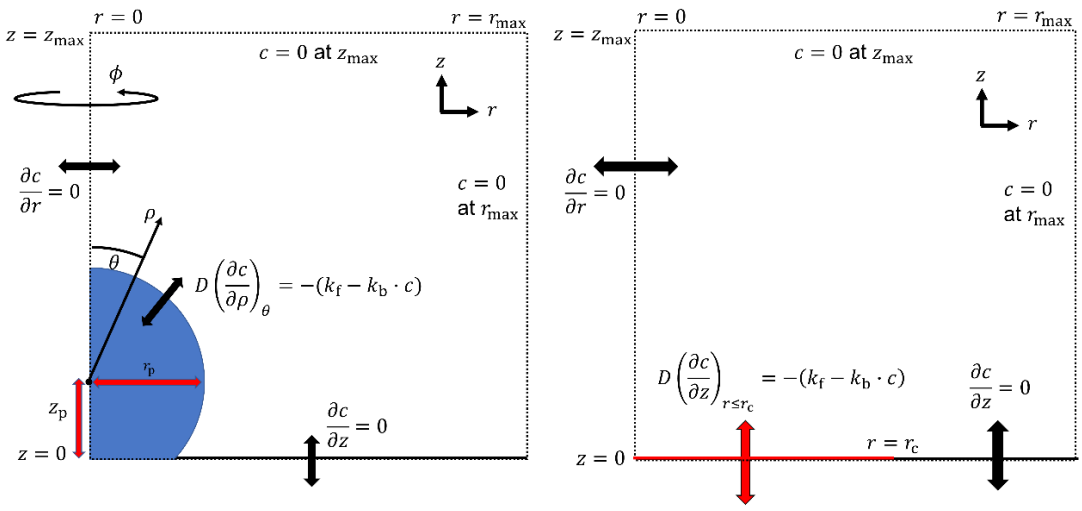


Figure 5.4: Illustration of model boundary conditions and coordinate systems

Processes are added sequentially to the model and simulation results are analyzed at each step. The order of processes introduced is: unbounded release from a spherical particle surrounded by solution; release from a truncated spherical particle constrained by an adjacent inert barrier; release from a circular particle-cuticle contact area into an infinite slab of finite thickness; and finally, surface-equilibrated partitioning of material between the aqueous and 'cuticle proper' phases, with and without simultaneous release via particle-cuticle contact. The direct and indirect pathways are simulated individually and then in tandem. A benefit of

the model's format is the ease of incorporation of additional processes and thus offering a physical foundation for further model development.

The particles are modelled as variably truncated spheres and cylindrical coordinates (r, z) are used to describe the system. $[A]^i$ and $[A]^i_{eq}$ are the concentration and equilibrium concentration in medium i, r_p is the radius of the particle, and D_{ref} is the reference diffusion coefficient (¿ D_i while media are simulated individually).

z_p is the perpendicular distance from the 'cuticle proper' to the particle's centre and θ_c is the angle from the particle's centre to the contact point, which is equivalent to the particle-cuticle-solution contact angle. z_{cut} is the 'cuticle proper' thickness. The model's spatial parameters are illustrated in Figure 5.5.

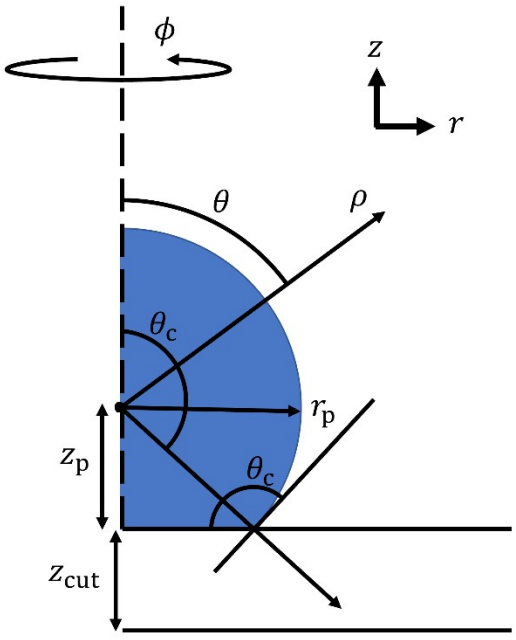


Figure 5.5: Schematic illustration of the spatial parameters describing a truncated sphere resting on a finite barrier under cylindrical coordinates (r, z). Parameters include angle from symmetry axis θ, angle to three-phase contact point θ_c (equivalent to the contact angle), particle radius r_p, shortest distance from particle centre ρ, distance from particle centre to barrier surface z_p, and barrier thickness z_{cut}.

Converting the parameters of the system into dimensionless forms simplifies the equations involved and generalizes the simulation results[62, 65]. The dimensionless conversions are provided in Table 5.1. $[A]^i_{eq}$ is the saturation concentration in medium i, D_{ref} is the reference diffusion coefficient, and r_{ref} is either the radius of the sphere r_p while only diffusion in the aqueous phase is being simulated or the radius of the disk contact area r_d while diffusion in the 'cuticle proper' is being simulated.

Applying the dimensionless conversions to Equation 5.3 produces:

$$\frac{\partial C}{\partial T} = \frac{\partial^2 C}{\partial Z^2} + \frac{\partial^2 C}{\partial R^2} + \frac{1}{R}\frac{\partial C}{\partial R} \qquad \text{Equation 5.6}$$

The boundary conditions at the particle surfaces are converted to:

$$\frac{\partial C}{\partial Z} = -K_{cut}(1-C) \text{ from the disk contact} \qquad \text{Equation 5.7}$$

$$R\left(\frac{\partial C}{\partial R}\right)_Z + Z\left(\frac{\partial C}{\partial Z}\right)_R = -K_{aq}(1-C) \text{ from the spherical surface} \qquad \text{Equation 5.8}$$

Table 5.1: Table of conversions from dimensional parameters to dimensionless parameters

Dimensional Parameter	Conversion to dimensionless form
Concentration, $[A]^i$	$C_i = [A]^i / [A]^i_{eq} = k^i_b \cdot [A]^i / k^i_f$
Diffusion coefficient, D_i	$d_i = D_i / D_{ref}$ (¿1)
Radial distance, r	$R = r / r_{ref}$
Distance from cuticle outer boundary, z	$Z = z / r_{ref}$
Thickness of the 'cuticle proper', z_{cut}	$Z_{cut} = z_{cut} / r_{ref}$
Distance from cuticle outer boundary to the particle's centre, z_p	$Z_p = z_p / r_{ref}$
Time, t	$T = D_{ref} \cdot t / r^2_{ref}$
Release rate constant into medium i, k^i_f Re-adsorption rate constant from medium i, k^i_b	$K_i = k^i_f \cdot r_{ref} / D_{ref} \cdot [A]^i_{eq}$ ¿ $k^i_b \cdot r_{ref} / D_{ref}$

Surface Flux at a point into medium i, j_i	$J_i = j_i \cdot r_{ref} / D_{ref} \cdot [A]_{eq}^{i}$ ¿ $j_i \cdot k_b^i \cdot r_{ref} / (D_{ref} \cdot k_f^i)$

Solution of Fickian diffusion within this chapter requires spatial and temporal discretization using the finite difference method[66]. The central three-point difference approximation is used for second order spatial derivative functions and the second-order central difference approximation is used for the first order spatial derivative functions. At the inner and outer boundaries, a forward or backward difference approximation is used for the spatial derivatives. Time discretization is achieved by backward difference approximation.

Space-time discretization is achieved using expanding grids[67, 68] to ensure a high density of points in regions of interest or where accurate simulation demands, while minimizing the total number of points used for the simulations. Specifically, exponentially expanding grids are implemented in this work according to Equation 5.9:

$$X_{i+1} - X_i = dX \times \omega_X^i = (X_i - X_{i-1})\omega_X \qquad \text{Equation 5.9}$$

where $0 \le i < n-1$ describes the point label, n is the number of points in dimension X, dX describes the initial step distance, and ω_X is the expansion factor in the X-direction. Illustrations of the grid schemes used are given in Figure 5.6.

The grid scheme around the truncated sphere should accurately describe the curved spherical surface and provide a high density of points at the spherical surface. We use the following scheme, introduced by Ward et al[69], to describe this problem (Figure 5.6A). A series of points on the surface of the sphere are distributed uniformly along the θ-coordinate (each separated by an angle $d\theta$). The R- and Z-grids are then set to contain these points. This describes the density of points around the sphere using one parameter: $d\theta$. The grid is expanded exponentially beyond $R = 1$ and $Z = 1 + Z_p$.

When the sphere is truncated, a greater demand on the density of points is observed for accurate simulation of diffusion below $Z=Z_p$. In this case, a second, smaller $d\theta_2$ is used between $\pi-\theta_c\leq\theta\leq\theta_c$ if $\frac{\pi}{2}<\theta_c<\pi$, where θ_c is the θ value at which the sphere and inert surface make contact. This is seen in Figure 5.6B, where the θ illustrated lies on the boundary between the two different θ-spacing regimes.

For the grid scheme around a disk, the Z-coordinate is discretized using a simple exponentially expanding grid. The R-coordinate requires a high density of points at the axis of symmetry and at the disk edge. The grid scheme expands and contracts such that $R=0$ and $R=1$ function as points around which the point density is maximized. For a low value of Z_{max}, the Z-grid contracts for $Z\geq\frac{Z_{max}}{2}$ to give a well-defined outer boundary. The expansions and contractions use the same ω factor.

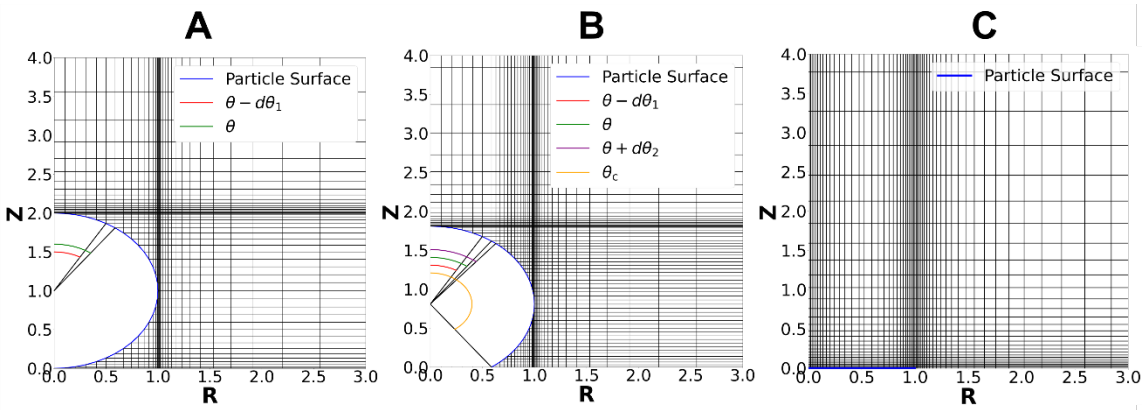


Figure 5.6: Illustration of spatial grid discretization schemes used in this work for: (A) the truncated sphere model when $Z_p=1$ (illustrated with $d\theta=\frac{\pi}{30}$ and $\omega_R=\omega_Z=1.3$) noting that the same scheme is used for $Z_p\leq 0$, (B) the truncated sphere model when $0<Z_p<1$ such that two θ-spacing regimes are used (illustrated with $Z_p=0.8$, $d\theta_1=\frac{\pi}{30}$, $d\theta_2=\frac{\pi}{60}$, and $\omega_R=\omega_Z=1.3$), and (C) the disk model (illustrated with $dR=dZ=0.01$ and $\omega_X=\omega_R=1.15$). The use of contraction in the z-direction for $Z>\frac{Z_{max}}{2}$ in small Z_{max} regimes is not illustrated in (C). Discretization parameters chosen for this illustration are purely illustrative.

For the one-dimensional simulation of an isolated sphere in solution, one exponentially expanding spatial grid is required only in the ρ-coordinate.

An exponentially expanding grid is applied in the T-dimension, as the greatest change in concentration occurs when the active surface is first exposed to the medium and decays as the concentration profile approaches the steady state solution.

To generate a time-dependent solution, the PDE is solved for each time step sequentially. The ADI method[70-72] divides each time-step into two halves. During the first half of the time-step, the derivative functions in one spatial direction are discretized implicitly, while the derivative functions in the perpendicular direction are discretized explicitly. During the second half of the time step, the direction in which the derivatives are solved implicitly is swapped with the explicit direction. Thus, each coordinate receives equal parts implicit and explicit discretization. This methodology is efficient while maintaining stability[71].

While the ADI method is useful for generating a time-dependent solution, it is also used in this chapter as an iterative process to converge upon steady-state solutions when $\frac{\partial c}{\partial t}=0$. In this case, each application of the ADI process results in an additional iteration towards the steady-state solution rather than resolving a discrete step in time. ADI iterations are repeated until the concentration at each point in space changes by less than $10^{-2}\%$.

Reliable simulation results must be converged and accurate[73]. Steady-state simulations are performed iteratively until the total mass varied by ¿0.01% and spatially converged until total surface flux is within 0.1% convergence error. Where analytical results were applicable, the total flux was accurate within 0.1%. The profiles of flux across the active surface are similarly accurate to literature. Time-dependent simulations used the same spatial grid as

time-independent solutions. Flux-time profiles are accurate within 1% of literature where available, and within 0.1% at long times. Time-dependent solutions have a total mass conservation error below 10^{-5}%. Where analytical results are not available, comparison to known cases and assessment of the continuity of results is used for validation.

Convergence testing was performed to find appropriate values for the parameters describing the discrete grids used in our simulations, balancing accuracy against simulation time. For modelling the disk geometry, these parameters are dZ, ω_Z, dR, ω_R, dT, and ω_T. For the truncated sphere geometry, these parameters are $d\theta$, $(d\theta_2)$, ω_Z, ω_R, dT, and ω_T. For simulations involving the truncated sphere, a convergence test must be performed for each Z_p value.

Results from these convergence tests were compared to analytical results where possible. The steady-state, diffusion-limited flux from a planar disk surrounded by inert surface in dimensionless coordinates is described analytically by Aoki[74] as

$$J = \frac{2}{\pi\sqrt{1-R^2}} \qquad \text{Equation 5.10}$$

Meanwhile Shoup and Szabo[75] provided an empirical, approximate expression for the total diffusion-limited flux in the regime where significant convergent diffusion acts:

$$J(T) = \frac{2}{\pi}\left[0.7854 + \frac{0.8863}{2\sqrt{T}} + 0.2146\exp\left\{\frac{-0.7823}{2\sqrt{T}}\right\}\right] \qquad \text{Equation 5.11}$$

The concentration profile at a dimensionless distance $P = \frac{\rho}{r_p} = \frac{\sqrt{r^2+(z-z_p)^2}}{r_p}$ from the centre of a hemisphere on a surface ($Z_p = 0$ within the truncated model) from which material releases into solution is given analytically by Crank[76] as

$$C(P,T)=\frac{K_j}{P(1+K_j)}\left[erfc\left(\frac{P-1}{2\sqrt{T}}\right)-\exp\left\{(K_j+1)(P-1)+(K_j+1\right.\right. \quad \text{Equation 5.12}$$

$$\frac{\partial C}{\partial P}(P=1,T)=\frac{K_j}{(1+K_j)}\left[-1-\frac{2}{\sqrt{\pi T}}\right. \quad \text{Equation 5.13}$$

$$-K_j\exp\left\{(K_j+1)^2T\right\}$$

$$\left.\left.erfc\left\{(K_j+1)\sqrt{T}\right\}\right]\right.$$

where P is the dimensionless distance from the centre of the sphere, T is the dimensionless time, and K_j is the dimensionless kinetic release rate constant into medium j. The steady-state, diffusion-limited flux from a sphere in point contact with a surface has been derived analytically by Bobbert, Wind and Vlieger[77]:

$$J_{Tot}=2\ln 2 \quad \text{Equation 5.14}$$

and the flux-versus-θ profile has been calculated by Streeter[78].

The simulations were performed using bespoke home-written *C++* programs with *OpenMP* used for parallel computing. The plotting of results was conducted in *Python* with the packages *NumPy*, *SciPy* and *matplotlib*. The plotting of 2D contour plots of concentration was carried out in *Origin 2020*.

5.3 Modelling release from the particle into the aqueous phase

In this section we consider steady-state results for the release from a truncated sphere on an inert surface under the release rate equation given in Equation 5.1. We initially present simulated results for a sphere releasing material into an unbounded volume and compare them to the analytical result proposed by Crank[76] (Equation 5.12 and Equation 5.13). We present results for the total flux, local flux profiles and the concentration profiles of

differently truncated spheres on a surface. These results overlap with results presented in Chapter 4 which are synonymous with results for $K_{aq} \gg 1$; the results from Chapter 4 serve as a benchmark and as a foundation for developing a model of the indirect uptake.

Simulation results for pesticide release from a spherical particle into an unbounded aqueous medium are presented as a function of K_{aq}. The plot in Figure 5.7 shows excellent agreement with the analytical prediction by Crank, demonstrating the thermodynamic ($K_{aq} \gg 1$) and kinetic ($K_{aq} \ll 1$) limits in the absence of a surface. Note that since the flux is uniform across the particle surface by symmetry, the dimensionless flux is presented, not the total flux integrated across the surface.

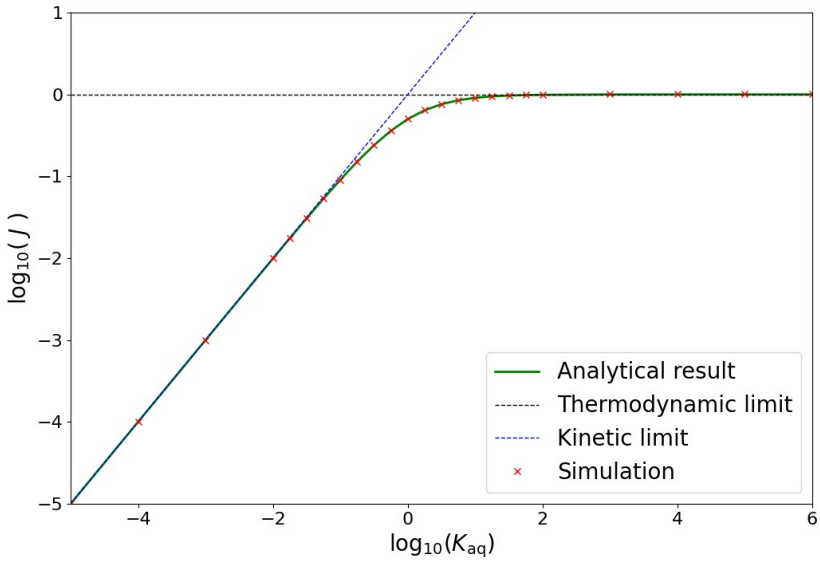


Figure 5.7: The logarithm of the steady-state dimensionless surface flux, J, as a function of the dimensionless release rate constant, K_{aq}, with limiting regimes illustrated, for a sphere in an unbounded medium, with analytical results from Crank's derivation.

The agreement of these results validates the simulation approach taken and provides insight into the analysis of later simulations by presenting a case for comparison for determining the effect of the cuticle surface on the pesticide release. Figure 5.8 further illustrates this limiting case.

It is evident that, for this geometry, the steady-state surface flux and concentration are equivalent, as expected from Crank's prediction. Under the thermodynamic limit, the rate at which material can be released is significantly greater than the rate at which it is transported away from the particle surface by diffusion, thus the surface flux and concentration become independent of K_{aq}. This limit is effectively modelled as an instantaneous equilibration of the concentration at the particle, as was done in Chapter 4. However, under the kinetic limit, the rate of diffusion dominates the rate of release and the steady-state surface flux and concentration vary linearly with K_{aq}. Finite time is required for the surface concentration to reach its steady-state limit. Using these simulation results and Crank's prediction, we hereby expect results for K_{aq}>10^{2} to reflect the thermodynamic limit and K_{aq}<10^{-2} to reflect the kinetic.

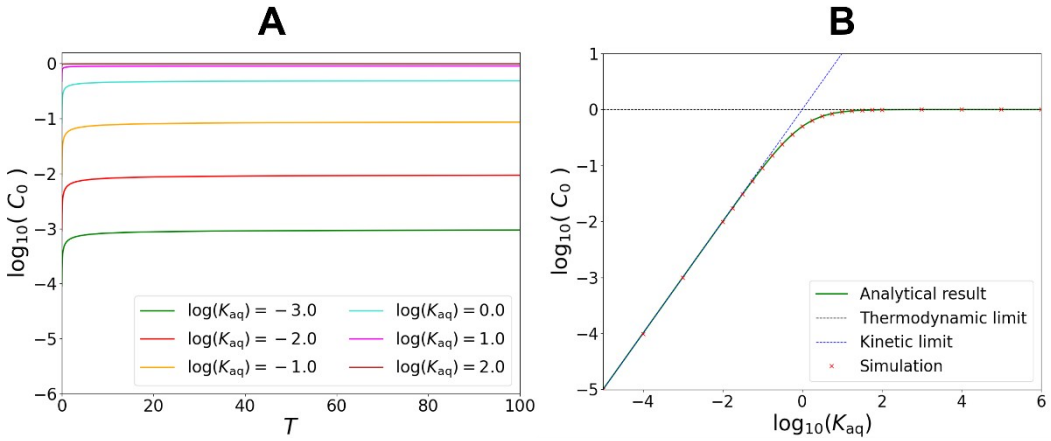


Figure 5.8: Further results for an isolated spherical particle releasing pesticide into an unbounded medium. (A) Dimensionless concentration on the particle surface C_0 as a function of dimensionless time T with varying values of K_{aq} illustrating finite time to attain the steady-state result for the surface concentration under the kinetic limit. (B) Steady-state dimensionless concentration on the particle surface as a function of K_{aq}, illustrating the limits. The analytical result derived by Crank is included as a green solid line. Note that this plot is identical to the plot of steady-state surface flux versus K_{aq}.

We next perform two-dimensional steady-state simulations of pesticide release into aqueous solution from truncated spheres supported on an inert surface. We consider how aqueous release is affected by the dimensionless aqueous release rate constant K_{aq} and the extent of truncation, parametrized by Z_p or θ_c.

We first perform simulations using $K_{aq}=10^6 \gg 10^2$ such that the surface is equilibrated, and the release is independent of K_{aq}: the thermodynamic limit. This is synonymous with the system simulated in Chapter 4, which used a different solution technique and is considered as a reference.

We consider the limiting cases of hemispherical ($Z_p=0$) and spherical particles ($Z_p=1$) on the surface with respect to their concentration profiles, presented in Figure 5.9. We also consider the dependence on Z_p of the dimensionless steady-state flux profiles $J(\theta)$ (Figure 5.10A) and the total dimensionless steady-state flux J_{Tot}, which is represented by the integral:

$\int_0^{\theta_c} J(\theta)\sin\theta\, d\theta = J_{Tot}/2\pi$ (Figure 5.10B).

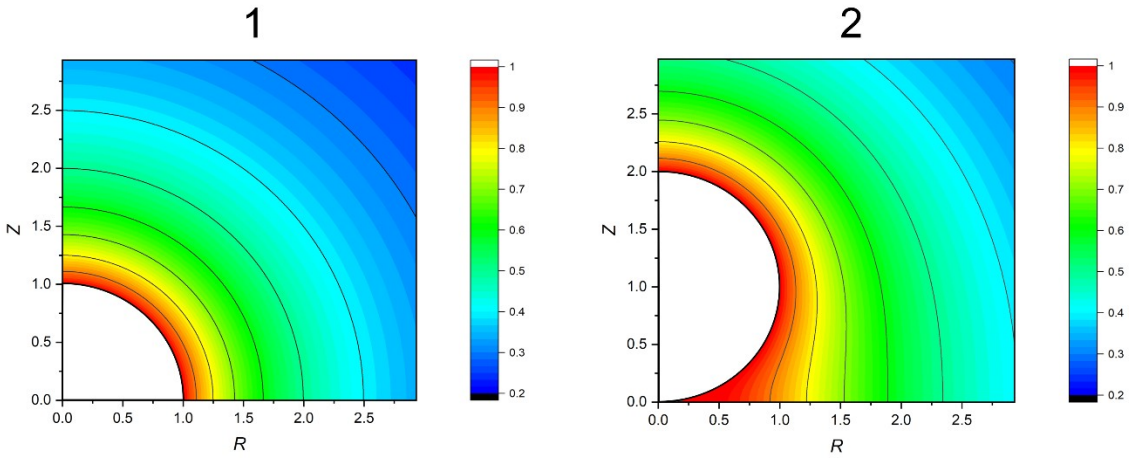


Figure 5.9: Dimensionless concentration profiles of aqueous, released material under thermodynamic limit for (1) a hemisphere on a plane ($Z_p=0$) and (2) a sphere on a plane ($Z_p=1$) represented as color maps. The white area is the particle. The spatial dimensions are normalized to the particle radius. Isoconcentration contour lines are included.

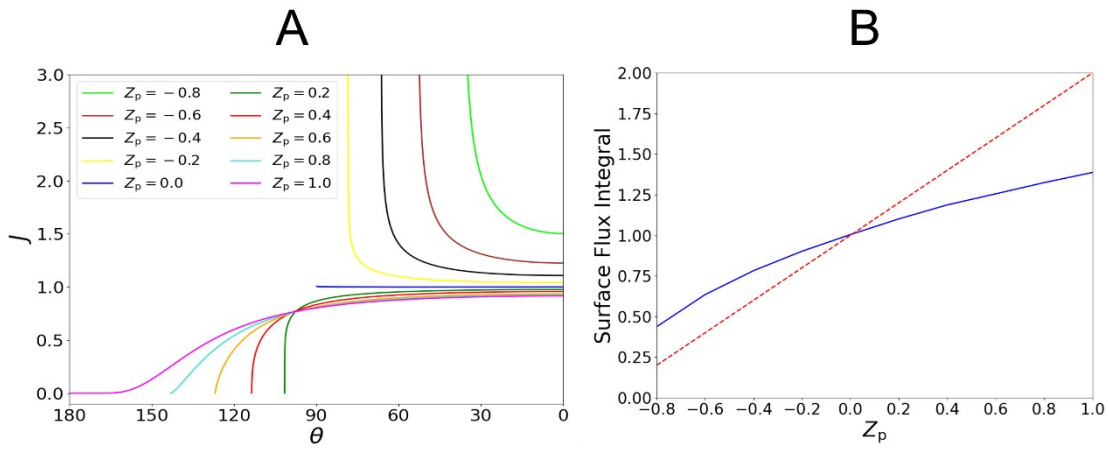


Figure 5.10: (A) The dimensionless steady-state flux profile for $-0.8 \le Z_p \le 1$ (B) The dimensionless steady-state surface flux integral $\int_0^{\theta_c} J(\theta)\sin\theta\, d\theta = J_{Tot}/2\pi$ for $-0.8 \le Z_p \le 1$, represented as a blue solid line, for a truncated sphere on a surface under thermodynamic release. The surface flux integral assuming a constant $J(\theta)=1$ is represented by a red dotted line in (B).

The diffusion of material from a hemisphere on a plane is isomorphic with a half-volume of release from an unbounded sphere. This is evident in Figure 5.9 as the concentration profile exhibits no θ-dependence and is spherically symmetric. Figure 5.10A corroborates this with a uniform local steady-state flux profile and Figure 5.10B does also since the hemisphere case occurs at the point where the total steady-state flux from a sphere on a surface crosses that for an unbounded sphere of equivalent surface area.

In contrast, the sphere on a plane does not give a θ-independent concentration profile. Figure 5.10A shows that the local flux is reduced at all points on the surface relative to the unbounded case. The reduction becomes increasingly prominent closer to the contact point. The steady-state release is being limited by the geometrically hindered diffusion. A diffusionally stagnant zone develops between the spherical particle and the cuticular plane, causing a build-up of material, as seen in Figure 5.9. Some diffusional stagnation persists around the entire particle. Figure 5.10B demonstrates that the total flux deviates by a factor of $\ln 2 \approx 0.69$ from that predicted for an isolated sphere. These results for the hemisphere and sphere are consistent with analytical and experimental results[2, 69, 77, 78], as well as the results

generated in Chapter 4 using fully implicit methods, providing validation to this model and simulation method.

Examples $0<Z_p<1$ exhibit a semi-stagnant zone of intermediate effect. As seen in Figure 5.10, the decay to $J(\theta)=0$ is sharp, becoming less sharp for larger Z_p. The development of a stagnant zone for which $J(\theta)\approx 0$ over a range of θ occurs only for $Z_p>0.8$. The non-uniform local diffusion effects are observed as a negative curvature in the surface flux integral in Figure 5.10B. These results are consistent with analytical results for the total flux[77], validating the local flux profiles which are novel contributions to the literature[2].

For $Z_p<0$ or $\theta_c<90°$, diffusion from the sphere near the contact point is enhanced. This is a contrasting phenomenon to that seen in the stagnant zone since the diffusionally accessible volume at the contact point is increased relative to the hemisphere case. This results in an enhanced local flux. The flux at the contact point tends toward infinity. This corroborates the understanding from Chapter 4 that the diffusional behaviour tends towards that of a disk. This model presents novel total flux calculations for spherical caps of $Z_p \leftarrow 0.4$ as well as local flux profiles for $Z_p<0$, overcoming the limitations of previous analytical approaches[77].

The non-linearity of the dependence of the release on truncation is relevant to fast-release dispersion-based formulation design with uptake across a bio-membrane: such as pure pesticide particles (wettable powders, water dispersible granules, suspension concentrates, oil dispersions)[79], rapid burst release particles[51, 52], and triggered release particles[80]. The correction to the total release rate needed for a given Z_p relative to a hemisphere is given in Figure 5.10B. Our model corrects the rate of aqueous release and gives the non-uniform release and concentration profiles. The stagnant zone close to the cuticle is highly pertinent to

the partitioning of material across the cuticle-solution interface and thus the indirect uptake pathway, which is further investigated later.

Reducing K_{aq} below 10^{-2} produces results for the kinetic regime. One observes a uniform steady-state surface flux $J=K_{aq}$ independent of the truncating surface. This is initially unintuitive as the diffusion layer still arrives at the inert surface; however, subsequent diffusional stagnation does not occur because material escapes from the confined area faster than it is replenished by the process at the particle surface. Similarly for $\theta_c<\frac{\pi}{2}$, no surface-parallel concentration gradients develop as the diffusional perturbation is too slight. We thus observe no deviation from the prediction by Crank for an unbounded sphere (Equation 5.13), given a correction accounting for a difference in surface area.

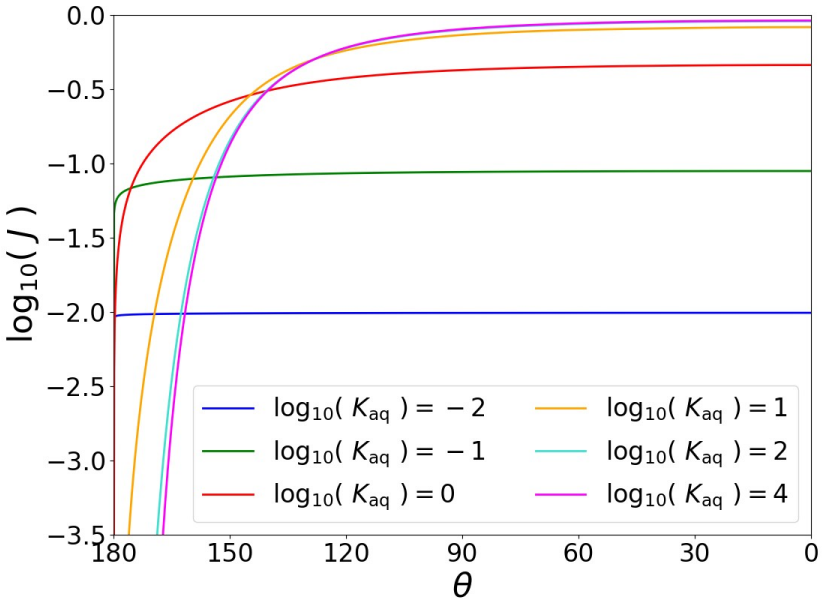


Figure 5.11: Variation of the logarithm of the dimensionless steady-state flux profile J across the surface of the sphere with $Z_p=1$ for different values of the dimensionless release rate constant K_{aq}, illustrating the thermodynamic and kinetic regimes for a sphere on an inert plane surface.

We can thus conclude that only particles with rapid release kinetics relative to diffusion exhibit deviations from unidimensional release models and thus benefit from tuning of the cuticle-particle contact angle. The local flux profiles across the particle surface in Figure 5.11

illustrate the thermodynamic-kinetic regime transition for a full sphere on a surface and the establishment of local flux uniformity as K_{aq} decreases. The same transition is observed for all Z_p.

5.4 Modelling direct uptake with perfect sink

In the previous section, we considered particle release into the aqueous phase, the precursor to indirect uptake. In this section we discuss direct transfer of pesticide into the 'cuticle proper', which is the direct uptake pathway. We approximate the area of particle-'cuticle proper' contact as a 2D disk through which uptake occurs exclusively. We simulate the release and diffusion from this disk contact across a barrier of finite thickness, $Z_{cut}=z_{cut}/r_p$, where z_{cut} and r_p are defined in Figure 5.5.

When considering direct uptake only, we simulate the disk and 'cuticle proper' only. The equations and methods used while modelling release from the truncated sphere are also applied here. However, the active surface is changed to a flat disk and the reference length used for converting to dimensionless parameters is changed from the particle radius r_p to the disk radius, $r_d=r_p\sin(\theta_c)$. The values of D and $[A]_{eq}$ are also changed; however, because of the conversion to dimensionless coordinates, their dimensionless counterparts are not affected while we simulate the cuticular medium independently from the aqueous. The distance between the planes in the Z-direction, which represents the thickness of the 'cuticle proper' is given by $Z_{cut}=z_{cut}/r_d$ which is equivalent to the Z_{max} of the simulation space. We apply a perfect sink boundary condition at the planar boundary opposite the disk contact area to represent the interface between the 'cuticle proper' and the 'sorption compartment', i.e. $C(R, Z=Z_{cut})=0$.

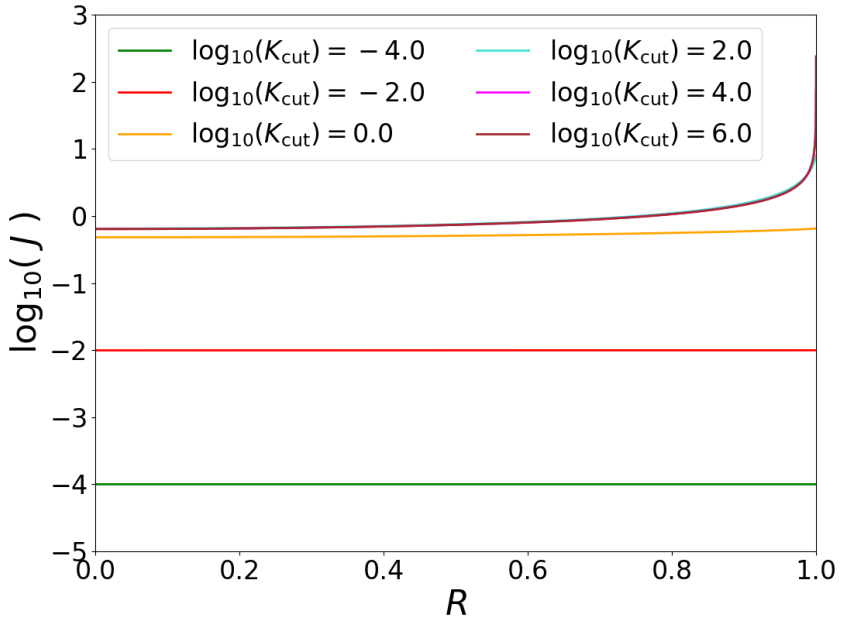


Figure 5.12: Steady-state surface flux profile J across the area of the particle-cuticle contact disk with $Z_{cut}=1000$ and varying K_{cut}.

We first simulate various K_{cut} values, the dimensionless rate constant for release into the 'cuticle proper', with a barrier thickness in the limit of infinite thickness ($Z_{cut}=1000 \gg 1$). The local flux profiles in Figure 5.12 distinguish the thermodynamic and kinetic limits. For the kinetic limit ($K_{cut} \leq 10^{-2}$), the steady-state flux is uniform across the disk: $J(R)=K_{cut}$ with no edge effect. The thermodynamic regime exhibits a steady-state surface flux accurate to the expression derived by Aoki[74] (Equation 5.10). The agreement of these results with literature provides validation for our model.

Diffusion at a disk into/from an infinite medium is well-described within the literature[81]. However, the 'cuticle proper' and particles are typically of a comparable size, on the scale of micrometers to tens of nanometers[11, 82-84]. This leads to marked differences from infinite-volume treatments or even simpler assumptions of unidimensional diffusion[31, 85].

We simulate varying Z_{cut} under the thermodynamic and kinetic regimes: the steady-state concentration profiles along the symmetry axis are given in Figure 5.13A and Figure

5.13B, respectively. The concentration profiles deviate from linearity as Z_{cut} increases, reflecting that diffusion in the *R*-direction increasingly contributes.

Figure 5.13C illustrates the effect of an increasing Z_{cut} on the steady-state surface flux under the thermodynamic regime. The release rate deviates from that of a linear concentration gradient: $J(R) \to \frac{\Delta C}{\Delta Z} = \frac{C(Z=0)}{Z_{cut}} = \frac{1}{Z_{cut}}$. An edge effect develops which affects the local flux increasingly far from $R=1$. The local surface flux increasingly resembles Aoki's prediction[81] and the total flux decreases to $J_{Tot}/r_p^2 = 4$.

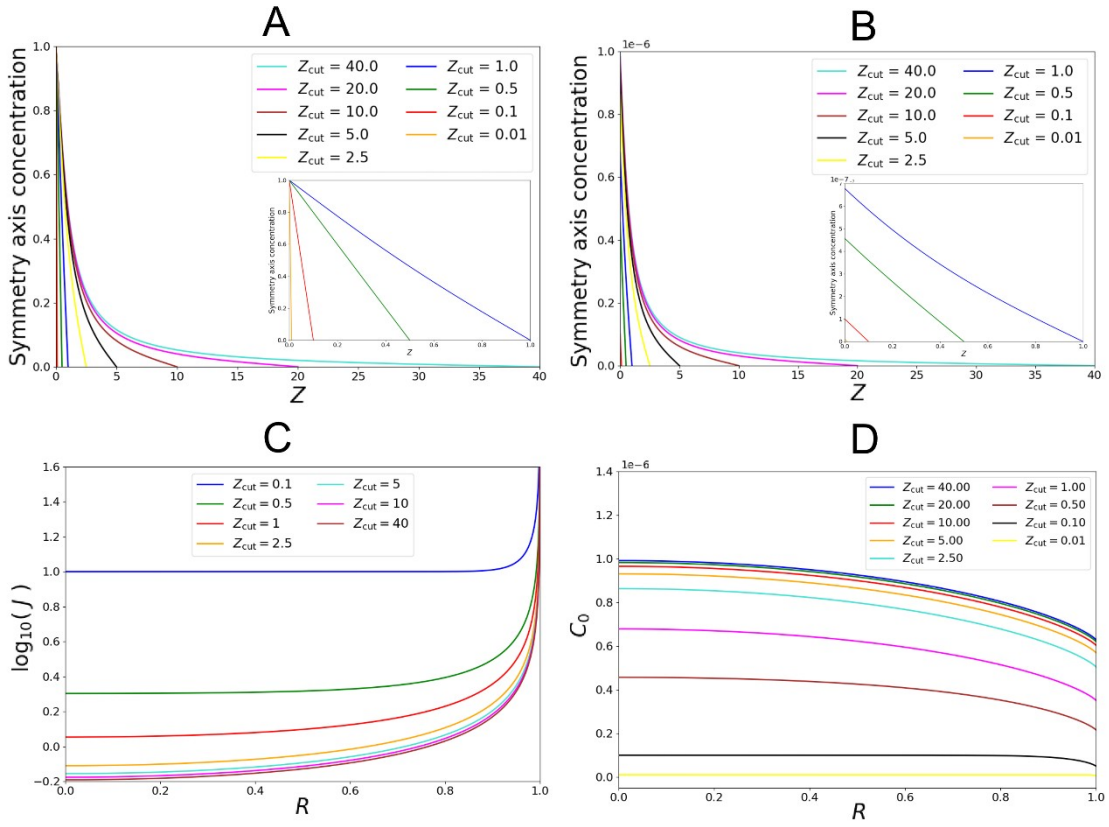


Figure 5.13: Results for the surface flux and cuticular concentration for varying Z_{cut} for a particle-cuticle disk interface. The steady-state concentration profile along the symmetry axis is presented for: (A) thermodynamic release ($K_{cut} = 10^6$) and (B) kinetic release ($K_{cut} = 10^{-6}$). Both demonstrate transitions from linear diffusion. Inlaid diagrams provide clearer illustration for small Z_{cut}. (C) presents the steady-state surface flux profile for varying Z_{cut} for $K_{cut} = 10^6$. (D) presents the surface concentration profile for varying Z_{cut} for $K_{cut} = 10^{-6}$.

Under the kinetic regime, the steady-state surface flux is unaffected by Z_{cut} and is uniform. As Z_{cut} decreases, the surface concentration of pesticide within the 'cuticle proper' decreases such that the flux at the surface remains equal to the dimensionless release rate constant, i.e. $J(R)=\frac{C(Z=0)}{Z_{cut}}=K_{cut}$. This can be seen in Figure 5.13 plots B and D for $Z_{cut}<1$. Interestingly, the surface concentration profile for the kinetic regime is non-uniform, unlike for the thermodynamic regime, with a decrease towards the disk edge. This reflects the increasing radial contribution to diffusion which provides a more efficient depletion of material at the surface. The edge effect on the surface concentration declines as Z_{cut} decreases.

Table 5.2: Summary of the 4 limiting cases alongside the points of transition.

	Thermodynamic limit	Transition point	Kinetic limit
Infinite media limit	$C_{Z=0}=1$ for all R $\left(\frac{\partial C}{\partial Z}\right)_{Z=0}=\frac{-2}{\pi\sqrt{1-R^2}}$ Non-linear diffusion $J_{Tot}/r_p^2=4$	$K_{cut}=4/\pi=$	$C_{Z=0}=f(R)$ $\left(\frac{\partial C}{\partial Z}\right)_{Z=0}=-K_{cut}$ Non-linear diffusion $J_{Tot}/r_p^2=\pi K_{cut}$
Transition point	$Z_{cut}=\pi/4$		$Z_{cut}=1$

Constrained media	$C_{Z=0}=1$ for all R $\left(\frac{\partial C}{\partial Z}\right)_{Z=0}=\frac{-1}{Z_{cut}}$ Linear diffusion $J_{Tot}/r_p^2=\frac{\pi}{Z_{cut}}$		$C_{Z=0}=K_{cut}Z_{cut}$ $\left(\frac{\partial C}{\partial Z}\right)_{Z=0}=-K_{cut}$ Linear diffusion $J_{Tot}/r_p^2=\pi K_{cut}$

For slow-release particles, this model predicts that reducing Z_{cut}, either by application to a thinner 'cuticle proper' or by increasing the particle-cuticle contact area through manipulation of the contact angle or particle size, results in a lower pesticide concentration within the 'cuticle proper' for the same uptake rate. This implies a reduced absorption of pesticide in the cuticle, a desirable formulation feature[86-89], so long as the direct uptake pathway is dominant.

For the case of diffusion across a finite, planar boundary, two pairs of limiting regimes exist: thermodynamic vs. kinetic and infinite thickness vs. constraining thickness. These regimes are summarized in Table 5.2. We use the total steady-state surface flux as the metric for determining the infinite-constrained transition under the thermodynamic limit and the thermodynamic-kinetic transition under the infinite limit, as it is stringent and most easily determined experimentally. The infinite-constrained transition for the kinetic limit is inferred from the steady-state concentration at the disk's centre. Plots illustrating these transitions are provided in Figure 5.14.

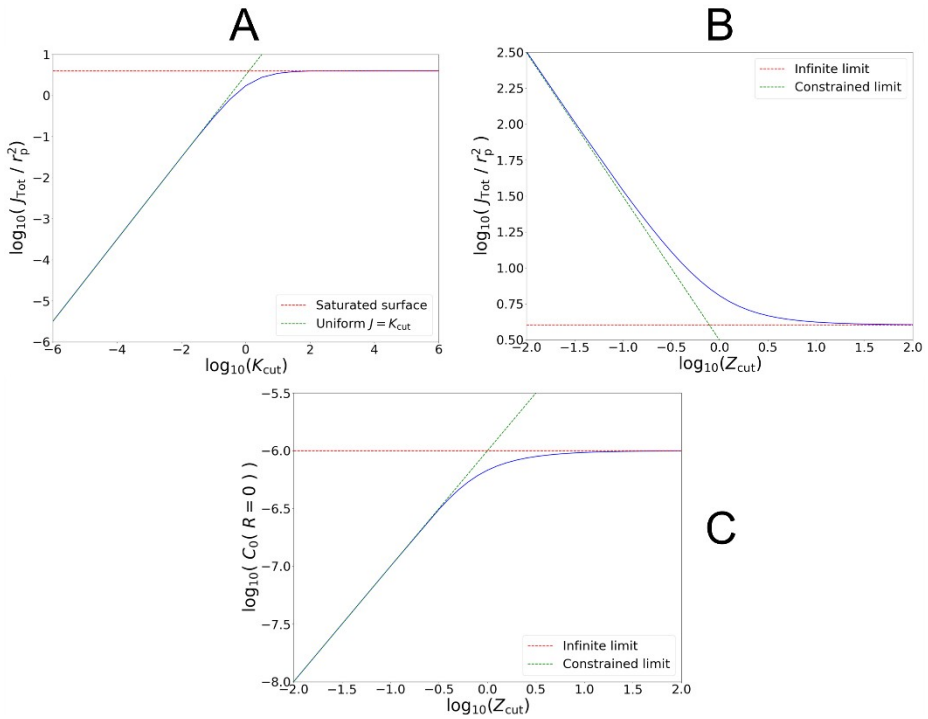


Figure 5.14: Illustration of, for direct uptake from a particle-cuticle disk contact area, (A) the thermodynamic-kinetic regime transition according to the total dimensionless particle-cuticle surface flux J_{Tot} in the infinite barrier limit, (B) the infinite-constrained regime transition according to the total dimensionless particle-cuticle surface flux J_{Tot} in the thermodynamic release limit, and (C) the infinite-constrained regime transition according to the dimensionless surface concentration at the symmetry axis $C_0(R=0)$ in the kinetic release limit.

The flux at the perfect sink boundary is a potential metric for the successful penetration of material through the ‘cuticle proper’. The flux into the ‘sorption compartment’ has a limiting case for small Z_{cut} of a step function from $J(R\leq 1)=1/Z_{cut}$ to $J(R>1)=0$. As Z_{cut} increases, this flux becomes less localized. Figure 5.15 illustrates the dependence of the flux on the barrier thickness under thermodynamic (A and C) and kinetic (B and D) release limits.

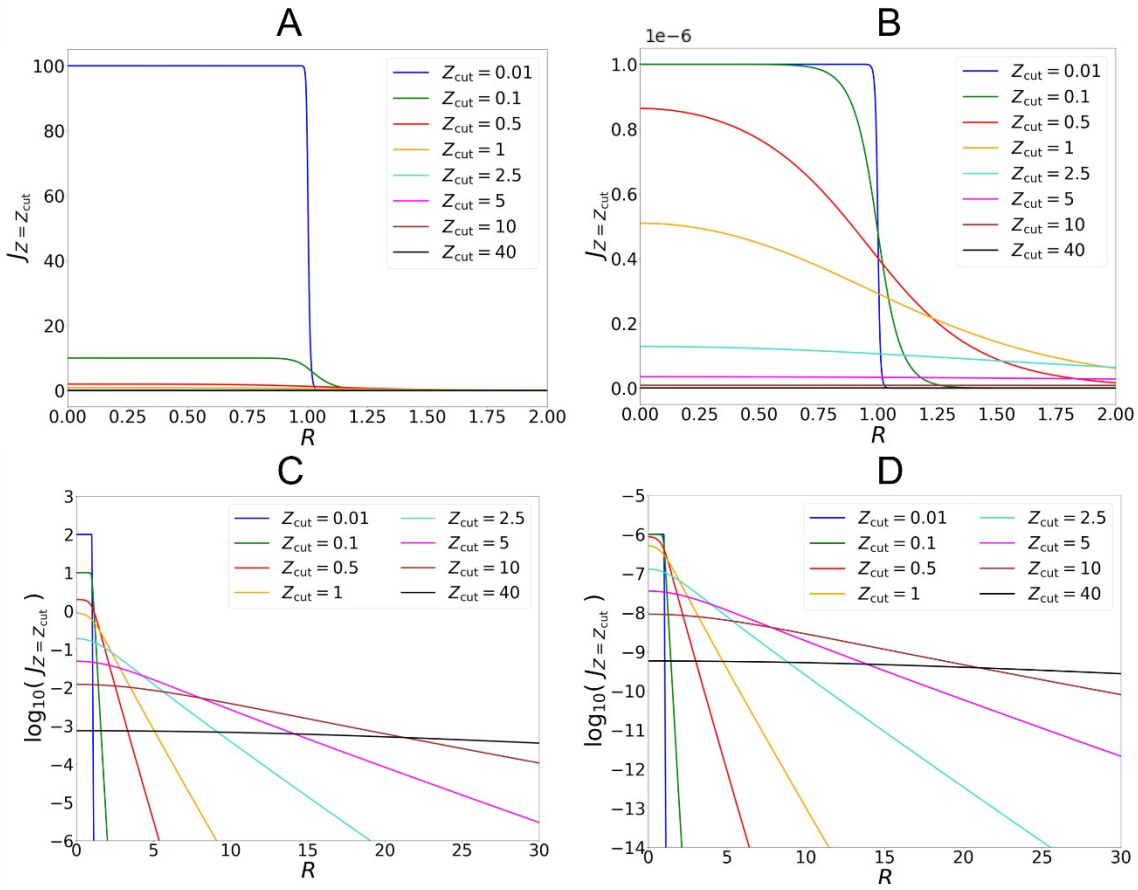


Figure 5.15: Dimensionless steady-state flux profile across the sink plane boundary $J_{Z=Z_{cut}}$ for varying barrier thicknesses Z_{cut} under (A) thermodynamic release ($K_{cut}=10^{6}$) and (B) kinetic release ($K_{cut}=10^{-6}$). Profile of the logarithm of the dimensionless steady-state flux across the sink plane boundary $\log_{10}\left(J_{Z=Z_{cut}}\right)$ for varying barrier thicknesses Z_{cut} under (C) thermodynamic release ($K_{cut}=10^{6}$) and (D) kinetic release ($K_{cut}=10^{-6}$).

Plot A illustrates the steady-state flux profile at the perfect sink plane boundary under the thermodynamic release regime at the particle-cuticle interface. As the diffusion becomes more constrained by a decreasing Z_{cut}, the flux at the sink boundary tends towards the predicted linear flux of $J(R\leq 1)=1/Z_{cut}$ and the flux decays increasingly sharply for $R>1$. Plot C highlights the difference in the sharpness of the decay in flux. As the barrier thickness grows, the rate of diffusion in the z-direction relative to the r-direction is reduced such that the flux profile extends to larger R. Under the steady state, the flux into the system must equal flux out of it, thus the total flux at the plane sink boundary must equal the total flux

from the disk. Thus, the principal effect of shortening the relative barrier thickness is the localization of material within $R \leq 1$.

We perform analogous simulations under the kinetic regime with $K_{cut} = 10^{-6}$. Plots B and D illustrate a similar trend as was observed for the thermodynamic regime whereby the flux profile tends towards a step function for decreasing Z_{cut}. However, the flux produced by linear diffusion is limited by the release kinetics and thus does not infinitely scale with the barrier thickness. The total flux remains equal to the total flux at the disk surface: $J_{Tot} / r_p^2 = \pi K_{cut}$ for all values of Z_{cut}.

Localization of the flux with respect to the r-dimension may have significant effects on the uptake beyond the 'cuticle proper', such as by reducing the sequestration of pesticidal material in intracuticular waxes due to the material diffusing over a smaller radial distance and thus encountering a smaller volume within the 'cuticle proper', or by maintaining a larger concentration gradient deeper into the leaf and thus a stronger driving force for uptake. This invites future study and may require potential revision of the perfect sink approximation at the 'cuticle proper'-'sorption compartment' interface when subcuticular effects are considered. Future study of the flux transient at this far boundary may also be of value for determining time-dependent uptake and uptake lag induced by transport across the membrane barrier.

Decreasing the value of Z_{cut} also decreases the time taken to achieve steady-state flux. This is illustrated in Figure 5.16. The flux is unchanged by the barrier thickness until the diffusion layer arrives at the sink boundary. Tuning the uptake rate decay towards a constant steady state uptake is significant for the design of formulations for which slow, continuous uptake is preferred from the moment of application. This is achieved sooner for particles with larger contact areas with the cuticle.

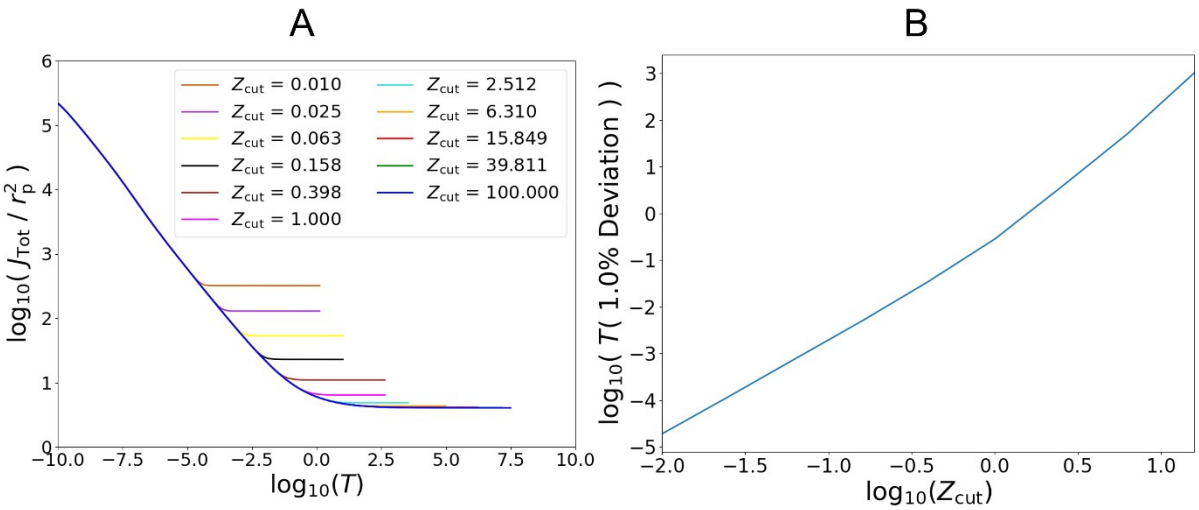


Figure 5.16: (A) Logarithm of the total flux J_{Tot} from a disk into a finite planar barrier under the thermodynamic regime ($K_{cut}=10^6$) with respect to dimensionless time T for varying relative barrier thicknesses Z_{cut} between constrained and infinite regimes. (B) Logarithm plot of the time taken for the flux transient to deviate from the infinite-volume limit by 1% as a function of Z_{cut}.

These results demonstrate that a greater contact area enhances direct uptake non-linearly: the area through which uptake occurs increases, the release kinetics accelerate ($K_{cut}=k_f^{cut}\cdot r_p/D_{cut}\cdot\left[A\right]_{eq}^{cut}$), and the *relative* barrier thickness Z_{cut} decreases. The flux into the cuticle is maximized under the thermodynamic, constrained regime. This non-linear dependence on area is not accounted for by unidimensional or partition-limited models.

While an 'effective' diffusion coefficient is used in our model, diffusion (and thereby transport) is treated here as homogeneous throughout the 'cuticle proper', which overly simplifies cuticles possessing highly tortuous structures[17, 26] or stratification of chemical components[19]. Further work is required to assess the validity of these results in such cases. Large tortuosity values will complicate assessments of transport rates based on the 'cuticle proper' thickness, as diffusion path lengths shall be greater[17]. Use of volume-averaged D_{cut} and $\left[A\right]_{cut}^{eq}$ may be inaccurate for modelling despite their experimental utility.

5.5 Modelling competing uptake pathways

In this section we discuss the competition between release into solution and transport across the cuticle-particle interface for typical physicochemical parameters related to foliar applied pesticides and cuticles. Thus far simulated results have been dimensionless and general to any system with the corresponding boundary conditions. In this section, we consider the dimensional results predicted by this model in the context of foliar pesticide uptake. Particular attention is given to the pesticide solubility in aqueous formulation solution, $[A]_{eq}^{aq}$, the partition coefficient between aqueous formulation solution and the 'cuticle proper', K_{cpw}, and the diffusion coefficient ratio, D_{cut}/D_{aq}.

5.5.1 Comparing release rates into aqueous and cuticular phases for typical pesticides

We are restricting the scope of this chapter to consider lipophilic pesticides only and so approximate the solubility in the aqueous formulation solution as the aqueous solubility, $[A]_{eq}^{aq} \approx [A]_{eq}^{H_2O}$, and estimate the aqueous-'cuticle proper' partition coefficient as $\log K_{cpw} \approx -1.108 + 1.01 \log K_{ow}$[90], where K_{ow} is the octanol-water partition coefficient. We consider a K_{ow} range between 1 (e.g. mesotrione: 1.29) and 10^7 (e.g. lambda-cyhalothrin)[91], which captures the full range of K_{ow} for commercially relevant lipophilic pesticides. We thus consider a K_{cpw} range between $10^{-1} - 10^6$. For the same reasons, we consider an aqueous solubility range between $10^{-7} mol/m^3$ and $10^2 mol/m^3$. Diffusion coefficients in water for small, organic species are $10^{-10} m^2 s^{-1}$, which is on the same scale as that for typical pesticides. Meanwhile, diffusion coefficients in the 'cuticle proper' are comparable to diffusion coefficients in reconstituted wax[18] $\approx 10^{-18} - 10^{-17} m^2 s^{-1}$. Relatively, diffusion through the 'cuticle proper' is very slow, reflecting the ratio $D_{cut}/D_{aq} \approx 10^{-8} - 10^{-7}$.

Comparing the particle-solution and particle-cuticle interfaces, several regimes are identified for each interface: either thermodynamically or kinetically limited release with highly linear or non-linear diffusion dependent on Z_{cut}. The interfacial fluxes also vary for different degrees of truncation.

We first consider the ratio of $A \times j_{SS}(i)$ (where A is the interfacial area and $j_{SS}(i)$ is the dimensional steady-state flux at the interface between the particle and medium i) of a $1\,\mu m$ radius particle which rests as a hemisphere on the 'cuticle proper' ($Z_p = 0$), with $Z_{cut} = 0.1$.

If both interfaces are under the thermodynamic regime:

$$\frac{A\, j_{SS}(cuticle)}{A\, j_{SS}(solution)} = \frac{\pi r_p D_{cut} [A]_{eq}^{cp}}{Z_{cut}} \times \frac{1}{2\pi D_{aq} [A]_{eq}^{aq} r_p} = \frac{K_{cpw} D_{cut}}{2 D_{aq} Z_{cut}} \qquad \text{Equation 5.15}$$

Considering typical values for lipophilic pesticides, we expect this ratio of interfacial fluxes to occupy a range between 5×10^{-9} and 5×10^{-1}.

If the interface with the aqueous solution medium is kinetic and the interface with the 'cuticle proper' is thermodynamic:

$$\frac{A\, j_{SS}(cuticle)}{A\, j_{SS}(solution)} = \frac{\pi r_p D_{cut} [A]_{eq}^{cp}}{Z_{cut}} \times \frac{1}{2\pi k_f^{aq} r_p^2} = \frac{D_{cut} [A]_{eq}^{cp}}{2 r_p k_f^{aq} Z_{cut}} \qquad \text{Equation 5.16}$$

where k_f^{aq} is the forward release rate constant from the particle into the aqueous medium. If we approximate $[A]_{eq}^{cp} = [A]_{eq}^{H_2O} \times K_{cpw}$, we shall expect this ratio of fluxes to vary between $5 \times 10^{-26} / r_p k_f^{aq}$ and $5 \times 10^{-9} / r_p k_f^{aq}$. For $r_p = 1\,\mu m$, the expected range is $5 \times 10^{-20} / k_f^{aq}$ to $5 \times 10^{-3} / k_f^{aq}$.

If we consider $K_{cut} = k_b^{cut} r_p / D_{cut}$, in order for $K_{cut} \leq 1$, for an $r_p = 1 \mu m$ and $D_{cut} = 10^{-17} m^2 s^{-1}$, $k_b^{cut} \leq 10^{-11} m/s$ is required. Thus, we do not consider cases in which the particle's interface with the 'cuticle proper' is under the kinetic regime since an unrealistic hindrance to the direct release is required for the kinetics to be rate-limiting relative to diffusion through the 'cuticle proper', even for designed particles.

We observe that the release of pesticide into the aqueous phase greatly outcompetes direct release into the 'cuticle proper' unless the pesticide is simultaneously extremely lipophilic, poorly water-soluble, *and* the release into water is under strict kinetic control: in the most lipophilic and poorly water-soluble case within the ranges considered, $k_f^{aq} < 5 \times 10^{-3} mol \cdot m^{-2} s^{-1}$ is required for direct release to outcompete aqueous release.

Though truncation does influence this ratio and must be considered for precise measurement of the rates of release and uptake, only the most extreme scenarios might produce results in which release into the aqueous phase does not markedly outcompete direct release into the 'cuticle proper'. As such, the influence of truncation on the general assessment of the competition between these processes in this section is neglected.

Both the direct and indirect pathways from the perspective of uptake into the leaf share a limiting step: diffusion-limited partitioning into the 'cuticle proper'. As described above, diffusion is so much faster within the formulation that the steady-state aqueous concentration at the cuticle-solution interface is established instantaneously relative to the timescale of diffusion through the 'cuticle proper'. By asserting mass balance at the interface:

$$\frac{\partial c_{aq}}{\partial z} = \frac{D_{cut}}{D_{aq}} \frac{\partial c_{cut}}{\partial z} \approx 10^{-8} \frac{\partial c_{cut}}{\partial z} \qquad \text{Equation 5.17}$$

This justifies the assumption that a concentration gradient that develops within the 'cuticle proper' at the aqueous interface due to partitioning shall negligibly impact the concentration gradient within the formulation's aqueous phase. With the dimensionless conversions and using $\frac{c_{cut}^{eq}}{c_{aq}^{eq}} \leq 10^4$:

$$\frac{\partial C_{aq}}{\partial Z} = \frac{D_{cut} c_{cut}^{eq}}{D_{aq} c_{aq}^{eq}} \frac{\partial C_{cut}}{\partial Z} \leq 10^{-4} \frac{\partial C_{cut}}{\partial Z} \qquad \text{Equation 5.18}$$

We can thus reasonably approximate that the diffusion within the formulation's aqueous phase is negligibly affected by the distribution of material in the 'cuticle proper'.

Recognizing this, simulating the concentration profile along an inert cuticle-solution interface for a releasing truncated sphere at steady-state, and using this profile as a constant boundary condition at the cuticle-solution interface (assuming surface equilibration), we present a model for the diffusion of material across the 'cuticle proper' which occurs via the direct and indirect pathways, assuming zero initial/bulk concentration in the droplet and highly disperse particles, which does not require simulation of the aqueous phase and 'cuticle proper' simultaneously.

5.5.2 Model of the indirect pathway

Analysis of the direct pathway acting alone under steady state is performed in Section 5.4. Consideration is now given to the case of the indirect pathway acting alone. The flux at the particle-cuticle interface is set to zero. The concentration along the solution-cuticle boundary is set as described above. Indirect uptake into the 'cuticle proper' from a hemispherical particle is simulated for varying K_{aq} with diffusion through the 'cuticle proper' under the infinite thickness regime and presented in Figure 5.17.

Comparison with the steady-state flux produced by direct uptake from a thermodynamic particle-cuticle interface of ($J_{Tot}/r_p^2=4$) suggests that an aqueous dimensionless release rate constant of 1.8 or less is required for the indirect pathway to be slower than the direct pathway for the case of a hemisphere with $Z_{cut} \gg 1$.

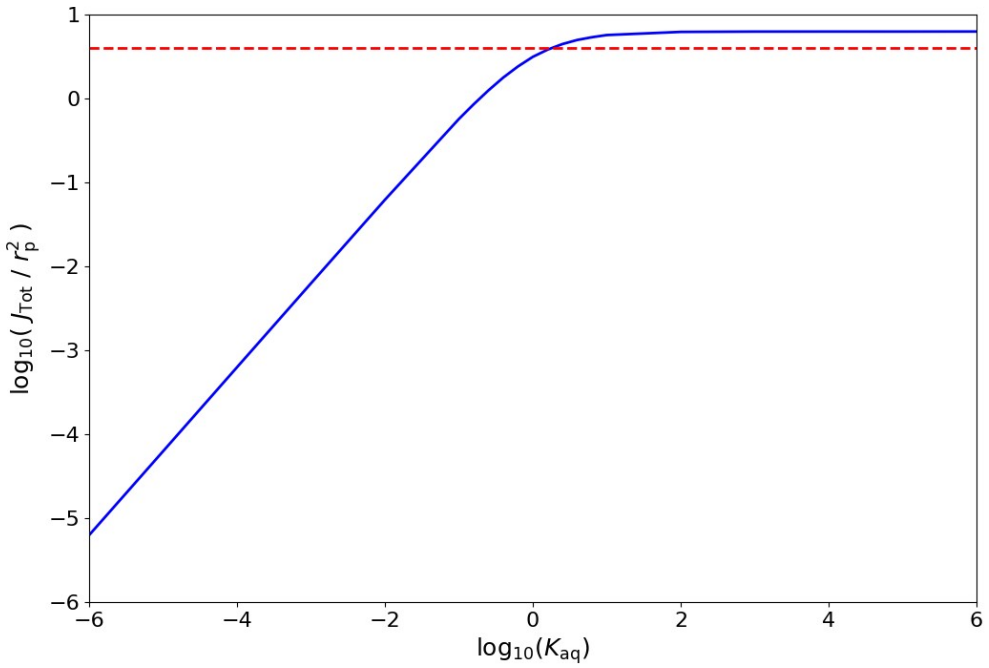


Figure 5.17: Logarithm of the dimensionless total steady-state flux J_{Tot}/r_p^2 via the indirect pathway into an infinite cuticle ($Z_{cut} \gg 1$) with zero direct flux from the disk contact area, assuming a surface-equilibrated cuticle-solution interface, a hemispherical particle ($Z_p=0$), and instant repletion of material at the cuticle interface by diffusion through the aqueous solution for varying K_{aq}. The red dotted line represents the dimensionless steady-state total flux predicted for direct uptake rate acting alone under the thermodynamic, infinite-thickness regime.

5.5.3 Competing direct and indirect pathways

If the two pathways are co-active, the total interfacial flux is not additive with respect to the indirect and direct uptake fluxes. In Figure 5.18, we present results of simulations performed under the assumptions described above with the cuticle-particle interface under thermodynamic control. The dimensionless aqueous release rate constant K_{aq} controls the rate of indirect uptake relative to direct uptake.

For high values of K_{aq}, i.e. thermodynamic aqueous release, the two pathways compete. The flux at the cuticle surface is positive both beneath and at a distance from the particle, as seen in Figure 5.18A. The resultant total flux approximates the indirect pathway acting alone, implying that direct uptake provides only a small contribution to the uptake from fast-releasing particles and thus that models treating the whole droplets as homogeneous sources can be applied accurately in these cases. In this high K_{aq} limit, the total flux and its contributions are independent of K_{aq}.

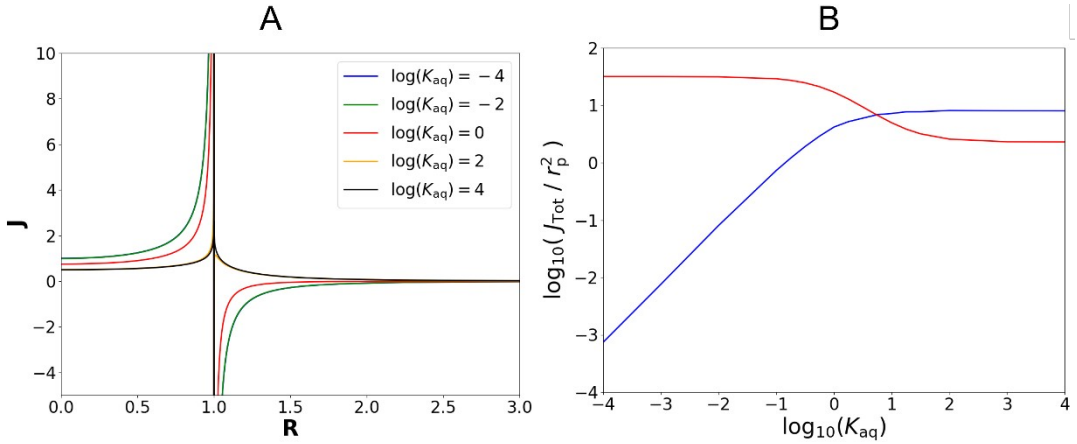


Figure 5.18: (A) Interfacial steady-state flux profile J for simultaneous direct and indirect uptake with varying dimensionless aqueous release rate constant, K_{aq}. (B) Logarithm of the total dimensionless steady-state flux for simultaneous direct and indirect pathways into an infinite cuticle ($Z_{cut} \gg 1$) assuming a thermodynamic cuticle-solution interface and instant repletion of material by diffusion through the solution for varying dimensionless particle-solution release rate constants K_{aq}. The blue line represents the total flux into the cuticle. The red line represents the total flux into the cuticle directly from the particle. The difference between the two corresponds to the flux at the solution-cuticle interface (note that this is negative for $K_{aq} < 10^{0.8}$).

As K_{aq} decreases, a transition occurs whereby the total flux into the cuticle becomes linearly dependent on K_{aq}. The flux from the particle-cuticle contact increases to a new limiting value, while the flux from indirect uptake decreases and even becomes negative. This is reflected in Figure 5.18A and Figure 5.18B.

A smaller K_{aq} results in an aqueous steady-state concentration profile that becomes smaller relative to the concentration profile generated by direct uptake alone along the outer cuticle surface and thus a smaller total flux. Reducing the rate at which pesticide enters the cuticle

along the indirect pathway leads to greater concentration gradient beneath the particle and hence an increased flux via the direct pathway. Once the aqueous concentration becomes less than what the direct uptake pathway can support within the cuticle after partitioning across the interface, pesticide material begins to 'leach' from the 'cuticle proper' back into the aqueous solution, rather than diffusing deeper into the cuticle. The alternative source hence becomes an alternative sink, which is closer to the disk source. We see that the positive and negative interfacial fluxes approach infinity at the disk boundary, which is unphysical outside of this idealized model, and decay. The flux at the disk is enhanced relative to if the cuticle-solution interface were a zero-flux boundary. The linear dependence of the total flux on K_{aq} in the limit of low K_{aq} reflects the linear dependence on K_{aq} of the aqueous concentration profile in the kinetic release limit and hence the extent of the 'leaching effect'. The 'leaching' of pesticide material greatly hinders the total uptake across the 'cuticle proper' so long as this alternative sink is available. The transition to a negative cuticle-solution interfacial flux occurs at $K_{aq}=10^{0.8}$.

This previously unrecognized 'leaching effect' is of great potential significance as it suggests a dependence of the uptake of lipophilic material on the persistence of the aqueous medium, which has otherwise been discounted. This effect cannot be characterized by other models which rely on simple permeability relationships or partition-limited uptake.

5.6 Additional insights

In this section, we discuss further insights that may be taken from this work to understand the processes active during foliar uptake. We consider what properties are required of the pesticide and particle for different contributions of the two uptake pathways and we discuss what implications our simulated results have when considered alongside co-occurrent droplet evaporation.

5.6.1 The G-factor

We identify the parameter G, where $G = \frac{D_{cut}[A]_{eq}^{cp}}{2 D_{aq}[A]_{eq}^{aq} Z_{cut}}$ under the constrained barrier regime

or $G = \frac{2 D_{cut}[A]_{eq}^{cp}}{D_{aq}[A]_{eq}^{aq}}$ if the barrier thickness is within the infinite regime. This parameter is derived from a comparison of the steady-state fluxes from the particle-solution interface and the particle-cuticle interface considering how long it will take for either to fully deplete a given particle when the particle is a hemisphere. We can conclude that if $K_{aq} \gg G$, the particle will be fully depleted of pesticide before direct uptake can meaningfully occur. If the aqueous release is slowed, such that $K_{aq} \leq G$, direct uptake can act meaningfully before particle depletion. If $G < 1$, then for direct uptake to occur before the complete depletion of material from the particle, the aqueous release must be slowed to such an extent that only direct uptake can be active. Thus, under this condition, the total uptake rate can be well-described as occurring by only the direct or indirect pathway and the two pathways cannot be simultaneously active. If $G > 1$ then a region in which the two pathways can compete simultaneously is accessible.

$G \ll 1$ throughout the ranges of physicochemical properties considered above for lipophilic pesticides on plant cuticles. We thus predict that lipophilic foliar pesticide uptake cannot meaningfully occur by both pathways simultaneously before particle depletion.

5.6.2 Considering evaporation times

Evaporation of solvent from a formulation droplet has a considerable influence on pesticide uptake[92, 93]. Evaporation shrinks the droplet size and concentrates the dissolved active ingredient along with any formulation additives. This eventually results in crystallization or

deposition of solid active ingredient onto the outer cuticular surface. Modelling has been reported of droplet evaporation in the context of foliar uptake and simulations have been performed in the literature for fully soluble pesticides[30, 32, 94]. The solid residue left after total droplet evaporation may be dry or partially hydrated. Lipophilic species are observed to continue to undergo uptake from such residues; however, at this stage, the rate of uptake is greatly slowed and the mechanism by which material continues to enter the 'cuticle proper' is obscure. Our results in Section 5.5.3 demonstrate a 'leaching effect' for slowly releasing particles while a surrounding medium is present which also complicates the dependence of lipophilic uptake on the solvent evaporation. Some consideration needs to be given to the evaporation time relative to the rates of uptake predicted within our model to assess the relevance of the indirect pathway and the 'leaching effect'. This initial and general consideration of the effects of evaporation on lipophilic foliar uptake also provides a foundation for the consideration of this process in Chapter 6.

Calculations were performed whereby the times taken for a particle to fully deplete under a given steady-state surface flux were found for release into the aqueous phase and release directly into the 'cuticle proper':

$$t^{i}_{dissolve} = \frac{V \times [A]^{s}}{A^{i} \times j^{i}_{SS}} \qquad \text{Equation 5.19}$$

where V is the particle volume, $[A]^{s}$ is the density of the pesticide within the particle ($mol \cdot m^{-3}$), A^{i} is the area of the particle exposed to medium i, j^{i}_{SS} is the dimensional steady-state flux into medium i, and $t^{i}_{dissolve}$ is the time taken to fully deplete the particle by release into medium i, assuming constant steady-state flux.

For solid lipophilic pesticide particles, with densities varying between 0.7 and $10\,mol\cdot dm^{-3}$, it is found that $10^{-2}\,s \le t_{dissolve}^{aq} \le 10^{8}\,s$ and $1\,s \le t_{dissolve}^{cut} \le 10^{7}\,s$ under the thermodynamic regime. If the particle-solution interface is under the kinetic regime, the corresponding result is $\frac{7}{30000 \times k_f^{aq}} s \le t_{dissolve}^{aq} \le \frac{1000}{3 \times k_f^{aq}} s$. These calculations assume relatively rapid attainment of the steady-state interfacial flux and neglects particle shrinking with associated moving boundary conditions.

The evaporation time of typical aqueous formulation droplets of $0.01-0.1\,\mu L$ is typically on the order of 10^2-10^3 seconds[95, 96]. Our results suggest that direct uptake from solid particles typically outlasts the evaporation time significantly even for lipophilic species. Similarly, the activity of indirect uptake may also give an uptake time that significantly outlasts the evaporation time. Thus we predict the general persistence of lipophilic pesticide deposits on the outer cuticular surface long after evaporation except in extreme cases. However, the presence of the indirect pathway still provides a means of accelerating uptake *within* this evaporation time, either by acting as an additional route into the cuticle or by reducing the 'leaching effect'. It is reasonable to assume that some form of direct uptake is the dominant pathway after complete droplet evaporation since rapid diffusion through a surrounding medium is no longer possible. A slower form of indirect uptake may still be possible for cases where significant additive material is co-deposited with the active ingredient to provide a continuous phase surrounding the particles through which diffusion may continue to occur.

Future work may assess how the 'leaching effect' inferred from this model affects the overall uptake in these cases and whether an accelerating transition is observed if this 'leaching' is ceased as a loss mechanism by the solvent's total evaporation for slow-releasing particles.

The results presented in this work are thus most applicable to dispersed-particle formulations before evaporation of the solvent completes. However, continued application of the direct uptake model may be relevant as a first approximation for uptake from a dried residue.

5.7 Comparison with other models

Our model builds upon unidimensional models that implicitly assume linear diffusion[18, 31] by demonstrating that this assumption is inaccurate for many modern application methods. Sufficiently small particle sizes on the sub-micrometre scale are now in commercial use[10, 11] that the contact area radius through which uptake occurs can no longer be generally assumed to be much greater than the cuticle or 'cuticle proper' thickness. This is crucial for slow-release, micro- and sub micro-particulate formulations for which uptake does not occur through the entire droplet area but from localised particle sources, illustrating this model's impact. Numerous other models demonstrate the importance of multi-dimensionality for the simulation of other aspects relevant to transcuticular uptake including the influence of droplet shape and evaporation[29, 32, 94], air-cuticle uptake for semi-volatile ingredients[33], and characterisation of diffusion about cuticular features[34, 97].

Additionally, several uptake models assume that the transport processes are partition-limited[85], including several mass-balanced multi-compartment models[88, 98]. Our work demonstrates the hitherto unrecognised importance of treating the particulate suspension and suspending solution as separate components in order to account for the competing direct and indirect pathways into the 'cuticle proper' and the 'leaching effect' we observe. Additionally, this is significant in the consideration of differential uptake rates before and after droplet evaporation. Relevant corrections to partition-limited models have been illustrated in this work in order to consider the kinetics of the particulate release, the particle-cuticle contact angle, and the 'cuticle proper' thickness relative to the particle-cuticle contact area.

While our model does not offer a complete estimation of uptake, it is nonetheless valuable for improving estimates of uptake into and across the ‘cuticle proper’ layer for larger whole-plant models of organic uptake and distribution[88, 98-100]. We expect that the use of our simulation results as relevant corrections to existing models will be impactful and useful in improving the accuracy of applying such models to particulate formulations. Furthermore, the results of this model are a valuable foundation for Chapter 6 in which we present and interpret experimental results relating to foliar uptake and in which we develop a simple, droplet-scale model based on this chapter’s results.

5.8 Conclusions

In this chapter, we have simulated the steps required for direct and indirect uptake of pesticidal material from a particulate formulation into the plant cuticle. The influence of the particle release rate constant for zero-order release kinetics and the imposition of thermodynamic and kinetic limits has been identified: the properties of these two limits have been investigated with respect to their associated concentration and flux profiles. We have investigated the influence of the thickness of the ‘cuticle proper’ relative to the particle size on the direct uptake pathway and identified the limits of infinite and constrained thickness.

The indirect uptake pathway is generally dominant over the direct uptake. The direct uptake pathway may be effectively neglected in favour of the indirect pathway even for highly lipophilic pesticides. The influence of the aqueous release rate constant, which may be controlled through particle design, on the interplay between the indirect and direct uptake pathways is vital for controlled release mechanisms.

We demonstrate that, counter to the intuition of literature, that lipophilic pesticides do diffuse through an aqueous carrying phase and engage in uptake at a distance from the particle itself. Furthermore, in scenarios where indirect uptake is hindered, we demonstrate the action of a 'leaching effect', compounding the reduction in uptake. We expect that the evaporation of the aqueous phase will have a significant impact on the diffusional processes available for lipophilic uptake, counter to the suggestion by literature, implying an additional process in effect or insufficient experimental investigation.

We have demonstrated the advantages of this multi-dimensional approach to modelling uptake and identifying hitherto unrecognized effects that arise from simple diffusion processes. The results from this modelling procedure provide key corrections for prior models and identifies key parameters for developing a deeper understanding of uptake in future studies.

Insights from the results generated from this chapter are applied in Chapter 6 in which we present experimental results for the study of foliar uptake paired with the development of a simplest viable uptake model and discussion of the considerations necessary for further development in this field of study.

References

1. Elliott, J. R.; Compton, R. G., Modeling Transcuticular Uptake from Particle-Based Formulations of Lipophilic Products. *ACS Agricultural Science & Technology* **2022,** *2* (3), 603-614.
2. Elliott, J. R.; Compton, R. G., Local diffusion indicators: A new tool for analysis of electrochemical mass transport. *Journal of Electroanalytical Chemistry* **2022,** *908*, 116114.
3. Shaner, D. L.; Beckie, H. J., The future for weed control and technology. *Pest Management Science* **2014,** *70* (9), 1329-1339.
4. Köhler, H.; Triebskorn, R., Wildlife Ecotoxicology of Pesticides: Can We Track Effects to the Population Level and Beyond? *Science* **2013,** *341* (6147), 759.
5. Malaj, E.; von der Ohe, P. C.; Grote, M.; Kühne, R.; Mondy, C. P.; Usseglio-Polatera, P.; Brack, W.; Schäfer, R. B., Organic chemicals jeopardize the health of freshwater ecosystems on the continental scale. *Proceedings of the National Academy of Sciences* **2014,** *111* (26), 9549.
6. Bradberry, S. M.; Proudfoot, A. T.; Vale, J. A., Poisoning Due to Chlorophenoxy Herbicides. *Toxicological Reviews* **2004,** *23* (2), 65-73.

7. Knoche, M., Effect of droplet size and carrier volume on performance of foliage-applied herbicides. *Crop Protection* **1994,** *13* (3), 163-178.
8. Graham-Bryce, I. J.; Cooke, G. W.; Pirie, N. W.; Bell, G. D. H., Crop protection: a consideration of the effectiveness and disadvantages of current methods and of the scope for improvement. *Philosophical Transactions of the Royal Society of London. B, Biological Sciences* **1977,** *281* (980), 163-179.
9. Matthews, G., *Pesticide application methods*. John Wiley & Sons: 2008.
10. Knowles, A., Recent developments of safer formulations of agrochemicals. *The Environmentalist* **2008,** *28* (1), 35-44.
11. Kumar, S.; Nehra, M.; Dilbaghi, N.; Marrazza, G.; Hassan, A. A.; Kim, K.-H., Nano-based smart pesticide formulations: Emerging opportunities for agriculture. *Journal of Controlled Release* **2019,** *294*, 131-153.
12. Schönherr, J., A mechanistic analysis of penetration of glyphosate salts across astomatous cuticular membranes. *Pest Management Science* **2002,** *58* (4), 343-351.
13. Shafer, W. E.; Schönherr, J., Accumulation and transport of phenol, 2-nitrophenol, and 4-nitrophenol in plant cuticles. *Ecotoxicology and Environmental Safety* **1985,** *10* (2), 239-252.
14. Schönherr, J.; Riederer, M., Desorption of chemicals from plant cuticles: Evidence for asymmetry. *Archives of Environmental Contamination and Toxicology* **1988,** *17* (1), 13-19.
15. Buchholz, A., Characterization of the diffusion of non-electrolytes across plant cuticles: properties of the lipophilic pathway. *Journal of Experimental Botany* **2006,** *57* (11), 2501-2513.
16. Kerstiens, G., Plant Cuticles — an Integrated Functional Approach. *Journal of Experimental Botany* **1996,** *47*, 50-60.
17. Baur, P.; Marzouk, H.; Schönherr, J., Estimation of path lengths for diffusion of organic compounds through leaf cuticles. *Plant, Cell & Environment* **2002,** *22*, 291-299.
18. Schreiber, L., Review of sorption and diffusion of lipophilic molecules in cuticular waxes and the effects of accelerators on solute mobilities. *Journal of Experimental Botany* **2006,** *57* (11), 2515-2523.
19. Li, Q.; Chen, B., Organic Pollutant Clustered in the Plant Cuticular Membranes: Visualizing the Distribution of Phenanthrene in Leaf Cuticle Using Two-Photon Confocal Scanning Laser Microscopy. *Environmental Science & Technology* **2014,** *48* (9), 4774-4781.
20. Staiger, S.; Seufert, P.; Arand, K.; Burghardt, M.; Popp, C.; Riederer, M., The permeation barrier of plant cuticles: uptake of active ingredients is limited by very long-chain aliphatic rather than cyclic wax compounds. *Pest Management Science* **2019,** *75* (12), 3405-3412.
21. Hock, B.; Elstner, E. F., *Plant Toxicology*. CRC Press: 2004.
22. Schönherr, J., Characterization of aqueous pores in plant cuticles and permeation of ionic solutes. *Journal of Experimental Botany* **2006,** *57* (11), 2471-2491.
23. Balneaves, J. M.; Gaskin, R. E.; Zabkiewicz, J. A., The effect of varying rates of glyphosate and an organosilicone surfactant on the control of gorse. *Annals of Applied Biology* **1993,** *122* (3), 531-536.
24. Zabkiewicz, J. A., Spray formulation efficacy—holistic and futuristic perspectives. *Crop Protection* **2007,** *26* (3), 312-319.
25. Schönherr, J.; Riederer, M., Foliar penetration and accumulation of organic chemicals in plant cuticles. In *Reviews of environmental contamination and toxicology*, Springer: 1989; pp 1-70.
26. Baur, P.; Buchholz, A.; Schönherr, J., Diffusion in plant cuticles as affected by temperature and size of organic solutes: similarity and diversity among species. *Plant, Cell & Environment* **1997,** *20* (8), 982-994.
27. Kerler, F.; Schönherr, J., Accumulation of lipophilic chemicals in plant cuticles: Prediction from octanol/water partition coefficients. *Archives of Environmental Contamination and Toxicology* **1988,** *17* (1), 1-6.

28. Kerstiens, G., Parameterization, comparison, and validation of models quantifying relative change of cuticular permeability with physicochemical properties of diffusants. *Journal of Experimental Botany* **2006,** *57* (11), 2525-2533.
29. Mercer, G. N., A simple diffusion model of the effect of droplet size and spread area on foliar uptake of hydrophilic compounds. *Pesticide Biochemistry and Physiology* **2007,** *88* (2), 128-133.
30. Tredenick, E. C.; Farrell, T. W.; Forster, W. A.; Psaltis, S. T. P., Nonlinear Porous Diffusion Modeling of Hydrophilic Ionic Agrochemicals in Astomatous Plant Cuticle Aqueous Pores: A Mechanistic Approach. *Frontiers in Plant Science* **2017,** *8* (746).
31. Pecha, J.; Fürst, T.; Kolomazník, K.; Friebrová, V.; Svoboda, P., Protein biostimulant foliar uptake modeling: The impact of climatic conditions. *AIChE Journal* **2012,** *58* (7), 2010-2019.
32. Tredenick, E. C.; Farrell, T. W.; Forster, W. A., Mathematical Modeling of Diffusion of a Hydrophilic Ionic Fertilizer in Plant Cuticles: Surfactant and Hygroscopic Effects. *Frontiers in Plant Science* **2018,** *9* (1888).
33. Riederer, M.; Daiß, A.; Gilbert, N.; Köhle, H., Semi-volatile organic compounds at the leaf/atmosphere interface: numerical simulation of dispersal and foliar uptake. *Journal of Experimental Botany* **2002,** *53* (375), 1815-1823.
34. Veraverbeke, E. A.; Verboven, P.; Van Oostveldt, P.; Nicolaï, B. M., Prediction of moisture loss across the cuticle of apple (Malus sylvestris subsp. mitis (Wallr.)) during storage: Part 1. Model development and determination of diffusion coefficients. *Postharvest Biology and Technology* **2003,** *30* (1), 75-88.
35. Siepmann, J.; Peppas, N. A., Higuchi equation: Derivation, applications, use and misuse. *International Journal of Pharmaceutics* **2011,** *418* (1), 6-12.
36. Ritger, P. L.; Peppas, N. A., A simple equation for description of solute release I. Fickian and non-fickian release from non-swellable devices in the form of slabs, spheres, cylinders or discs. *Journal of Controlled Release* **1987,** *5* (1), 23-36.
37. Muro Suñé, N.; Gani, R.; Bell, G.; Shirley, I., Computer-aided and predictive models for design of controlled release of pesticides. In *Computer Aided Chemical Engineering*, Barbosa-Póvoa, A.; Matos, H., Eds. Elsevier: 2004; Vol. 18, pp 301-306.
38. Roy, A.; Singh, S. K.; Bajpai, J.; Bajpai, A. K., Controlled pesticide release from biodegradable polymers. *Central European Journal of Chemistry* **2014,** *12* (4), 453-469.
39. Grassi, M.; Grassi, G., Mathematical Modelling and Controlled Drug Delivery: Matrix Systems. *Current Drug Delivery* **2005,** *2* (1), 97-116.
40. Lin, C.-C.; Metters, A. T., Hydrogels in controlled release formulations: Network design and mathematical modeling. *Advanced Drug Delivery Reviews* **2006,** *58* (12), 1379-1408.
41. Amsden, B., Solute Diffusion within Hydrogels. Mechanisms and Models. *Macromolecules* **1998,** *31* (23), 8382-8395.
42. Masaro, L.; Zhu, X. X., Physical models of diffusion for polymer solutions, gels and solids. *Progress in Polymer Science* **1999,** *24* (5), 731-775.
43. Siepmann, J.; Peppas, N. A., Modeling of drug release from delivery systems based on hydroxypropyl methylcellulose (HPMC). *Advanced Drug Delivery Reviews* **2012,** *64*, 163-174.
44. Wu, N.; Wang, L.-S.; Tan, D. C.-W.; Moochhala, S. M.; Yang, Y.-Y., Mathematical modeling and in vitro study of controlled drug release via a highly swellable and dissoluble polymer matrix: polyethylene oxide with high molecular weights. *Journal of Controlled Release* **2005,** *102* (3), 569-581.
45. Hopfenberg, H. B., Controlled Release from Erodible Slabs, Cylinders, and Spheres. In *Controlled Release Polymeric Formulations*, American Chemical Society: 1976; Vol. 33, pp 26-32.
46. Heller, J., Controlled release of biologically active compounds from bioerodible polymers. *Biomaterials* **1980,** *1* (1), 51-57.
47. Katzhendler, I.; Hoffman, A.; Goldberger, A.; Friedman, M., Modeling of Drug Release from Erodible Tablets. *Journal of Pharmaceutical Sciences* **1997,** *86* (1), 110-115.

48. Göpferich, A.; Langer, R., Modeling monomer release from bioerodible polymers. *Journal of Controlled Release* **1995,** *33* (1), 55-69.
49. Lu, S.; Fred Ramirez, W.; Anseth, K. S., Modeling and optimization of drug release from laminated polymer matrix devices. *AIChE Journal* **1998,** *44* (7), 1689-1696.
50. Lu, S.; Ramirez, W. F.; Anseth, K. S., Photopolymerized, multilaminated matrix devices with optimized nonuniform initial concentration profiles to control drug release. *Journal of Pharmaceutical Sciences* **2000,** *89* (1), 45-51.
51. Sagiv, A.; Parker, N.; Parkhi, V.; Nelson, K. D., Initial Burst Measures of Release Kinetics from Fiber Matrices. *Annals of Biomedical Engineering* **2003,** *31* (9), 1132-1140.
52. Huang, X.; Brazel, C. S., On the importance and mechanisms of burst release in matrix-controlled drug delivery systems. *Journal of Controlled Release* **2001,** *73* (2), 121-136.
53. Bhushan, B.; Jung, Y. C., Wetting, adhesion and friction of superhydrophobic and hydrophilic leaves and fabricated micro/nanopatterned surfaces. *Journal of Physics: Condensed Matter* **2008,** *20* (22), 225010.
54. Koch, K.; Bhushan, B.; Barthlott, W., Diversity of structure, morphology and wetting of plant surfaces. *Soft Matter* **2008,** *4* (10), 1943-1963.
55. Dzierżanowski, K.; Popek, R.; Gawrońska, H.; Sæbø, A.; Gawroński, S. W., Deposition of Particulate Matter of Different Size Fractions on Leaf Surfaces and in Waxes of Urban Forest Species. *International Journal of Phytoremediation* **2011,** *13* (10), 1037-1046.
56. Xu, X.; Yu, X.; Mo, L.; Xu, Y.; Bao, L.; Lun, X., Atmospheric particulate matter accumulation on trees: A comparison of boles, branches and leaves. *Journal of Cleaner Production* **2019,** *226*, 349-356.
57. Beckett, K. P.; Freer-Smith, P. H.; Taylor, G., Urban woodlands: their role in reducing the effects of particulate pollution. *Environmental Pollution* **1998,** *99* (3), 347-360.
58. Vogg, G.; Fischer, S.; Leide, J.; Emmanuel, E.; Jetter, R.; Levy, A. A.; Riederer, M., Tomato fruit cuticular waxes and their effects on transpiration barrier properties: functional characterization of a mutant deficient in a very-long-chain fatty acid β-ketoacyl-CoA synthase. *Journal of Experimental Botany* **2004,** *55* (401), 1401-1410.
59. Jetter, R.; Riederer, M., Localization of the Transpiration Barrier in the Epi- and Intracuticular Waxes of Eight Plant Species: Water Transport Resistances Are Associated with Fatty Acyl Rather Than Alicyclic Components *Plant Physiology* **2015,** *170* (2), 921-934.
60. Zeisler-Diehl, V.; Müller, Y.; Schreiber, L., Epicuticular wax on leaf cuticles does not establish the transpiration barrier, which is essentially formed by intracuticular wax. *Journal of Plant Physiology* **2018,** *227*, 66-74.
61. Fick, A., V. On liquid diffusion. *The London, Edinburgh, and Dublin Philosophical Magazine and Journal of Science* **1855,** *10* (63), 30-39.
62. Compton, R. G.; Kätelhön, E.; Laborda, E.; Ward, K. R., *Understanding voltammetry: Simulation of electrode processes*. Second ed.; World Scientific Europe: 2020.
63. Einstein, A., Über die von der molekularkinetischen Theorie der Wärme geforderte Bewegung von in ruhenden Flüssigkeiten suspendierten Teilchen. *Annalen der Physik* **1905,** *322* (8), 549-560.
64. von Smoluchowski, M., Zur kinetischen Theorie der Brownschen Molekularbewegung und der Suspensionen. *Annalen der Physik* **1906,** *326* (14), 756-780.
65. Woodside, C., Scaling analysis and dimensional analysis of simulation models. *Simulation* **1972,** *19* (2), 51-54.
66. Smith, G. D., *Numerical Solution of Partial Differential Equations: Finite Difference Methods*. Third ed.; Oxford University Press: Oxford, 1985.
67. Rudolph, M., Digital Simulations on unequally spaced grids. Part 1. Critical remarks on using the point method by discretisation on a transformed grid. *Journal of Electroanalytical Chemistry* **2002,** *529*, 97-108.

68. Gavaghan, D. J., An exponentially expanding mesh ideally suited to the fast and efficient simulation of diffusion processes at microdisc electrodes. 1. Derivation of the mesh. *Journal of Electroanalytical Chemistry* **1998,** *456* (1), 1-12.
69. Ward, K. R.; Lawrence, N. S.; Hartshorne, R. S.; Compton, R. G., Modelling the steady state voltammetry of a single spherical nanoparticle on a surface. *Journal of Electroanalytical Chemistry* **2012,** *683*, 37-42.
70. Alden, J. A.; Compton, R. G., A general method for electrochemical simulations. 1. Formulation of the strategy for two-dimensional simulations. *The Journal of Physical Chemistry B* **1997,** *101* (44), 8941-8954.
71. Gavaghan, D. J.; Rollett, J. S., Correction of boundary singularities in numerical simulation of time-dependent diffusion processes at unshielded disc electrodes. *Journal of Electroanalytical Chemistry and Interfacial Electrochemistry* **1990,** *295* (1), 1-14.
72. Peaceman, D. W.; Rachford, J., H. H. , The Numerical Solution of Parabolic and Elliptic Differential Equations. *Journal of the Society for Industrial and Applied Mathematics* **1955,** *3* (1), 28-41.
73. Kätelhön, E.; Compton, R. G., Testing and validating electroanalytical simulations. *Analyst* **2015,** *140* (8), 2592-2598.
74. Aoki, K., Several Derivations for I = 4Fc*Da. *Review of Polarography* **2017,** *63* (1), 21-28.
75. Shoup, D.; Szabo, A., Chronoamperometric current at finite disk electrodes. *Journal of Electroanalytical Chemistry and Interfacial Electrochemistry* **1982,** *140* (2), 237-245.
76. Crank, J., *The Mathematics of Diffusion*. Clarendon Press: 1979.
77. Bobbert, P. A.; Wind, M. M.; Vlieger, J., Diffusion to a slowly growing truncated sphere on a substrate. *Physica A: Statistical Mechanics and its Applications* **1987,** *141* (1), 58-72.
78. Streeter, I.; Compton, R. G., Diffusion-Limited Currents to Nanoparticles of Various Shapes Supported on an Electrode; Spheres, Hemispheres, and Distorted Spheres and Hemispheres. *The Journal of Physical Chemistry C* **2007,** *111* (49), 18049-18054.
79. Hazra, D. K.; Karmakar, R.; Poi, R.; Bhattacharya, S.; Mondal, S., Recent advances in pesticide formulations for eco-friendly and sustainable vegetable pest management: A review. *Archives of Agriculture and Environmental Science* **2017,** *2* (3), 232-237.
80. Esser-Kahn, A. P.; Odom, S. A.; Sottos, N. R.; White, S. R.; Moore, J. S., Triggered Release from Polymer Capsules. *Macromolecules* **2011,** *44* (14), 5539-5553.
81. Aoki, K.; Osteryoung, J., Diffusion-controlled current at the stationary finite disk electrode: Theory. *Journal of Electroanalytical Chemistry* **1981,** *122* (C), 19--35.
82. Magasitz, E.; Lakatos, Á.; Dombay, Z., Effect of particle size distribution on the stability of pesticide suspensions. *Periodica Polytechnica Chemical Engineering* **1984,** *28* (3-4), 281-292.
83. Zhao, X.; Cui, H.; Wang, Y.; Sun, C.; Cui, B.; Zeng, Z., Development Strategies and Prospects of Nano-based Smart Pesticide Formulation. *Journal of Agricultural and Food Chemistry* **2018,** *66* (26), 6504-6512.
84. Jeffree, C. E., Structure and ontogeny of plant cuticles. In *Plant Cuticles*, Kerstiens, G., Ed. BIOS Scientific Publishers: Oxford, 1996; pp 33-82.
85. Li, H.; Sheng, G.; Chiou, C. T.; Xu, O., Relation of Organic Contaminant Equilibrium Sorption and Kinetic Uptake in Plants. *Environmental Science & Technology* **2005,** *39* (13), 4864-4870.
86. Nzengung, V. A.; Jeffers, P., Sequestration, Phytoreduction, and Phytooxidation of Halogenated Organic Chemicals by Aquatic and Terrestrial Plants. *International Journal of Phytoremediation* **2001,** *3* (1), 13-40.
87. Liu, Z., Confocal laser scanning microscopy – an attractive tool for studying the uptake of xenobiotics into plant foliage. *Journal of Microscopy* **2004,** *213* (2), 87-93.
88. Trapp, S., Plant uptake and transport models for neutral and ionic chemicals. *Environmental Science and Pollution Research* **2004,** *11* (1), 33-39.
89. Sharp, D. S.; Eskenazi, B.; Harrison, R.; Callas, P.; Smith, A. H., Delayed health hazards of pesticide exposure. *Annual Review of Public Health* **1986,** *7* (1), 441-471.

90. Schönherr, J.; Baur, P., Modelling penetration of plant cuticles by crop protection agents and effects of adjuvants on their rates of penetration. *Pesticide Science* **1994,** *42* (3), 185-208.
91. Zhang, Y.; Lorsbach, B. A.; Castetter, S.; Lambert, W. T.; Kister, J.; Wang, N. X.; Klittich, C. J. R.; Roth, J.; Sparks, T. C.; Loso, M. R., Physicochemical property guidelines for modern agrochemicals. *Pest Management Science* **2018,** *74* (9), 1979-1991.
92. Ramsey, R. J. L.; Stephenson, G. R.; Hall, J. C., A review of the effects of humidity, humectants, and surfactant composition on the absorption and efficacy of highly water-soluble herbicides. *Pesticide Biochemistry and Physiology* **2005,** *82* (2), 162-175.
93. Matsumoto, S.; Suzuki, S.; Tomita, H.; Shigematsu, T., Effect of humectants on pesticide uptake through plant leaf surfaces. In *Adjuvants for Agrichemicals*, CRC Press: 2018; pp 261-271.
94. Tredenick, E. C.; Farrell, T. W.; Forster, W. A., Mathematical Modelling of Hydrophilic Ionic Fertiliser Diffusion in Plant Cuticles: Lipophilic Surfactant Effects. *Plants* **2019,** *8* (7), 202.
95. Yu, Y.; Zhu, H.; Frantz, J. M.; Reding, M. E.; Chan, K. C.; Ozkan, H. E., Evaporation and coverage area of pesticide droplets on hairy and waxy leaves. *Biosystems Engineering* **2009,** *104* (3), 324-334.
96. Li, H.; Travlos, I.; Qi, L.; Kanatas, P.; Wang, P., Optimization of Herbicide Use: Study on Spreading and Evaporation Characteristics of Glyphosate-Organic Silicone Mixture Droplets on Weed Leaves. *Agronomy* **2019,** *9* (9), 547.
97. Veraverbeke, E. A.; Verboven, P.; Van Oostveldt, P.; Nicolaï, B. M., Prediction of moisture loss across the cuticle of apple (Malus sylvestris subsp. mitis (Wallr.)) during storage: Part 2. Model simulations and practical applications. *Postharvest Biology and Technology* **2003,** *30* (1), 89-97.
98. Satchivi, N. M.; Stoller, E. W.; Wax, L. M.; Briskin, D. P., A Nonlinear Dynamic Simulation Model for Xenobiotic Transport and Whole Plant Allocation Following Foliar Application. I. Conceptual Foundation for Model Development. *Pesticide Biochemistry and Physiology* **2000,** *68* (2), 67-84.
99. Rein, A.; Legind, C. N.; Trapp, S., New concepts for dynamic plant uptake models. *SAR and QSAR in Environmental Research* **2011,** *22* (1-2), 191-215.
100. Grafahrend-Belau, E.; Junker, A.; Eschenröder, A.; Müller, J.; Schreiber, F.; Junker, B. H., Multiscale Metabolic Modeling: Dynamic Flux Balance Analysis on a Whole-Plant Scale *Plant Physiology* **2013,** *163* (2), 637-647.

6 Foliar uptake: experiment and modelling

In this chapter we present experimental results for the uptake of an agronomically relevant, lipophilic fungicide into the cuticle compartment of living maize when applied as droplets of a simple, non-adjuvant, suspension concentrate (SC) formulation and the behaviour of those deposits after dry-down. Using information inferred here, in Chapter 5, and in literature, we present a model for the uptake behaviour. By applying this model to our experimental data, we predict values for the diffusion coefficient within the cuticle and the inferred cuticle-water partition coefficient and compare these values to literature. Two limiting kinetic uptake regimes are identified for short and long times and are corroborated by the model. We discuss what can be inferred from this case study and discuss the generalisability of this model for the uptake of lipophilic particulate residues within a 'cuticle reservoir' approximation. The work presented in this chapter closely follows work that has been published in ACS Agricultural Science & Technology[1].

6.1 Introduction

Understanding the uptake of lipophilic pesticides into the cuticles of agronomically significant plant species is of vital importance from the perspectives of agrochemical efficiency[2-4], environmentalism[5-8] and toxicology[8-11], including risk assessment and food quality. The lipidic cuticle is the plant's primary barrier against the uptake of potentially hazardous material, including pesticides[3, 4, 12, 13]. Not only does it sequester lipophilic material[14], and thus can reduce uptake into the underlying tissue, but it also acts as a diffusional barrier[3], slowing the mass transport. Agrochemicals, especially pesticides, are frequently applied as water-based foliar sprays[15], and thus must interact with the cuticle prior to their function. Understanding the behaviour of lipophilic material in and on the cuticle facilitates the design of these products for efficiency and safety. Generally, rapid and

effective uptake into the cuticle is preferred, either as a precursor to transport into the plant tissue[3] (e.g. systemic herbicides) or to enhance the pest resistance of the cuticle itself (e.g. certain fungicides and insecticides). Rapid uptake from the leaf surface may also help to mitigate loss processes from the leaf surface, such as washing off by rain which also adds to the environmentally damaging effects of pesticide runoff[8, 16]. Additionally, cuticular uptake is vital for modelling the movement and accumulation of pesticides and other pollutants in the biosphere[9-11, 14, 17-20] and thus assessing their threat to humans[9-11] or to the environment[14], such as through crop consumption.

Developing effective models for the interaction of pesticide residues with plant cuticles[21-26] provides insight into how future formulations can be tuned to demonstrate desired behaviour[2, 27], such as reduced risk profiles and greater food quality and yield, as well as identifying and explaining the observed behaviours of formulations used today. In particular, further work is required for modelling the behaviour of particulate- and suspension-based formulations on cuticle surfaces, as these represent significant potential for delivery control, ease of use and safety for the user and environment[15, 28-30].

For this purpose, this chapter builds upon work presented in Chapter 5. The work presented in each of these chapters has been published in ACS Agricultural Science & Technology[1, 31]. While in Chapter 5 we have focussed on the interaction between individual particles and the uppermost layer of the cuticle, the ‘cuticle proper’, in this chapter we consider the interaction between a droplet of suspended particles and the cuticle whole for a specific case study, based on inferences from Chapter 5 as applied to understanding experimental results.

We first describe the methods used to acquire data on the foliar uptake rate of a relevant fungicide in simple, non-adjuvant suspension concentrate formulation and the microscopy used to characterise the surface and evaporated deposit. We present relevant results and their

analysis. We then consider theory underlying the simplest viable model for explaining these results, present the dimensionless simulation results it predicts and consider what predictions are made when applying the model to the experimental data. We finally discuss the generalisability of the model and the parameters required for its use.

6.2 Experimental methods

In this section, we describe the methods that were used to gather data on the rate of uptake of fungicide from droplets of simple, non-adjuvant formulation on the leaf surface. We also describe the microscopy techniques that were used to acquire images of the resulting deposits after evaporation to dry residue. The analysis techniques employed on these data are also described here.

6.2.1 Uptake study

Experiments to kinetically monitor the uptake of lipophilic fungicide were made by applying aqueous micro-droplets containing known concentrations of fungicide to the leaves of two varieties of living maize plants.

Stock fungicidal formulation was acquired from Syngenta Ltd as non-adjuvant suspension concentrate (SC). The formulation was chosen to minimise additive effects that might influence the uptake, such as adjuvancy, and thus complicate our analysis and modelling.

Coxximo and Farmfire maize (Syngenta) were grown under ideal greenhouse conditions of 24 °C (day) and 18 °C (night) with ~15 daylight hours and 55% humidity. 24 hours before application of fungicide, they were transferred to a *Weiss Gallenkamp Fitotron CE* growth room, where prior conditions were maintained but at 70% humidity. 600 lumen light substituted daylight. Plant positions were randomised after transfer and before droplet application to mitigate inhomogeneity in the growth conditions.

20 $0.2\,\mu L$ droplets were applied in a regular array to the leaf surface as approximate hemispheres of $460\,\mu m$ radius. The droplets were applied to the adaxial surface halfway along the 2nd oldest leaf at the plant age of 9 days old. The SC formulation was diluted to $375\,ppm$ using 90:10 v/v water/isopropyl alcohol. Droplets were applied with $\geq 3\,mm$ separation to ensure diffusional independence in the leaf, as discussed below. A *Sartorius Picus Biohit Single-Channel* Electronic pipette was used.

To monitor the transfer of fungicide from the leaf surface into the leaf cuticle, the fungicide within each of these two compartments – surface and cuticle - was extracted after an exposure time. Each exposure timepoint refers to the time between application and extraction. 2 batches of 3 repeats were used for each timepoint and the batch order was randomised. The time taken for the droplets to evaporate to dryness was also noted.

For extracting from the leaf surface, the whole leaf was washed for 20 seconds with $5\,mL$ of 80:20 water/acetonitrile. For extracting from within the leaf, the leaf was dried, macerated with $5\,mL$ of 20:80 water/acetonitrile ($2 \times 20\,s$ at $6000\,RPM$ using *Precellys Lysing* tube *CK28* and *Precellys Evolution* homogeniser), and centrifuged (15 minutes at $4000\,RPM$ using *Heraeus Multifuge 3C*). $1\,mL$ subsamples were taken. Quantitation of the fungicide in a subsample was performed by calibrated LC-MS using *Vanquish LC* system feeding into *ThermoFisher Q-Exactive UHMR*.

Preliminary experiments involved washing with heptane after the surface wash to differentiate fungicide within the cuticle from fungicide within the subcuticular tissue, but this was observed to not provide statistically valuable quantitative information, as shall be described in the Experimental results section.

Statistical analysis involved ANOVA testing[32] followed by post-hoc Tukey testing and calculation of covariance and Pearson and Spearman correlation coefficients; this analysis

was performed in *Python* using the *numpy*, *scipy* and *statsmodels* packages with the *matplotlib* package for plotting.

6.2.2 Microscopy

Imaging was used to characterise the distribution of solid material remaining on the leaf surface following complete evaporation of water from the droplet arrays (described above) as well as the leaf surface structure itself.

Two techniques were applied: reflected light microscopy (RLM) using *Zeiss Axio Zoom. V16* and *Zeiss ZEN* software and cryogenic scanning electron microscopy (cryo-SEM) whose preparation procedure is described below. All leaves for both techniques were imaged 1 hour after droplet application.

To perform the cryo-SEM, ca. $1\,cm \times 1\,cm$ sections were mounted on a *Quorum* specimen shuttle using *Tissue-Tek* O.C.T. compound. The sample was plunge-cooled in a liquid nitrogen slush before transfer to the *Quorum PP3010T* preparation chamber. The specimen holder was located onto the nitrogen gas-cooled sample stage maintained under vacuum at -120 °C. The sample was sublimated at -90 °C for 3 mins prior to coating with gold/palladium for 60 seconds with a current of 5 mA and a temperature of -120 °C. The specimen shuttle was transferred to the *Hitachi SU8220* Field Emission Scanning Electron Microscope (FESEM), and the sample was maintained at a temperature of -160 °C. The image acquisition using cryo-SEM was performed by Dr Giovambattista Depietra, a collaborator and co-author on the submitted manuscript sent for publication.

The open-source *Fiji* package[33] for *ImageJ2*[34] was used for image analysis. Semi-automated segmentation of cryo-SEM images using *Trainable Weka Segmentation*[35] was trained by manual segmentation of a representative image into four classes: cuticle above palisade cell,

cuticle above cuticular peg, damaged cuticle, and fungicide particle. The classifier consisted of a random forest of 200 trees using mean and bilateral filters. Definitions of the palisade cell and cuticular peg are given in Section 6.3.1 and an example of an image classified by this method is given in Figure 6.6.

6.3 Experimental Results

In the following we first present results for the characterization of the adaxial Coxximo variety maize leaf surface using the cryo-SEM technique described above. We then discuss the results of observations of the evaporation times of the fungicidal droplets on this surface, followed by characterization of the resultant deposition of solid material by RLM and cryo-SEM, using the methods described above. These data are essential for the interpretation of the uptake kinetics and the development of suitable models, both of which are considered below.

6.3.1 Characterisation of leaf surface by microscopy

Characterisation of the leaf surface, performed by cryo-SEM and subsequent image analysis, is essential for informing the surface topology through which uptake occurs. The leaf surface of Coxximo maize was differentiated into pavement and stomatal cells only, with cuticular pegs evident between these cells. No trichomes were observed. Epicuticular wax crystals were observed across the entire surface. Figure 6.1 demonstrates the leaf structure as observed by cryo-SEM.

Pavement cells provide protection for the more specialised cells beneath them and spacing between the stomata. We observe that the cuticle above pavement cells makes up the majority of the leaf's surface area[36] and is thus the predominant barrier to astomatous lipophilic uptake[12, 37, 38]. The pavement cells were approximately rectangular with rounded vertices, major axes parallel to the leaf's major vein, waviness in the shape outline and a mean axis length ratio of 3. The cells were approximately organised into rows of alternating phase.

Stomatal cells are specialised epidermal cells ubiquitous to plants which control the exchange of gas and water vapor between the environment and the leaf's porous interior through the opening and closing of stomatal pores[36]. They introduce surface inhomogeneity and potentially provide a stomatal uptake route for low-surface-tension mixtures[39-41]. The stomatal complexes were observable by the two guard cells at the surface. All stomata observed by cryo-SEM were closed. The complexes were generally aligned with the pavement cell rows and shared the same width. The stomata were generally separated by one pavement cell only. The rows that contained stomata were randomly distributed but non-clustered.

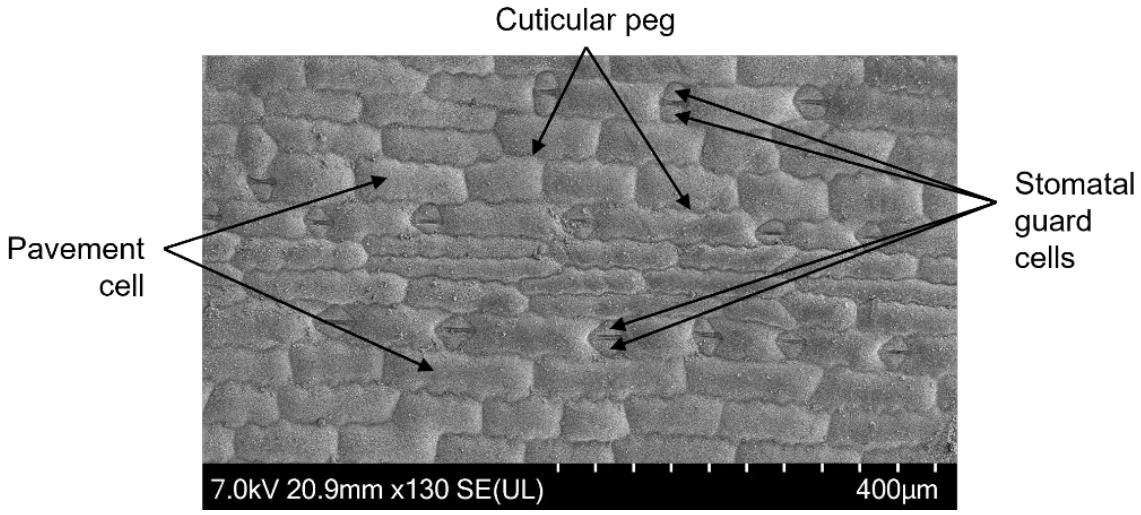


Figure 6.1: Cryo-SEM image of the interior of a dried deposit illustrating the cuticle above a leaf structure consisting of rows of pavement cells, stomatal complexes and cuticular pegs. Image magnification was 130×. A scale bar of 400 μm is included at the bottom of the image.

The cuticular peg between all epidermal cells can be observed by its deformation of the cuticular topography into a slight trough. The width of the trough indicates the peg's width at the leaf's surface and may be used in approximating the cuticular peg volume. This deformation allows differentiation of the cells below the cuticle[36]. The cuticular peg represents a region of greater cuticular depth and roughness of the internal cuticle-cell interface[42].

The epicuticular waxes provide a barrier to surface wetting and reduce direct contact between solid particles and the cuticle. Epicuticular wax crystals were observed as plate-like

fragments and needles with their major axes perpendicular to the underlying smooth wax surface. The exposed lengths of each were $1\,\mu m$ and their thicknesses were $0.05\,\mu m$. An example image of these epicuticular wax crystals is presented in Figure 6.2.

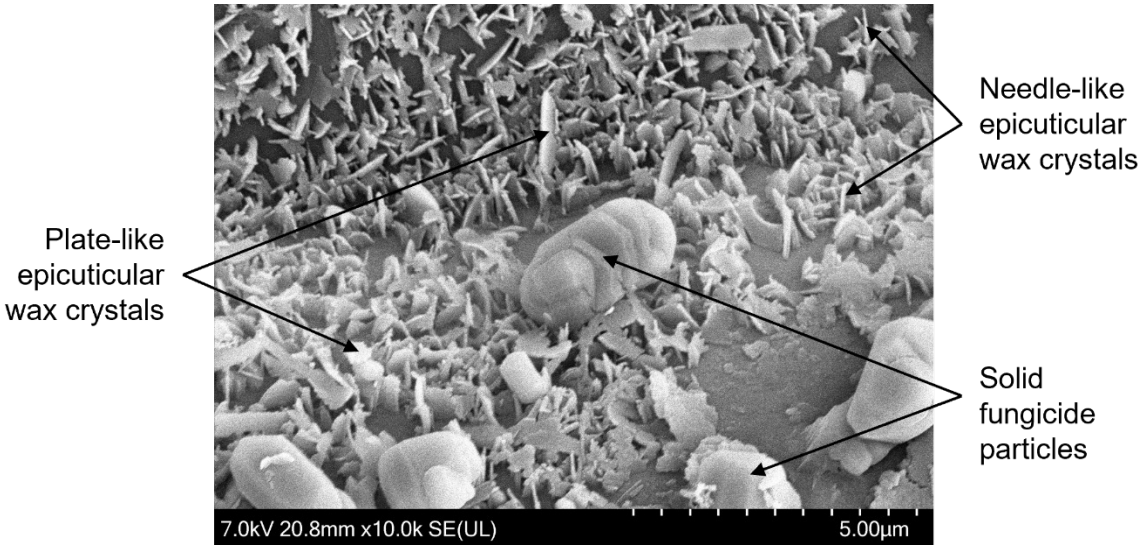


Figure 6.2: Cryo-SEM image of solid fungicide particles on cuticle near a cuticular peg induced surface trough. This illustrates the size and shape of the epicuticular crystals relative to the size and shape of the fungicide particles and their effect on the contact with the underlying smooth cuticle. Image magnification was 10,000x. A scale bar of 5 μm has been included at the bottom of the image.

Quantitative details for the leaf characterisation are provided in Table 6.1 as average values and standard errors extracted from cryo-SEM images.

Table 6.1: Leaf surface properties extracted from scanning electron microscopy images for 0.2 μL 375 ppm droplet deposit on Coxximo via semi-automated ML segmentation. Results are given as averages with standard errors.

Cuticular peg width at outer surface (μm)	Pavement cell length (μm)	Pavement cell width (μm)	Stomatal complex length (μm)	Stomatal complex width (μm)
4.0 ± 2.7	124 ± 6	42 ± 3	30.5 ± 0.97	42 ± 1.4

6.3.2 Droplet evaporation

Visual observation of the evaporation of the fungicidal droplets was performed to measure the window of time in which the formulation's aqueous phase is present on the surface after application. The aqueous phase contributes to the uptake by offering an indirect pathway via dissolution and aqueous transport. The evaporation of the droplet induces convective flow which mixes any dissolved material and directs the deposition of solid material.

The evaporation times of 5 arrays of 20 $0.2\mu L$ droplets containing fungicide on living Coxximo leaves, with $\geq 3\,mm$ separation, were recorded. Droplet evaporation to dryness occurred, on average, 652 ± 3 seconds (10.9 ± 0.05 minutes) after application. For each droplet, a ring of deposited solid was visible by eye after complete evaporation, with a predominance of material at the edge of the droplet's contact area. Microcrystals of fungicide were randomly deposited within the interior area. Figure 6.3 demonstrates representative RLM images at 40× and 150× magnifications. The ring shape of the deposit is visible as is the presence of microcrystals within the interior. The significance of the ring shape of the deposit after evaporation is discussed further in the following section.

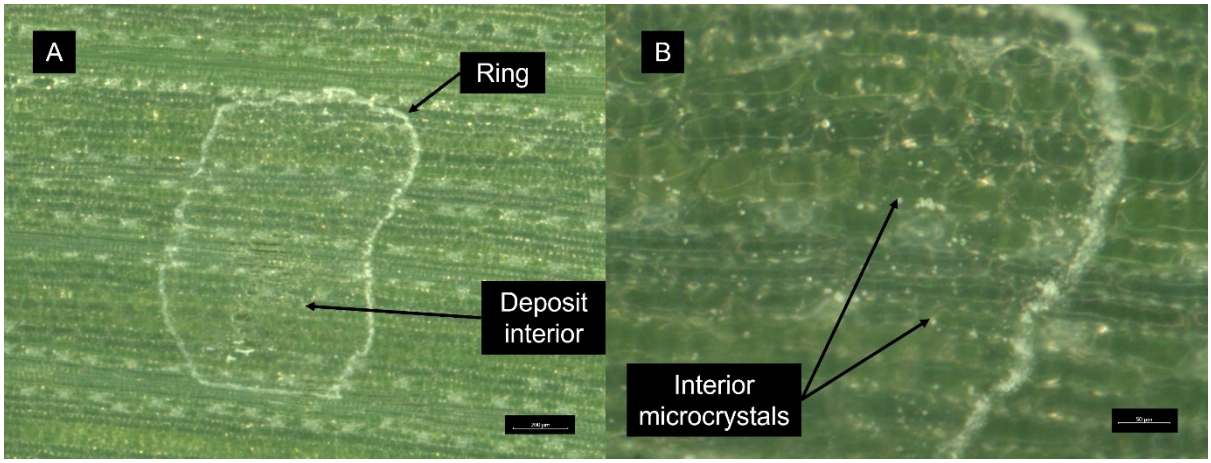


Figure 6.3: Annotated Reflected Light Microscopy images of dried deposits one hour after application. Image A is at 40× magnification and image B is at 150× magnification. Scale bars are in the lower right of each image ($200\,\mu m$ for A and $50\,\mu m$ for B). Image B shows the presence of microcrystals within the ring's interior though at greater sparsity than within the ring itself.

6.3.3 Characterisation of deposit by microscopy

The deposition of solid material after droplet drying indicated incomplete fungicide uptake prior to drying and the deposit's characterisation by microscopy informs the uptake modelling, the physical processes that occur during evaporation, and the fungicide's behaviour after drying.

The deposit was characterised using RLM, where the deposit area was identified by its contrasting whiteness and high reflectivity, and cryo-SEM imaging, where the ring was seen as a greater surface concentration of particles and additive film with a relative sparsity of particles in the shape's interior.

Through manual segmentation of RLM images into deposit exterior, ring and deposit interior, averages for the size and shape of the overall deposit and ring thickness were measured and are provided in Table 6.2 alongside standard errors.

Table 6.2: Properties extracted from optical microscopy images for 0.2 μL 375 ppm droplet deposits on Coxximo via manual segmentation. Results are given as averages with standard errors.

Total deposit area (mm^2)	Interior deposit area $(m\,m^2)$	Deposit aspect ratio	Deposit Circularity	Deposit Roundness	Deposit Solidity	Average ring thickness (μm)
0.64 ± 0.06	0.54 ± 0.06	1.40 ± 0.05	0.55 ± 0.06	0.72 ± 0.02	0.91 ± 0.02	32 ± 2

An example of the segmentation and analysis of the ring and deposit interior from an RLM image is provided in Figure 6.4. We tested several methods for measuring the ring's thickness from RLM images after manual segmentation into ring, deposit interior and deposit exterior. The radial thickness was measured relative to the centroid of the deposit to give a radial thickness distribution across the range $0 \leq \theta < 2\pi$. The histogram of the local thickness

heatmap of the mask of the ring segment gives the distribution of the local thickness across the whole ring area. However, it over-represents the large local thickness regions (greater local thickness results in more pixels within that area) and so the number of pixels in each bin was normalised against the local thickness value of that bin to measure the distribution of the local thickness around the deposit perimeter. The distance-to-nearest-edge heatmap was generated for the mask of the ring segment. A midline around the ring was generated following the maximum cusp of the distance-to-nearest-edge heatmap. The distribution along this midline of local thickness and double-distance-to-nearest-edge (which equals the edge-to-edge distance at the maximum) provides alternative measures of the ring thickness around the deposit perimeter. Example results are presented in Figure 6.5.

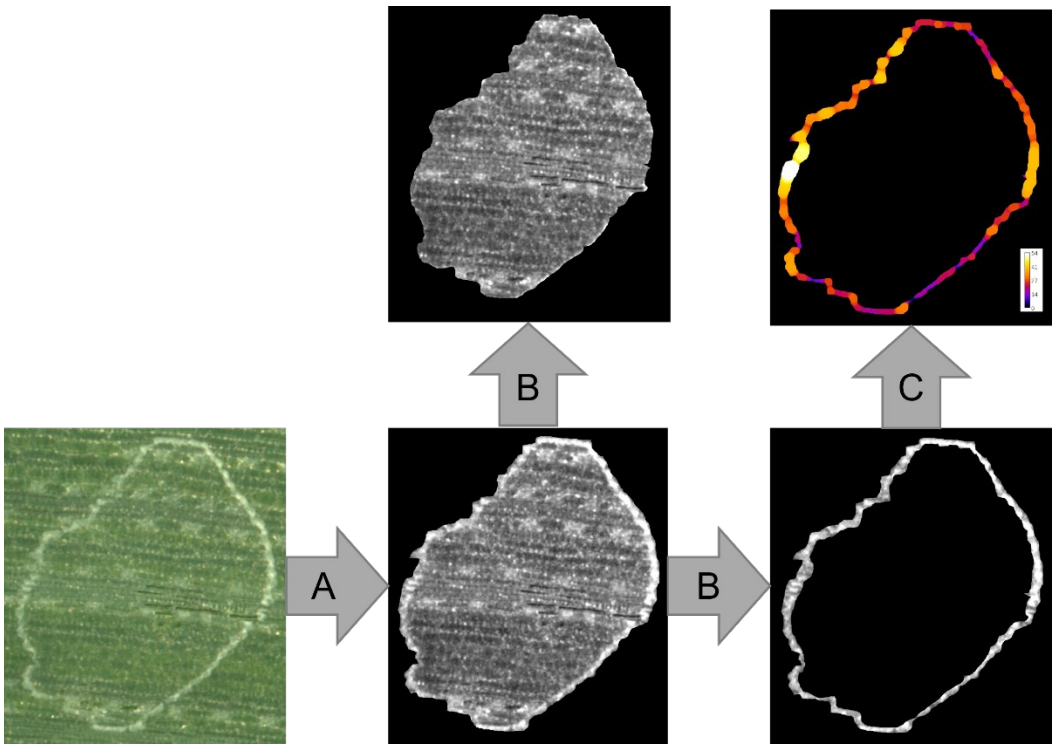


Figure 6.4: Illustration of the analysis workflow of RLM images at 40× magnification for extraction of data related to size and shape of deposits. Step A applies blue filter and manual segmentation of deposits from leaf background. Step B involves the manual segmentation of the deposit interior from the ring. Step C involves the conversion of the ring segmentation to a mask and the calculation of the local thickness map from which a histogram is derived for the calculation of the ring thickness distribution around the deposit perimeter. A colour scale is included.

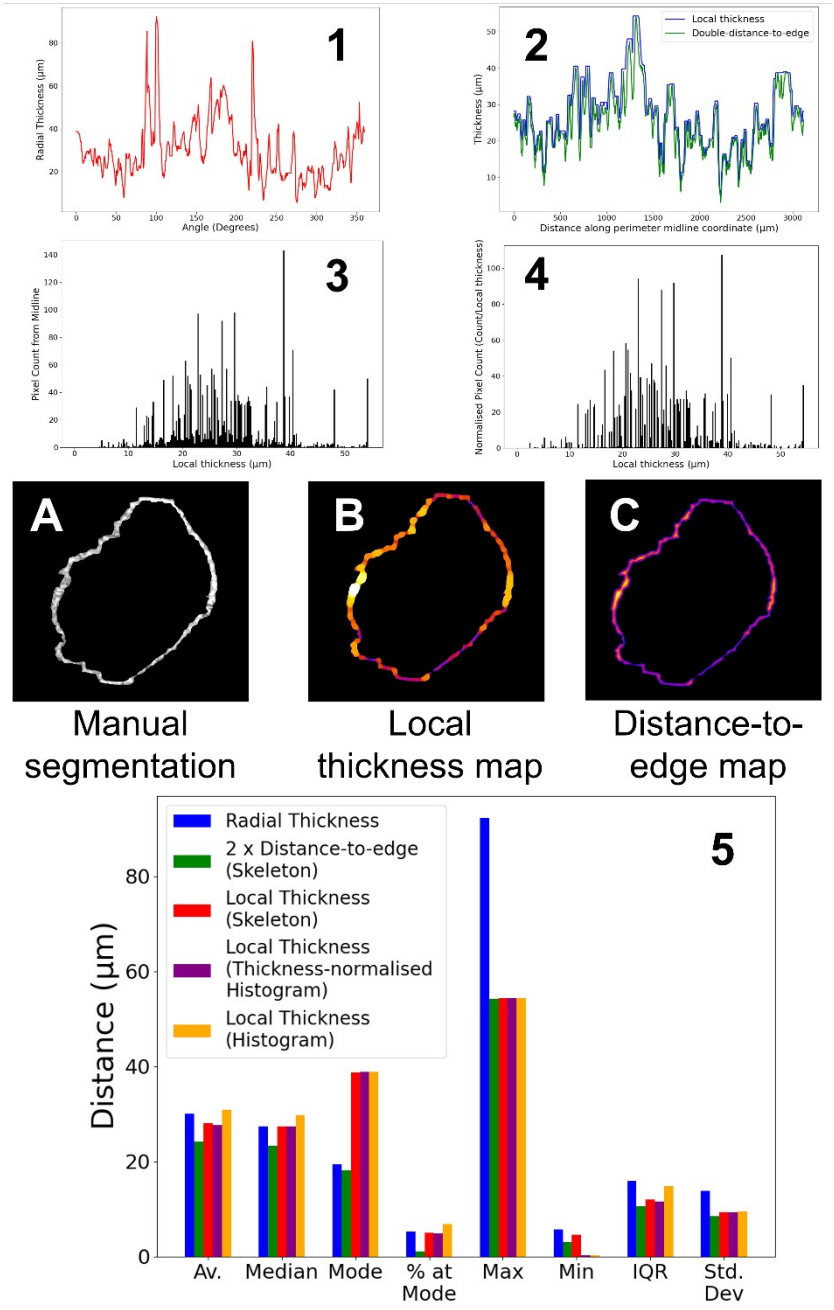


Figure 6.5: Image A is the manually segmented ring of a 40× magnification optical microscopy image of a $375\ ppm$ 10 % IPA $0.2\ \mu L$ deposit on a Coxximo leaf. Image B is the local thickness heat-map of the ring. Image C is the distance-to-nearest-edge heat-map of the ring. Plot 1 is the radial thickness profile from the deposit's centroid. The distance-to-nearest-edge map is used to manually generate a midline. Plot 2 is the profile of local thickness (blue) and double-distance-to-nearest-edge along the midline coordinate. Plot 3 is the histogram of local thickness of pixels on this midline. Plot 4 is the histogram of local thickness of all pixels in the heat-map normalised against the thickness. Plot 5 are the statistics of the thickness distributions produced by these methods: radial thickness is blue, double-distance-to-nearest-edge along the midline is green, local thickness along midline is red, local thickness histogram normalised against the local thickness is purple, and non-normalised local thickness histogram is orange.

The radial thickness measurement overestimates the thickness due to its high sensitivity to the non-circularity of the deposit's ring; this results in larger values of the average, median, maximum, minimum, IQR and standard deviation, and is discarded as a viable measurement.

The local thickness histogram similarly overestimates the ring's thickness distribution as it considers the local thickness distribution across the ring area instead of its perimeter, resulting in overestimates of the average, median and IQR values. This measurement is less valuable and thus discarded.

The average, median and standard deviation values of the distributions of the double-distance-to-edge along midline skeleton, local thickness along midline skeleton and normalised local thickness histogram are generally in close agreement with each other. The double-distance-to-edge distribution has a larger maximum, smaller mode, and smaller % of distribution at the mode value. These three measurements are each viable. We use the normalised local thickness histogram value as it avoids the generation of the midline, which is an additional source of error and increases the characterisation time.

The average total deposit area (including interior) was $0.64 \pm 0.06\, mm^2$ and 16% of that was constituted by the deposited ring, whose thickness distribution had a mean of $32 \pm 2\, \mu m$ (averaged over observations). The high average solidity and roundness imply that an approximation of the deposit as circular may be suitable for modelling.

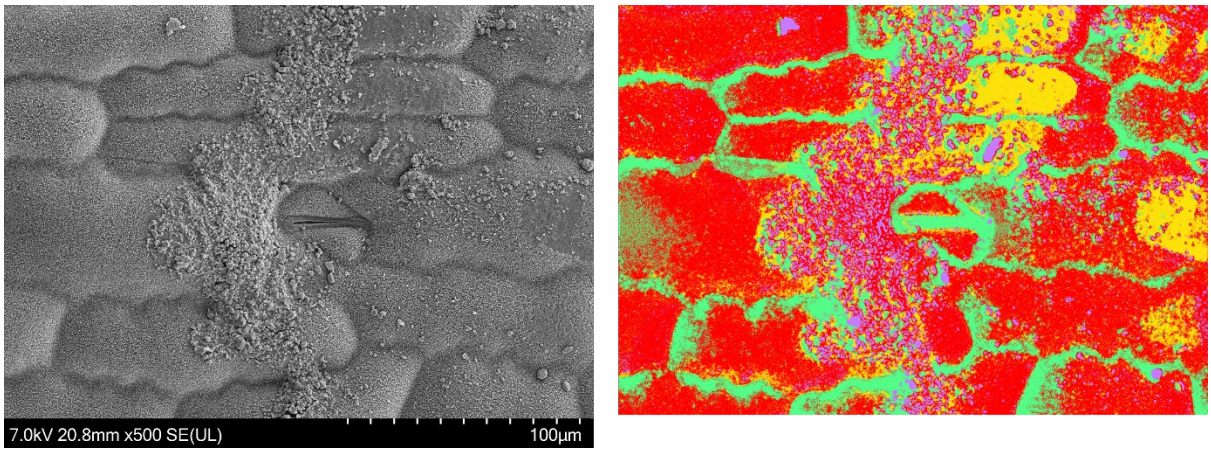


Figure 6.6: Example of semi-automated segmentation of a SEM image at 500× magnification. The 4 classes we segment into are cuticle above palisade cell (red), cuticle above cuticular peg (green), damaged cuticle (yellow) and solid particle (purple).

The greater resolution of cryo-SEM allowed characterisation of the solid fungicide particles themselves. Semi-automated segmentation using the *Trainable Weka Segmentation* plug-in[35] for *Fiji*[33, 34] classified images into 4 classes: cuticle above palisade cell, cuticle above cuticular peg, damaged cuticle and solid particle, an example of which is shown in Figure 6.6.

Table 6.3: Deposited particle properties extracted from scanning electron microscopy images for 0.2 μL 375 ppm droplet deposit on Coxximo via semi-automated ML segmentation. Results are given as averages with standard errors.

Projected area per particle in interior region $\left(\mu m^2\right)$	Particle minor axis length in interior region $\left(\mu m\right)$	Particle volume for particles in interior region $\left(\mu m^3\right)$	Particle aspect ratio
1.93 ± 0.03	1.44 ± 0.01	2.30 ± 0.04	1.8 ± 0.2
Inferred particle density in interior region $\left(\mu g\, cm^{-2}\right)$	Inferred particle density in ring $\left(\mu g\, cm^{-2}\right)$	Leaf area per particle in the interior region $\left(\mu m^2\right)$	Interparticle separation in the interior region $\left(\mu m\right)$
1.2 ± 0.03	58.4 ± 7.1	295 ± 8	17.2 ± 0.5

Table 6.3 contains values that were calculated rather than directly measured from the images. The volumes of particles in the interior region were calculated by approximating the particles as ellipsoids on a flat surface and using the measured values for the particles' projected area, A_{proj}, and minor axis length, x_{minor}, in the following equation:

$$V\left(\mu m^3\right) = \frac{4}{3} A_{proj} \times \frac{x_{minor}}{2} \qquad \text{Equation 6.1}$$

The inferred particle density in the interior region, $\Gamma_{particle}^{interior}$, was calculated from the particle volume, the density of solid fungicide $\left(\rho = 1.5 g/cm^3\right)$, and the number of particles observed in a representative area, N_{rep}, of size, A_{rep}:

$$\Gamma_{particle}^{interior}\left(\mu g\, cm^{-2}\right)=\frac{\rho \times N_{rep} \times V}{A_{rep}}$$ Equation 6.2

From this, the total mass of particles in the interior (measured area of $A^{interior}$) was calculated:

$$M^{interior}=\Gamma_{particle}^{interior} \times A^{interior}$$ Equation 6.3

The particle density in the coffee ring, $\Gamma_{particle}^{ring}$ was then calculated by comparison to the total mass measured on the surface from the uptake studies (presented below), $M^{surface}$, and the average area of the deposit constituting the coffee ring, A^{ring}:

$$\Gamma_{particle}^{ring}=\frac{M^{ring}}{A^{ring}}=\frac{M^{surface}-M^{interior}}{A^{ring}}$$ Equation 6.4

Calculation of the particle volumes and thus density in the coffee ring by direct measurement of the particles' projected area and minor axis lengths in that region was not performed due to the stacking of particles complicating the semi-automated segmentation of individual particles and invalidating the approximation of particles as ellipsoids on a *flat* surface.

A particle density of $1.2 \pm 0.03\, \mu g\, cm^{-2}$ in the interior of the deposit was estimated from the mean particle volume of $2.3\, \mu m^3$, the density of solid fungicide of $1.5\, g/cm^3$ (calculated from the relative density and weight fraction of the formulation and corroborated by literature[43]), and the number of particles observed in a representative area of the deposit interior. The average area of the deposit interior of $0.54 \pm 0.06\, mm^2$ (presented in Table 6.2) was used to infer the total mass of particles in the deposit interior, from which a particle density of $58.4 \pm 7.1\, \mu g\, cm^{-2}$ within the ring was calculated using the total mass expected on the surface derived from the uptake kinetics study (presented below). An interparticle separation of $17.2 \pm 0.5\, \mu m$ in the interior region was measured. We calculate that $90\,\%$ of the deposit material by mass is in the ring after drying. Direct inference of the particle volumes and thus

density in the coffee ring region from the images was not performed due to the stacking of particles complicating the segmentation, alongside the inaccuracy of approximating these particles as on a flat surface when calculating their individual volumes.

The observation of deposits forming rings of high particle density in the microscopy images provide evidence for a significant coffee-ring effect[44-47] during droplet drying. This is commonly seen for colloidal suspensions during drying whereby fluid evaporation induces flow towards the droplet edge, preferentially depositing suspended particles at the triple-interface point, leading to the formation of a “coffee ring”. Surface heterogeneity also results in pinning of the droplet radius, leading to predominant Constant Contact Radius (CCR) drying[46, 47] when the coffee-ring effect is active; this was seen during our observations of the droplet evaporation. The dimensions of the coffee ring thus evidence the size and shape of the droplet-cuticle contact during CCR drying. We thus infer significant convection within the droplet during drying and a predominantly constant contact area. The effect of the convection is expected to cause homogenisation of the concentration of dissolved fungicide within the droplets, permitting helpful simplification in the modelling of the kinetics of uptake, the experimental measurements of which we next turn to.

6.3.4 Uptake data & analysis

Measurement of the transfer of fungicide from the surface into the leaf via uptake was undertaken for developing and fitting a kinetic model for the uptake. By measuring the mass of material within different leaf ‘compartments’ over time after application of fungicide as a droplet array, as described in the Experimental methods section (Section 6.2), experimental data is obtained to inform model design and fit simulation.

First, the uptake behaviour of the fungicide within the 24 hours after droplet application was assessed. The study consisted of three sampling processes as described in the Experimental

methods section: a leaf surface wash (LW) involving washing the surface of the treated leaf with 80:20 water/acetonitrile, a leaf surface wash with heptane (HW), and an extraction from the remaining leaf (Ext) after maceration and centrifugation with 20:80 water/acetonitrile. Two varieties of maize were studied – Farmfire and Coxximo – in order to assess the generality of the uptake results. Figure 6.7 presents the results as percentages of the total mass recovered for a given plant for each sampling process. The percentage recovery from sample i is defined as m_i/m_{Tot}, where m_i is the mass of material recovered from sample i and m_{Tot} is the total mass recovered from all samples of the plant. Results for the masses contained in each sample are presented in Figure 6.8.

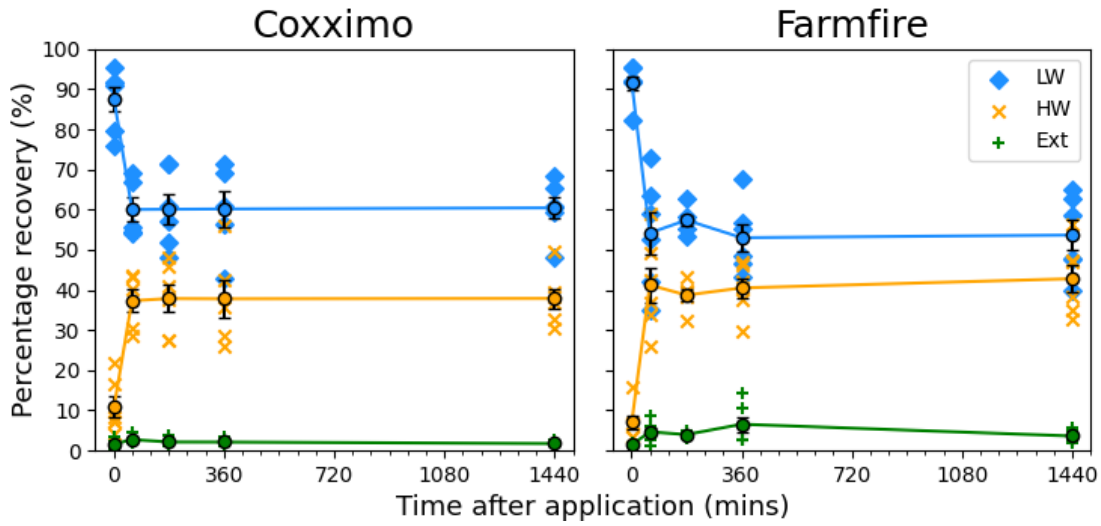


Figure 6.7: Percentage of total mass recovered from the leaf wash (LW), from the heptane wash (HW) and extracted from the remaining leaf (Ext). Averages at each time-point are plotted as coloured circles with black borders and the interpolated line between them is included. Standard error bars are included in black. The result for Farmfire at the 360 mins timepoint appears anomalous due to demonstrating a statistically significant difference in mean ($p<0.05$) while being inconsistent with the lower Ext mass percentage values recorded at the 1440 mins timepoint.

There was a short initial period of uptake within the first hour (defined as a decrease in LW fraction with a corresponding increase in HW fraction) after which the mass taken up from the surface relative to total mass recovery plateaued to a constant value within experimental error. It has previously been observed that uptake into HW fraction does continue beyond 24 hours [unpublished data, Syngenta] but with a very much reduced uptake rate. This

corroborates our observations. Additionally, results presented as percentage recovery are more consistent and corroborate the qualitative trends observed for raw data. The mass recovered from the extract after the heptane wash is negligible and no statistically significant variation in time can be established.

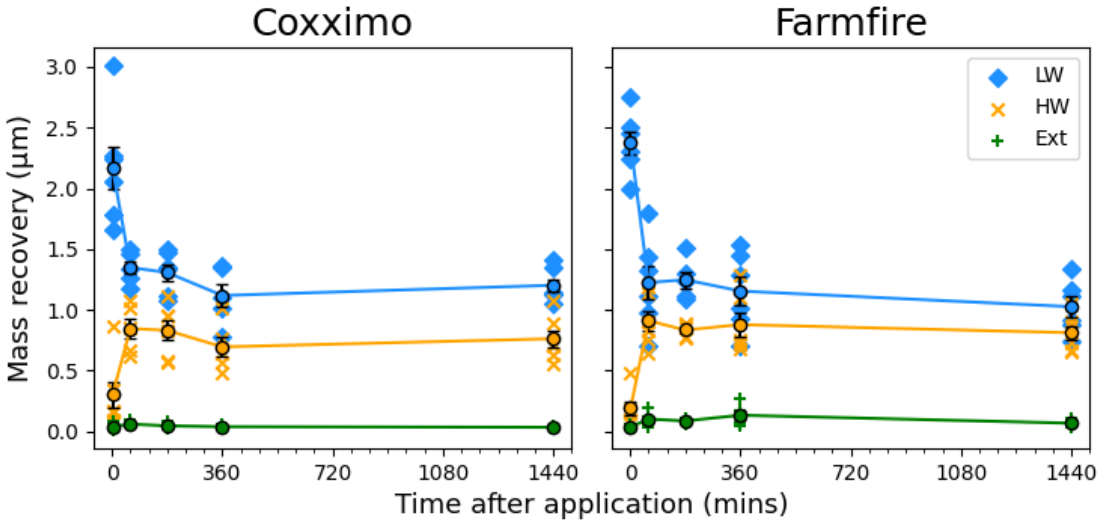


Figure 6.8: Raw data for masses recovered from each sampling process (LW: blue diamond, HW: orange ×, Ext: green +¿) for Coxximo (left) and Farmfire (right) maize varieties. Averages at each time-point are plotted as coloured circles with black borders and the interpolated line between them is included. Standard error bars are included in black.

We conclude that differentiation between material bound in cuticle and material bound in the sub-cuticle using a heptane wash was not valuable for further study. The percentage recovery of fungicide from the Ext fraction was negligible (for reliable data) relative to the other fractions and did not increase noticeably with time, implying that negligible penetration into the sub-cuticle occurs on this timescale. Additionally, there is evidence that a heptane wash may not fully remove the cuticular bound material reliably.

Figure 6.9 shows the results for the percentage recovery of the TL $\left(\frac{m_{TL}}{m_{LW}+m_{HW}+m_{TL}}\right)\times 100\,\%$ against the HW $\left(\frac{m_{HW}}{m_{LW}+m_{HW}+m_{TL}}\right)\times 100\,\%$ sampling methods for this preliminary study,

where m_X is the mass recovered from sampling process X. From this we can assess visually the presence of correlation between these two values. Correlation, if any, would imply that the recovery of material using the heptane wash is incomplete and that a significant proportion of the material recovered from the extract is truly material in the cuticle compartment that had not been recovered by the heptane wash.

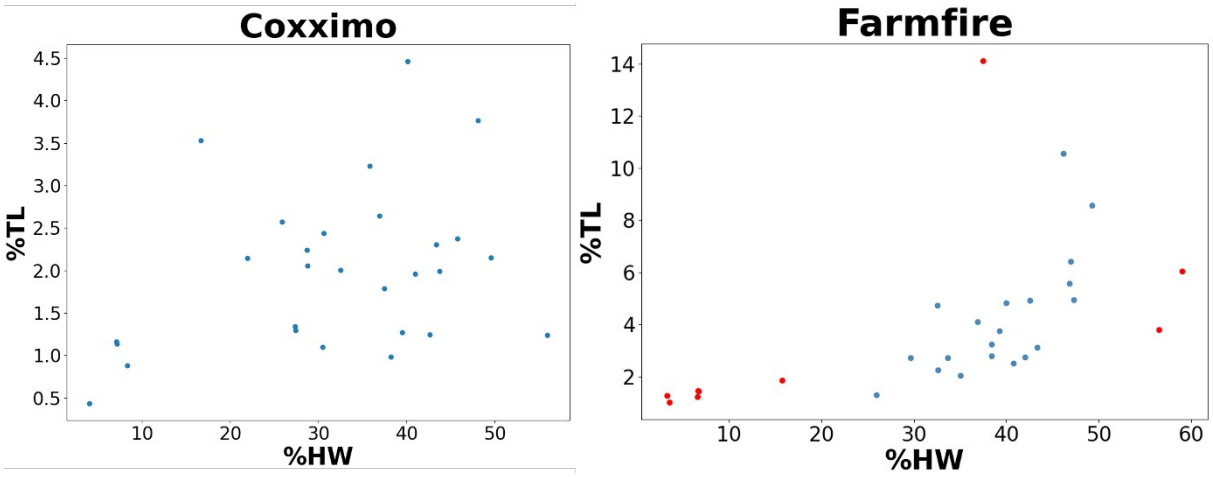


Figure 6.9: Results from the Preliminary study of uptake of percentage recovery from the remaining leaf extract (%TL) versus percentage recovery from the heptane wash sampling (%HW) for Coxximo (left) and Farmfire (right).

There is not a strong correlation for the Coxximo results but there is a correlation for the Farmfire results whereby a large %HW corresponds to a large %TL. This is quantitatively evidenced by the Pearson and Spearman correlation coefficients, which measure the degree of linear and non-linear correlation respectively, presented in Table 6.4. We see a strong positive non-linear correlation for the Farmfire case. This provides evidence that the recovery of material from the cuticle using a heptane wash is incomplete, particularly when %HW is large, and that this leads to correlatively increased %TL values, since cuticular material has been left behind to be extracted from the remaining leaf. The %TL values for Farmfire are also significantly larger than those for Coxximo with respect to their paired %HW, with an increasing difference as %HW increases. This evidence suggests that the heptane wash is an

unreliable technique for extracting material from the cuticle in the case of Farmfire, which is a driver for the exclusion of the heptane wash from the later uptake study.

Table 6.4: Correlation coefficients between %HW and %TL for Coxximo and Farmfire.

Correlation (%HW:%TL)	Pearson	Spearman
Coxximo	0.34	0.29
Farmfire	0.55	0.81

We next sought to test whether the uptake results for the Coxximo and Farmfire maize varieties were statistically significantly different. P-tests were performed between the results of the two varieties at each timepoint. No significant differences ($p \gg 0.05$ at every timepoint) were observed. We infer that these two maize varieties do not have a statistically significant effect on the fungicide uptake for studies of this scale and that uptake results can be generalised across maize varieties to this level of experimental error.

We then collected low-variance, short-timepoint data in order to accurately characterise the fungicide's uptake behaviour within 1 hour of application and thus develop a testable uptake model. Short-timepoint data has larger variance due to greater relative uncertainty in the time domain for a given experimental procedure, as such the methodology for the following studies was adjusted as follows: removal of the heptane wash for greater throughput and improved time precision; total randomisation of the batch order for greater data robustness; and recording of timings for droplet application and leaf sampling individually to give greater accuracy and a measure of uncertainty in time.

We quantified the masses of material removed by a wash of the leaf surface with 80:20 water/ acetonitrile (LW), the masses of material extracted from the remaining leaf after washing (TL), and the percentage of the total mass recovered from the TL fraction (%TL). The method for the application of the fungicidal droplets was unchanged. Results for Coxximo are presented in Figure 6.10.

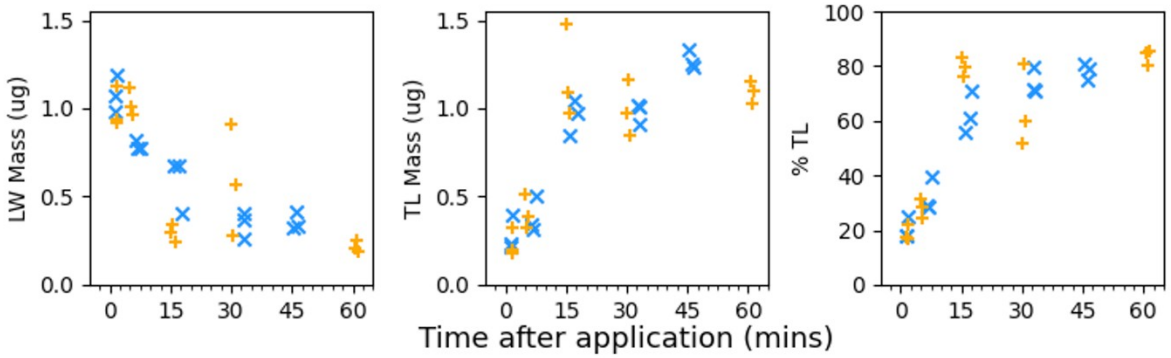


Figure 6.10: Data derived from a study of uptake of SC fungicide on Coxximo maize. The first plot presents masses recovered from the leaf wash (LW), the second plot presents masses recovered from remaining leaf (TL), and the third plot presents percentage of total mass recovered as TL (%TL). The 2 batches for each timepoint are differentiated by marker colour and shape (× and +¿). There is no correlation between marker selection and batch order.

The uptake followed a rapid initial uptake within the first 15 minutes, a similar timescale to dry-down for the formulation $(10.9 \pm 0.05 mins)$.

We conclude that there are two uptake regimes: an initially rapid uptake rate within the first 15 minutes before a transition to a much slower uptake rate. The uptake appears to be confined within the cuticular layer with minimal penetration to the sub-cuticle during this timeframe. The timescale of the initial uptake regime effectively coincides with the dry-down time for this formulation. This insight, alongside the quantitative data and surface characterisations, will inform the development of a model.

6.4 Theory

In this section we develop a “simplest viable model” to describe the uptake behaviour of this lipophilic fungicide. We present a model of the leaf-cuticle system in Figure 6.11 in which it

is assumed that the uptake occurs from the liquid droplet during the period from application to the point at which the droplet has evaporated. The droplet-leaf contact area during this time is pinned by the coffee-ring effect. The system is modelled as 4 homogeneous compartments: air, formulation droplet, cuticle and sub-cuticular tissue. The cuticle and sub-cuticle are modelled as uniformly flat. The contact area between the formulation droplet and cuticle is modelled as constant. The uptake through the cuticle is modelled as diffusional. The concentration within the droplet is modelled as saturated and homogeneous due to convective currents induced by evaporation and the overlapping of diffusion zones even without this convective consideration, further discussed below.

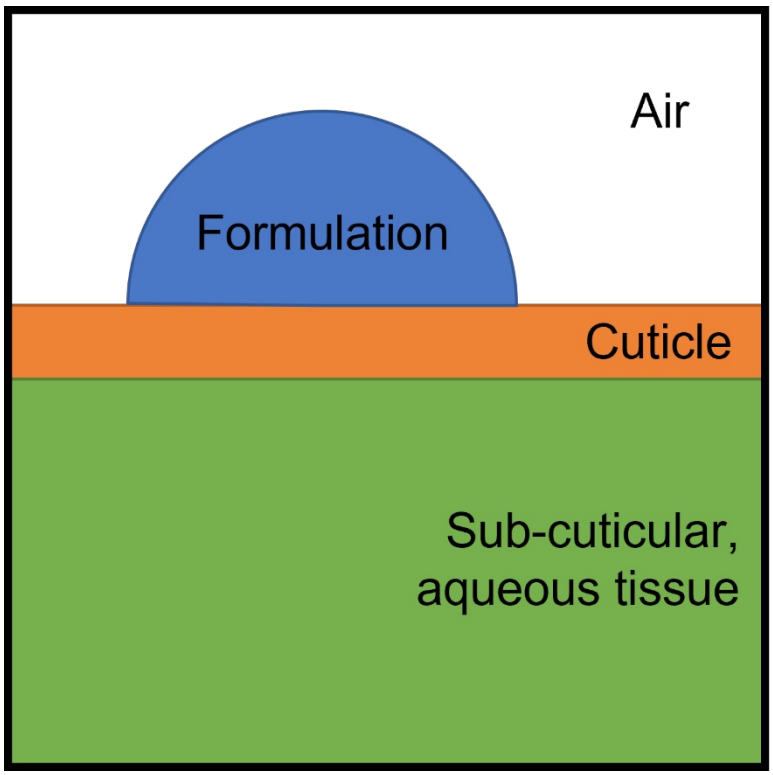


Figure 6.11: Schematic illustration of model formulation-plant system as homogeneous compartments. Not to scale.

Our approach follows that commonly utilised in the literature, including by Mercer[21], Trapp[20] and our prior related work[31], also presented in Chapter 5. However, we approach this as a two-dimensional system as opposed to one and consider the uptake of a highly lipophilic

compound confined to the cuticle space, rather than hydrophilic species that readily permeate into the sub-cuticle at the internal cuticle boundary.

A droplet separation of $\geq 3\,mm$ was used to ensure that uptake from each droplet was independent. Considering that the uptake pathway in this case is astomatous diffusion through the cuticle, we can assess at what distance apart droplets must be to ensure that their diffusion zones within the cuticle do not overlap. According to the Einstein-Smoluchowski equation[48, 49], the expected square displacement of a diffusing particle after time t is: $\langle x^2 \rangle = 6\,Dt$ in three dimensions. As such, we can consider the root mean square displacement of the fungicide through the cuticle after 24 hours to be: $\sqrt{\langle x^2 \rangle} = 7.2 \times 10^{-7} m = 0.7\,\mu m$, where we have used $D_{cut} = 10^{-18}\,m^2\,s^{-1}$ as a typical value for pesticides in the cuticular environment, inferred from literature experiments on diffusion through reconstituted cuticles[3]. If we consider the droplet radii are $450\,\mu m$, a separation of $1\,mm$ is required to avoid two droplets coalescing. If we include two diffusion zones, then one must include an additional $1.5\,\mu m$ separation at least to avoid the diffusion zones significantly overlapping. However, to ensure no interference, a minimum centre-to-centre separation of $3\,mm$ was used. This ensures that over the course of 24 hours, a diffusing particle would not expect to interfere with the uptake at an adjacent droplet if its diffusion coefficient is $2 \times 10^{-12}\,m^2\,s^{-1}$ or less. Given the expected values of the diffusion coefficient (and the value we infer below) we conclude that uptake from a single droplet is independent of the other droplets and that total uptake during our study occurs as a sum of independent uptakes from droplets. The total uptake behaviour reflects the average individual droplet behaviour summed over 20 droplets.

A relatively dense and thick coffee ring deposit shape was observed for each droplet after drying. From this we can infer two key insights for building a simplest viable model: strong flow effects are active within the droplet during drying[44], which will encourage

homogenisation of soluble material within the droplet, and the drying is predominantly under the constant contact radius (CCR) regime[50-52] at a radius equivalent to the coffee ring's.

Additionally, our uptake data illustrates the predominant uptake occurs before evaporation is complete ¿ for the formulation observed) and thus while the particulate material is surrounded by aqueous solution. Modelling in Chapter 5 has demonstrated that foliar uptake from a particulate system within an aqueous external environment involves the competition of two uptake pathways[31]: a direct pathway directly through the particle-cuticle contact and an indirect pathway via dissolution into and diffusion through the aqueous environment surrounding the particles. It was predicted that the indirect uptake pathway dominates the direct uptake pathway for typical pesticides according to their physicochemical properties. By applying the G-factor described in Chapter 5, we observe that $G<1$, therefore dominant indirect uptake is predicted for the fungicide investigated in this study and the more localised uptake from direct particle-cuticle contact is not expected to influence the uptake meaningfully.

The average separation of the particles in the interior region of the dried deposit was extracted from SEM images: $x_{sep}=17\,\mu m$. From this, and the approximate aqueous diffusion coefficient of $D_{aq}=10^{-10}m^2s^{-1}$, we can conclude that the aqueous diffusional zones between these particles significantly overlap once $t \;\; x_{sep}^2/D_{aq}=3\,s$ have passed[53-55]. Once significant aqueous diffusional zone overlap has been established, the transfer into the cuticle from the area interior to the coffee ring is effectively equivalent to uniform transfer across the entire droplet contact area, since the diffusion coefficient in the cuticle is several orders of magnitude lower than in an aqueous medium[3]. A schematic illustration is given in Figure 6.12. Initially after application, the concentration of material at the cuticle interface is localised around individual particles, but after the transition to significant aqueous diffusion

zone overlap at 3 seconds, the concentration at the cuticle surface, and thus the uptake rate at the surface, is uniform, assuming the uptake is partition-limited. Since this transition occurs early in the 24-hour timescale we investigated, we model the second regime as being dominant throughout. Furthermore, the observation of average separation of $17\,\mu m$ is performed after accumulation of material in the coffee ring, implying that this is the largest average particle separation experienced before drying.

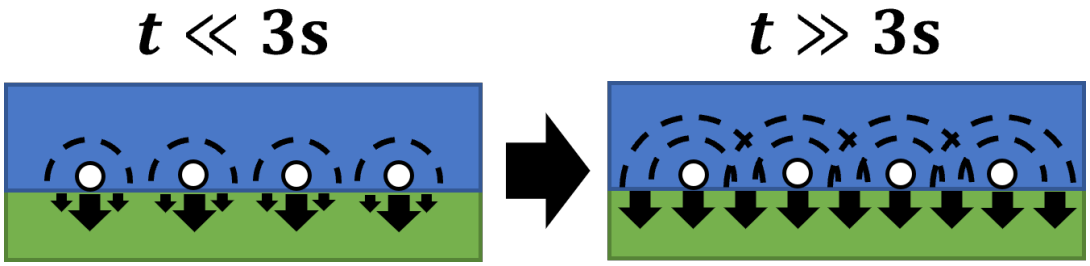


Figure 6.12: Schematic of aqueous (blue) diffusion zone (black dotted lines) overlap transition from localised to uniform aqueous concentration at the cuticle interface and its effect on the homogeneity of the transfer (black arrows) into the cuticle (green). Not to scale.

We thus model the uptake as occurring by the indirect pathway uniformly across a disk of droplet-cuticle contact and neglect the distribution of particles on the surface beyond the above consideration of their average separation. This approximation is evidently applicable before dry-down. However, as shall be demonstrated in the next section, longitudinal saturation of the cuticle coincides with the dry-down and thus the uptake becomes restricted to the edge of the original droplet-cuticle interface, at which radial diffusion is available. The potential localisation of uptake to individual particles deposited in the ringed interior does not have an effect on the total uptake rate since the local uptake rate here is zero due to the saturation and so does not depend on the local boundary conditions. As such, the approximation of a disk of uniform surface concentration remains viable. In cases where dry-down occurs significantly earlier than longitudinal saturation while depositing a low density of particles on the leaf surface within the coffee ring interior (such that their cuticular diffusion zones poorly overlap) with no co-deposited medium through which indirect uptake

may continue, such as a non-volatile additive film, a more complex boundary condition may be required.

We next test the simplest model that fits these observations, presented schematically in Figure 6.13. We approximate the droplet-cuticle interface as a uniform disk at which thermodynamic equilibrium holds (maintained by convection effects and the large ratio between the aqueous and cuticular diffusion coefficients). Within the cuticle, modelled as a thin, homogeneous layer, the material diffuses longitudinally and radially. Considering we are working with a highly lipophilic active ingredient, we apply a "wax reservoir" condition to the model whereby material does not escape the cuticle into the air or sub-cuticle. We have not distinguished the 'cuticle proper' and 'sorption compartment' for greater simplicity.

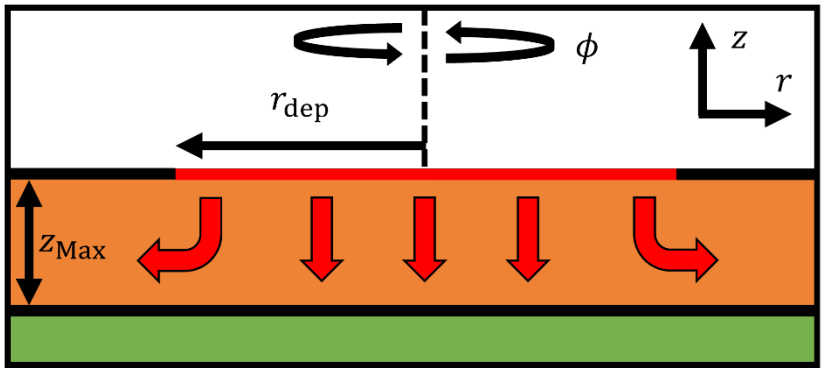


Figure 6.13: Schematic of model cuticle system for simple simulation within cylindrical coordinates $\{r, z, \phi\}$. A uniform, saturated disk (red) represents the cuticle-droplet contact area with constant contact radius. Diffusion then occurs through the cuticle (orange), with the potential for a radial component to diffusion at the disk edge (represented by red arrows). Zero escape into air (white) or subcuticular tissue (green) through zero-flux interfaces (black) corresponds to the 'wax reservoir' limit. Not to scale.

This problem can be represented as a partial differential equation corresponding to Fick's 2nd Law of Diffusion[56]. The interface between the cuticle and droplet is assumed to be saturated while each other cuticle interface does not allow transfer of active ingredient across it. Our model is conceived to be dimensionless and thus the predicted uptake curve is dependent on:

- $Z_{Max} = z_{Max} / r_{dep}$, the ratio of the cuticle thickness, z_{Max}, and the radius of the deposit, r_{dep};

- $t_{ref} = \frac{r_{dep}^2}{D_{cut}} = \frac{t}{T}$, which determines the dimensional timescale, where D_{cut} is the space-averaged diffusion coefficient in the cuticle, T is the dimensionless time, and t is the dimensional time;

- $m_{ref} = c_{sat}^{cut} \cdot r_{dep}^3 = \frac{m}{M}$, the reference mass which converts between dimensionless and dimensional results for the penetrated mass, where c_{sat}^{cut} is the space-averaged saturation concentration of the active ingredient within the cuticle, M is the dimensionless total mass in the cuticle, and m is the dimensional total mass in the cuticle.

A larger value of Z_{Max} corresponds to a larger cuticle relative to the contact area with the applied formulation and fundamentally changes the uptake curve shape. The reference time is six times the time taken for a pesticidal molecule engaging in three-dimensional Brownian motion within the cuticle to have an expected square displacement equal to r_{dep}, according to the relation $\langle r^2 \rangle = 6\,Dt$. The reference mass is the mass of pesticide within a cube of saturated cuticle with a side length of r_{dep}. Increasing t_{ref} corresponds to a slower timescale and a more slowly evolving uptake profile. Increasing m_{ref} corresponds to a larger mass of material taken up for an equivalent dimensionless uptake curve.

The model developed is based on Fick's 2nd Law of diffusion[56] in two-dimensional cylindrical coordinates, r, perpendicular distance from axis of symmetry, and z, distance from reference plane perpendicular to symmetry axis:

$$\frac{\partial c}{\partial t} = D\left(\frac{\partial^2 c}{\partial z^2} + \frac{\partial^2 c}{\partial r^2} + \frac{1}{r}\frac{\partial c}{\partial r}\right) \qquad \text{Equation 6.5}$$

where c is the concentration and D is the diffusion coefficient.

We implement a complete set of boundary conditions, presented schematically in Figure 6.14.

We apply zero-flux boundaries at the flat cuticle's longitudinal interfaces (top and bottom boundaries as illustrated in Figure 6.14), thereby applying the "wax reservoir" limit such that no material is lost from the cuticle into the air or sub-cuticle. We define a r_{Max} value as the simulation's radial limit at which we also apply a zero-flux boundary. r_{Max} is defined in relation to t_{Max}, the largest value in time to which we simulate, such that we are within the infinite limit and r_{Max} does not affect the solution: $r_{Max}=6\sqrt{D\,t_{Max}}$. This is justified in the above section by the diffusional independence of the uptake from adjacent droplets. The axis of symmetry must, by definition, also have a zero-flux boundary through it such that there is no concentration gradient across this axis. We implement a zero-concentration condition at $t=0$, assuming no fungicide is already present within the cuticle. We implement a uniform constant-concentration boundary condition at the cuticle-droplet contact disk area, assuming that thermodynamic equilibrium is held and that the cuticle here is saturated such that $c=c_{sat}$.

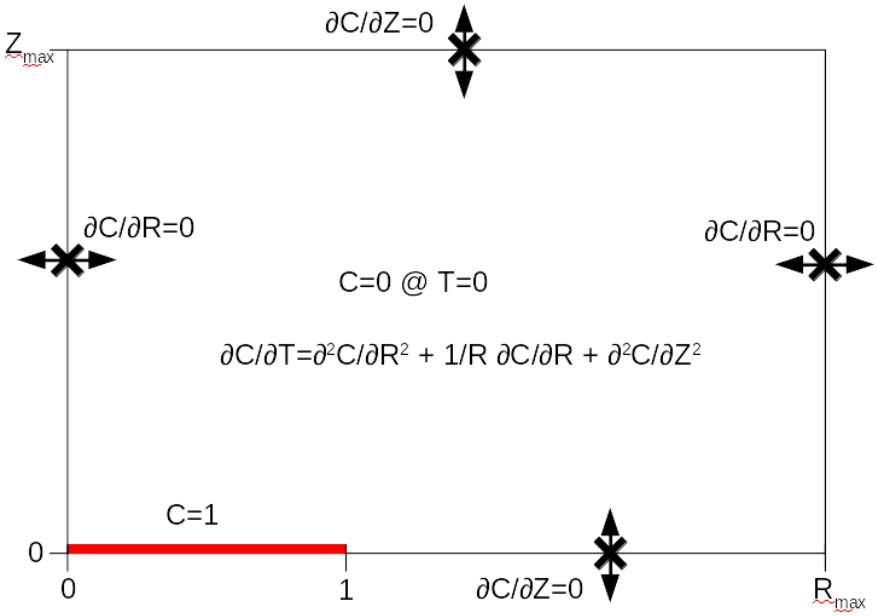


Figure 6.14: Schematic of simulation space with associated boundary conditions and PDE in dimensionless form.

This set of boundary conditions is summarised as:

$$\begin{cases} \frac{\partial c}{\partial z}=0\, at\,(r,z)=(r>r_{dep},0)\wedge(r,z_{Max}) \\ \frac{\partial c}{\partial r}=0\, at\,(r,z)=(0,z)\wedge(r_{Max},z) \\ c=0\;\forall\,(r,z)\, at\, t=0 \\ c=c_{sat}\, at\,(r,z,t)=(r\le r_{dep}, z=0, t>0) \end{cases}$$

where r_{dep} is the radius of the disc through which uptake occurs, corresponding to the radius of the cuticle-droplet contact area, z_{Max} is the maximum simulation longitudinal distance, which corresponds to the cuticle thickness, and c_{sat} is the saturation concentration of the fungicide in the cuticle.

In order to simplify the mathematics and generalise the results of a simulation, we convert these parameters to dimensionless values using the conversions presented in Table 6.5.

Table 6.5: Table of dimensionless conversions for model parameters

Dimensional parameter	Dimensionless conversion

r	$R = r / r_{dep}$
z	$Z = z / r_{dep}$
r_{dep}	$R_{dep} = r_{dep} / r_{dep} = 1$
r_{Max}	$R_{Max} = r_{Max} / r_{dep}$
z_{Max}	$Z_{Max} = z_{Max} / r_{dep}$
D_{cut}	$d_{cut} = D_{cut} / D_{cut} = 1$
c	$C = c / c_{sat}^{cut}$
t	$T = D_{cut} \cdot t / r_{dep}^2 = t / t_{ref}$
$m = 2\pi \int_0^{r_{Max}} \int_0^{z_{Max}} c\, r\, dz\, dr$	$M = 2\pi \int_0^{R_{Max}} \int_0^{Z_{Max}} C\, R\, dZ\, dR$ ¿ $m / c_{sat}^{cut} r_{dep}^3 = m / m_{ref}$
j	$J = r_{dep} \cdot j / D_{cut} \cdot c_{sat}^{cut}$
$j_{Tot} = 2\pi \int_0^{r_{dep}} j\, r\, dr$	$J_{Tot} = 2\pi \int_0^1 J\, R\, dR = j_{Tot} / D_{cut} \cdot c_{sat}^{cut} \cdot r_{dep}$

where m is the total dimensional mass in the cuticle, j is the dimensional flux at a given position $\left(mol\, m^{-2} s^{-1}\right)$ given by Fick's First Law $\left(j = -D \frac{\partial c}{\partial x}\right)$, j_{Tot} is the increase in total mass in the cuticle over time according to the integration of flux at the disk $\left(mol\, s^{-1}\right)$, and $t_{ref} = r_{dep}^2 / D_{cut}$ and $m_{ref} = c_{sat}^{cut} \cdot r_{dep}^3$ are dimensionless conversion factors for mass and time, which are orthogonal for a given r_{dep}. We can now express the PDE and boundary conditions in dimensionless terms:

$$\begin{cases} \dfrac{\partial C}{\partial T} = \dfrac{\partial^2 C}{\partial Z^2} + \dfrac{\partial^2 C}{\partial R^2} + \dfrac{1}{R}\dfrac{\partial C}{\partial R} \; \forall (R, Z, T) \\ \dfrac{\partial C}{\partial Z} = 0 \; at \; (R, Z) = (R > 1, 0) \wedge (R, Z_{Max}) \\ \dfrac{\partial C}{\partial R} = 0 \; at \; (R, Z) = (0, Z) \wedge (R_{Max}, Z) \\ C = 0 \; \forall (R, Z) \; at \; T = 0 \\ C = 1 \; at \; (R, Z, T) = (R \leq 1, Z = 0, T > 0) \end{cases}$$

For numerical simulation, we discretise these equations onto points on a grid and represent the PDE and boundary conditions using the finite difference method. The discretisation scheme is illustrated in Figure 6.15.

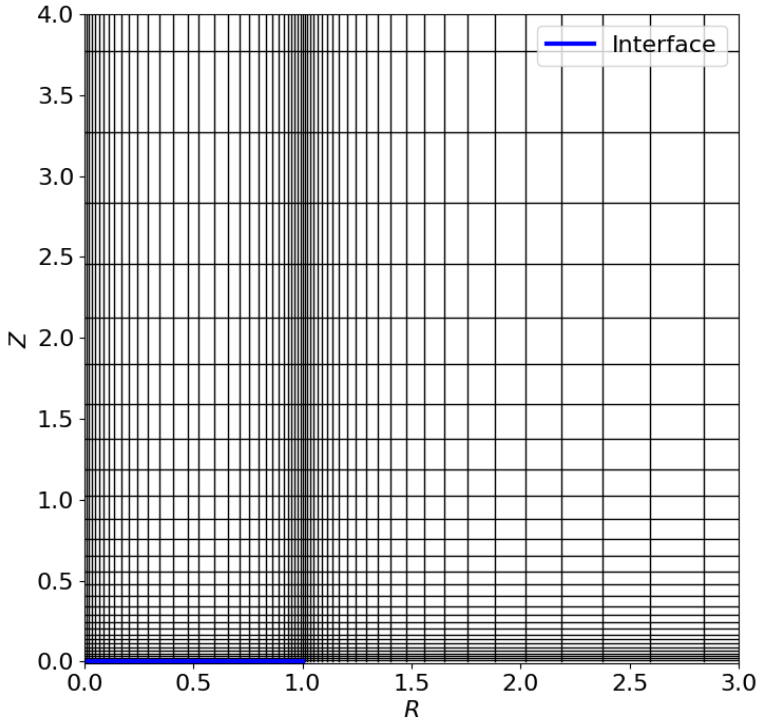


Figure 6.15: Illustration of the discretisation scheme used. Parameters used are $h_R = h_Z = 0.01$ and $\omega_R = \omega_Z = 1.15$. These values are chosen to be illustrative only.

An exponentially expanding grid[57-60] was used since the concentration gradients decrease with distance from the source disc and so the density of the grid required to achieve accurate simulation also decreases with distance. The distribution of points in such a grid for a generic coordinate X is given as:

$$X_i = X_{i-1} + h_X \times \left(\omega_X\right)^{i-1} \qquad \text{Equation 6.6}$$

where h_X is the initial step distance $\left(X_1 - X_0\right)$ and ω_X is the expansion factor. The Z and T grid-steps are monotonically expanding. The R grid-steps expand until $R = 0.5$, then contract to $R = 1$ (to give a symmetric distribution about $R = 0.5$), before expanding to $R = R_{Max}$. This is done to ensure high density of points around the disc edge where concentration gradients are largest. A backward implicit discretisation[61-63] is used to resolve the steps in time.

This discretised, finite difference system is then solved fully implicitly and iteratively using the Biconjugate Gradient Stabilised method (BICGSTAB), with a relative convergence tolerance of 1×10^{-6}, with a semi-coarsening multigrid (SMG) preconditioner. The numerical simulation was performed on a *Linux(Centos)* machine with an *Intel Core i7-6800K* CPU (3.40GHz, 6 cores), 32GB of RAM, and an *Nvidia Quadro GP100*. The simulation program was written in C++, utilising the *HYPRE* software package (version 2.18.2)[64, 65] executed with *CUDA* enabled GPU support. Construction of the discretised grid, data analysis, and plotting were performed with *python*, including the *NumPy*, *SciPy* and *matplotlib* packages.

6.5 Simulation results

Dimensionless results were generated from simulation of the above model showing the dependence of the uptake rate on Z_{Max}. These results are presented in Figure 6.16 where the uptake rate is presented as $\log_{10}\left(\frac{dM}{dT}\right)$, where M is the dimensionless mass within the cuticle and T is the dimensionless time, against $\log_{10}\left(T\right)$ for a series of Z_{Max} values between 10^{-4} and 100. This is done to show uptake rate curves which display log-log linear initial decay before a transition to a new regime and ones that show a positive deviation from the log-log linear decay before that transition.

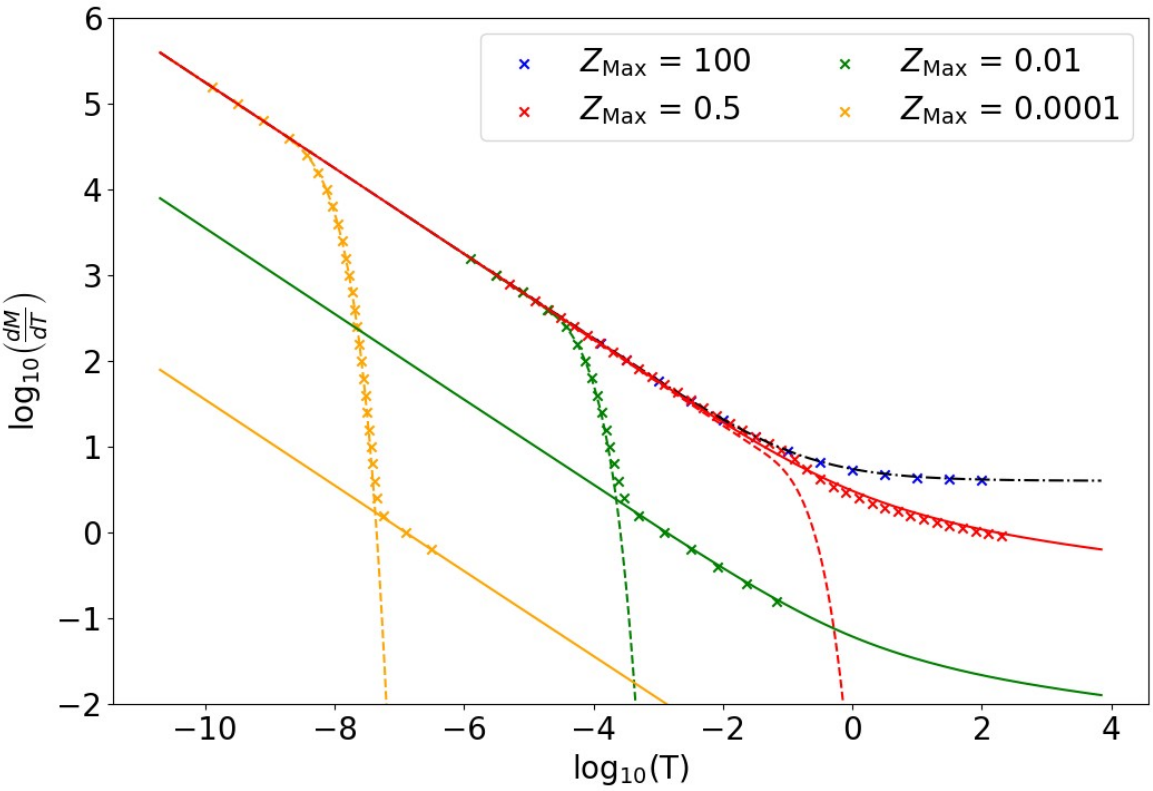


Figure 6.16: Gradient of the dimensionless total flux with dimensionless time as a function of the cuticle thickness Z_{Max} from simulated results. Plots of the Shoup-Szabo (dot-dashed black) and scaled Aoki equations (solid lines of colours corresponding to respective Z_{Max} values) are included. The analytical result for a 1D system with no radial diffusion is also included as dashed lines whose colour correspond with Z_{Max}.

The dimensionless results demonstrate two limiting uptake rate regimes with several orders of magnitude difference. The first is the Cottrell equation[66]:

$$\frac{dM}{dT} = \frac{A_d}{\sqrt{\pi T}} \qquad \text{Equation 6.7}$$

where A_d is the dimensionless area of the disk contact (¿ π in the dimensionless system). This equation analytically describes linear diffusional uptake and therefore the uptake rate predicted by a one-dimensional, semi-infinite model. For longer times, edge diffusion at the disk circumference develops, as described by the Shoup-Szabo equation[67]:

$$\frac{dM}{dT} = \frac{4\,A_d}{\pi}\left(0.7854 + \frac{0.8863}{2\sqrt{T}} + 0.2146\,e^{\frac{-0.7823}{2\sqrt{T}}}\right) \qquad \text{Equation 6.8}$$

which describes the uptake rate by diffusion from a disk into an infinite volume. The equation initially follows the Cottrell equation but increases at intermediate time due to the increasing relative radial contribution to diffusion. This leads to an eventual steady-state uptake rate. This is presented in Figure 6.16 as a black dot-dashed line and describes the early uptake behaviour.

Once $T \quad 0.5 \times Z_{Max}^2$, the uptake curve predicted by the model decreases. This is caused by the longitudinal saturation of the cuticle whereby the volume directly below the disk contact becomes saturated and thus no more material can be taken up into it. This problem has been solved analytically in one-dimension by Crank[68] to give the following co-convergent infinite series, which have been included in Figure 6.16 as coloured dashed lines:

$$\frac{dM}{dT} = \begin{cases} \dfrac{A_d}{\sqrt{\pi T}}\left(1+2\sum_{n=1}^{\infty}(-1)^n e^{\frac{-n^2 Z_{Max}^2}{T}}\right) \\ \dfrac{2A_d}{Z_{Max}}\sum_{n=0}^{\infty} e^{\frac{-(2n+1)^2\pi^2 T}{4 Z_{Max}^2}} \end{cases} \qquad \text{Equation 6.9}$$

The first infinite series converges most rapidly for $T < Z_{Max}^2$ and the second converges most rapidly for $T > Z_{Max}^2$. However, unlike these equations, which neglect radial diffusion, we see that the simulated uptake rates do not decay to zero but instead tend to a different limit. All uptake rate curves for this model at long dimensionless times tend to scaled versions of the Aoki equation[69], included in Figure 6.16 as coloured solid lines:

$$\frac{dM}{dT} = A_c\left(0.422+\frac{1}{\sqrt{\pi T}}-0.0675\log_{10}T\right. \qquad \text{Equation 6.10}$$

$$\left.+0.0058\left(\log_{10}T-1.47\right)\times\left|\log_{10}T-1.47\right|\right)$$

where $A_c = 2\pi Z_{Max}$ is the dimensionless surface area of a cylinder extruded from the disk contact to the internal cuticle boundary. The Aoki equation describes the uptake rate curve for diffusion from a uniform, cylindrical surface. Once longitudinal saturation occurs, the only means by which uptake can continue is by radial diffusion, and thus the limiting step to uptake is diffusion from a saturated cylinder of material beneath the contact area, with a radius of r_{dep} and a length of z_{Max}. This is the uptake rate's limiting regime at long times.

The larger the value of Z_{Max}, the later the transition from the short- to the long-time limits, since the transition begins once $T \quad 0.5 \times Z_{Max}^2$. The short-time limit is a uniform disk in infinite volume (Equation 6.8) and the long-time limit is a uniform cylindrical surface of length z_{Max} and radius r_{dep} (Equation 6.10). Small Z_{Max} values ($\lll 0.5$) have a transition described by Equation 6.9 until $\frac{dM}{dT}$ approaches Equation 6.10. $Z_{Max} = 0.5$ corresponds to the case where Equation 6.7 and Equation 6.10 overlap at short times. For increasing Z_{Max}, the transition to the long-time limit is more prolonged as the cylinder beneath the droplet contact/ disk requires more time to saturate.

For fitting to experimental data, we adopted the measured average $r_{dep} = 450 \pm 30\,\mu m$, approximating the droplet contact as a disk with the same deposit area as characterised from the images presented in the Experimental Results section. The z_{Max} for cuticles of maize is reported[70] as $50\,nm$. From this we infer a value of $Z_{Max} = 1.1 \times 10^{-4}$. The transition from a high uptake regime to a slow uptake regime observed in the experimental data can thus be explained as longitudinal saturation in the cuticle, according to this model. By fitting the dimensionless uptake rate curve simulated for this Z_{Max} to our experimental data, we can derive values for expected t_{ref} and m_{ref} values, and thus predict D_{cut} and $[A]_{sat}^{cut}$ values, which

can be compared with expected values to assess the feasibility of this model. This is done in the following section.

6.6 Model application to experimental data

For a fixed value of r_{dep}, t_{ref} and m_{ref} are orthogonal and independently scale the time and mass-dimensions respectively. We performed a simple fitting of the simulated uptake rate curve for $Z_{Max}=1.1\times10^{-4}$ using the Trust Region Reflective algorithm to minimise the least-squares error against the experimental data for the uptake study using *Python* and the *scipy* package. This fitting is presented in Figure 6.17. We have included the inferred D_{cut} and c_{sat}^{cut} values with standard errors and the R^2 value in the Figure legend.

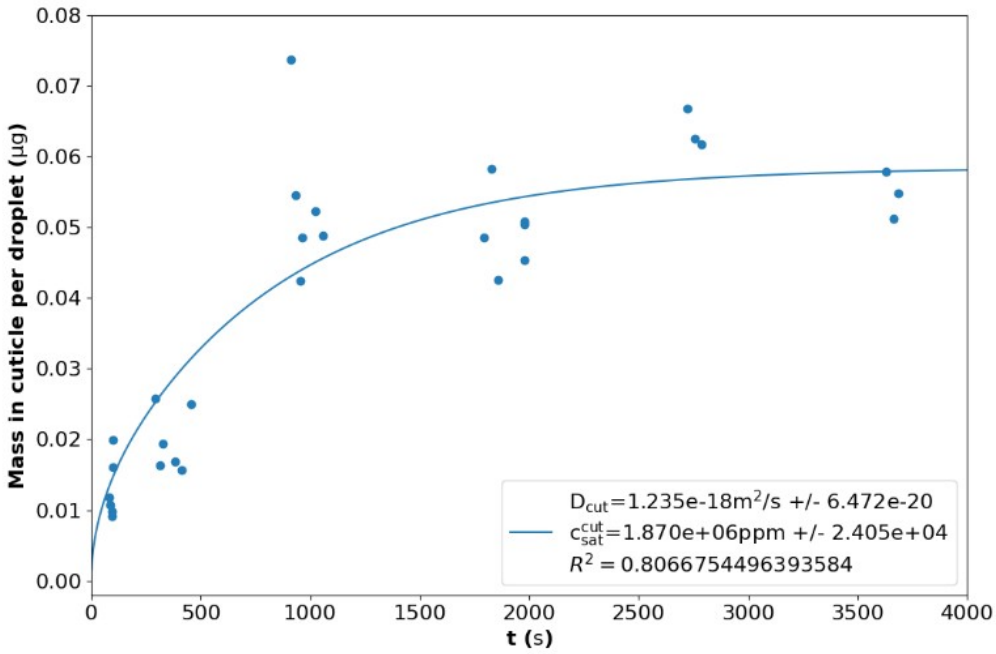


Figure 6.17: Fitting the simulated uptake rate curve for $Z_{Max}=1.1\times10^{-4}$ to experimental data from the uptake assay study. The D_{cut} and c_{sat}^{cut} values inferred from the fitted $K\square_t$ and K_m values, their inferred errors and the R^2 value of the fitting are presented in the Figure Legend.

A large value for R^2 suggests that this model provides a good fit for this data. The model implies $D_{cut}=(1.24\pm0.06)\times10^{-18}m^2s^{-1}$ and $c_{sat}^{cut}=(1.87\pm0.02)\times10^6\,ppm$ from fitting to our experimental data. Our value for D_{cut} aligns well with literature measurements for diffusion

through reconstituted cuticles[3], suggesting that the timescale of uptake is well-described within this model and that longitudinal saturation of the cuticle is a viable explanation for the change in uptake rate.

We now consider the inferred c_{cut}^{sat} value. A simple and common method to estimate the saturation concentration in the cuticle is to multiply the experimentally determined aqueous solubility by the partition coefficient from water into the cuticle: K_{cw}. K_{cw} is often approximated using the partition coefficient of the chemical from water into a system that models the cuticular environment[3, 71-74]. If we use ethyl acetate as the model system, we expect $c_{sat}^{cut} = 1.3 \times 10^5\, ppm$, which is almost within one order of magnitude of the value inferred from the model. This is despite the possible limitations of using ethyl acetate as a solubility model, which lacks the chain lengths and secondary alcohol groups of the esters found in maize cuticle wax and cutin[70] and thus is an encouraging comparison for the feasibility of this model.

We justify ethyl acetate as a cuticular model in this case due to the dominant presence of esters in the cuticle wax and cutin of mature maize leaves[70]. While K_{ow}, the octanol-water partition coefficient, is a standard model parameter to use for estimating K_{cw} and thus the cuticular solubility, it would predict a c_{sat}^{cut} value of $9.5 \times 10^3\, ppm$, which is much lower than predicted by the model and impossible to justify considering the cuticular volume accessible per droplet in the measured timeframe and the mass measured as taken up within it. This implies that comparison to octanol would be inappropriate for the case of this lipophilic fungicide and maize leaf, and that ethyl acetate acts as a more suitable solubility model.

An aspect which is currently neglected by the model is the cuticular peg between the epidermal cells, an area which has a greater cuticular depth than the main cuticle proper. This

provides an additional volume into which the lipophilic fungicidal material may be taken up and may explain the larger than expected mass of fungicide taken up, leading to an erroneously large, inferred value for c_{sat}^{cut}. The area of the cuticle above which there is cuticular peg can be observed from SEM images and has been characterised. The cuticular pegs have an average width at the outer surface of $4 \pm 0.1\,\mu m$. If we assume that the cuticular peg volume below the deposit is also saturated after longitudinal saturation, we predict an average cross-sectional area of $19\,\mu m^2$, suggesting that the depth of the cuticular peg would need to be on the order of $5\,\mu m$, which is viable for the maize cuticle.

As such, the fitted behaviour of this model is entirely consistent with partitioning of fungicide into ethyl acetate and the presence of cuticular pegs. We propose this model as a simplest viable solution for predicting the foliar uptake of lipophilic species. The model can be generalised for any r_{dep}, z_{Max}, D_{cut} and c_{sat}^{cut} or used to infer these values from measured uptake. We present two limiting regimes for the "wax reservoir" mode of uptake and inferred equations for the calculation of their uptake rates (Equation 6.8 and Equation 6.10) without the need for numerical simulation. For the case of $z_{Max} \lll r_{dep}$, Equation 6.9 is also provided to describe the transition between the two limiting regimes.

6.7 Conclusions

We have observed that uptake into maize of the lipophilic fungicide from droplets of non-adjuvant suspension concentrate formulation occurs unexpectedly rapidly initially but has a well-defined transition to a second, much slower uptake regime. We have shown that transfer of fungicide from the cuticle into plant tissue is negligible within 24 hours after application of the formulation droplets to the leaf surface.

Semi-automated image segmentation has been demonstrated as a rapid and effective means to gather data on particle sizes and distributions on the leaf surface from microscopic images. These images and their analysis confirm and characterise a “coffee ring” effect active during the droplet drying on the cuticle surface.

The simplest viable model to explain the results for this case study involves a ‘wax reservoir’ approximation and uniform equilibration across the droplet-cuticle contact area, justified by strong overlap of diffusional zones around the suspended particles. This predicts that the transition between uptake regimes is a consequence of longitudinal cuticle saturation with continuous uptake occurring by radial diffusion. This is consistent with the majority of uptake occurring beneath the coffee ring, even after drying. We further predict that an initial rapid uptake regime is universal to such formulations and shall closely follow the Shoup-Szabo equation and that this has been underappreciated by the literature. The predicted results for the cuticular diffusion coefficient and saturation concentration are within expectations, helping to validate this model.

This chapter concludes this thesis’ investigation into the foliar uptake of lipophilic pesticides from the perspective of diffusional processes. We have provided a model and relevant simulation results for considering uptake on the scale of individual particles on a diffusional barrier membrane in Chapter 5 and, in this chapter, we have considered the processes involved for a particular case study and developed a simple, generalisable model on the droplet scale which explains experimental results. While future work is required to build a comprehensive understanding of foliar uptake, the models described in these two chapters, and the results they predict, cover the influence of diffusional processes on the uptake behaviour of particulate systems beyond what has been presented in literature, and thus are highly valuable for further study.

References

1. Elliott, J. R.; Cortvriend, J.; Depietra, G.; Brennan, C.; Compton, R. G., Kinetics of Lipophilic Pesticide Uptake by Living Maize. *ACS Agricultural Science & Technology* **2023,** *3* (5), 445-454.
2. Shaner, D. L.; Beckie, H. J., The future for weed control and technology. *Pest Management Science* **2014,** *70* (9), 1329-1339.
3. Schreiber, L., Review of sorption and diffusion of lipophilic molecules in cuticular waxes and the effects of accelerators on solute mobilities. *Journal of Experimental Botany* **2006,** *57* (11), 2515-2523.
4. Kirkwood, R. C., Recent developments in our understanding of the plant cuticle as a barrier to the foliar uptake of pesticides. *Pesticide Science* **1999,** *55* (1), 69-77.
5. Köhler, H.; Triebskorn, R., Wildlife Ecotoxicology of Pesticides: Can We Track Effects to the Population Level and Beyond? *Science* **2013,** *341* (6147), 759-765.
6. Malaj, E.; von der Ohe, P. C.; Grote, M.; Kühne, R.; Mondy, C. P.; Usseglio-Polatera, P.; Brack, W.; Schäfer, R. B., Organic chemicals jeopardize the health of freshwater ecosystems on the continental scale. *Proceedings of the National Academy of Sciences* **2014,** *111* (26), 9549-9554.
7. Bradberry, S. M.; Proudfoot, A. T.; Vale, J. A., Poisoning Due to Chlorophenoxy Herbicides. *Toxicological Reviews* **2004,** *23* (2), 65-73.
8. de Perre, C.; Williard, K. W. J.; Schoonover, J. E.; Young, B. G.; Murphy, T. M.; Lydy, M. J., Assessing the fate and effects of an insecticidal formulation. *Environmental Toxicology and Chemistry* **2015,** *34* (1), 197-207.
9. Jones, K. C.; Keating, T.; Diage, P.; Chang, A. C., Transport and Food Chain Modeling and Its Role in Assessing Human Exposure to Organic Chemicals. *Journal of Environmental Quality* **1991,** *20* (2), 317-329.
10. McKone, T. E.; Ryan, P. B., Human exposures to chemicals through food chains: an uncertainty analysis. *Environmental science & technology* **1989,** *23* (9), 1154-1163.
11. Nzengung, V. A.; Jeffers, P., Sequestration, Phytoreduction, and Phytooxidation of Halogenated Organic Chemicals by Aquatic and Terrestrial Plants. *International Journal of Phytoremediation* **2001,** *3* (1), 13-40.
12. Buchholz, A., Characterization of the diffusion of non-electrolytes across plant cuticles: properties of the lipophilic pathway. *Journal of Experimental Botany* **2006,** *57* (11), 2501-2513.
13. Kerstiens, G., Plant Cuticles — an Integrated Functional Approach. *Journal of Experimental Botany* **1996,** *47*, 50-60.
14. Li, H.; Sheng, G.; Chiou, C. T.; Xu, O., Relation of Organic Contaminant Equilibrium Sorption and Kinetic Uptake in Plants. *Environmental Science & Technology* **2005,** *39* (13), 4864-4870.
15. Knowles, A., Recent developments of safer formulations of agrochemicals. *The Environmentalist* **2008,** *28* (1), 35-44.
16. Chen, C.; Guo, W.; Ngo, H. H., Pesticides in stormwater runoff—A mini review. *Frontiers of Environmental Science & Engineering* **2019,** *13* (5), 72.
17. Legind, C. N.; Kennedy, C. M.; Rein, A.; Snyder, N.; Trapp, S., Dynamic plant uptake model applied for drip irrigation of an insecticide to pepper fruit plants. *Pest Management Science* **2011,** *67* (5), 521-527.
18. Rein, A.; Legind, C. N.; Trapp, S., New concepts for dynamic plant uptake models. *SAR and QSAR in Environmental Research* **2011,** *22* (1-2), 191-215.

19. Grafahrend-Belau, E.; Junker, A.; Eschenröder, A.; Müller, J.; Schreiber, F.; Junker, B. H., Multiscale Metabolic Modeling: Dynamic Flux Balance Analysis on a Whole-Plant Scale *Plant Physiology* **2013,** *163* (2), 637-647.
20. Trapp, S., Plant uptake and transport models for neutral and ionic chemicals. *Environmental Science and Pollution Research* **2004,** *11* (1), 33-39.
21. Mercer, G. N., A simple diffusion model of the effect of droplet size and spread area on foliar uptake of hydrophilic compounds. *Pesticide Biochemistry and Physiology* **2007,** *88* (2), 128-133.
22. Pecha, J.; Fürst, T.; Kolomazník, K.; Friebrová, V.; Svoboda, P., Protein biostimulant foliar uptake modeling: The impact of climatic conditions. *AIChE Journal* **2012,** *58* (7), 2010-2019.
23. Riederer, M.; Daiß, A.; Gilbert, N.; Köhle, H., Semi-volatile organic compounds at the leaf/atmosphere interface: numerical simulation of dispersal and foliar uptake. *Journal of Experimental Botany* **2002,** *53* (375), 1815-1823.
24. Tredenick, E. C.; Farrell, T. W.; Forster, W. A.; Psaltis, S. T. P., Nonlinear Porous Diffusion Modeling of Hydrophilic Ionic Agrochemicals in Astomatous Plant Cuticle Aqueous Pores: A Mechanistic Approach. *Frontiers in Plant Science* **2017,** *8*, 746.
25. Tredenick, E. C.; Farrell, T. W.; Forster, W. A., Mathematical Modeling of Diffusion of a Hydrophilic Ionic Fertilizer in Plant Cuticles: Surfactant and Hygroscopic Effects. *Frontiers in Plant Science* **2018,** *9*, 1888.
26. Tredenick, E. C.; Farrell, T. W.; Forster, W. A., Mathematical Modelling of Hydrophilic Ionic Fertiliser Diffusion in Plant Cuticles: Lipophilic Surfactant Effects. *Plants* **2019,** *8* (7), 202.
27. Zabkiewicz, J. A., Spray formulation efficacy—holistic and futuristic perspectives. *Crop Protection* **2007,** *26* (3), 312-319.
28. Hazra, D. K.; Karmakar, R.; Poi, R.; Bhattacharya, S.; Mondal, S., Recent advances in pesticide formulations for eco-friendly and sustainable vegetable pest management: A review. *Archives of Agriculture and Environmental Science* **2017,** *2* (3), 232-237.
29. Vurro, M.; Miguel-Rojas, C.; Pérez-de-Luque, A., Safe nanotechnologies for increasing the effectiveness of environmentally friendly natural agrochemicals. *Pest Management Science* **2019,** *75* (9), 2403-2412.
30. Hazra, D. K.; Purkait, A., Role of pesticide formulations for sustainable crop protection and environment management: A review. *J Pharmacogn Phytochem* **2019,** *8* (2), 686-693.
31. Elliott, J. R.; Compton, R. G., Modeling Transcuticular Uptake from Particle-Based Formulations of Lipophilic Products. *ACS Agricultural Science & Technology* **2022,** *2* (3), 603-614.
32. Cox, D. R., *Planning of Experiments*. Wiley: 1992.
33. Schindelin, J.; Arganda-Carreras, I.; Frise, E.; Kaynig, V.; Longair, M.; Pietzsch, T.; Preibisch, S.; Rueden, C.; Saalfeld, S.; Schmid, B.; Tinevez, J.-Y.; White, D. J.; Hartenstein, V.; Eliceiri, K.; Tomancak, P.; Cardona, A., Fiji: an open-source platform for biological-image analysis. *Nature Methods* **2012,** *9* (7), 676-682.
34. Rueden, C. T.; Schindelin, J.; Hiner, M. C.; DeZonia, B. E.; Walter, A. E.; Arena, E. T.; Eliceiri, K. W., ImageJ2: ImageJ for the next generation of scientific image data. *BMC Bioinformatics* **2017,** *18* (1), 529.
35. Arganda-Carreras, I.; Kaynig, V.; Rueden, C.; Eliceiri, K. W.; Schindelin, J.; Cardona, A.; Sebastian Seung, H., Trainable Weka Segmentation: a machine learning tool for microscopy pixel classification. *Bioinformatics* **2017,** *33* (15), 2424-2426.
36. Glover, B. J., Differentiation in plant epidermal cells. *Journal of Experimental Botany* **2000,** *51* (344), 497-505.

37. Wang, C. J.; Liu, Z. Q., Foliar uptake of pesticides—Present status and future challenge. *Pesticide Biochemistry and Physiology* **2007,** *87* (1), 1-8.
38. Staiger, S.; Seufert, P.; Arand, K.; Burghardt, M.; Popp, C.; Riederer, M., The permeation barrier of plant cuticles: uptake of active ingredients is limited by very long-chain aliphatic rather than cyclic wax compounds. *Pest Management Science* **2019,** *75* (12), 3405-3412.
39. Roth-Nebelsick, A., Computer-based Studies of Diffusion through Stomata of Different Architecture. *Annals of Botany* **2007,** *100* (1), 23-32.
40. Burkhardt, J.; Basi, S.; Pariyar, S.; Hunsche, M., Stomatal penetration by aqueous solutions – an update involving leaf surface particles. *New Phytologist* **2012,** *196* (3), 774-787.
41. Fernández, V.; Gil-Pelegrín, E.; Eichert, T., Foliar water and solute absorption: an update. *The Plant Journal* **2021,** *105* (4), 870-883.
42. Holloway, P. J. In *Plant Cuticles: Physicochemical Characteristics and Biosynthesis*, Berlin, Heidelberg, Springer Berlin Heidelberg: Berlin, Heidelberg, 1994; pp 1-13.
43. http://www.chemspider.com. (accessed Jan 3 2023).
44. Mampallil, D.; Eral, H. B., A review on suppression and utilization of the coffee-ring effect. *Advances in Colloid and Interface Science* **2018,** *252*, 38-54.
45. Deegan, R. D.; Bakajin, O.; Dupont, T. F.; Huber, G.; Nagel, S. R.; Witten, T. A., Capillary flow as the cause of ring stains from dried liquid drops. *Nature* **1997,** *389* (6653), 827-829.
46. Eral, H. B.; 't Mannetje, D. J. C. M.; Oh, J. M., Contact angle hysteresis: a review of fundamentals and applications. *Colloid and Polymer Science* **2013,** *291* (2), 247-260.
47. Han, W.; Lin, Z., Learning from "Coffee Rings": Ordered Structures Enabled by Controlled Evaporative Self-Assembly. *Angewandte Chemie International Edition* **2012,** *51* (7), 1534-1546.
48. Einstein, A., Über die von der molekularkinetischen Theorie der Wärme geforderte Bewegung von in ruhenden Flüssigkeiten suspendierten Teilchen. *Annalen der Physik* **1905,** *322* (8), 549-560.
49. von Smoluchowski, M., Zur kinetischen Theorie der Brownschen Molekularbewegung und der Suspensionen. *Annalen der Physik* **1906,** *326* (14), 756-780.
50. Erbil, H. Y., Evaporation of pure liquid sessile and spherical suspended drops: A review. *Advances in Colloid and Interface Science* **2012,** *170* (1), 67-86.
51. Schönfeld, F.; Graf, K.-H.; Hardt, S.; Butt, H.-J., Evaporation dynamics of sessile liquid drops in still air with constant contact radius. *International Journal of Heat and Mass Transfer* **2008,** *51* (13), 3696-3699.
52. Weon, B. M.; Je, J. H., Self-Pinning by Colloids Confined at a Contact Line. *Physical Review Letters* **2013,** *110* (2), 028303.
53. Davies, T. J.; Compton, R. G., The cyclic and linear sweep voltammetry of regular and random arrays of microdisc electrodes: Theory. *Journal of Electroanalytical Chemistry* **2005,** *585* (1), 63-82.
54. Belding, S. R.; Compton, R. G., Transient Voltammetry at Electrodes Modified with a Random Array of Spherical Nanoparticles: Theory. *The Journal of Physical Chemistry C* **2010,** *114* (18), 8309-8319.
55. Sliusarenko, O.; Oleinick, A.; Svir, I.; Amatore, C., Validating a Central Approximation in Theories of Regular Electrode Electrochemical Arrays of Various Common Geometries. *Electroanalysis* **2015,** *27* (4), 980-991.
56. Fick, A., V. On liquid diffusion. *The London, Edinburgh, and Dublin Philosophical Magazine and Journal of Science* **1855,** *10* (63), 30-39.

57. Gavaghan, D. J., An exponentially expanding mesh ideally suited to the fast and efficient simulation of diffusion processes at microdisc electrodes. 1. Derivation of the mesh. *Journal of Electroanalytical Chemistry* **1998,** *456* (1), 1-12.
58. Rudolph, M., Digital Simulations on unequally spaced grids. Part 1. Critical remarks on using the point method by discretisation on a transformed grid. *Journal of Electroanalytical Chemistry* **2002,** *529*, 97-108.
59. Seeber, R.; Stefani, S., Explicit finite difference method in simulating electrode processes. *Analytical Chemistry* **1981,** *53* (7), 1011-1016.
60. Feldberg, S. W., Optimization of explicit finite-difference simulation of electrochemical phenomena utilizing an exponentially expanded space grid: Refinement of the Joslin-Pletcher algorithm. *Journal of Electroanalytical Chemistry and Interfacial Electrochemistry* **1981,** *127* (1), 1-10.
61. Alden, J. A.; Compton, R. G., A general method for electrochemical simulations. 1. Formulation of the strategy for two-dimensional simulations. *The Journal of Physical Chemistry B* **1997,** *101* (44), 8941-8954.
62. Compton, R. G.; Kätelhön, E.; Laborda, E.; Ward, K. R., *Understanding Voltammetry: Simulation of Electrode Processes*. Second ed.; World Scientific Europe: 2020.
63. Laasonen, P., Über eine Methode zur Lösung der Wärmeleitungs-gleichung. *Acta Mathematica* **1949,** *81*, 309-317.
64. Falgout, R. D.; Yang, U. M., hypre: A Library of High Performance Preconditioners. In *Computational Science — ICCS 2002*, Springer Berlin Heidelberg: Berlin, Heidelberg, 2002; Vol. 2331, pp 632-641.
65. Falgout, R. D.; Jones, J. E.; Yang, U. M., The Design and Implementation of hypre, a Library of Parallel High Performance Preconditioners. In *Numerical Solution of Partial Differential Equations on Parallel Computers*, Bruaset, A. M.; Tveito, A., Eds. Springer: Berlin, Heidelberg, 2006; Vol. 51, pp 267-294.
66. Cottrell, F. G., Der Reststrom bei galvanischer Polarisation, betrachtet als ein Diffusionsproblem. *Zeitschrift für Physikalische Chemie* **1903,** *42U* (1), 385-431.
67. Shoup, D.; Szabo, A., Chronoamperometric current at finite disk electrodes. *Journal of Electroanalytical Chemistry and Interfacial Electrochemistry* **1982,** *140* (2), 237-245.
68. Crank, J., *The Mathematics of Diffusion*. Clarendon Press: 1979.
69. Aoki, K.; Osteryoung, J., Diffusion-controlled current at the stationary finite disk electrode: Theory. *Journal of Electroanalytical Chemistry* **1981,** *122* (C), 19--35.
70. Bourgault, R.; Matschi, S.; Vasquez, M.; Qiao, P.; Sonntag, A.; Charlebois, C.; Mohammadi, M.; Scanlon, M. J.; Smith, L. G.; Molina, I., Constructing functional cuticles: analysis of relationships between cuticle lipid composition, ultrastructure and water barrier function in developing adult maize leaves. *Annals of Botany* **2019,** *125* (1), 79-91.
71. Kerler, F.; Schönherr, J., Accumulation of lipophilic chemicals in plant cuticles: Prediction from octanol/water partition coefficients. *Archives of Environmental Contamination and Toxicology* **1988,** *17* (1), 1-6.
72. Popp, C.; Burghardt, M.; Friedmann, A.; Riederer, M., Characterization of hydrophilic and lipophilic pathways of Hedera helix L. cuticular membranes: permeation of water and uncharged organic compounds. *Journal of Experimental Botany* **2005,** *56* (421), 2797-2806.
73. Shafer, W. E.; Schönherr, J., Accumulation and transport of phenol, 2-nitrophenol, and 4-nitrophenol in plant cuticles. *Ecotoxicology and Environmental Safety* **1985,** *10* (2), 239-252.
74. Satchivi, N. M.; Stoller, E. W.; Wax, L. M.; Briskin, D. P., A Nonlinear Dynamic Simulation Model for Xenobiotic Transport and Whole Plant Allocation Following Foliar

Application. I. Conceptual Foundation for Model Development. *Pesticide Biochemistry and Physiology* **2000,** *68* (2), 67-84.